Department of Mechanical Engineering

Factors Affecting the Development of Sprays Produced by Multihole Injectors for Direct-Injection Engine Applications

Ritsaert Zane van Romunde

This thesis is submitted for the fulfilment of the requirements for the Degree of Doctor of Philosophy

UCL

2011

I, Ritsaert Zane van Romunde confirm that the work presented in this thesis is my own. Where information has been derived from other sources, I confirm that this has been indicated in the thesis.

Abstract

The spray form development from a state of the art multi-hole injector for gasoline direct injection internal combustion engines is examined to attempt to determine the thermo-fluid dynamics affecting the spray development. The current state of knowledge regarding spray break-up and the interactivity of the factors on spray form are detailed. The spray under investigation was injected into purposely designed quiescent chambers to decouple the effects of the fluid mechanics on spray development from any in-engine effects. The pressure chambers, experimental apparatus and techniques used to characterise and measure the spray properties are described along with an assessment of any sources of variability in the measurement and analysis methodologies and hardware. Initial spray images of the spray produced by a range of multi-component "retail" fuels as well as single component non-oxygenated and oxygenated hydrocarbons with a range of boiling ranges and points for different injector body (and hence assumed fuel) temperatures and chamber gas pressures are presented. The experimental measurements show the strong interaction between the operational conditions in relation to the fuel properties and the physical spray form. A large amount of deviation from the nominal "ambient" spray form is observed for conditions where the fuel's bubble point (boiling temperature at given gas pressure) is exceeded by a multiple of 10, termed spray collapse. The dependence of a multi-component fuel on the boiling characteristics of its highest volatility components suggest that it is these components which drive the fuel spray development formation, which is further illustrated by comparing different single component fluids. This suggests that higher volatility fluids are better representatives of full range, multi-component fuels for modelling or other investigative work when a single component fuel is required to be used. The onset of spray collapse was found to be gradual with no sudden "threshold" condition at which collapse occurred, also illustrated by a gradual reduction in measured spray droplet size with increasing injector body temperature and/or reducing gas pressure. The physical factors affecting spray development and break-up, and their effects are examined including the fluid flow inside a real size transparent, optically accessed nozzle, illustrating the effect of cavitation supplying nucleation sites for the subsequent vaporisation of the fuel. The scales of local air turbulence are found to affect the local vapour concentration, and hence vaporisation rate, and hence the interaction of these factors is shown to determine the spray formation.

Acknowledgements

This work has only been made possible by the extremely generous support of a number of key people and organisations, the support from each which has been, and will always remain to be, hugely appreciated.

From an operations view, I would like to thank everyone at Jaguar Cars ltd, Shell Global Solutions, and the Engineering and Physical Sciences research Council (EPSRC) for making this project financially possible. In particular, thanks go to Stan Wallace, Steve Richardson, Xiang Dong Chen and Dave Richardson at Jaguar for providing the engine related hardware to the project, as well as project management and general communications. From Shell, Roger Cracknell and Harold Walsmey contributed the range of fuel blends, as well as expertise to bring this work together.

For all the mentoring and supervisory aspects, I have to start by thanking Paul Williams for initiating this project and generally getting me into this caper in the first place. In addition, everyone at UCL Department of Mechanical Engineering, both academic and workshop staff, deserve to be recognised for providing the academic background and craftsmanship to enable this project to succeed. Leeds University should also be thanked for their hospitality and use of facilities. The largest thanks should of course go to Pavlos Aleiferis, my supervisor for the majority of this work. Pavlos' perseverance and belief in me has made this possible, and I would very much like to thank him for all the time and effort he has personally devoted to enabling this work to be completed.

On a personal level, there are a huge number of "thank yous", which can only really be repaid by returning the favour, if that is at all possible: Firstly, my fantastic parents and brothers, for all the years of love and laughter; not to mention the generous financial support over many years, a few more than expected! Also, to all the great friends over the years, and especially in relation to this work to the chaps in "the hole", without whom the labs would certainly have been a less bright place. And lastly, to Harriet, to whom I owe more than these pages can ever tell.

As a small token of my humble thanks and love for you all, this work is dedicated to you all.

Table of Contents

1 Literature Survey 20
1.1 Introduction 20
1.1.1 Fuel Metering in Spark Ignition Engines 22
1.1.2 Gasoline Direct Injection Fuel Delivery Strategies 23
1.2 Fuel Injectors for Gasoline Direct Injection 25
1.2.1 Pressure Swirl Injectors 25
1.2.2 Multihole Injectors 27
1.3 Spray Development 28
1.3.1 Break-Up Mechanisms 29
1.4 Cavitation 34
1.4.1 Cavitation Number 35
1.4.2 In Nozzle Flow Visualisation 37
1.5 Spray Collapse 39
1.5.1 Flash Boiling 39
1.5.2 Spray Collapse 40
1.6 Objectives 41
2 Spray and Experimental Characterisation 44
2.1 Injector and Nominal Spray Form 44
2.1.1 Nozzle Geometry 47
2.1.2 Spray Wetted Footprint 48
2.1.3 Fuel Flow Rate 49
2.2 Optical Nozzle 50
2.2.1 Optical Nozzle Mounting 50
2.2.2 Optical Nozzle 52
2.3 Injector Control 57
2.3.1 Injection Hardware Variability 58
2.4 Pressure Chambers 60
2.4.1 Cylindrical Pressure Chamber 61
2.4.2 Octagonal Pressure Chamber 62
2.4.3 Chamber Optical Access Windows 66
2.4.4 Chamber Mounting 68
2.4.5 Chamber Condition Monitoring 69
2.4.6 Chamber Pressurisation System 69

2.4.7 Fuel System 71
2.4.8 Injector Mounting 73
2.5 Fuels Tested and Their Properties 76
2.6 Spray Characterisation Techniques 84
2.6.1 Shadowgraph Imaging 84
2.6.2 Schlieren Imaging 84
2.6.3 Mie Scattering Imaging 85
2.6.4 High Speed Imaging 86
2.6.5 Image processing 88
2.6.6 Droplet Sizing 94
2.6.7 Refractive Index 102
2.6.8 Comparison of Drop Size Measurements Obtained with Different Techniques 103
3 Spray Development 118
3.1 Experimental Conditions 118
3.1.1 Operating Conditions 118
3.1.2 Imaging 119
3.2 Global Spray Development 121
3.2.1 Standard Gasoline 121
3.2.2 Spray Collapse 126
3.2.3 Heavy Gasoline 130
3.2.4 *iso*-Octane 135
3.2.5 *n*-Pentane 140
3.2.6 Extreme Conditions 142
3.2.7 Spray Variability 145
3.2.8 Summary of Images Spray Development Trends 148
4 Spray Parameter Measurement 152
4.1 Spray Characteristic Parameter Measurement 152
4.1.1 Spray Plume Penetration 152
4.1.2 Spray Velocity 160
4.1.3 PDA Velocity Measurement 165
4.1.4 Spray Cone Angle 170
4.1.5 Base View Spray Areas 174
4.2 Droplet Sizing 176
4.2.1 Phase Doppler Anemometry 176

4.2.2 Laser Diffraction Droplet Sizing 186
4.2.3 Comparison of Results from Droplet Size Measurement Techniques 190
4.2.4 Summary of Drop Size Measurements 192
4.2.5 Correlation between Droplet Size and Velocity 194
4.2.6 Droplet Size Distribution Modelling 197
4.3 Summary 200
5 Spray Break-Up 202
5.1 Near Nozzle Imaging 202
5.1.1 Flash Bulb Illumination 203
5.1.2 Laser Sheet Illumination 210
5.1.3 Spray Development Relationship to Fuel Properties 217
5.1.4 Flash Boiling 219
5.2 Summary 220
6 Oxygenated Fuels 221
6.1 Fuel Selection 222
6.2 Spray Development 222
6.3 Comparison of Spray Characteristics 225
6.3.1 Spray Penetration 225
6.3.2 Spray Velocity 229
6.3.3 Spray Cone Angles 231
6.4 Summary 232
7 Cavitation 235
7.1 Cavitation 235
7.1.1 Cavitation Number 236
7.2 In-Nozzle Flow Imaging 239
7.2.1 In-Nozzle Flow Condition Matching 239
7.2.2 Cavitation Numbers of Experimental Nozzles 241
7.3 Imaging of Flow in Optical Nozzle 248
7.4 General Conclusions With Respect to Cavitation 264
7.4.1 Effect of Fuel Properties 265
7.5 Summary 267
8 Gas Turbulence Effect on Spray Development 269
8.1 Consideration of In-Cylinder Turbulence 269
8.2 Leeds Combustion Chamber 270
8.3 Spray Development in Turbulent Gas Body 272

8.3.1 Effect of Turbulence on Fuel Evaporation Rate 278
8.4 Spray Interaction with Turbulent Gas Motion 281
8.4.1 Stokes Number 282
8.4.2 Prediction of Turbulence Effect for Different Fuels 286
8.5 Spray Combustion 289
8.5.1 Flame Growth 292
8.6 Summary 295
9 Conclusions and Further Work 297
9.1 Factors Affecting Multihole Fuel Spray Development 297
9.1.1 In-Nozzle Flow 299
9.1.2 Spray Break-Up 299
9.1.3 Spray Formation 300
9.1.4 Effect of Gas Turbulence 300
9.1.5 Biogenic Fuels 301
9.2 Further Work 301
9.2.1 Investigation of Biogenic Fuels 302
9.2.2 In-Nozzle Fuel Flow Visualisation 303
9.2.3 Spray Interaction with In-Cylinder Gas Turbulence 304
9.2.4 Fuel Spray Vaporisation Rate 305
9.3 Summary 306
10 References 308

Table of Figures

Figure 1-1 Schematic Representation of a Swirl Nozzle, Zhao et al [2002]..... 26
Figure 1-2 Spray Break-Up Mechanisms – (A) Rayleigh Regime, (B) Wind-Induced Regime , (C) Atomisation Regime..... 30
Figure 1-3 Spray Break-Up Regimes..... 32
Figure 1-4 Anatomy of Break-Up of Full Cone Spray, Baumgarten [2006] 33
Figure 2-1 Spray Definition for Project Injectors 45
Figure 2-2 Model Image of Injector and Nominal Spray..... 46
Figure 2-3 Spray Plume Nominal Angles 46
Figure 2-4 Backlit Nozzle Hole Showing Inner and Outer Orifices..... 47
Figure 2-5 Diagram of Nozzle Geometry 48
Figure 2-6 Injector Manufacturer Measured Fuel Distribution..... 49
Figure 2-7 Injector Stem, Pintle and Attachment Ring..... 50
Figure 2-8 Mounted Injector with Removable Stem 51
Figure 2-9 Injector with Stem and Pintle Removed..... 51
Figure 2-10 Optical Nozzle Adaptor..... 52
Figure 2-11 Optical Nozzle Adaptor Attached to Injector Body and Pintle..... 52
Figure 2-12 Optical Nozzle Blank Attached to Adaptor and Injector 53
Figure 2-13 Optical Injector and Mounting Assembly 54
Figure 2-14 Optical Injector and Nozzle Blank in-situ In Pressure Chamber 54
Figure 2-15 Initial Optical Nozzle Design Showing Bowl Cut-Out..... 55
Figure 2-16 Development of Optical Nozzle Showing Groove..... 56
Figure 2-17 CAD Drawings of Nozzle A (d=0.5 mm) and Nozzle B (d=0.2 mm) 56
Figure 2-18 Injector Trigger Circuit 57
Figure 2-19 Trigger and Injector Pulses..... 59
Figure 2-20 Probability of Fuel at Injector Tip. 60
Figure 2-21 Cylindrical Pressure Chamber Dimensions..... 61
Figure 2-22 Cylindrical Pressure Chamber..... 62
Figure 2-23 Schematic Diagram of Octagonal Pressure Chamber Showing Multi Technique Analysis Capabilities..... 64
Figure 2-24 Octagonal Pressure Chamber 65
Figure 2-25 Photographs of Octagonal Pressure Chamber..... 65
Figure 2-26 Variable Angle Window..... 67
Figure 2-27 Variable Angle Window Components 68
Figure 2-28 Schematic of Fuel Separation and Evacuation System 70

Figure 2-29 Schematic of Air Control Unit 72
Figure 2-30 Image showing Cylindrical Pressure Chamber and Schematic of Injector Mounting 74
Figure 2-31 Schematic of Injector and Mounting 75
Figure 2-32 Schematic of Cylindrical Pressure Chamber 76
Figure 2-33 Distillation Curves for Fuels Tested in this Work 81
Figure 2-34 Fuel Vapour Pressures 81
Figure 2-35 Graph of Bubble Point Pressures for Fuels 83
Figure 2-36 Graph of Dew Point Pressures for Fuels 83
Figure 2-37 Schematic of Schlieren Imaging Technique 85
Figure 2-38 Schematic of High Speed Imaging Equipment 86
Figure 2-39 Plume Penetration Length Measurement Variation with Threshold Value 90
Figure 2-40 Normalised Plume Penetration Variation with Threshold Value 91
Figure 2-41 Spray Detection and Measurement Methodology 93
Figure 2-42 Effect of Droplet Size on Scattering Angle 95
Figure 2-43 Spray Separator 97
Figure 2-44 Schematic Representation of Light Reflection and Refraction of a Spherical Droplet 99
Figure 2-45 Droplet Size Measurement Validation Rig 104
Figure 3-1 Spray Development Standard Gasoline 20 °C 1.0 bar 122
Figure 3-2 Spray Development Standard Gasoline 120 °C 0.5 bar 123
Figure 3-3 Spray Development Standard Gasoline 120 °C 1.0 bar 124
Figure 3-4 Spray Development Standard Gasoline 120 °C 5.0 bar 125
Figure 3-5 Different Views of Nominal and Collapsed Spray Form 128
Figure 3-6 Standard Gasoline, 777 µs ASOI 129
Figure 3-7 Spray Development Heavy Gasoline 20 °C 1.0 bar 131
Figure 3-8 Spray Development Heavy Gasoline 120 °C 0.5 bar 132
Figure 3-9 Spray Development Heavy Gasoline 120 °C 1.0 bar 133
Figure 3-10 Heavy Gasoline, 777 µs ASOI 134
Figure 3-11 Spray Development *iso*-Octane 20 °C 1.0 bar 136
Figure 3-12 Spray Development *iso*-Octane 120 °C 0.5 bar 137
Figure 3-13 Spray Development *iso*-Octane 120 °C 1.0 bar 138
Figure 3-14 *iso*-Octane, 777 µs ASOI 139
Figure 3-15 *n*-Pentane, 777 µs ASOI 141
Figure 3-16 High Temperature Spray Development: Standard Gasoline, 0.3 bar 142

Figure 3-17 High Temperature Spray Development: *iso*-Octane, 0.3 bar 143
Figure 3-18 High Temperature Spray Development: *n*-Pentane, 0.3 bar 144
Figure 3-19 Mean and RMS Spray Images at 777 μs ASOI for 20 °C Fuel Temperature, 1.0 bar Gas Pressure 147
Figure 3-20 Mean and RMS Spray Images at 777 μs ASOI: 120 °C, 0.5 bar 148
Figure 3-21 Global Spray Form for All Fuels – 1.0 bar Gas Pressure 150
Figure 3-22 Global Spray Form for All Fuels – 0.5 bar Gas Pressure 151
Figure 4-1 Spray Plume Penetration: 20 °C, 1.0 bar 153
Figure 4-2 Spray Plume Penetration: 20 °C, 0.5 bar 154
Figure 4-3 Spray Plume Penetration: 20 °C, 5.0 bar 154
Figure 4-4 Spray Plume Penetration: 90°C, 1.0 bar 155
Figure 4-5 Spray Plume Penetration: 120°C, 1.0 bar 156
Figure 4-6 Spray Plume Penetration: 90 °C, 0.5 bar 157
Figure 4-7 Spray Plume Penetration: 120 °C, 0.5 bar 158
Figure 4-8 Spray Plume Penetration: 120 °C, 5.0 bar 159
Figure 4-9 Spray Tip Velocity: 20 °C, 1.0 bar 161
Figure 4-10 Spray Tip Velocity: 120 °C, 0.5 bar 162
Figure 4-11 Spray Tip Velocity: 120 °C, 1.0 bar 162
Figure 4-12 Spray Tip Velocity for Standard Gasoline 163
Figure 4-13 Spray Tip Velocity for *iso*-Octane 165
Figure 4-14 Plume 6 Droplet Velocity: *iso*-Octane 20 °C, 1.0 bar PDA 167
Figure 4-15 Plume 6 Droplet Velocity: *iso*-Octane 20 °C, 0.5 bar PDA 168
Figure 4-16 Plume 6 Droplet Velocity: *iso*-Octane 120 °C, 1.0 bar PDA 169
Figure 4-17 Plume 6 Droplet Velocity: *iso*-Octane 120 °C, 0.5 bar PDA 170
Figure 4-18 Measure of Spray Cone Angle (End View) 172
Figure 4-19 Overall Spray Cone Angle: 0.5 bar Gas Pressure, End View 173
Figure 4-20 Base View Spray Area Normalised to Engine Bore 175
Figure 4-21 PDA Droplet Measurement Location 177
Figure 4-22 PDA Drop Size Characteristics (Standard Gasoline, 20 °C, 1.0 bar) 178
Figure 4-23 PDA Droplet Sizes with Instantaneous Mean over Injection Duration (Standard Gasoline, 20 °C, 1.0 bar) 179
Figure 4-24 PDA Droplet Sizes with Instantaneous Mean over Injection Duration (Standard Gasoline, 120 °C, 1.0 bar) 180
Figure 4-25 PDA Droplet Sizes with Instantaneous Mean over Injection Duration (Standard Gasoline, 120 °C, 0.5 bar) 180

Figure 4-26 PDA Droplet Sizes with Instantaneous Mean over Injection Duration (*iso*-Octane, 20 °C, 1.0 bar) 181
Figure 4-27 PDA Droplet Sizes with Instantaneous Mean over Injection Duration (*iso*-Octane, 120 °C, 1.0 bar) 182
Figure 4-28 PDA Droplet Sizes with Instantaneous Mean over Injection Duration (*iso*-Octane, 120 °C, 0.5 bar) 182
Figure 4-29 PDA Droplet Sizes with Instantaneous Mean over Injection Duration (*n*-Pentane, 20 °C, 1.0 bar) 183
Figure 4-30 PDA Droplet Sizes with Instantaneous Mean over Injection Duration (*n*-Pentane, 120 °C, 1.0 bar) 184
Figure 4-31 PDA Droplet Sizes with Instantaneous Mean over Injection Duration (*n*-Pentane, 120 °C, 0.5 bar) 184
Figure 4-32 Collated Mean Trend Lines for PDA droplet sizing over Injection Duration for Range of Experimental Conditions 186
Figure 4-33 Laser Diffraction Technique Spray Droplet Size Measurement Locations 187
Figure 4-34 Laser Diffraction Droplet Size Measurements at Different Locations (1.0 bar Gas Pressure) 188
Figure 4-35 Laser Diffraction Droplet Size Measurements at Different Locations (0.5 bar Gas Pressure) 189
Figure 4-36 Sauter Mean Diameters - Standard Gasoline 191
Figure 4-37 Sauter Mean Diameters - *iso*-Octane 192
Figure 4-38 Sauter Mean Diameters - *n*-Pentane 192
Figure 4-39 Droplet Velocity with Respect to Size: *iso*-Octane 20 °C, 1.0 bar 195
Figure 4-40 Droplet Velocity with Respect to Size: iso-Octane 20 °C, 0.5 bar 195
Figure 4-41 Droplet Velocity with Respect to Size: iso-Octane 120 °C, 1.0 bar 196
Figure 4-42 Droplet Velocity with Respect to Size: iso-Octane 120 °C, 0.5 bar 197
Figure 4-43 SMD Drop Sizes Calculated From Eq. 4.1, 0.5 bar Gas Pressure 198
Figure 4-44 SMD Drop Sizes Calculated From Eq. 4.1, 1.0 bar Gas Pressure 199
Figure 4-45 SMD Drop Sizes Calculated From Eq. 4.1, 5.0 bar Gas Pressure 199
Figure 5-1 High Magnification Imaging of Very Early Spray Development 204
Figure 5-2 Standard Gasoline, High Speed, High Magnification Imaging 206
Figure 5-3 Heavy Gasoline, High Speed, High Magnification Imaging 207
Figure 5-4 *iso*-Octane, High Speed, High Magnification Imaging 208
Figure 5-5 *n*-Pentane, High Speed, High Magnification Imaging 209

Figure 5-6 Spray at Injector Nozzle with Laser Sheet Illumination 211
Figure 5-7 Schematic of Laser Sheet Illuminated High Magnification Imaging Set-Up 212
Figure 5-8 Laser Sheet Illumination, Standard Gasoline 213
Figure 5-9 Laser Sheet Illumination, Heavy Gasoline 214
Figure 5-10 Laser Sheet Illumination, *iso*-Octane 215
Figure 6-1 Butanol, 777 μs ASOI 223
Figure 6-2 Ethanol, 777 μs ASOI 224
Figure 6-3 Oxygenated and Non-Oxygenated Fuels: Plume Penetration: 20 °C, 0.5 bar 226
Figure 6-4 Oxygenated and Non-Oxygenated Fuels: Plume Penetration: 20 °C, 1.0 bar 226
Figure 6-5 Oxygenated and Non-Oxygenated Fuels: Plume Penetration: 90 °C, 0.5 bar 227
Figure 6-6 Oxygenated and Non-Oxygenated Fuels: Plume Penetration: 90°C, 1.0 bar 227
Figure 6-7 Oxygenated and Non-Oxygenated Fuels: Plume Penetration: 120 °C, 0.5 bar 228
Figure 6-8 Oxygenated and Non-Oxygenated Fuels: Plume Penetration: 120°C, 1.0 bar 228
Figure 6-9 Spray Tip Velocity: 20 °C, 1.0 bar 229
Figure 6-10 Spray Tip Velocity: 120 °C, 0.5 bar 230
Figure 6-11 Spray Tip Velocity: 120 °C, 1.0 bar 230
Figure 6-12 Overall Spray Cone Angles – Side View 232
Figure 6-13 Summary of Fuel Sprays under Range of Test Conditions 234
Figure 7-1 Graph of Flow Rate vs. Back Pressure (Gilles-Birth [2006]) with Current Work Super-Imposed 238
Figure 7-2 Flow Reynolds Numbers Optical Nozzles A and B 240
Figure 7-3 Experimental Cavitation Numbers (Ca Eq.7.1), Nozzle A 242
Figure 7-4 Experimental Cavitation Numbers (CN Eq.7.2), Nozzle A, 0.5 bar 243
Figure 7-5 Experimental Cavitation Numbers (CN Eq.7.2), Nozzle A, 1.0 bar 243
Figure 7-6 Experimental Cavitation Numbers (Ca Eq.7.1), Nozzle B 244
Figure 7-7 Experimental Cavitation Numbers (CN Eq.7.2), Nozzle B, 0.5 bar 244
Figure 7-8 Experimental Cavitation Numbers (CN Eq.7.2), Nozzle B, 1.0 bar 245
Figure 7-9 Weber Number (liquid) Nozzle A 246

Figure 7-10 Weber Number (liquid) Nozzle B 246
Figure 7-11 Ohnesorge Number Nozzle A 247
Figure 7-12 Ohnesorge Number Nozzle B 247
Figure 7-13 Ohnesorge Diagram Nozzle A 248
Figure 7-14 Ohnesorge Diagram Nozzle B 248
Figure 7-15 Nozzle A Fuel Flow, 30 bar Fuel Pressure, Standard Gasoline 251
Figure 7-16 In-Nozzle Fuel Flow, Standard Gasoline 254
Figure 7-17 In-Nozzle Fuel Flow, *iso*-Octane 255
Figure 7-18 In-Nozzle Fuel Flow, *n*-Pentane 256
Figure 7-19 In-Nozzle Fuel Flow, Butanol 257
Figure 7-20 In-Nozzle Fuel Flow, Ethanol 258
Figure 8-1 Photograph of Leeds University Combustion Bomb 271
Figure 8-2 Effect of turbulence on spray – 0.5 bar 273
Figure 8-3 Effect of turbulence on spray – 5.0 bar 274
Figure 8-4 Effect of Turbulence on Spray Penetration; Standard Gasoline, 120 °C, 5.0 bar 276
Figure 8-5 Effect of Turbulence on Spray Penetration; Standard Gasoline, 120 °C, 0.5 bar 277
Figure 8-6 Projected Spray Volume Cone 278
Figure 8-7 Evaporated Fuel Mass, 120 °C, 0.5 bar 280
Figure 8-8 Evaporated Fuel Mass, 120 °C, 5.0 bar 280
Figure 8-9 Integral Length Stokes Numbers for Gasoline Sprays 284
Figure 8-10 Probability of Droplet Clustering in relation to Stokes Number (Generalised) 285
Figure 8-11 Integral Scale Stokes Numbers for Injector Body Temperatures at u' = 2 m/s (1.0 and 5.0 bar) 287
Figure 8-12 Integral Scale Stokes Numbers for Injector Body Temperatures at u' = 2 m/s (0.5 bar) 287
Figure 8-13 Integral Scale Stokes Numbers for Injector Body Temperatures at u' = 4 m/s (1.0 and 5.0 bar) 288
Figure 8-14 Integral Scale Stokes Numbers for Injector Body Temperatures at u' = 4 m/s (0.5 bar) 288
Figure 8-15 Injection and Spray Combustion Images 291
Figure 8-16 Flame Radius 292

Figure 8-17 Flame speeds of *iso*-Octane-air mixtures at □ = 1.2, near atmospheric conditions and at different flame radii. Inset: the corresponding schlieren images at radius of approximately 48mm (Reproduced from Lawes *et al.* [2006]) 293
Figure 8-18 Flame Speed of Standard Gasoline Spray at □ = 0.8 294
Figure 9-1 Functional Relationships between Factors Affecting Spray Development. 298

Table of Tables

Table 2-1 Composition of Multi-Component Model Fuel (Fuel 3) 78
Table 2-2 Selected Fuel Properties for Gasoline and Single Component Fuels (Kaye [1995], Yaws [2006]) 80
Table 2-3 Fuel Boiling Characteristics 82
Table 2-4 Threshold Values for Average Background Pixel Intensity 92
Table 2-5 TSI PDA System Settings 102
Table 2-6 Refractive Index Values for Fuels 103
Table 2-7 Comparison of Droplet Measurements 104
Table 3-1 Test Matrix 119
Table 6-1 Properties of Oxygenated (Alcohol) Fuels 221
Table 6-2 Fuel Boiling Characteristics 233

Nomenclature

Abbreviations

AFR	Air-Fuel Ratio
ASOI	After Start of Injection
ATDC	After Top Dead Centre
BTDC	Before Top Dead Centre
BDC	Bottom Dead Centre
CA	Crank Angle
CAD	Computer Aided Design
CCD	Charge-Coupled Device
Ca	Cavitation Number
CN	Cavitation Number (alternative formulation)
CFD	Computational Fluid Dynamics
DI	Direct Injection
EVC	Exhaust Valve Closed
EVO	Exhaust Valve Open
FSTF	Fuel System Test Facility
ICE	Internal Combustion Engine
IMEP	Indicated Mean Effective Pressure
IVC	Intake Valve Closed
IVO	Intake Valve Open
LDA	Laser Doppler Anemometry
Nd:YLF	Neodymium: Yttrium Lithium Fluoride
Oh	Ohnesorge Number
PDA	Phase Doppler Anemometry
PDPA	Phase Doppler Particle Analyzer
PFI	Port Fuel Injection
PIV	Particle Image Velocimetry
PPI	Probability Presence Image
QPLIF	Quantitative Planar Laser Induced Fluorescence
Re	Reynolds Number
RMS	Root Mean Squared
RVP	Reid Vapour Pressure
SMD	Sauter Mean Diameter
SOF	Start of Fuel

SOI	Start of Injection
St	Stokes Number
TDC	Top Dead Centre
UCL	University College London
uHC	Unburned Hydro-Carbons
We	Weber Number
WOT	Wide-Open-Throttle
WWMP	World-Wide-Mapping-Point

Symbols

D	Nozzle hole diameter [m]
p	Pressure [Pa]
u	Velocity component [m/s]

Greek letters

μ	Dynamic viscosity [(N s)/m^2]
ρ	Density [kg/m^3]
σ	Surface tension [N/m]
Φ	Equivalence ratio

Subscripts and Superscripts

Cr	Critical
g	gas
l	liquid
vap	vapour

Graph Nomenclature

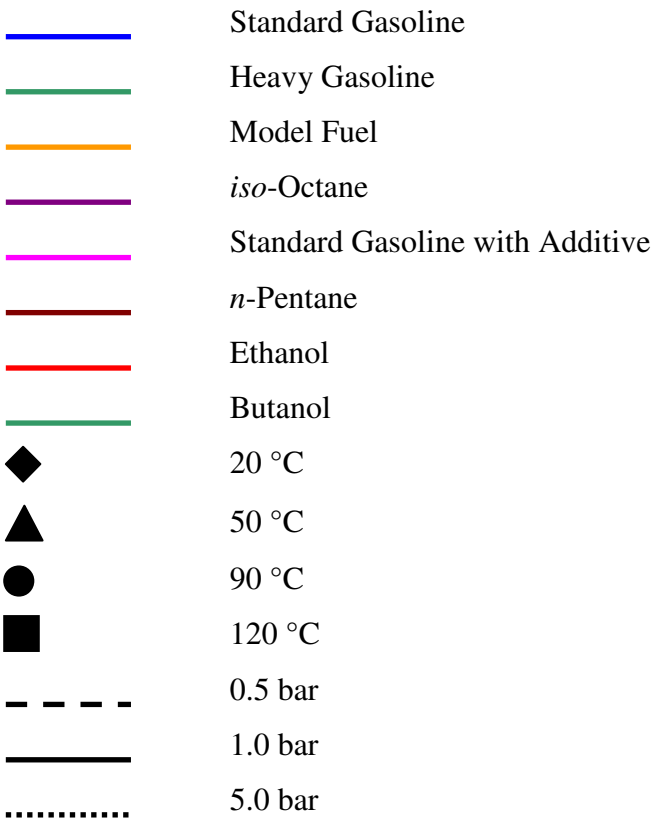

1 Literature Survey

1.1 Introduction

Since its inception and demonstration in the latter half of the 19th century, the internal combustion engine (ICE) has provided convenient, affordable and reliable conversion of chemical energy into motive power. Due to these benefits its application to personal transport has provided mobility to billions of people around the world. The popularity of the engine has led to its continual development in search of increased performance through the more efficient combustion of the fuel.

Whilst a number of concepts exist for the cycle of events leading to the conversion of the fuel chemical energy to motion, all ICEs have in common that this conversion occurs through the combustion of fuel. The real world demands placed on engines has led to the widespread deployment of the four stoke engine, whereby the piston makes 4 passes along the cylinder axis for each power cycle. In brief, fluids are "sucked" into the cylinder in the induction stroke through the open valve(s) by the motion of the piston away from the valve(s); the fluids are compressed against a sealed cylinder by the motion of the piston towards the closed valve(s) during the compression stroke; the compressed fluid mixture is ignited and combusts forcing the piston away from the valve(s) during the expansion stroke; and finally the exhaust gases are expelled from the chamber through the exhaust valve(s) by the motion of the piston back towards the valve(s) during the exhaust stroke. This entire process takes place in a small fraction of a second. To further complicate the situation, the completeness of combustion and its rate, which determine the engine performance and composition of the exhaust gases, is dependant on the relative amounts of fuel and air, and the quality of their mixing. Therefore, extremely close control is required over these parameters to ensure the desired engine performance.

While the use of gaseous fuels is widespread in ICEs, especially for stationary electric power generation, the higher energy density of liquid fuels as well as their convenience

of storage and distribution have made their use in mobile applications near universal. Traditionally, these fuels have been derived from fossil-fuel sources. However, due to current concerns over the environmental impact and availability of fossil fuels, the use of fuels derived from biogenic sources is currently being examined commercially and by the engine research community (*e.g.* Balabin *et al*. [2007], Aleiferis *et al*. [2008]). In all cases, the mixing and combustion demands by the engine will continue to be of paramount importance to the efficient use of fuel resources.

For liquid fuelled engines, the requirements for suitable charge metering and mixing may be achieved by a number of different methods. Likewise, the energy required to ignite the fuel and initiate combustion may either be provided by the pressure (and associated temperature) rise caused by the compression of the chamber contents in a compression ignition ("Diesel") engine, or by an electronically produced spark in a spark ignition (SI, gasoline) engine. In modern diesel engines, named after the inventor of the compression ignition engine Dr. Rudolf Diesel, the fuel is injected directly into the combustion chamber during the compression stroke. To enable a sufficient compression-induced temperature rise to ignite the fuel, the compression ratio for diesel engines is required to be high, increasing the thermal efficiency of the engine. A high compression ratio is only possible, however, due to the direct injection of the fuel into the combustion chamber at the desired time just prior to ignition, as any pre-mixed air/fuel mixture would auto-ignite prematurely, causing performance and physical degradation. Whilst diesel engine operation offers many combustion efficiency advantages, these also carry associated penalties such as poor transient performance and limited engine speed due to the time required for the in-cylinder mixing prior to ignition.

By metering the air and fuel mixtures prior to induction into the cylinder and independently controlling ignition through the timing of the spark event, traditional spark ignition, gasoline engines operating on the Otto Cycle do not have the constraints associated with the diesel engine. However, these benefits carry the penalty of a reduction in thermal efficiency. An imperfect balance between the air and fuel entering the engine commonly also results in high exhaust gas emissions. Whilst these exhaust emissions can be successfully captured and converted using catalysts in the exhaust system, the lower efficiency of the spark ignition engine relative to the compression ignition engine has increasing implications at the current time of resource and

environmental awareness. Today, both compression-ignition and spark-ignition engines compete in the automotive market on their relative merits.

1.1.1 Fuel Metering in Spark Ignition Engines

Initial attempts were made to overcome some of the inherent difficulties in fuel metering in spark ignition engines by the use of ever increasingly complex designs of carburettor; whereby the fuel is induced into the airflow by the depression occurring as the inducted air flows through a venturi. More recently, the mass production of compact electronics has allowed for the low pressure injection of fuel into the airflow, most commonly onto the back of the hot intake valves (known as port fuel injection, PFI) to aid fuel vaporisation and hence mixing. Both of these techniques, however, require the throttling of the intake air to meter the mixed fuel-air charge volume entering the engine (and hence the engine power), imparting a parasitic load on the engine. Furthermore, as mixing occurs outside of the cylinder, and hence prior to the power stroke for which the charge is required, neither of these techniques allow perfect accuracy in metering of the air-fuel ratio (AFR) from engine cycle to cycle. Both techniques also necessitate that the entire combustion chamber is filled with the fuel-air mixture.

To counter these known drawbacks, as well as capitalise on the advantages of both spark ignition and compression ignition engines, the concept of a direct injection (DI) spark ignition engine has been developed. Initially developed for fighter aircraft during the Second World War and produced in small numbers for specialist applications by both Mercedes Benz and Ford in the 1950s – 1970s (Zhao [2002]), the high cost and immaturity of electronics for injectors and their control systems have until recently largely prevented this concept being explored further in research or production. In a direct injection spark ignition engine a metered volume of gasoline-type fuel is injected directly into the combustion chamber prior to spark ignition. By doing so, the exact quantity of fuel required for that cycle can be metered accurately, allowing for operation in different modes depending on the load demands on the engine. For low load operation, careful direction of the fuel spray injected late in the compression stroke just prior to ignition may be used to establish a region of suitable fuel concentration around the spark plug at time of ignition, whilst maintaining a very lean (low fuel concentration) mixture in the rest of the combustion chamber, known as stratified charge operation. Whilst a premixed spark ignition engine requires the entire chamber to be maintained at or near stoichiometry (14.1:1 AFR for most gasoline blends), a

much lower overall AFR of up to 25:1 can be maintained in a stratified charge operated DI engine, thereby minimising the volume of fuel required for engine operation and reducing combustion emissions. At high load operation, injection during the induction stroke may be used to fill the entire chamber with a homogeneously mixed charge at the time of ignition. By directly injecting the liquid spray into the inducted air early during the cycle the latent energy of vaporisation of the liquid spray acts to cool the air charge and hence increase its density, increasing the engine volumetric efficiency, Iwamoto *et al.* [1997].

The necessity for fine control of both the location and mixture qualities of the fuel injected into the engine brings about its own challenges to enable robust engine performance over the range of real world engine operation demands. To enable engineers to address these challenges requires precise knowledge of the fuel injection process, and especially of the fuel spray development and break-up in the cylinder under all the demanded operating conditions. The factors which influence this spray formation and its subsequent mixing with the air charge are therefore required to be known in relation to the fuel properties to allow prediction of the fuel location and mixing, and hence of engine performance with the use of both current and potential future fuels.

This chapter summarises the main findings published in the literature to date relevant to the presented work. A brief overview of direct injection spark ignition engine operation is given followed by fuel supply demands for such engines. The injector types available to supply the fuel are then discussed along with their operating principles and principal spray characteristics. The analytical methods developed for spray characterisation are examined and finally the objectives of this work are identified from the extent of current knowledge of the factors affecting spray development from state of the art fuel injectors.

1.1.2 Gasoline Direct Injection Fuel Delivery Strategies

For any engine, achieving the correct AFR at ignition is critical to engine operation, as illustrated by studies into the strong relationship between the AFR, the rate of initial flame-kernel development and the cycle indicated mean effective pressure (IMEP) for a "stratified charge" PFI engine by Aleiferis *et al.* [2004]. The establishment of a homogeneous charge at the appropriate AFR may be achieved in a gasoline Direct Injection engine through the injection of an accurately metered fuel volume during the induction stroke, provided the spray is suitably atomised to promote complete mixing

with the in-cylinder air flow. However, several strategies have been proposed for establishing a localised region at the appropriate AFR at the spark plug at the time of ignition for stratified charge operation, Zhao *et al*. [1999]. Each strategy uses a different mechanism to direct the injected fuel towards the spark plug, with the intention of the vaporisation and mixing of the fuel with the air as it migrates to the spark plug region. The main strategies that may be employed are:

- Wall guided - fuel spray interaction with the piston crown or other solid combustion chamber boundary
- Air guided - interaction with the in-cylinder air motion
- Spray guided - direction of the spray itself towards the spark plug

The wall guided concept has to date been the most widely examined, as it is the simplest to instigate through mounting the injector on the cylinder circumference and directing the spray to a suitably shaped bowl on the piston crown. The predictable nature of the piston motion then forces the accurately timed spray towards the spark plug. However, the necessary interaction of the fuel with the cylinder boundary (piston crown) can result in fuel pooling and poor mixing with the air charge, resulting in large concentrations of unburned hydrocarbons (uHC) in the exhaust gases. Wall guided systems are also limited in their timing of stratified charge establishment by their reliance on the piston bowl to guide the fuel charge to the spark-plug.

Air guidance of the spray offers the potential advantage of negating any cylinder wall interactions, but requires precise control of the in-cylinder charge motion at the time of injection. However, the cycle to cycle variability inherent of in-cylinder flows, as detailed by Ozdor [1994] and examined for a modern engine designed for gasoline direct injection by Jarvis *et al*. [2006] and Justham [2009], can lead to variability in the success of stratified charge operation of an engine using this technique.

In a spray guided system the injector and its spray are positioned so as to direct the fuel towards the spark plug, relying on the momentum and simultaneous atomisation and vaporisation of the spray to carry the fuel to the spark plug in the appropriate mixture quality and AFR for complete combustion.

In theory, spray guided systems offer relative advantages in reduced wall wetting and independence from the variations in in-cylinder air motion. To attempt to realise these advantages, injectors for spray guided systems been developed with the benefit of Diesel injection system knowledge, to utilise ever increasing fuel pressures to aid spray direction as well as break-up and hence mixing. However, the multiple demands placed on the spray are not without their drawbacks; Hung *et al.* [2003] summarise that misfires, poor combustion and excessive emission products may potentially be linked to the pulse to pulse variation of the fuel spray, leading to wetting of the spark plug and/or cylinder surfaces, and building up liquid films on the piston top. However, their in-engine investigation of a pressure swirl spray using a probability presence image (PPI) analysis technique showed that the variability in in-cylinder air-motion is a greater contributor to spray variability than the spray itself. Spray variations can also adversely influence the mixture preparation resulting in combustion instability. Therefore, whilst the spray guided method potentially offers the largest benefits, its successful implementation requires great control, and hence understanding, of the factors affecting the fuel spray formation.

1.2 Fuel Injectors for Gasoline Direct Injection

To satisfy customer requirements, automotive engines must be capable of robust operation over a wide range of conditions from cold start to heat soaked. As alternative fuels become more widely available the engine must achieve all of these requirements using a range of fuel blends, which will have different physical and chemical properties within certain boundaries. To satisfy these demands a number of injector designs with different resultant spray forms have been applied to direct injection engines. A full description of all of these injector types and their variants is outside the scope of this work and the reader is guided to Zhao [2002] for an excellent overview. The main types of injectors which have been used to date, both commercially and in research, are the pressure swirl and multihole types.

1.2.1 Pressure Swirl Injectors

The largest volume of research to date in gasoline direct injection engine injectors and their sprays has been conducted into the use of pressure swirl injectors for wall guided systems, (*e.g.* Araneo *et al.* [2000], Hochgreb and van der Wege [2000], Loustalan *et al.* [2003] etc.) In a pressure swirl injector a small swirl plate over the orifice produces a swirling liquid cone when the injector is opened, as illustrated in Figure 1-1. Williams

et al. [2001] also observed the injection of an initial, poorly atomised volume of liquid, remnant from the previous injection event, often causing significant wall wetting on the piston crown and leading to high uHC exhaust emissions. Upon injection, the swirling liquid cone interacts with the ambient gas, which has the effect of establishing a vortex around the outside of the cone as well as an inwardly spiralling air motion in its centre. The rate of break-up of the sheet is increased over a non swirling cone due to the added shear stress imposed on the liquid cone by these vortices, Loustalan *et al.* [2003].

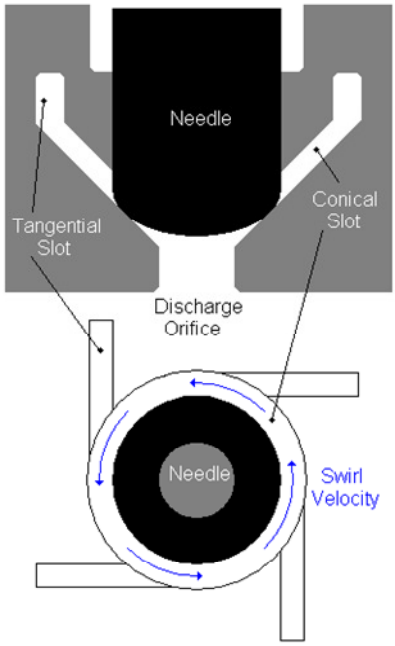

Figure 1-1 Schematic Representation of a Swirl Nozzle, Zhao et al [2002]

In relation to the fuel properties, the effect of altering the fuel temperature and gas pressure for pressure-swirl atomisers have both been examined by several researchers, including Araneo *et al*. [2000], Hochgreb and van der Wege [2000] and Loustalan *et al*. [2003]. These studies have shown that increasing the fuel temperature relative to the fuel's boiling point for a given gas pressure affects the spray cone in distinct phases. These studies have also shown that if the fuel temperature is well below the fuel's boiling point, normal evaporation will occur and the gas pressure effects are predominant in affecting the spray form. An increase in gas pressure, such as that associated with late injection, stratified charge operation, increases the drag force on the spray, reducing the leading edge penetration and widening the swirl cone. An increase in fuel temperature to near its boiling point induces increased levels of evaporation, whereby the more volatile components in the fuel evaporate and are drawn to the low pressure cone core, narrowing the spray cone. A further increase in fuel temperature

leads to the onset of disruptive or “flash” boiling in which the rapid vaporisation of the low volatility components and their suction into the low pressure cone core acts to affect the initial liquid spray, greatly narrowing the spray cone and forming a single axial jet in the extreme case. This effect was found to be augmented by an increase in gas pressure, where by the pressure differential between the low pressure cone core and the external gas volume is increased.

The operational mechanism of the injector nozzle for a pressure swirl injector determines that the spray cone is aligned with the injector axis, although Zhao [2002] notes that an axial deviation of 5° may be achieved. Whilst careful positioning of the injector does enable the realisation of wall and even spray guided systems using these injectors, the co-axial nature of the spray and injector inevitably does constrain the engine packaging and system design parameters.

1.2.2 Multihole Injectors

A multihole injector and its spray potentially offer advantages over a pressure swirl layout as it produces full cone spray jets through holes positioned at the nozzle. These nozzle holes may be located on a flat nozzle or on a three-dimensional feature on the nozzle, such as on the periphery of a cone. This design allows potential realisation of the benefits offered by spray guided systems without being subject to packaging constraints as the spray direction is independent of injector axial orientation. The nozzle holes are commonly round although can also be slits to produce fan-like sprays and may be regularly or irregularly spaced in a geometric shape (such as a circle or crescent), or in any other manufacturable arrangement thought to present the fuel to the required locations in the engine cylinder. Indeed, Preussner *et al.* [1998] note that nearly any spatial distribution of the fuel mass can be obtained. Under engine running conditions, Ortmann *et al.* [2001] found further advantages of multihole injector spray characteristics in relation to engine-out emissions for wall-guided DI systems. Using the multihole injector at constant injection timing whilst increasing the fuel pressure, they found that unburned Hydrocarbons (uHC) and soot emissions decreased with increasing fuel pressure. This reduction in soot is explained as being due to the presence of more air inside the spray of a multihole injector (than a pressure swirl spray), which increases the rate of vaporisation of the fuel and was found to lead to more complete combustion.

These advantages of multihole sprays have led to further recent research into these sprays being conducted, e.g. Mitroglou *et al*. [2009]. In parallel, the similarity of these sprays to diesel injection systems and their increasing fuel pressures have led to a growing overlap in these fields of study, Nouri *et al*. [2007]. However, whilst these and other recent works have developed an initial understanding of specific aspects of the development of these sprays, their commercial deployment requires an in-depth understanding of the fundamental mechanisms affecting the entire process of fuel flow, spray development and break-up over the full range of different operating conditions and fuels which may be encountered by state of the art multihole injectors designed specifically for gasoline direct injection engines.

1.3 Spray Development

For any spray, its development and break-up are governed by the liquid flow properties and their interaction with those of the gaseous medium into which the flow is injected. As well as the fluid properties themselves, the relative magnitudes of these properties can be characterised by certain dimensionless relationships. For the liquid phase (subscript l), the principal properties are its density, ρ, and dynamic viscosity, μ. The effect of these properties on a flow in relation to the liquid velocity u and a characteristic dimension D (usually the injector nozzle hole diameter) may be characterised by the Reynolds Number, Re, as expressed in Eq.1.1.

Eq.1.1
$$\mathrm{Re} = \frac{uD\rho_l}{\mu_l}$$

When the liquid is injected into a volume of gas, the balance of the liquid inertia force (a function of ρ and u) relative to its surface tension, σ, acts at the boundary of the liquid spray. This balance of forces may be represented by the dimensionless Weber number, We, as expressed in Eq.1.2.

Eq.1.2
$$We_l = \frac{\rho_l u^2 D}{\sigma_l}$$

Similarly, a gas phase Weber number may be defined for the gas-liquid interface by considering the gaseous properties instead of those of the liquid, denoted by a "g" subscript of the appropriate properties.

The first quantitative description of the liquid break-up process upon release into a volume of gas was given by Ohnesorge in 1931, who performed measurements of the intact jet length, and showed that the break-up process can be described by the dimensionless ratio of the liquid flow Re and We, in the process deriving the Ohnesorge Number, Oh, which incorporates all the main fluid properties, Ohnesorge [1931]. This ratio is expressed in Eq.1.3.

Eq.1.3
$$Oh = \frac{\sqrt{We_l}}{\mathrm{Re}} = \frac{\mu}{\sqrt{\rho\sigma D}}$$

Classical spray break-up theory has been based purely on the Ohnesorge number as it incorporates all the main liquid properties. However, as noted by Hiroyasu and Arai [1990], it does not incorporate any of the gas properties, which also act to influence the spray break-up. Hence a fuller characterisation of the spray break-up should consider these gas phase properties, such as related by the gas phase Weber number (We_g) or, as suggested by Rietz and Bracco [1982], by the gas to liquid density ratio. However, to date no single descriptor has been derived which incorporates all of these properties, and so a combination of the above referenced dimensionless numbers are used to characterise ranges of spray break-up behaviour.

1.3.1 Break-Up Mechanisms

As described above, the break-up process of a liquid jet from a straight, circular nozzle injected into a volume of gas is determined by the liquid and gaseous properties as well as the relative velocity between the liquid and gas. The spray formation resultant from this process may be characterised by the distance between the nozzle and the point of first droplet formation, the "break-up length," and by the size of the droplets that are produced, Baumgarten [2006]. As would be expected, different mechanisms act as the relative magnitudes of the liquid and gas forces acting on the spray change, with increasing rapidity of break-up with an increase in liquid flow velocity, and hence with increasing Reynolds number. As such, different break-up regimes may be identified at which different break-up mechanisms act. The break-up regimes commonly differentiated are the Rayleigh regime, the first and second wind-induced regimes and the atomisation regime. A schematic representation of these spray characteristics for each of the main break-up regimes is shown in Figure 1-2.

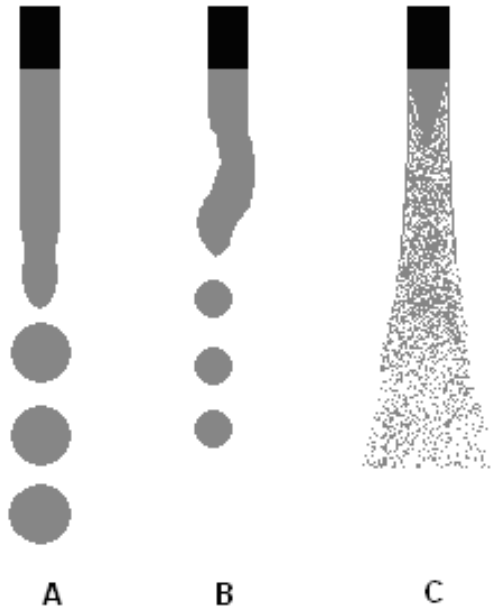

Figure 1-2 Spray Break-Up Mechanisms – (A) Rayleigh Regime, (B) Wind-Induced Regime , (C) Atomisation Regime

The Rayleigh regime occurs at very low flow velocities; the flow drips from an unbroken liquid jet length, which increases in length with increasing flow velocity. Break-up occurs due to the growth and eventual meeting of troughs of axis-symmetric surface oscillations, the result of the imbalance between liquid inertia and surface tension forces, Rayleigh [1878]. This break up produces droplets with a diameter of a constant multiple of 1.98 of the liquid jet diameter.

A further increase in liquid flow velocity results in the onset of the wind-induced regimes. In the first wind-induced regime, the relevant forces acting in the Rayleigh regime are amplified by the aerodynamic force of the gas acting at the liquid boundary, as represented by the gas phase Weber number. This break-up regime is characterised by a decrease in the jet break-up length, and the droplets are no longer a constant multiple of the liquid jet diameter; the average droplet size is approximately that of the nozzle diameter. A further increase in the liquid velocity causes the flow inside the nozzle to become turbulent as the critical Reynolds number is surpassed, and leads to the onset of the second wind induced regime. In an extension of the first wind induced regime, the increase in the magnitude of the aerodynamic forces in the second wind-

induced regime causes jet break-up to occur due to the instable growth of short wavelength surface waves that are initiated by turbulence. Increasing the Reynolds number leads to increasingly turbulent flow and rapid and chaotic droplet separation and spray break-up processes. As a result, this leads to a reduction in droplet diameter to below that of the liquid jet, as well as to a decrease in the intact liquid spray length. This intact length will be surrounded by small separated droplets, and so two break up lengths may be defined; the length from the nozzle to the end of the intact liquid core, and the length to the end of the jet break-up. While the intact surface length decreases with increasing jet velocity, the overall break-up length may increase as the spray velocity increases. However, as noted by Baumgarten [2006], the accurate measurement of either of these characteristic lengths becomes increasingly difficult with increasing Reynolds numbers due to surrounding dense region of separated droplets.

Finally, a further increase in Reynolds number beyond the second wind-induced regime leads to intact liquid core length approaching zero, at which stage the spray breaks-up in the atomisation regime. This regime is characterised by a conical spray, and spray divergence begins immediately after the jet leaves the nozzle, although as noted by Baumgarten [2006] an intact liquid core, or at least a dense core consisting of large liquid fragments, may still be present several nozzle diameters downstream from the nozzle. The resulting droplets are much smaller than the nozzle diameter. The theoretical description of spray break-up in the atomisation regime is much more complex than any other regime, because the disintegration process strongly depends on the flow conditions inside the nozzle hole (*i.e.* turbulence and cavitation), Faeth *et al.* [1995]. Chigier and Reitz [1996] also noted the importance of liquid cavitation in the nozzle in this regime, usually resulting in a shorter break-up length, except under fully detached flow (so called “supercaviation”) conditions, which were found to produce sprays with longer break-up lengths. Due to the high injection pressures and resulting Reynolds numbers used in gasoline direct injection systems, the sprays of relevance to this work usually operate in this regime.

Each of these spray break-up regimes may be depicted on a graphical plot of the Ohnesorge Number against Reynolds Number, known as the Ohnesorge diagram, as detailed in Lefebvre [1989] and illustrated in Figure 1-3. The Ohnesorge diagram shows that increasing Re or Oh results in a more rapid and intense spray break-up.

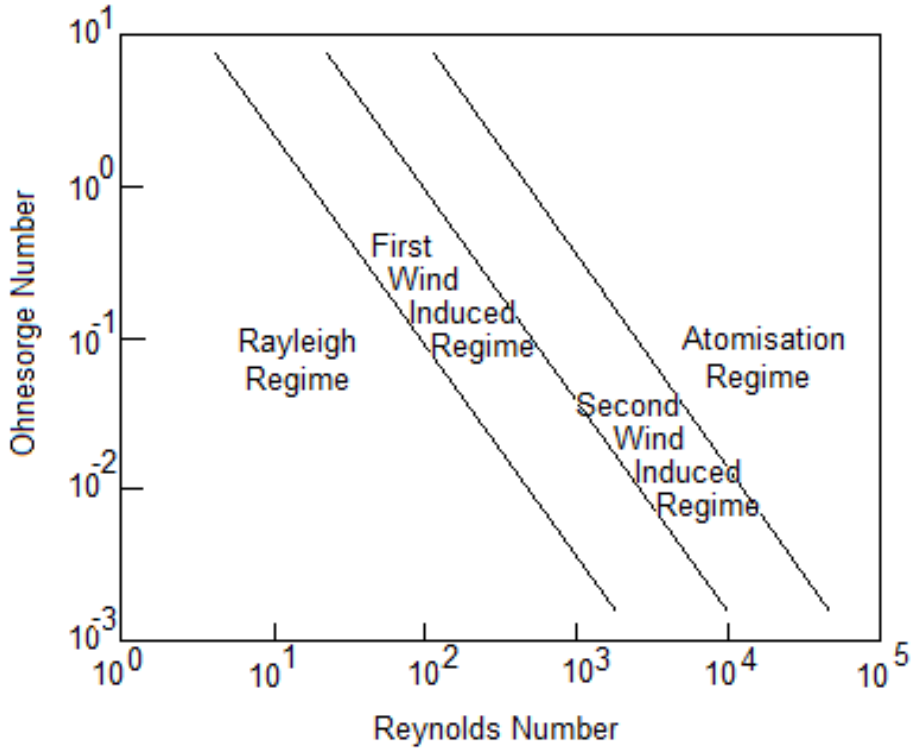

Figure 1-3 Spray Break-Up Regimes

As described above, the primary spray break up approaching and in the atomisation regime is rapid and intense. The exact mechanisms at work to bring about the break-up of the liquid body are also dependant on the nature of the in-nozzle flow, and hence the entire process is highly coupled, (Hiroyasu [2000], Sou *et al.* [2007]). The result is a multiphase flow with complex gaseous structures of different origins that merge aspects of turbulent primary and secondary break-up (Dumouchel [2008]).

If the radial turbulent velocity fluctuations inside the liquid jet are strong enough, the turbulent eddies can overcome the surface tension and leave the jet to form primary droplets. Cavitation structures developed inside the nozzle holes result in the formation of bubbles, and hence a two phase flow inside the nozzle holes. The intensity and spatial structure of the cavitation zones depends on nozzle geometry and pressure boundary conditions. Implosion of the cavitation bubbles increases the turbulence level and thus also intensifies the spray disintegration, as determined by Hiroyasu *et al*. [1991] and Soteriou *et al*. [1995]. This process is shown schematically in Figure 1-4. Studies by Yue *et al*. [2001] on Diesel sprays with 20–80 MPa injection pressures using X-rays showed that the bulk of the spray near the nozzle was composed of a liquid/gas mixture with liquid content not exceeding 50% by volume. However, in general the

phenomenon of in-nozzle cavitation is not well understood as to date it has been largely invisible, and hence theoretical postulations on the mechanism of cavitation have not been validated, Baumgarten [2006].

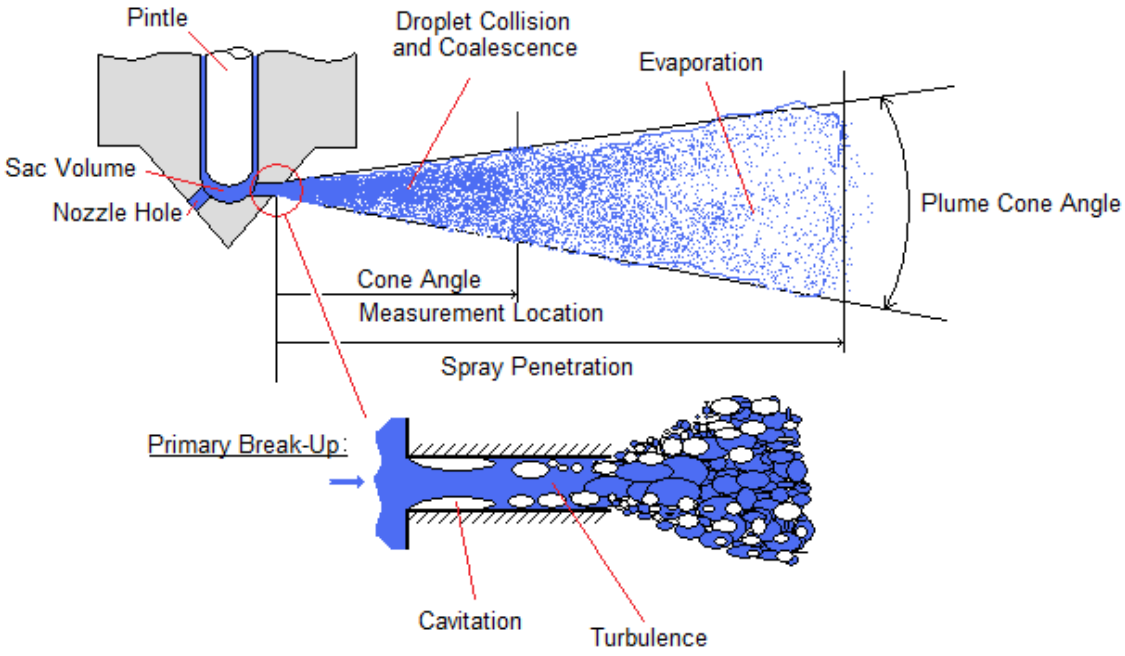

Figure 1-4 Anatomy of Break-Up of Full Cone Spray, Baumgarten [2006]

As summarised by Hiroyasu [2000], the importance of aerodynamic effects on primary break-up has been a topic of debate in the spray research community. Initial postulations were that the gas phase Weber number, We_g, could be used to determine the boundary between the second wind-induced and atomisation regimes. However, this notion has been superseded by work which has shown that aerodynamic effects contained within the We_g term are not the dominant mechanisms in primary atomisation, but that aerodynamic interactions can contribute to droplet formation at the liquid surface and droplet transport away from the surface via large-scale recirculating vortices. Wu and Faeth, [1993] showed that this was particularly the case for situations where the liquid-gas density ratio (ρ_l/ρ_g) was less than 500. Furthermore, Sallam *et al.* [2002] showed that for turbulent flow at the jet exit for water and ethanol liquids with properties of turbulent primary break-up, the non-dimensional break up length (defined as the intact liquid core length divided by the nozzle hole diameter (L_c/d)) first increases with an increase in We_l and then becomes independent of We_l at large values of We_l. Sallam *et al.* [2002] derived a relationship between the liquid-gas density ratio (ρ_l/ρ_g) and the

break-up length for the range of We_l over which the relationship is valid as noted in Eq.1.4.

Eq.1.4 $$L_c/d = C_b(\rho_L/\rho_G)^{1/2}$$

Where C_b is an empirical parameter that describes the nozzle flow conditions. In the literature C_b takes values in the range 3.3–15 (Baumgarten, [2006]). Specifically, Sallam *et al.* [2002] identified a value of C_b=11.0 for shear-type break-up of a liquid-ethanol jet in quiescent air.

For engines, the concept of spray break-up length is important because given the finite time scales available for adequate mixture preparation it indicates the rate of the mixing process. Historically, break-up length correlations have been limited to simplified analysis of either Rayleigh type break-up or fully developed turbulent flow break-up using large nozzle diameters and l/d ratios, under non-cavitating conditions and with fluids such as water (*e.g.* Chen and Davis [1964], Grant and Middleman [1966]). Indeed the idea of an 'intact liquid core' for engine injectors was initially developed by Hiroyasu *et al.* [1991] in order to characterise the inner structure of Diesel sprays. More recent studies such as those by Wu *et al.* [1995] and Sallam *et al.* [2002] have continued the investigation of liquid column surface break-up at more intense break-up regimes, but have not accounted for cavitating flows or realistic engine injector nozzle geometries. However, for gasoline direct injection fuel sprays, the in-nozzle flow at even higher liquid Weber numbers than those studied limit the applicability of these studies in determining the precise spray break-up length.

1.4 Cavitation

Cavitation occurs in a flowing liquid when a pressure drop causes the local static pressure to reduce below the liquid's vapour pressure (at its local temperature), resulting in a phase change initiated at appropriate nucleation sites. In an injector nozzle, if the in-nozzle flow is assumed to be one dimensional, stationary, frictionless, incompressible and isothermal, the Bernoulli equation (Eq.1.5) illustrates that an increase in velocity, which occurs at the inlet of an injector nozzle, results in a localised decrease in static pressure;

Eq.1.5
$$p_1 + \frac{\rho}{2}u_1^2 = p_2 + \frac{\rho}{2}u_2^2$$

The large velocity gradients established over cavitation regions by the axial flow lead to a strong shear flow in this area, leading to the creation of small turbulent vortices in the flow. Cavitation may also occur at the centre of these vortices due to the centrifugal static pressure differentials in the vortices. Under extreme conditions, such as those found in diesel injector nozzles, von Kuensberg Sarre *et al.* [1999] showed that these cavitation regions can collapse and cause spray break-up inside the injector nozzle, although Berkwerk [1959] had first shown that cavitation phenomena occur inside Diesel injector nozzles some time ago. Although cavitation is not desirable on many occasions since the collapse of the cavitation bubbles can have a negative effect on the mechanical integrity of components through surface erosion, cavitation in injection nozzles is recognised as a phenomenon that can be beneficial to the development of the fuel spray. This is due to the fact that the primary break-up and subsequent atomisation of the liquid fuel jet at the nozzle exit can be improved by the disruption of the flow and enhanced turbulence caused by the cavitation patterns within the flow, (Schmidt and Corradini [2001]). In addition, the dynamics of cavitation inside the nozzle is expected to enhance fuel atomisation through generation of smaller droplets which vaporise more rapidly, thereby enhancing the air and fuel mixing.

1.4.1 Cavitation Number

A dimensionless cavitation number may be defined to characterise the sensitivity to cavitation in a particular liquid flow arrangement. Cavitation is predicted to occur if the cavitation number is above the critical cavitation number for the system. A number of definitions for the cavitation number exist, which all relate the in-nozzle flow to the upstream and downstream pressures. A number of commonly used definitions of the cavitation number (CN) are presented in Eq.1.6 to Eq.1.8:

Eq.1.6
$$CN = \frac{\left(p_{inj} - p_g\right)}{p_g}$$ (*e.g.* Chaves and Schuhbauer [2006])

Eq.1.7
$$CN = \frac{p_{inj} - p_v}{p_{inj} - p_g}$$ (*e.g.* Schmidt *et al.* [1996])

Eq.1.8 $$CN = \frac{\left(p_{inj} - p_g\right)}{\left(p_g - p_v\right)}$$ (*e.g.* Gilles-Birth *et al*. [2006])

Where p_{inj} is the injection pressure, p_g is the gas pressure and p_v is the liquid vapour pressure at the prevailing liquid temperature in all cases. A full discussion of the derivation of these definitions of the cavitation number is outside the scope of this work and the reader is guided to Hu and Ruiz [1995] and Efthymiou [2004] for further details. However, all of the above stated definitions of CN fail to account for the effect of the fluid flow kinetic energy on the system, which acts to suppress the formation of cavitation bubbles through turbulence. In addition, the above definitions assume that the vapour pressure for the liquid is either constant at all temperatures, or that vapour pressure at the fluid temperature is used. Lastly, whilst cavitation is usually considered along the length of the injector hole, and hence the "inj" and "g" locations may be used as boundary conditions, the cavitation number may be considered at any location within the fluid system. Hence, incorporating the effect of turbulence, explicitly stating the liquid vapour pressure dependence on temperature and accounting for the location of interest at "∞", a more physically correct definition of the cavitation number (differentiated by the nomenclature Ca) may be defined as presented in Eq.1.9:

Eq.1.9 $$Ca = \frac{p_\infty - p_v(T_\infty)}{\frac{1}{2}\rho_L u_\infty^2}$$ (*e.g.* Liggett [1994])

Where p_∞ is the pressure at a reference point in the flow, p_v is the vapour pressure of the liquid at the reference temperature T_∞, ρ_L, is the liquid density and u_∞ is the characteristic velocity at the reference point.

Whereas the pressure difference associated with cavitation is manifest in a high value for cavitation number for the definitions given in Eq.1.6, Eq.1.7 and Eq.1.8, the onset of cavitation is associated with a low value of Ca in the formal definition given in Eq.1.9. At large values of Ca, flows will be single-phase due to either p_∞ being very large compared to $p_v(T_\infty)$, or the flow velocity u_∞ being very small. As Ca decreases however, nucleation will first occur at a value dependent on the physical geometry and fluid properties. This is usually denoted as incipient cavitation and defined by a critical cavitation number, Ca_{cr}. A further reduction in the cavitation number below this value will cause an increase in the number of vapour bubbles. The rate of growth of bubbles is

radically affected by the thermodynamic properties of the liquid and vapour, which are also functions of the temperature of the liquid, and consequently the value of Ca_{cr} will also depend on the liquid temperature. In a hypothetical flow where the liquid cannot resist any tension, vapour bubbles would appear immediately when p reaches p_v. However, nucleation does not typically happen instantaneously due to the varying levels of nuclei present in the test liquid – from contaminant gas or otherwise – and the fact that growth rates are finite, requiring a certain 'residence time' when $p < p_v$. These fundamental relationships are significant in the current application but have yet to be recorded or characterised fully in real-sized gasoline injector nozzles.

1.4.2 In Nozzle Flow Visualisation

The limited number of previous studies on cavitation in multi-hole injectors have focused largely on flow imaging in scaled-up optical models of Diesel nozzles, *e.g.* Soteriou [1995] and Aleiferis *et al.* [2007] in a 20× models, Nouri *et al.* [2007] in a 29× model, with few studies on real-size nozzles. Real size nozzle images are mainly limited to those of pressure swirl injectors (*e.g.* Allen and Hargrave [2000], Allen *et al*. [2003], Khoo and Hargrave [2006] and Moon *et al*. [2007]) or diesel injector geometry (Walther *et al*. [2000a] and Walther *et al*. [2000b]).

Nouri *et al.* [2007] examined the sac volume and nozzle flow of a large scale (29 x) transparent acrylic nozzle using water as the working fluid. Matching the Re and CN to actual size flows allowed for high speed examination of the cavitation flow structures in the nozzle for a range of needle lifts. The authors observed the staged onset of cavitation with increasing cavitation number. Cavitation was first observed at cavitation numbers of 0.5 to 0.7 (as per Eq.1.7) with the formation of a “needle string” from the needle surface into one of the nozzle holes. An increase in CN to 0.7 – 0.9 was found to lead to the development of unstable cavitation bubbles at the top of the nozzle hole inlets. Further increases in cavitation number were observed to lead to a corresponding increase in flow turbulence as well as cavitation. At CN greater than 1.0, the needle string cavitation dissipated, and pre-film and film cavitation along the nozzle hole boundary, emanating from the nozzle inlet, were observed to form along with a vortex string cavitation along the central axis of the injector hole. At CN above 2.5, film cavitation was seen along the surface of the nozzle hole whilst the flow through the hole was formed of a highly turbulent 2 phase fluid.

However, research conducted in comparing the results and observations of cavitation inside real-size and large-scale model injectors has questioned the direct scaling of cavitation phenomena in injectors, even when relevant non-dimensional parameters have been matched on models. In one of the earliest studies on injector nozzles, Bergwerk [1959] conducted experiments with simplified large-scale and real-size single-hole Diesel nozzles and observed that for the large-scale nozzle, increasing cavitation continuously led to a transition into hydraulic flip resulting in a poorly atomised, "pencil spray"; on the contrary, increased cavitation in the real-sized nozzle brought about a more atomised spray. More recently, Arcoumanis *et al.* [2000] found that cavitation in large scale nozzle models occurred in the form of foamy clouds of bubbles, similar to those observed by Soteriou *et al.* [1999]. However, in real-size injectors, cavitation appeared in the form of large clear voids, similar to those detailed by Chaves *et al.* [1995]. These results suggest that the nature of cavitation inception may change in scaled-up models and that bubble scaling factors are still not well understood.

Gilles-Birth *et al.* [2005, 2006] investigated the effect of cavitation in multi-hole DISI injectors. They used a real injector body coupled to a real-size optical nozzle with a single angled orifice 0.2 mm in diameter. They identified three types of cavitating structures: bubble, film and string cavitation. The latter was found for nearly all operating conditions and started at the injector needle due to strong rotational flow at the nozzle inlet, growing towards the nozzle exit but was very unstable in its development, shape and shot-to-shot repeatability. Film cavitation and supercavitation were the dominant modes, the former observed to have stronger regions on the top side of the nozzle as bubbles were created at the nozzle inlet and flushed away and the latter used to define conditions where bubbles completely filled the nozzle. The effect of the presence of cavitation at the nozzle exit on spray form was also shown by Gilles-Birth *et al.* [2005, 2006], to the extent that cavitation at certain regions around the circumference of the nozzle was shown to produce an asymmetric spray formation and thus affect the spray primary break-up. Similarly, Suh and Lee [2008] also investigated the effect of nozzle exit cavitation on the spray form and conclude that cavitation has the effect of producing a wider cone angle and reducing values of the droplets' Sauter Mean Diameter (SMD, $D_{3,2}$).

Apart from a recent study on flash boiling inside pressure-swirl injectors by Moon *et al*. [2007], none of these studies using optical injectors were extended to compare various fuels, temperatures or examine flows at conditions close to flash boiling. However, such phenomena are very important because gasoline direct injection injectors are mounted in the engine head and experience a wide range of operating conditions. While the effect of liquid temperature on cavitation may not be significant at low vapour pressures compared to the downstream pressure, at injector (fuel) temperatures of more than 70 °C and in-cylinder pressures below 0.5 bar (*i.e.* conditions representative of early injection, homogeneous charge engine operation), changes in vapour pressure and vapour and liquid density do become significant, although no experimental results exist to explain such effects in multi-hole type nozzles.

1.5 Spray Collapse

1.5.1 Flash Boiling

Early studies on the sprays from low pressure port fuel injection injectors observed certain conditions at which the spray spontaneously evaporated upon injection, a phenomenon termed "flash boiling". Early fundamental studies like those of Brown and York [1962], Lienhard [1966] and Lienhard and Day [1970] identified two types of flash boiling: internal, where bubble nucleation occurs within the nozzle; and external, where the jet exits the nozzle as a superheated liquid, followed by sudden bubble nucleation and growth a short distance beyond the nozzle exit. Since nucleation is promoted by factors such as surface roughness and turbulence, they found that nozzles with smooth orifice walls which promoted a laminar jet were most likely to suppress nucleation within the nozzle and exhibit external flashing. The onset of flashing for both types was correlated with the degree of liquid superheat. The effect of flashing on the jet shape and final droplet size were related to the amount of available energy in the liquid within the nozzle, and the dynamic stability of the non flashing jet.

Areneo *et al.* [2000] observed that if the fuel temperature is increased to exceed its boiling point for the ambient conditions, the phenomenon of flash boiling is observed to affect the spray form for pressure swirl sprays. Flash boiling was observed by measuring the very initial spray cone angle at different ambient pressures for fuel at 293 and 393 K. At the higher fuel temperature, the fuel (Shell Optimax) was superheated at lower pressures, and the cone angle was observed to collapse rapidly. Hochgreb and van der Wege [2000] showed that the flash vaporisation at warm fuel conditions of the

volatile components in fuel leads to a change from the hollow cone structure observed under cold conditions to a solid cone distribution due to the entrainment of the smaller fuel droplets into the centre of the jet by the induced air flow. Image intensity comparisons showed a droplet diameter decrease in the order of 40% due to flash vaporisation. Bubble point calculations suggested that superheat of about 20 °C was sufficient for flash vaporisation. Williams *et al.* [2001] summarised that flash boiling in pressure swirl sprays occurs due to the reduction in the boiling temperature that results from the rapid depressurisation of the fuel as it is injected. van der Wege and Hochgreb [2000] also postulate a third intermediate phase in the flash boiling process, termed "Non-disruptive Evaporation". Here 10-20% of the fuel volume spontaneously evaporates, without noticeable disruption to the liquid phase or centre of the spray.

1.5.2 Spray Collapse

The phenomena of spray collapse can be observed for all injector types, given conditions which are adverse to their usual operation modes. Spray collapse is the term given to the large scale deviation from the usual spray formation, to a spray in which the geometric parameters and the atomisation quality are markedly altered. As such, spray collapse is the result of a rapid vaporisation of all or some of the fuel, such as flash boiling. In relation to a typical multihole spray, a collapsed spray would typically be observed as a single, poorly defined large jet as opposed to a number of clearly defined smaller, angled, jets. Zhao [2002] details the collapse of a multihole spray formation into a reduced number of plumes as being the extreme limit of individual plume spray interaction. To this end the critical geometric parameter is the relative spacing of the individual plume nozzles. Here the author postulates that holes orientated relatively at 30° will allow plume interaction under adverse circumstances, whilst those relatively orientated at 40° will not allow interaction. Although the author acknowledges that these values are dependant largely on the individual plume angles, further details of the spray in which these limits of interaction were observed are not given. Spray collapse is accompanied not only by a more compact wetted footprint, but also by a more rapidly penetrating spray tip.

Zhao [2002] notes that the main influencing conditions on spray collapse are those of the injector/fuel operating temperature and the ambient air/gas pressure. The tendency observed was for multihole injector sprays to collapse when the temperature was increased to around 75 °C or more and the back (ambient) pressure was decreased to

below atmospheric pressure. Although usually the result of a combination of these conditions, spray collapse also occurred if one of the conditions was altered in the extreme. Zhao described the spray collapse process in a number of stages. The initial starting point was a normal spray consisting of a single jet from each hole in the nozzle. As the temperature was increased from ambient to 75 °C or more the individual plumes became wider with less well defined spray boundaries. If at the elevated fuel temperature the back pressure was decreased from typical late injection values of 0.45 to 0.25 MPa, the plumes broadened further and began to combine, until a single plume was evident at approximately 0.15 MPa (1.5 Bar) back pressure. This single plume produced a wetted footprint which was reduced in area by approximately 15% over the sum areas of the individual jets. The single jet was also surrounded by a torodial vortex, not unlike a normal pressure swirl spray. A further decrease in back pressure to 0.1 MPa brought about a complete spray collapse and a single, rapidly penetrating jet was produced.

1.6 Objectives

This chapter has shown the highly complex interaction of the fuel flow properties and the nozzle geometry in affecting the spray development and break-up. For engine developers and researchers to be able to predict the real world performance of fuel systems and engines, including by the use of computational fluid dynamic (CFD) modelling, the fuel spray development is required to be understood in terms of the fuel physical and chemical properties in relation to the demanded operating conditions.

Although multi-hole injectors are common in Diesel engines and have been used for many years, they have only recently been applied to gasoline DISI engines. As a result the majority of work published to date on multi-hole injectors concerns Diesel nozzle geometries, with particular experimental features and analysis targeted at this combustion system. Although there is much that can be learned from these studies in terms of optimising injector design and understanding fundamental spray behaviour from such atomizers, much also remains to be understood. For example, there are still many uncertainties about the role of in-nozzle phenomena on spray formation and the description of the underlying mechanisms is still too simplistic to allow accurate simulations to be built for development and optimisation purposes in real gasoline engines, where in-nozzle phase change phenomena are coupled to flash-boiling phase change upon spray development downstream of the nozzle exit. Furthermore, the

sensitivities to geometrical differences of the injector nozzles and piston design, the varied operating conditions for the DISI combustion system and its particular mixture preparation requirements merit specific attention and are the motives behind continued research in this field.

To date spray development and break-up have been examined largely independently from the in- and near-nozzle fuel flow structures for high pressure gasoline injectors. The effects of fuel evaporation characteristics on spray development in relation to the prevailing operating conditions have been mostly examined separately to the effect of these conditions on the upstream flow. Because of the ability of multi-hole injectors to target fuel directly to the spark-plug for stratified operation and to different areas around the cylinder to produce robust mixture formation under early injection homogeneous mode, it is important to understand whether strict design criteria are maintained when fluids other than those used to test the injectors at design and optimisation stage are employed in real engines and when extreme conditions of temperature and pressure found during engine operation are experienced. These requirements are further emphasised by the trend towards using biogenically derived fuels such as ethanol in increasing proportions with gasoline. There is also a limited understanding about the role that liquid transport properties such as surface tension (σ), viscosity (μ), density (ρ), boiling point and vapour pressure (p_v) have on in-nozzle phenomena and overall spray development, and how these are affected by the wide operating envelope of gasoline engine injectors; *e.g.* gasoline injectors must inject fuel at conditions of low ambient pressure, typically from ~0.2 bar to ~5 bar or more, and at liquid temperatures of -10 °C or lower, to over 150 °C at the injector tip under high-load firing conditions.

An improved understanding of the atomisation behaviour of high-pressure sprays is also necessary both inside and outside the engine combustion chamber in order to decouple the competing effects. The effects of fuel-specific spray break-up phenomena on combustion must also be explored to put the results into context. For example, one of the drawbacks of ethanol as an automotive fuel is its lower energy density compared to gasoline and lower stoichiometric Air/Fuel Ratio (AFR) which increases the fuel mass that must be injected per cycle to achieve the same fuel equivalence ratio (typical AFR at stoichiometry for gasoline is 14.7, for pure ethanol 9.0). To deal with these issues, either the flow rate of injectors has to be increased, which may reduce the accurate fuel metering capabilities required for stratified operation, or standard injectors are typically

used and the fuel is injected over a longer period of time during the cycle, increasing the probability of wall-wetting and reducing the effective time available for good mixing and evaporation before ignition.

Whilst the study of sprays and liquid jet break up has been the subject of many years of research, the recent advent of DI engine spray guided systems along with developments of Diesel engine injection systems has led to the need for further investigations, including the current work, into the interaction of the spray break up mechanisms with the fluid properties at operating conditions hitherto not deemed feasible.

To meaningfully add to the existing body of knowledge regarding the above, this work has sought to fulfil the following objectives:

- Investigate the effect of fuel temperature on spray formation and break-up in relation to fuel properties for a multihole injector spray
- Investigate the effect of gas pressure into which the spray is injected in relation to fuel temperature and properties
- Investigation of effect of fuel properties, such as viscosity and vapour pressure on spray development and break-up for the range of fuel temperature and gas pressure conditions representative of engine operating conditions
- Investigation of emerging biogenic oxygenated fuels Ethanol and Butanol and comparing their spray formation with those of fossil derived, multi-component gasoline fuels to indicate likely engine operation compatibility
- Investigate near nozzle spray break-up
- Investigate the effect of in-nozzle cavitation on spray break-up and atomisation rate and quality for real sized nozzle geometries and flow conditions.

In summary, this work seeks to contribute to the knowledge regarding spray development and break-up by linking the in nozzle flow, cavitation and near-nozzle spray development for a state of the art multi-hole injector designed for commercialisation in a high performance gasoline direct injection engine developed for both homogeneous charge and spray guided stratified charge operation in relation to the fuel properties.

2 Spray and Experimental Characterisation

This chapter details the techniques, hardware and methodology used to analyse the spray produced by the multihole injector examined for this work. The test equipment and rigs used to take the measurements presented in this work are described, followed by a discussion of each of the spray measurement and analysis techniques employed including major sources of measurement variability. The fuels used in this work are also described in relation to their physical properties.

2.1 Injector and Nominal Spray Form

Prior to beginning spray characterisation, information relating to the injector's nominal spray form was supplied by Jaguar Cars, the supplier of the injector hardware to this work. The information provided by Jaguar Cars was in the form of the spray plume axis angles, as illustrated in Figure 2-1. The spray definition supplied shows a 6 hole multihole (full cone) injector type. Although the off-axis nozzle angles could induce swirl within the liquid flow path, further details of the spray form were not supplied, and the design of the injector flow path with respect to swirl was unknown.

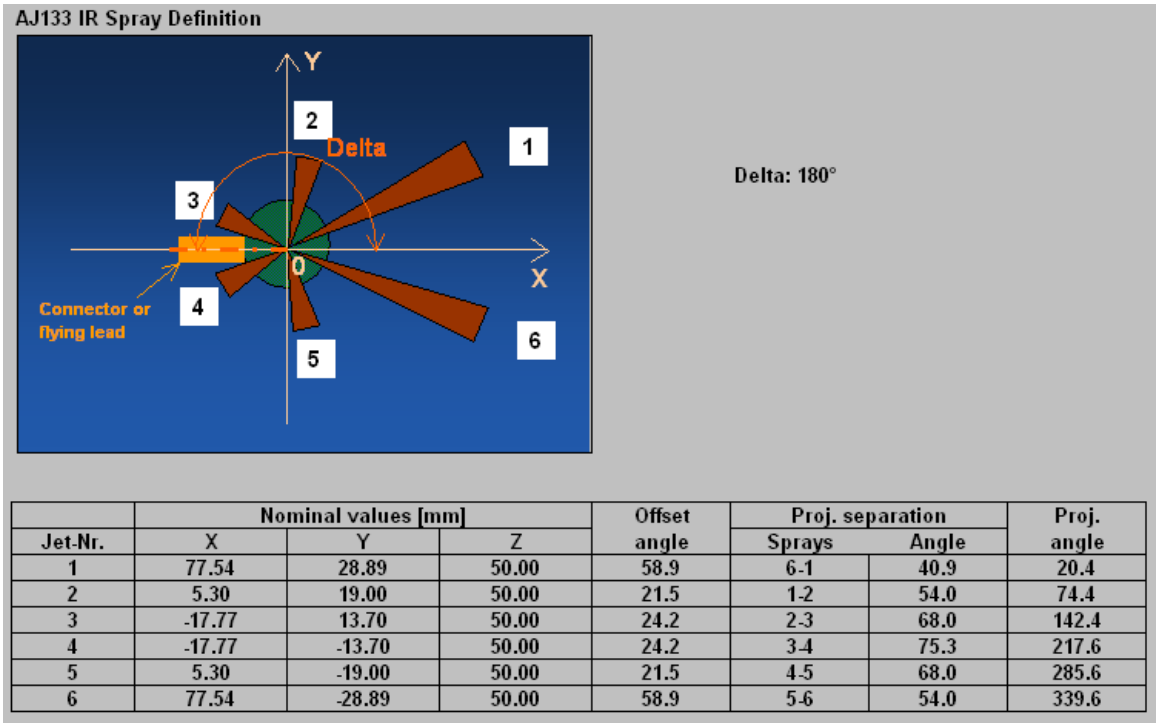

	Nominal values [mm]			Offset	Proj. separation		Proj.
Jet-Nr.	X	Y	Z	angle	Sprays	Angle	angle
1	77.54	28.89	50.00	58.9	6-1	40.9	20.4
2	5.30	19.00	50.00	21.5	1-2	54.0	74.4
3	-17.77	13.70	50.00	24.2	2-3	68.0	142.4
4	-17.77	-13.70	50.00	24.2	3-4	75.3	217.6
5	5.30	-19.00	50.00	21.5	4-5	68.0	285.6
6	77.54	-28.89	50.00	58.9	5-6	54.0	339.6

Figure 2-1 Spray Definition for Project Injectors

To further visualise the spray and enable the design of the characterisation chambers and rig, the provided information was used to model the spray in three dimensions. Due to the asymmetry of the spray, each projection was labelled in relation to the orientation of the injector to the chamber optical access to enable each view to be easily differentiated and described. The modelled spray and the view designation labels are shown in Figure 2-2. Note that in Figure 2-2 the injector has been tilted by an angle of 19° to reflect its orientation as mounted in the chamber and that the projected spray plumes are shown to be cut at a plane perpendicular to the injector axis and not the plume axis, as would be the case for a real spray.

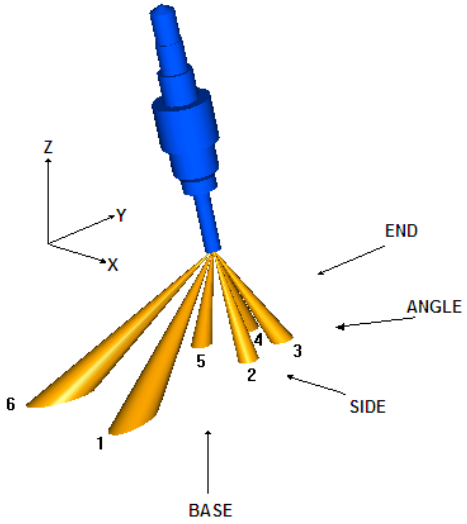

Figure 2-2 Model Image of Injector and Nominal Spray

Further projections of the spray along the injector axis, as interpolated from the data provided in Figure 2-1, are illustrated below in Figure 2-3 (a, b, c) for each of the principle characterisation views of “end”, “side” and “base”.

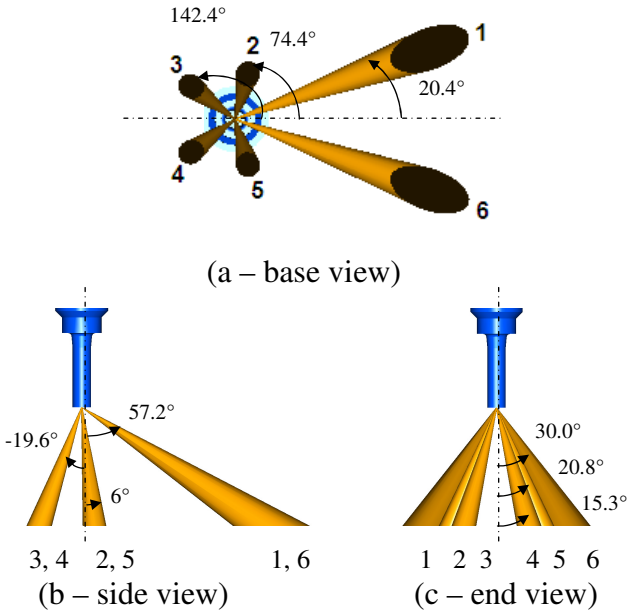

Figure 2-3 Spray Plume Nominal Angles

High magnification images using a digital camera mounted onto an optical microscope to give a magnification of 100× were taken of each of the injector holes to examine whether any deposits or other effects of their previous usage were present,

and are presented in Appendix A to this Chapter. The images appeared to show an outer nozzle diameter of 0.5 mm, and appear to show no major manufacturing differences. Although some irragulaties can be seen at the outer nozzle perimeter, possibly signs of deposits, these were not found to affect the fuel spray (in terms of expected form or variability in the form), likely due to this outer nozzle not being the actual injector nozzle, as described below.

2.1.1 Nozzle Geometry

At the time of receipt of the injector, it was stated that the injector had been used for experimental purposes, although its operating history was unknown. Confidentiality agreements in place during the experimental duration of this work prevented internal investigation of the injector or its nozzle. However, towards the end this work these confidentiality agreements had lapsed and a similar injector to that used in this work was cut open for internal examination. The timing of the availability of this data meant that it could only be used in retrospective interpretation of the experimental results. In addition, many experimental conditions and designs were based on the initial, external measurement of the injector dome diameter of 0.5 mm. Upon examination, the injector nozzle holes were found to be internally stepped, presumably to attempt to prevent the build-up of in-nozzle deposits during engine operation. A backlit image of the opened nozzle shown in the photograph in Figure 2-4 clearly shows the larger outer nozzle periphery as well as the smaller inner nozzle hole.

Figure 2-4 Backlit Nozzle Hole Showing Inner and Outer Orifices

The dimensions of the nozzle and step, as best as could be measured using standard engineering tools, are shown in Figure 2-5. It should be noted that the accuracy of the dimensions in Figure 2-5 is limited by the manual measurement technique, and that the hole lengths are estimates based on the measurement instrument limitations. A particular word of caution is attached to the accuracy of these measurements as Morgan *et al.* [2001] found noticeable spray penetration differences were observed for hole diameter differences of as little as 0.05 mm.

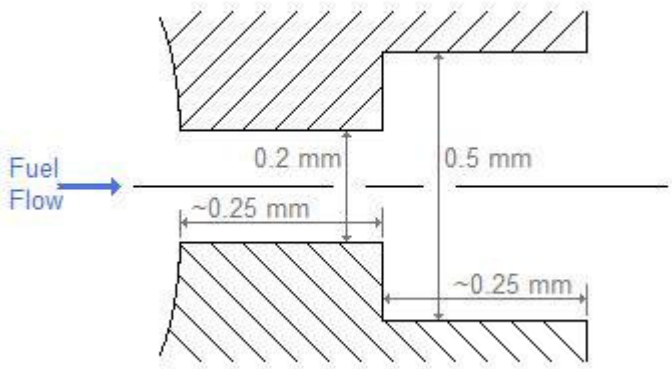

Figure 2-5 Diagram of Nozzle Geometry

Of particular note in relation to the nozzle geometry is the sharp edge at the nozzle entrance (with respect to the fuel flow) as it has been shown that rounded nozzle inlets can act to prevent flow separation (*e.g.* Kolokotronis [2007]). The nozzle length is also of interest, as long nozzles can lead to the reestablishment of a laminar flow structure. Honda *et al.* [2004] manufactured similar injectors with different L/D nozzles and noted an individual jet angle increase of 9° to 15° when the L/D ratio was reduced from 5 to 2, as compared to a value of ~1.25 for the nozzle used in the current work.

2.1.2 Spray Wetted Footprint

Some rudimentary information regarding the volume distribution of the wetted footprint was also made available at the start of this work in terms of the fuel footprint distribution shown in Figure 2-6. This distribution was measured by the injector manufacturer at a sampling distance of 23 mm and a fuel pressure of 117.6 bar (1176 kPa). However, this data carried no correlation as to which actual injector was used,

such as serial number. Note the volume axis (z axis) is in terms of percentage collected as no further information of flow rate or injection duration for designed operating conditions was supplied.

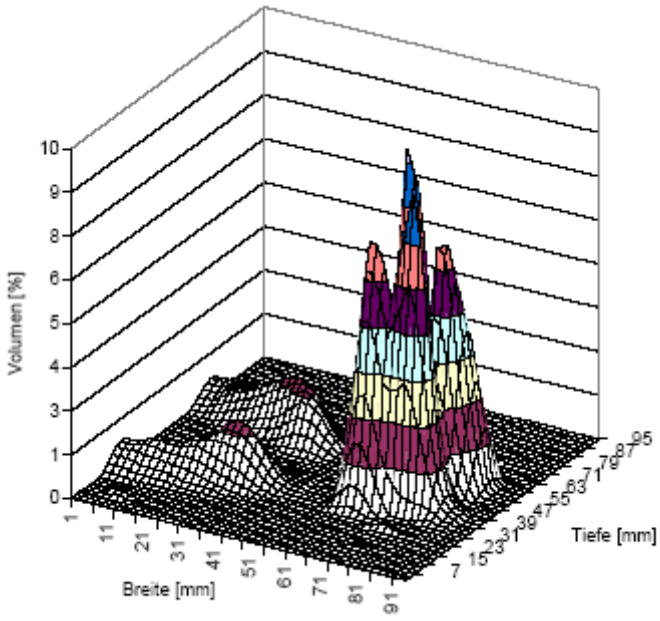

Figure 2-6 Injector Manufacturer Measured Fuel Distribution

2.1.3 Fuel Flow Rate

The fuel flow rate was measured by mounting the injector over a dry conical flask. Tissue was wrapped around the injector nozzle to prevent evaporation of the fuel but allow displacement of air in the flask by the fuel. The fuel used was *iso*-Octane due to its low volatility at room temperature. All tests were carried out at a fuel pressure of 150 bar into ambient gas pressure, for 600 injections of 2 ms duration each. The mass of the flask was found using high accuracy digital scales of the appropriate scale (milligrams), before and after the injections. The difference in mass was taken to be the mass of fuel collected, which was converted to a volume measurement by dividing by the density of *iso*-Octane. Measurement was made of the pulsed injected volume as opposed to the steady state flow rate to correlate the injection duration to the volume of fuel injected. The volumetric flow rate for *iso*-Octane was measured to be 0.3 g per injection event of 2 ms, which equates to 0.222 litres / second if the flow rate is averaged over the injection duration.

2.2 Optical Nozzle

As discussed in the previous chapter, a number of recent studies have shown the importance of the in-nozzle fuel flow on subsequent spray development and break-up for gasoline direct injection nozzles (*e.g.* Gilles-Birth [2005, 2006]). In order to image the flow inside the nozzle, a real size optically accessible nozzle was designed and manufactured to replicate the injector used for the spray investigation in as far as the nozzle dimensions could be measured or estimated without damaging the injector. To accommodate the injector with the optical nozzle attachment in the pressure chambers in a similar manner to the production injector, a new injector mounting block and clamp were also designed and manufactured. Due to the complexities of the design, and the requirement to only image the spray inside the nozzle and hence not requiring optimisation of the length over which the spray plumes could be imaged, the mounting for the optical nozzle injector was designed to align the injector body axis with that of the pressure chamber.

2.2.1 Optical Nozzle Mounting

The optical nozzle was mounted to an additional injector supplied by the project sponsors. This additional injector was of a similar type as used for the main experiments for this work, but with a removable nozzle stem which was held in place with a threaded ring. The assembly of the stem, pintle and ring is shown in Figure 2-7. The pintle is the needle structure that sits inside the stem and is lifted by the electro mechanical actuator in the injector body to open the nozzle orifice at the injector tip, thereby allowing for the injection of fuel.

Figure 2-7 Injector Stem, Pintle and Attachment Ring

The nozzle assembly with the steel stem as would be used in an engine is shown in Figure 2-8 as mounted in the injector mounting.

Figure 2-8 Mounted Injector with Removable Stem

Figure 2-9 Injector with Stem and Pintle Removed

The injector body with the stem, pintle and ring removed is shown in its mounting in Figure 2-9. With these metallic parts removed from the injector, an adaptor was designed to allow the optical nozzle to be mounted to the injector body. This adaptor was designed to screw in to the injector body in place of the fixing ring, and to thereby locate the pintle and enable the fuel to flow to the nozzle while allowing for the attachment of the optical version of the stem. The adaptor as manufactured in steel is shown in Figure 2-10. The adaptor is shown mounted to the injector body with the pintle protruding in Figure 2-11.

Figure 2-10 Optical Nozzle Adaptor

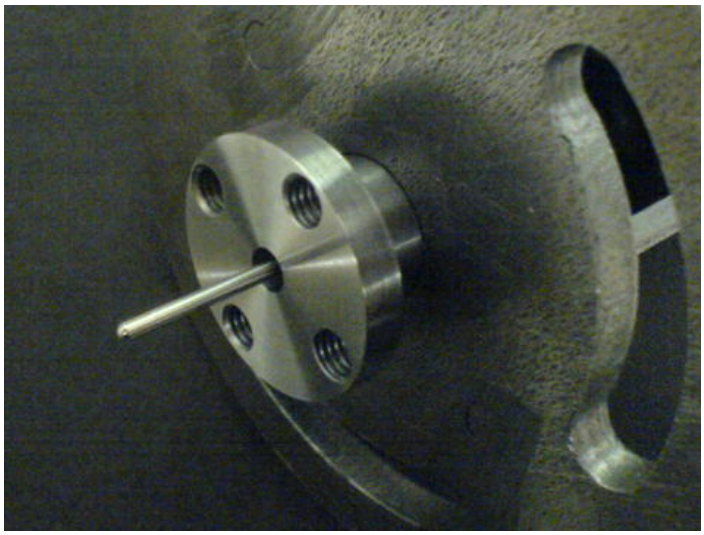

Figure 2-11 Optical Nozzle Adaptor Attached to Injector Body and Pintle

2.2.2 Optical Nozzle

The optical nozzle itself was manufactured in acrylic Perspex. The refractive index of Perspex is 1.495, and the melting point typically in the range 90–115 °C (363–388 K). Matching of the refractive index between the nozzle material and the fuel was especially important to detect fuel flow voids. The refractive index of the tested fuels is presented in Table 2-2 and is similar to that of Perspex for all fuels. The sides of the optical nozzle stem were required to be flat for the avoidance of refraction of the imaged light. A number of blanks were made of the nozzle in case of breakage, into which the nozzle holes were drilled at a later stage. A blank attached to the injector is shown in Figure 2-12. The nozzle was attached to the adaptor using 4 M5 x 10 mm

bolts, and was sealed at the joint with the adaptor using an o-ring at the mating surface.

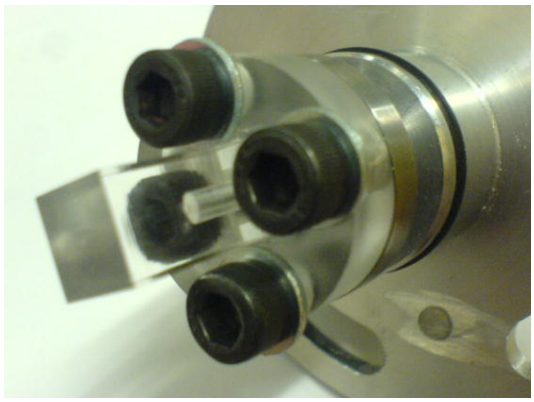

Figure 2-12 Optical Nozzle Blank Attached to Adaptor and Injector

To relate the in-nozzle flow phenomena to the global spray formation as produced by the production injector, similar test conditions were replicated for experiments using the optical nozzle. One of the principal test parameters varied in this work was the fuel temperature, and so the mounting for the optical nozzle was designed to incorporate a band heater and feedback thermocouple in a similar manner as used for the production injector mounting.

The band heater can be seen surrounding the injector body and clamp at the top of the assembly in Figure 2-13. The assembly is also shown mounted in the octagonal pressure chamber in Figure 2-14, where the adaptor and nozzle can be seen inside the pressure chamber and the rest of the assembly is located in the injector mounting crucible above the reflective insulation.

Figure 2-13 Optical Injector and Mounting Assembly

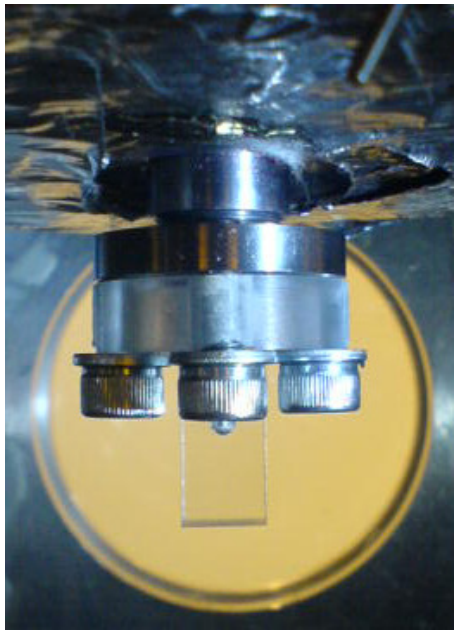

Figure 2-14 Optical Injector and Nozzle Blank in-situ In Pressure Chamber

Although the production injector nozzle orifices had a measured depth of 0.5 mm, it was calculated that the minimum wall thickness required for the Perspex nozzle was 2.5 mm for the fuel pressures used for these tests. To enable the force exerted by the fuel pressure inside the nozzle to be spread throughout the overall wall thickness, whilst allowing the minimum length nozzle with a diameter of 0.5 mm, the initial

design of the optical nozzle used a bowl cut-out at the nozzle orifice. This bowl was designed to spread the load exerted by the fuel pressure at the nozzle entry over the entire thickness of the material, while allowing the nozzle length to be similar to the real-size steel nozzle. A schematic diagram of this nozzle design is shown in Figure 2-15. Although this nozzle design was found to work very well in practice, the bowl cut-out obscured the spray at the emergence from the nozzle, and hence masked the link between in nozzle flow effects and the emergent spray form. To enable viewing of the emergent spray while maintaining material integrity a development of this bowl cut-out design was successfully tested with the bowl cut-out extended along the axis of the nozzle hole to produce an arched groove, as illustrated in Figure 2-16.

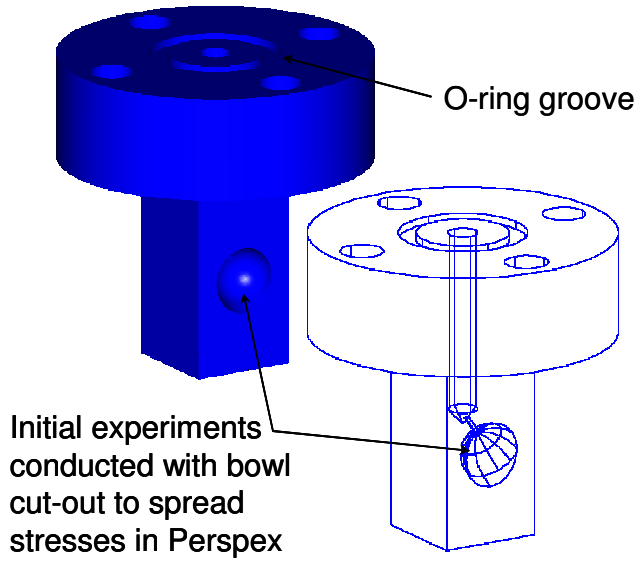

Figure 2-15 Initial Optical Nozzle Design Showing Bowl Cut-Out

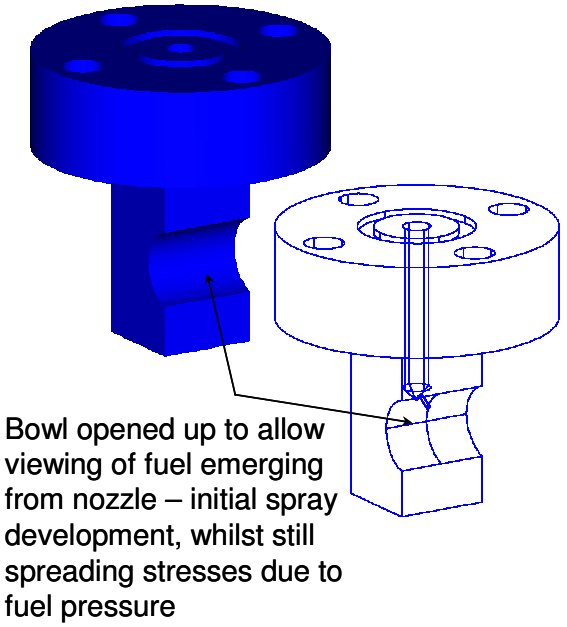

Figure 2-16 Development of Optical Nozzle Showing Groove

Following the success of the first optical nozzle with the groove cut-out, a further evolution of this design of optical nozzle was designed and manufactured. Where the first nozzle (Nozzle A) had a diameter of 0.5 mm and a length of 2.5 mm (l/d=5), the second nozzle (Nozzle B) was an even more faithful representation of the real sized nozzle, with a diameter of 0.2 mm and a length of 1.0 mm (also l/d=5), with a hole position closer to the bottom of the needle seat. The hole was designed at 60° angle to the vertical for both nozzles as an approximate to the 58.8° offset of plumes 1 and 6 in the real injector. Computer Aided Design (CAD) drawings of the two optical nozzles are presented in Figure 2-17.

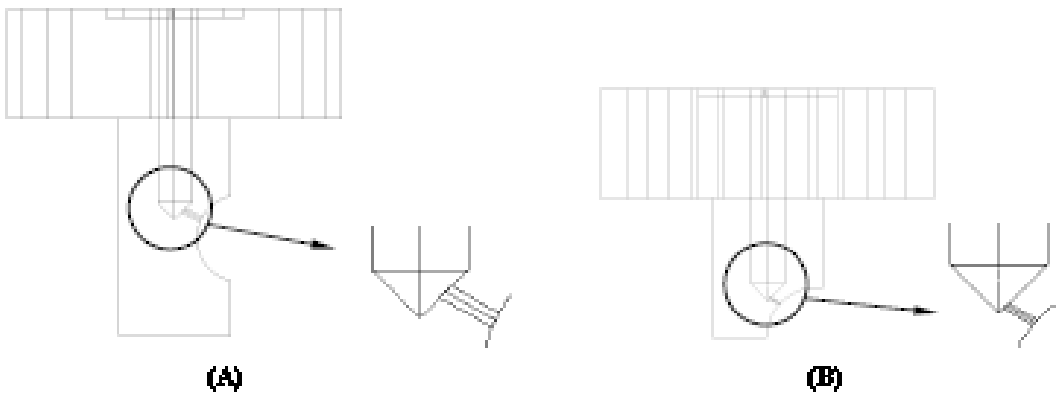

Figure 2-17 CAD Drawings of Nozzle A (d=0.5 mm) and Nozzle B (d=0.2 mm)

2.3 Injector Control

The precise control of the timing and duration of the injection event for gasoline direct injection engine operation under any strategy demands control of the timing, voltage and current signal sent to the injector by the injector control unit, commonly known as the "driver." The driver unit supplied to this work was pre-programmed with the required current and voltage characteristics, which would trigger the injector to open or close at the command of an external electronic trigger. The design of the driver unit used was such that pin 44 was required to be held at the supply voltage to hold the injector closed. Grounding the connection to this pin triggered the injector to open.

Due to the purchase of new equipment during this work, two methods of triggering the driver unit were used although in both cases the electrical and triggering connections to the driver unit were identical. The supply power and triggering pin connection, along with the triggering method used for the first part of this work, is shown in Figure 2-18. For later experiments, the positive voltage to pin 44 was supplied directly by an AVL 327 Timing Unit and hence the opto-isolator was no longer required to be used.

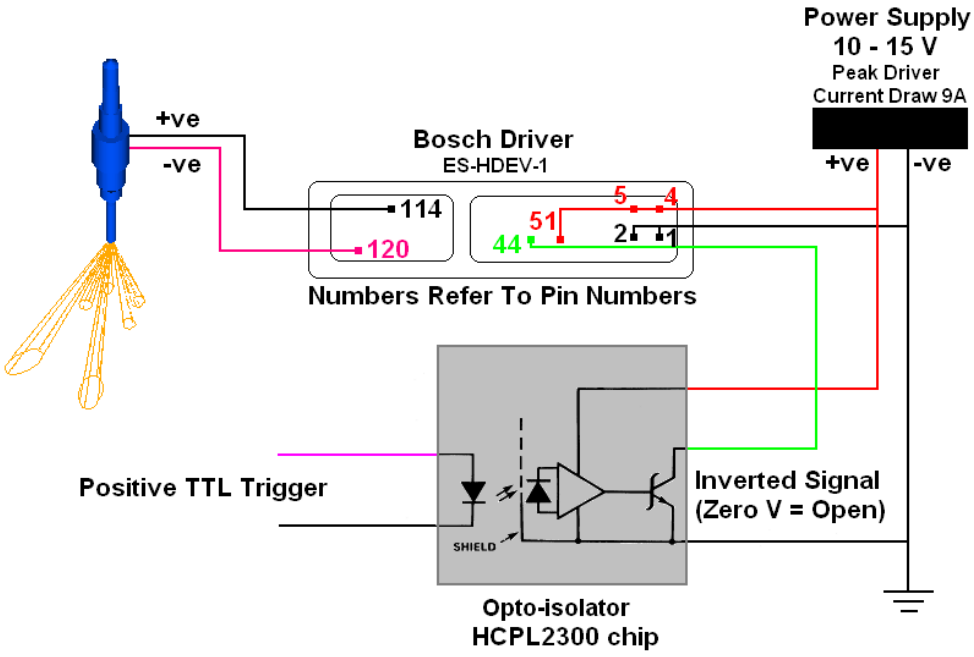

Figure 2-18 Injector Trigger Circuit

For all triggered injection events for this work an injection duration (trigger duration) of 2 ms was used. This duration was selected to enable spray formation, steady state and disintegration to be captured over the course of the characterisation equipment operability (*i.e.* flash lamp duration and high speed camera total memory availability), and to be comparable to engine spray durations. Engine injector pulse width durations are determined by the fuel flow characteristics of the injector and the volume of fuel required for the operational strategy, and are commonly in the range of 1.2 to 1.9 ms for single injection DISI operation.

2.3.1 Injection Hardware Variability

Prior to commencing the spray characterisation experimentation for this work, variability in the repeatability of the injection hardware was examined using the injector triggering arrangement as illustrated in Figure 2-18. Whilst variability in the hardware and in the spray parameters measured cannot be decoupled, an understanding of the source and extent of variability present in the hardware aids in interpreting subsequent experimental results.

The repeatability of the injector driver unit in terms of delays between triggering and signal outputs was measured at a constant power supply of 13 volts, which was the supply voltage used throughout this work. The output injector signal timing was measured using a LEM PR30 current probe with a reaction time of 2 μs around the positive wire of the injector lead connected to the driver. Trigger signals sent to the driver and the pulses sent by the driver to the injector were recorded on a digital storage oscilloscope over 100 pulses. These traces were then individually recalled and the delay between them measured using the on-screen cursors.

In common with other high-pressure injectors the current pulse supplied to the injector over the injection event was found to comprise of two sections. Initially the current rose rapidly to ensure rapid opening of the injector nozzle. The current then reduced to an intermediate level to hold the nozzle open, thereby enabling a quick closing of the nozzle at the end of the injection event. This current trace as recorded on the oscilloscope is shown in the top trace of Figure 2-19. The lower trace in Figure 2-19 is a magnification of the initial section of the trace, and shows the measured

delay between the trigger signal and initial current rise. The average delay between these events was measured to be 12.28 μs with a standard deviation of 3.97 μs. For an engine running at the standard test condition of 1500 rpm, such a delay corresponds to only 0.11° crank angle, with a standard deviation of 0.036° crank angle.

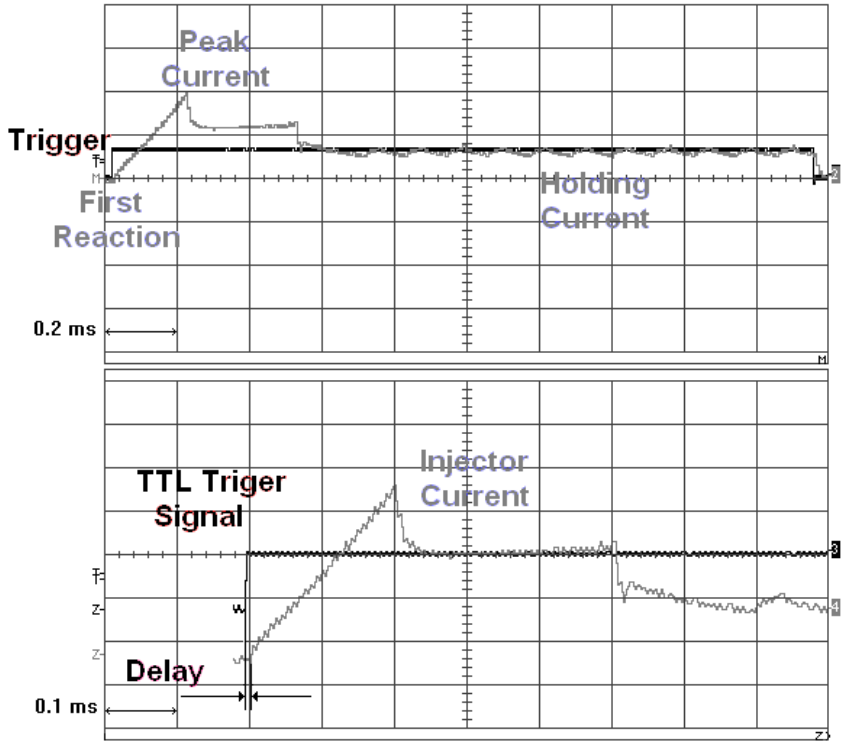

Figure 2-19 Trigger and Injector Pulses.

The time interval between the injector trigger pulse and first fuel seen at the injector nozzle tip was measured by imaging the back-lit injector nozzle using a single-shot PCO Pixelfly CCD camera at constant gas pressure of 1.0 bar. The delay between the injector and camera trigger was varied until an image was recorded in which fuel could just be seen emanating from the injector nozzle tip. This delay was then reduced in 10 μs increments until no fuel was seen at the tip over 100 injection events. The delay was then increased incrementally and 100 injection events were recorded for each delay interval until fuel was evident in each image. A tally chart of the probability of fuel seen at tip for each injector was built up, indicating the probability of fuel present at the tip for each delay interval as shown in Figure 2-20.

The injector used for the work, in conjunction with the driver unit, showed a delay of 301.4 µs to 100% probability of first fuel, with a 4.0 µs standard deviation, which would correspond to 2.7° crank angle (with a standard deviation of 0.036° crank angle) for an engine running at 1500 RPM.

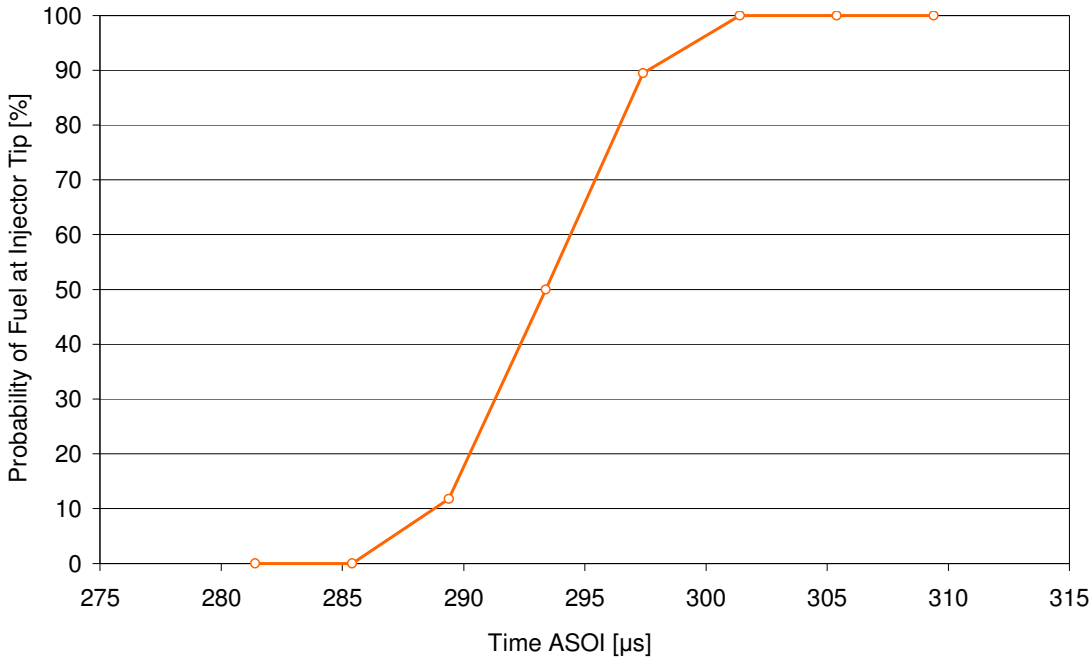

Figure 2-20 Probability of Fuel at Injector Tip.

In general, the levels of variability were measured to be extremely low in the injector operating hardware. The voltage dependence of the injector driver units was also measured to be negligible with the overall rate of reaction remaining steady with respect to the supply voltage over a range of 10 to 15 V, as may commonly be found in commercially produced vehicles.

2.4 Pressure Chambers

To isolate the injection system and spray development from any engine in-cylinder conditions such as gas motion or vibrations, measurements of the spray were carried out in optically accessed pressure chambers. Two sealed pressure chambers were used to image and analyse the injected spray for this work. Both of the chambers were mounted in the same manner in the purpose designed FSTF (Fuel System Test

Facility) located at UCL and consisting of a separate control room, test cell and plant room.

2.4.1 Cylindrical Pressure Chamber

The majority of spray imaging, as well as system delay and variability analysis and laser diffraction droplet sizing were carried out in a cylindrical pressure chamber as previously installed at UCL and described comprehensively by Loustalan [2004]. The chamber is formed from a machined stainless steel cylinder with an internal diameter of 180 mm and a wall thickness of 60 mm. A lid and base stud mount at each end of the cylinder to seal the chamber. The chamber features two pairs of orthogonal round openings on its circumference into which imaging windows can be placed and clamped by stud mounted rings. The chamber and its main dimensions are shown in Figure 2-21 and a photograph of the chamber body without the lid or windows mounted is presented in Figure 2-22.

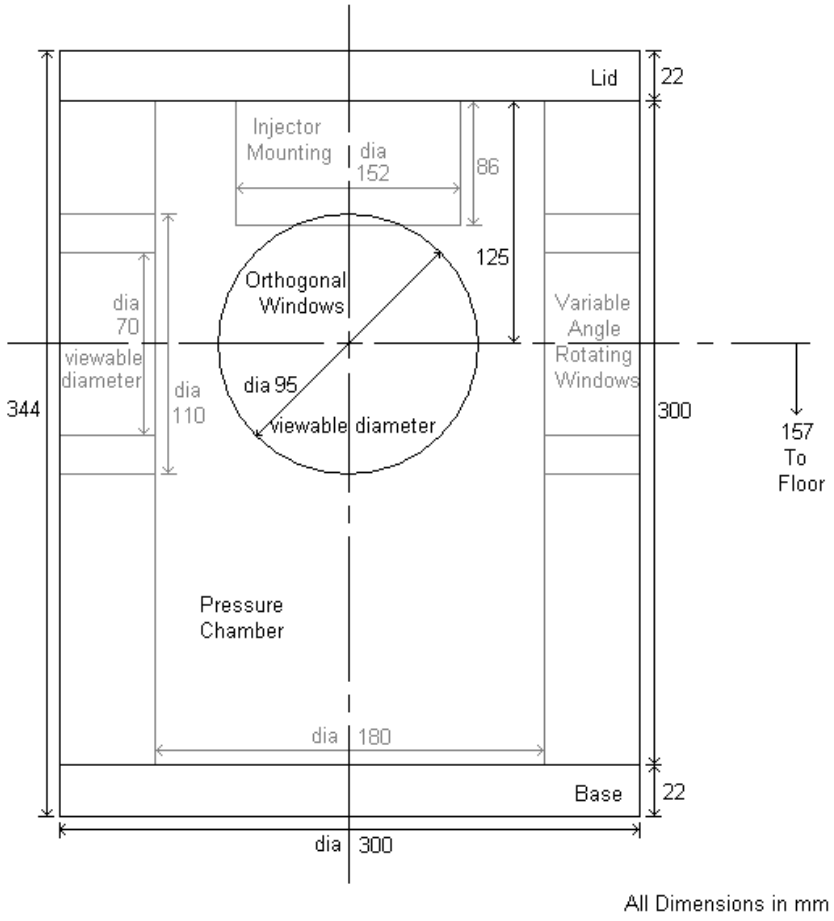

Figure 2-21 Cylindrical Pressure Chamber Dimensions

Figure 2-22 Cylindrical Pressure Chamber

The chamber lid accommodated an adaptor for the gas inlet and injector mounting, as well as a thermocouple and pressure transducer for monitoring of the chamber gas temperature and pressure. The base of the chamber contained an adaptor for the connection of the depressurisation and fuel evacuation hose and equipment. The chamber was sealed using o-rings around the circumference of the cylinder body at the lid and base, and by using rubberised gaskets at the window seating locations. Using these seals, the chamber was designed to maintain a positive pressure of 10 bar.

2.4.2 Octagonal Pressure Chamber

As discussed in Section 2.6.6, for optimum Phase Doppler droplet sizing measurement the detector is required to be mounted at a forward scattering angle to the measuring beams. Whilst the orthogonal window arrangement of the cylindrical pressure chamber allows the detector to be mounted at the opposite side of the chamber to the emitter, and hence at 0° or low forward scattering angles, detection of the reflected and refracted light fringes with the minimum sensitivity to changes in droplet refractive index is at higher scattering angles of around 40°. Even using the variable angle windows to ensure perpendicularity between the window and beam, such detection angles could not be achieved within the geometrical confines of the

cylindrical chamber and its window orientation. To enable the detection of scattered light at the desired angles, as well as the simultaneous use of other spray characterisation techniques, a new pressure chamber was designed and manufactured for this work. The new chamber was required to accommodate the opposing nature of most spray characterisation techniques (e.g. flash lamp and camera are most commonly mounted opposite each other) as well as the obtuse PDA detection angle requirement whilst maintaining the positive and negative pressure containing ability of the cylindrical chamber. In addition, it was desired to enable multiple characterisation techniques to be used simultaneously and for the spray to be photographically captured over a longer penetration length. Based on these requirements an octagonal arrangement for the new chamber sides was selected with a longer axial planar imaging window, as illustrated in Figure 2-23.

The octagonal chamber design was based on interchangeable sides with a thickness of 20 mm with a tongue and groove join, to make for an easily configurable chamber for use with a range of spray characterisation techniques, both for this work and for adaptability to future experiments. The octagonal structure of the sides was designed to be maintained by the seating of the sides in a groove in both the lid and base. The lid and base maintain the same injector and instrumentation mounting facilities as for the cylindrical pressure chamber so that these aspects could be carried over without further modification.

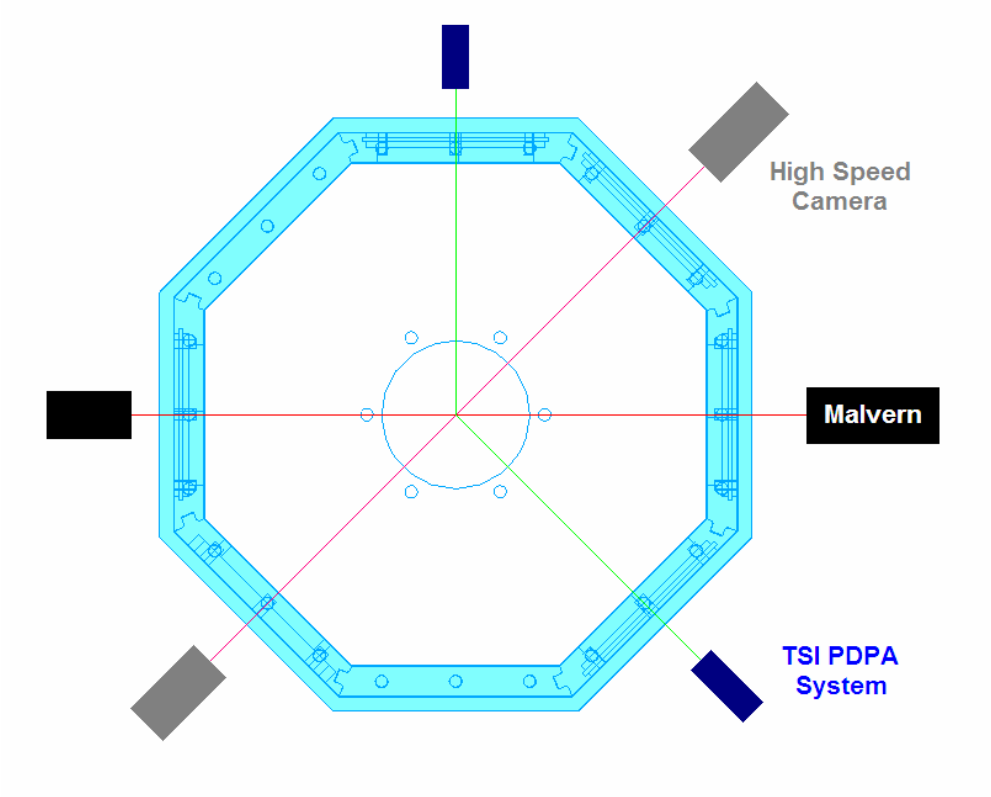

Figure 2-23 Schematic Diagram of Octagonal Pressure Chamber Showing Multi Technique Analysis Capabilities

In designing the octagonal pressure chamber, detailed calculations were carried out to ensure adequate pressure containment capabilities and safe operation of the chamber, whilst also ensuring its cost effective construction. An overview of these calculations is provided in Appendix B to this chapter. The main section engineering drawings used in the construction of the chamber are presented in Appendix C to this chapter whilst the modelled octagonal pressure chamber is shown in Figure 2-24 and the completed and assembled chamber is shown photographically in Figure 2-25.

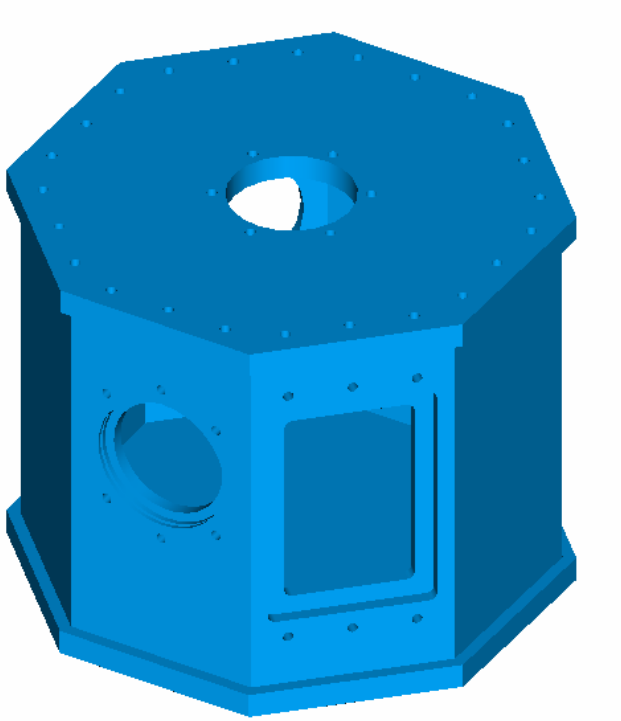

Figure 2-24 Octagonal Pressure Chamber

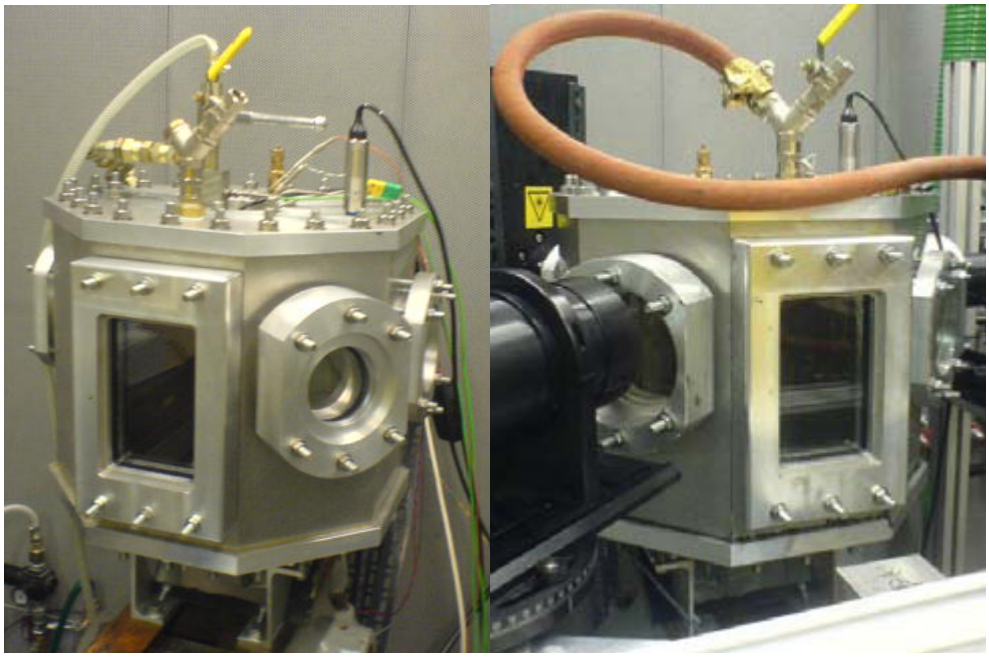

Figure 2-25 Photographs of Octagonal Pressure Chamber

Following manufacture and assembly of the octagonal chamber, extensive baseline testing was carried out to ensure the sealing and safety of the new chamber. An

imaging investigation was also conducted with a variety of fuels under various conditions to ensure consistency of image quality and subsequent measurement with those obtained from the cylindrical pressure chamber.

An additional imaging window orifice was machined into the chamber base to replicate an engine piston crown view of the spray using an angled mirror placed beneath the chamber and the camera suitably directed to capture this view. Whilst a new planar imaging window with increased length along the axis of the chamber has also been designed and manufactured to allow for imaging of the spray over a longer penetration, the scope remains for this window to be mounted in a custom holder to align it parallel to any spray plume angle, and therefore for un-distorted images of that plume to be captured in future experimental work.

2.4.3 Chamber Optical Access Windows

To image the spray successfully and clearly whilst maintaining the pressurisation capabilities of the chambers, optical quality quartz windows were used to allow optical access to the chambers. Whilst the cylindrical chamber was machined for round windows, the design and manufacture of the octagonal chamber allowed for the incorporation of a rectangular imaging window with the longer dimension parallel to the axis of the chamber, allowing the spray to be viewed over a greater distance before it became obscured by the window boundaries.

The spray droplet sizing techniques employed in this work required the precise alignment of light beams, their effectiveness being reduced by planar reflections of the light from the reflective surfaces of the chamber optical windows. To avoid external and internal reflections of the measurement beam for both laser diffraction droplet sizing and for the achievement of the appropriate forward scattering angle for Phase Doppler Anemometry (as discussed below), variable pitch windows were designed and manufactured. These windows were designed so that the quartz disc was mounted at an angle in an annular ring, which in turn was mounted at the same angle in another annular carrier ring, as illustrated in Figure 2-26. The pitch of the window could then be altered from between 0° (parallel to the chamber wall) to twice the mounting angle by rotating the ring in which the window is held.

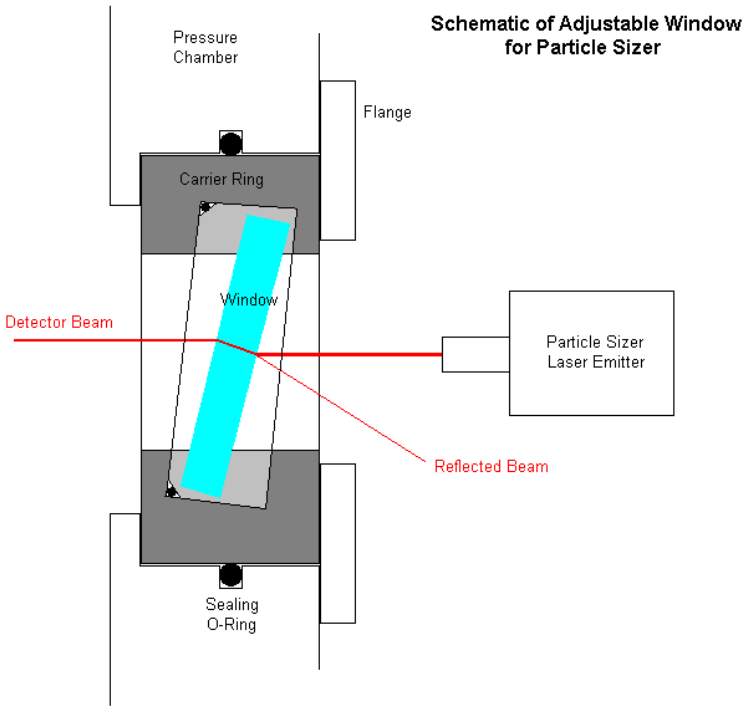

Figure 2-26 Variable Angle Window

The components of the variable pitch window and the final assembly are illustrated in Figure 2-27. The window was bonded into the upper and lower holding rings using a Loctite 3442, which is resistant to fuels and adhered to and sealed both the metallic and quartz elements of the assembly. Sealing of the movable components of the assembly was achieved by an o-ring located in a recess in the lower holder ring. Locating lugs were incorporated into the design of the holder ring to allow fine adjustment of the window angle with a custom designed spanner.

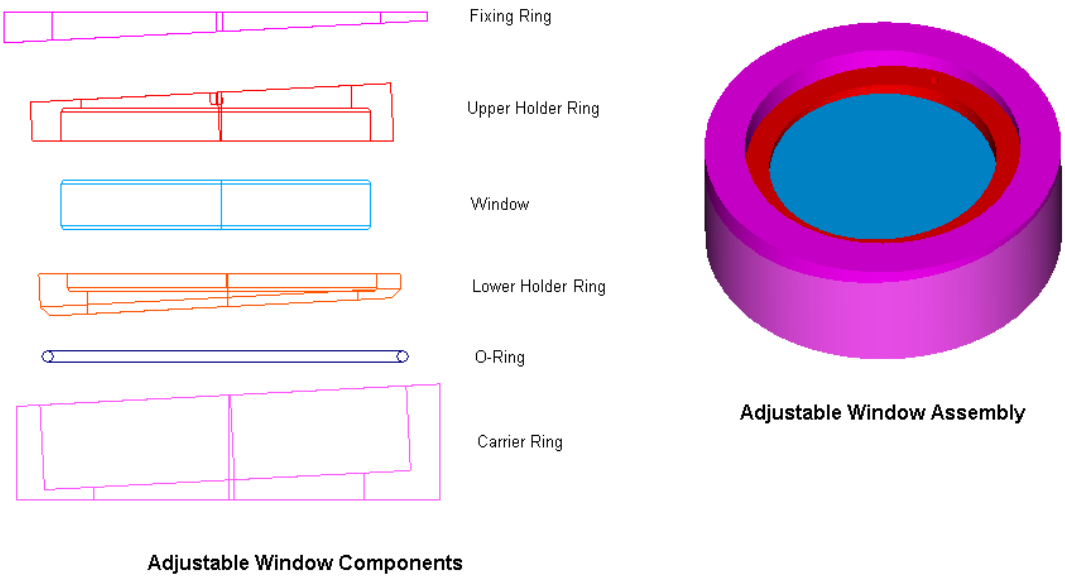

Figure 2-27 Variable Angle Window Components

Additional variable angle windows, designed on the same principle as those described above, but with an angle of 10°, were also designed and manufactured for use in the octagonal pressure chamber. By mounting these high variability angle windows in the octagonal arrangement, the actual angle between the windows diagonally "across" the chamber could be varied between 35° and 55°.

2.4.4 Chamber Mounting

To enable accurate single and simultaneous multi technique spray analysis and characterisation, the pressure chambers described above was mounted on a reclaimed milling machine. The chamber was mounted in place of the machine head, with the measurement equipment mounted to the adjustable work bed. As such, the measuring equipment could be firmly mounted to the bed using t-nuts as a work piece would be clamped for machining, and adjusted around the chamber using the fine control of the original machine. A platform was manufactured and mounted on the back of the milling machine to mount the imaging light source. Cantilevered arms either side of the chamber were fixed to the bed onto which the droplet sizing hardware was attached, maintaining a fixed position of both the emitter and receiver relative to each other, and to the imaging hardware.

2.4.5 Chamber Condition Monitoring

In both the cylindrical and octagonal pressure chambers the gas pressure and temperature were monitored to enable the desired experimental conditions to be established and to ensure consistency between experiments at similar conditions. For both chambers, a Druck PMP 4100 pressure sensor was mounted in the lid of the pressure chamber and the output displayed on an oscilloscope. For practical reasons the chamber gas temperature was not controlled but was monitored using a K-type thermocouple mounted in the lid of the chambers with the sensing tip located near the injector mounting crucible.

2.4.6 Chamber Pressurisation System

The pressure of the gas into which the spray was injected was shown in the previous chapter to be one of the fundamental aspects governing the spray's development and break-up. The chamber gas supply therefore had to provide pressurised air and/or inert gas to the chamber, and to create sub-atmospheric pressure conditions inside the chamber. The injection of multiple fuel sprays into the sealed chamber also presented the possibility of explosive mixtures being established inside the chamber, and so the chamber contents had to be evacuated in a sealed manner to allow for the safe separation and disposal of the fuel.

The pressurisation and evacuation systems are shown schematically in Figure 2-28. Valve 1 represents the nitrogen inlet valve, whilst Valve 2 is the air intake. The injector is not represented but can be taken to be a fuel valve in line with the gas inlet to the chamber. Valve 3 was located along the gas/fuel evacuation line which exits at the bottom of the chamber. Valve 4 is the bypass valve for Valve 3 and was used to regulate the vacuum pressure in the chamber and as the air inlet to the settling chamber during the running of experiments, ensuring the pump did not suck against a pure vacuum, which would lead to overheating of the motor.

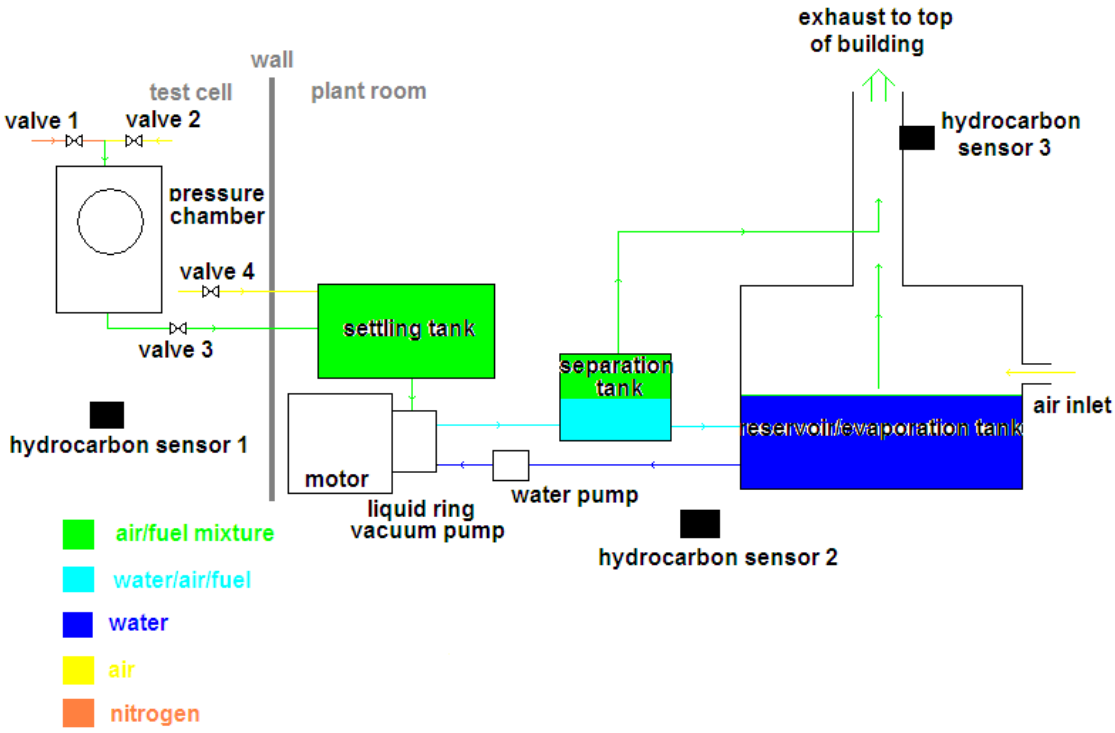

Figure 2-28 Schematic of Fuel Separation and Evacuation System

To increase the gas pressure inside the chamber for above atmospheric pressure experiments, nitrogen from a compressed cylinder was released into an otherwise sealed chamber through a connection in the chamber lid. At the desired pressure the nitrogen feed valve was closed to seal the chamber. A settling time of 30 seconds was allowed between setting the gaseous conditions within the chamber and running experiments to ensure a quiescent environment.

A liquid ring vacuum pump was located in a plant room adjacent to the test cell and attached to a fuel separator. The pump was connected to the bottom of the chamber by a fuel corrosion resistant rubber pipe through a valved connection pipe which ran through the wall between the rooms. The vacuum pump was operated during all experiments to evacuate liquid and vapour fuel between experimental batches and to create below-atmospheric pressures within the chamber; during experimentation the valve at the base of the chamber was closed to maintain a quiescent environment in the chamber at the desired test gas pressure. During chamber purging, a valve in the chamber lid was opened to allow air to pass through the chamber. This valve was

closed to allow depressurisation to the desired pressure for sub atmospheric conditions, prior to closing the vacuum valve.

In all cases, the base vacuum valve was opened prior to the top atmospheric or pressurisation valves following experimentation to prevent the release of fuel vapours into the test cell.

During chamber purging, the fuel/air mixture (liquid and vapour) was drawn into the settling tank, and then through the liquid ring vacuum pump, where it was mixed with water supplied by the water pump which forms the liquid sealing ring in the pump. The water/air/nitrogen/fuel mixture was then pumped to the separation tank, where any vaporised fuel and gas bubbles were drawn off into the system gas exhaust by the slight depression in the exhaust system. The remaining fuel/water mixture was pumped into the large water tank, which had an air feed which directs the air along the surface of the water. Baffles ensured the air covered the entire surface of the water. Due to the difference in density of the two liquids, the mixed liquid fuel rises to the surface and is vaporised by the air moving across the liquid surface. The vaporised fuel and air was drawn into the main system exhaust, which exited to the environment at the top of the building.

Hydrocarbon sensors were located near to floor level in the test cell, plant room and in the system exhaust duct. These were linked to an alarm and electrical system shutdown, which also cut the fuel pressure to prevent the build up of fuel vapour to dangerous or explosive concentrations.

2.4.7 Fuel System

To supply the high pressure fuel demanded by the injector here examined, as well as for future work using similar injectors, a high pressure fuel delivery system and associated safety features were designed and manufactured for this work. To enable the fuel pressure to be adjusted and potentially increased in the future, a Heypac GX30 pneumatic-hydraulic pump was used to pressurise the fuel. This pump uses compressed air through a pressure magnification piston to pressurise the hydraulic fluid, in this case the test fuel. By adjusting the pressure of the compressed air supply, the pressure of the fuel can be adjusted within the bound of the magnification ratio

and above the minimum air pressure required to overcome the pump's internal friction.

Compressed air was supplied to the pump through an air supply control unit, illustrated in Figure 2-29. In the presence of an electrical supply, the valves' nominal positions are reversed (i.e. Normally Closed Valve opens and vice versa), and the compressed air passes through the control unit. In absence of an electrical supply, as would be effected by an emergency shutdown, the valves revert and cut off and release the air supply to the pump, rapidly depressurising the fuel and preventing further fuel injection

.

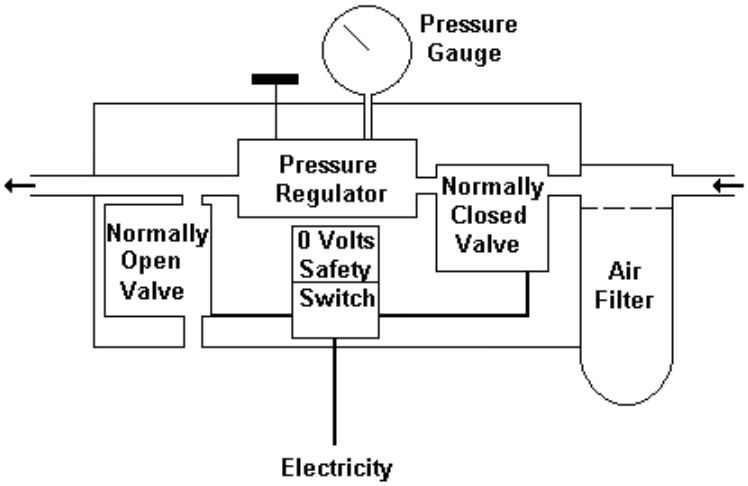

Figure 2-29 Schematic of Air Control Unit

A removable 5 litre fuel reservoir formed an integral part of the pump, and was attached directly to the base of the pump. To change fuels, the reservoir was removed and excess fuel emptied into an appropriate disposal container. The reservoir was then thoroughly dried and reinstalled. The new fuel was then pumped into the tank through the filler hole using a small hand pump. Following this procedure, the pump was pressurised to its lowest hydraulic pressure, and the rest of the fuel system flushed with the new fuel.

The output from the pump was directly connected to the injector clamp using flexible high pressure fuel hosing. A valve at the top of the injector clamp, the highest point of

the system, was attached to a clear pipe which drained into the waste fuel disposal tank as well as to remove any air trapped in the fuel lines. When changing fuels, this top valve was opened and the fuel system flushed until the new fuel was seen to flow in the clear pipe. By coincidence the fuel types tested for this work all had different colours (or were clear), allowing for the fuel test order to be such that consecutive fuels always had different colours to allow differentiation. When only new fuel could be seen to flow through the clear pipe, the top valve was sealed and the pump returned to operational pressure by increasing the air pressure. The injector trigger system was then set to fire the injector 200 times at 2 ms duration. This allowed for 4 full flushes of the injector, which was measured to hold approximately 50 injections at 2 ms duration volume of fuel.

2.4.8 Injector Mounting

The injector was mounted at the top of the pressure chambers in a custom designed and manufactured stainless steel mounting block, which in turn was fixed into a stainless steel crucible suspended from the chamber lid. By placing the mounting in the fixed crucible, the injector could be rotated to align the spray to the characterisation hardware as required by the experiment to be carried out. Furthermore, the injector could be easily removed for cleaning without the need to dismantle the chamber. The mounting was sealed in the crucible using rubber o-rings at the mating surfaces to ensure sealing of the chamber.

As detailed previously, the injector examined for this work was of a multi-hole nozzle design, with the nozzle orifices being located on a cone at the injector tip. The injector was of “production intent” for a spray guided system. As such, the orifices and hence spray were not aligned to the central axis of the injector in all planes. To maximise the viewable portion of the spray through the round chamber imaging windows, the injector was mounted at the angle subtended between the spray symmetry axis and the injector body axis, which was measured to be 19°. A schematic representation of the injector in its mounting is superimposed on a photograph of the cylindrical chamber in Figure 2-30 to illustrate the angled mounting of the injector. Due to the high fuel pressure and hence spray momentum, it is not expected that this angle if inclination will have affected the spray formation or development in any way.

Figure 2-30 Image showing Cylindrical Pressure Chamber and Schematic of Injector Mounting

The injector was clamped in the mounting by a stainless steel custom designed clamp, through which pressurised fuel was also supplied to the injector. A Kistler 4065A500A0 piezo-resistive pressure sensor (0 – 500 bar) was also mounted in the injector clamp to measure the fuel pressure at inlet to the injector. Figure 2-31 shows a schematic diagram of the injector clamped in its instrumented mounting.

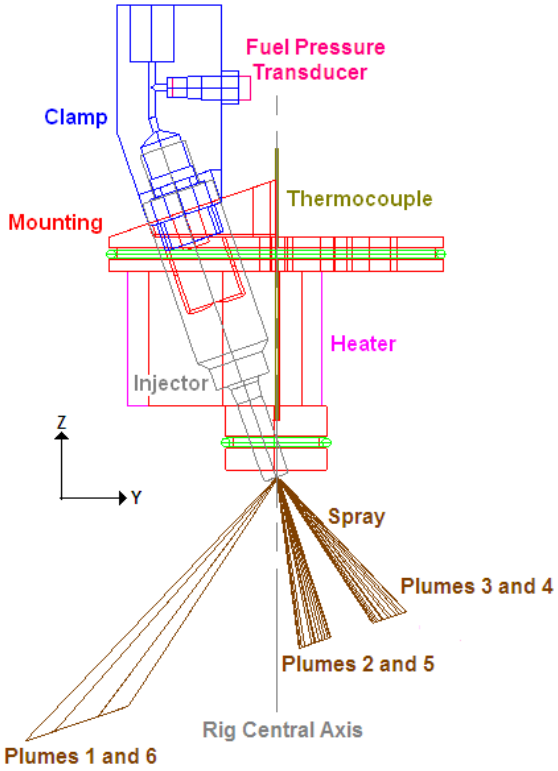

Figure 2-31 Schematic of Injector and Mounting

To enable the injector and hence the fuel to be heated as it would be in an operating, firing engine, the main section of the mounting was surrounded by an Omega MB1 150W band heater. A fine tip temperature feedback K-type thermocouple was located as near to the injector tip as could be managed through a blind hole in the centre of the mounting block. Closed loop control of the heater was made from the thermocouple using a Desin Instruments BS-1100 programmable temperature controller. As the thermocouple was located near the tip and not inside the fuel passage itself, the temperature quoted throughout this work is that of the injector body and surrounding mounting. The assumption has been made throughout that, given a heat soak time of at least half an hour and a low injection frequency of < 1 Hz, the fuel temperature is that of the injector body. Using a similar heating, temperature measurement and injection frequency arrangement on a pressure swirl injector, and measuring the in-nozzle temperature prior to injection, Moon *et al.* [2007] measured a temperature difference between the fuel and injector body of less than 3 K. Heat insulation wadding was packed between the crucible and injector mounting to minimise heat transfer. The crucible was covered in a further 2 layers of insulating matting which

was secured with reflective tape to minimise heat transfer from the crucible to the chamber gas volume. The entire instrumented injector mounting assembly is labelled and shown schematically in Figure 2-32.

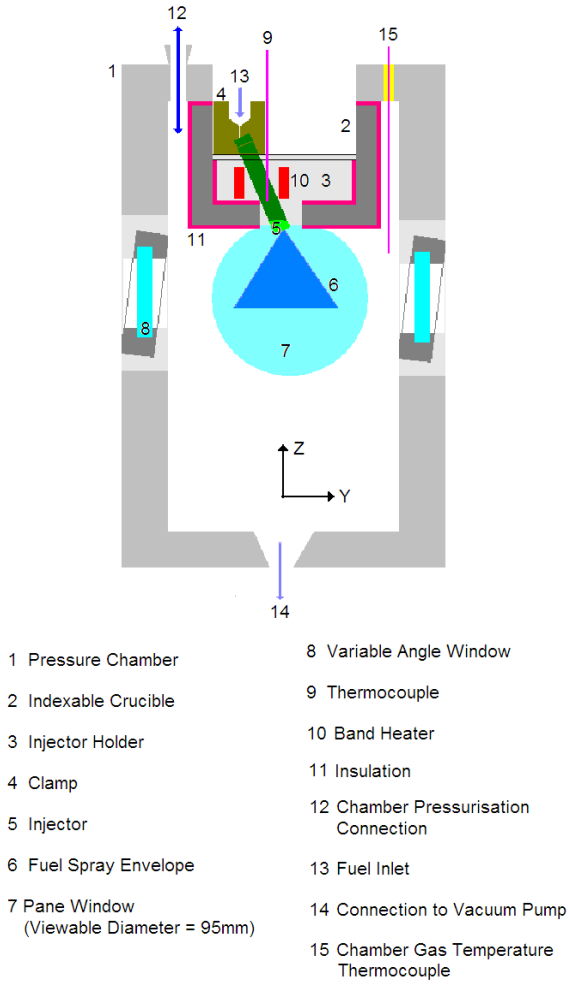

Figure 2-32 Schematic of Cylindrical Pressure Chamber

2.5 Fuels Tested and Their Properties

The transport properties of the liquid fuel injected may be expected to play a significant role in the development and break-up of the spray. To investigate the effect of these properties, a range of multi- and single-component fuels were examined in this work.

The multi-component fuels tested were:

- Standard Gasoline – a retail pump grade fuel which was marketed by Shell in the Netherlands until 2004 and has a number of light components
- Standard Gasoline with Additives – the same fuel as above but with an undisclosed amount of detergent additives designed to enable more efficient engine operation. This fuel was also a retail pump fuel, usually sold under a premium brand.
- Heavy Gasoline – a retail pump gasoline with fewer high volatility components designed for use in warmer climates.
- Model Fuel – a multi-component purpose blended "pseudo-fuel" designed to mimic the distillation properties of a full boiling range gasoline, but free from aromatics so that it would not fluoresce under laser illumination for quantitative Laser Induced Fluorescence (LIF) measurements carried out in a sister project to the presented work. However, it's volatility properties provide a comparative multi-component fuel for this work with properties part way between those of Standard Gasoline and Heavy Gasoline.

The constituents of the Model Fuel are listed in Table 2-1. The listed components account for 99.19% of the total analysed volume, the remaining 0.81% consists of a variety of hydrocarbon components in concentrations below 0.07%. It should be noted that any in-cylinder laser induced fluorescence work using the Model Fuel would require the addition of one of three dopants, acetone, toluene and trimethylbenzene, to trace the desired co-evaporative molecules within the fuel (Stevens *et al*. [2006]). These dopants would be added by volume to make-up up to 5% of the fuel. Whilst such a low concentration is not expected to greatly alter the fuel properties, there might be a slight change in spray behaviour, although examination of these effects was beyond the scope of this study.

Component	% by volume
Propane	0.55
iso-Butane	1.86
n-Butane	4.90
iso-Pentane	16.91
n-Pentane	0.18
iso-Octane	48.09
2,2-Dimethylhexane	1.09
2,5-Dimethylhexane	0.37
2,3,4-Trimethylpentane	0.59
2,3,3-Trimethylpentane	0.14
n-Octane	11.09
iso-Dodecane	9.58
n-Decane	2.34
3-Ethylnonane	0.54
p-*n*-Propyltoluene + 1,4-Dietbz	0.40
1,2-Diethylbenzene	0.28
1-Methyl-4-*t*-Butylbenzene	0.17
o-*n*-Propyltoluene	0.11
Total	99.19

Table 2-1 Composition of Multi-Component Model Fuel (Fuel 3)

Interpretation of quantitative results obtained with these multi-component fuels, such as the calculation of the Weber and Ohnesorge numbers for these fuels, is not trivial, particularly at the range of fuel temperature and gas pressure conditions necessary for a constructive analysis. Therefore, specific single components fuels for which the Weber and Ohnesorge numbers could be calculated were also tested. These reference single-component fuels were chosen to be *n*-Pentane and *iso*-Octane. *o*-Xylene, a heavier gasoline component with boiling temperature 144 °C is also included in graphical representation of the results from this work to aid discussion of the results. *o*-Xylene was not included in the experimental test matrix because its high viscosity

and very low volatility properties make it insensitive to the phenomena investigated. The use of this component served only to define the range of gasoline's thermo-physical properties, which is useful when discussing the effects of different chemical components on the observed behaviour of gasoline as a fuel.

Finally, oxygenated fuels Ethanol and Butanol were also tested to compare the fuel spray development and break-up of these "novel" single component fuels with those of traditional multi-component Standard Gasoline.

The principal physical and thermodynamic properties of all these fuels, where available, are summarised in Table 2-2 at standard conditions (1 bar ambient pressure). The Reid Vapour Pressure (RVP) is the pressure exerted by the vapour at standard conditions of 4 volumes of air to 1 of liquid, at 100 F (37.8 °C) and indicates the volatility of the fuel. The vapour pressures were calculated using correlations obtained from Yaws [2006] within valid temperature ranges for *iso*-Octane, *n*-Pentane, *o*-Xylene, Ethanol and Butanol. For gasoline the vapour pressure was obtained experimentally using the standard ASTM D5190 (Dry Vapour Pressure Equivalent, DVPE) test methodology as carried out by Shell Global Solutions (UK) Ltd; further properties were obtained from Kaye [1995]. It should be noted the refractive index has implications for both the imaging of the fuel flows in the nozzle and the measurement of droplet diameters by optical means. The value of a liquid's refractive index is temperature dependent, and reduces by approximately 1.4–1.7% with an increase in fuel temperature to 90 °C (363 K).

The distillation curves for the fuels are shown in Figure 2-33, which clearly shows the single component nature of *iso*-Octane, *n*-Pentane, Butanol and Ethanol in relation to the multi component, and hence temperature spread, fuels. A fuel's vapour pressure is also temperature dependant, with higher volatility fuels exerting a higher vapour pressure at low temperatures. The vapour pressure with respect to liquid temperature for the main fuel types tested is presented in Figure 2-34.

Fuel Properties	Standard Gasoline (with additives)	Standard Gasoline (without additives)	Heavy Gasoline	Model Fuel	*iso*-Octane	*n*-Pentane	Butanol	Ethanol	*o*-Xylene
Density [kg/m^3] (20 °C)	719	720	766	681	692	626	809	794	876
Viscosity [cP] (25 °C)	0.4–0.8	0.4–0.8	0.4–0.8	0.4–0.8	0.51	0.24	3.64	1.08	8.10
Surface Tension [mN/m] (20 °C)	25.8	-	-	-	14.7	15.82	25.4	22.4	29.6
Latent Heat [MJ/kg] (25 °C)	0.364	-	-	-	0.305	0.363	0.430	0.902	0.347
Energy Density [MJ/kg], [MJ/lt]	44, 32	-	-	-	45, 31	48, 30	37, 30	29, 23	42, 38
Boiling Point [°C]	30–190	30–190	35–105	30–190	99.8	36.1	117.2	78.5	144.4
Reid Vapour Pressure [bar]	0.56	0.56	0.67	0.79	0.14	1.08	0.02	0.16	0.17
H:C, O:C	1.92, 0	1.92, 0	-, 0	-, 0	2.25, 0	2.4, 0	2.5, 0.25	3, 0.5	1.25,0
Refractive Index (25 °C)	1.427	-	-	-	1.388	1.358	1.395	1.362	1.496

Table 2-2 Selected Fuel Properties for Gasoline and Single Component Fuels (Kaye [1995], Yaws [2006])

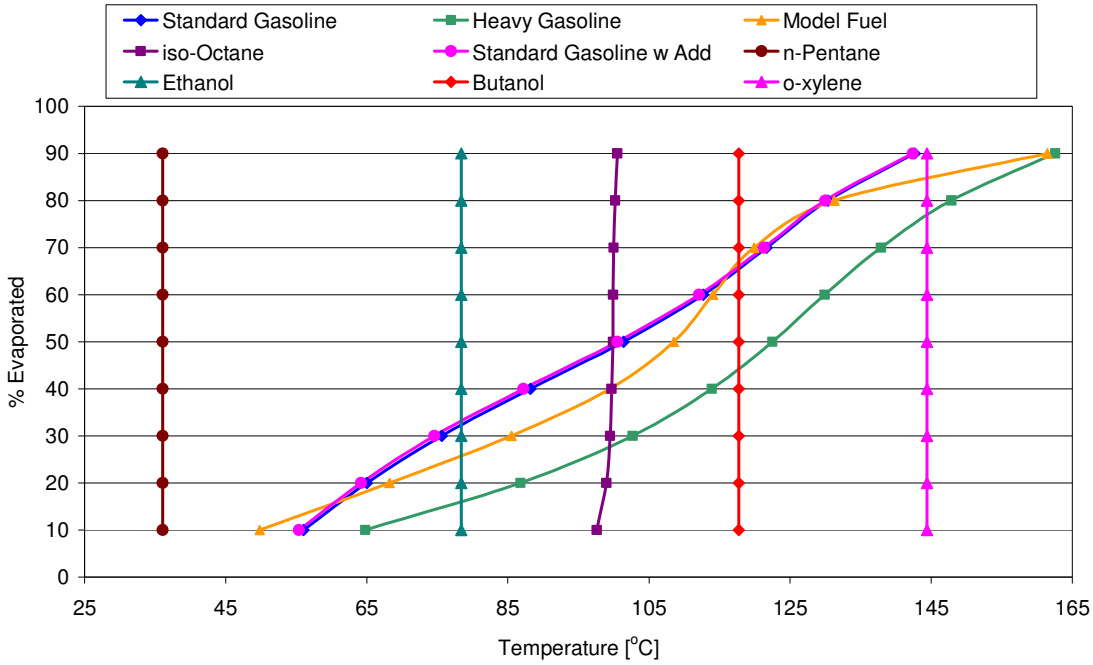

Figure 2-33 Distillation Curves for Fuels Tested in this Work

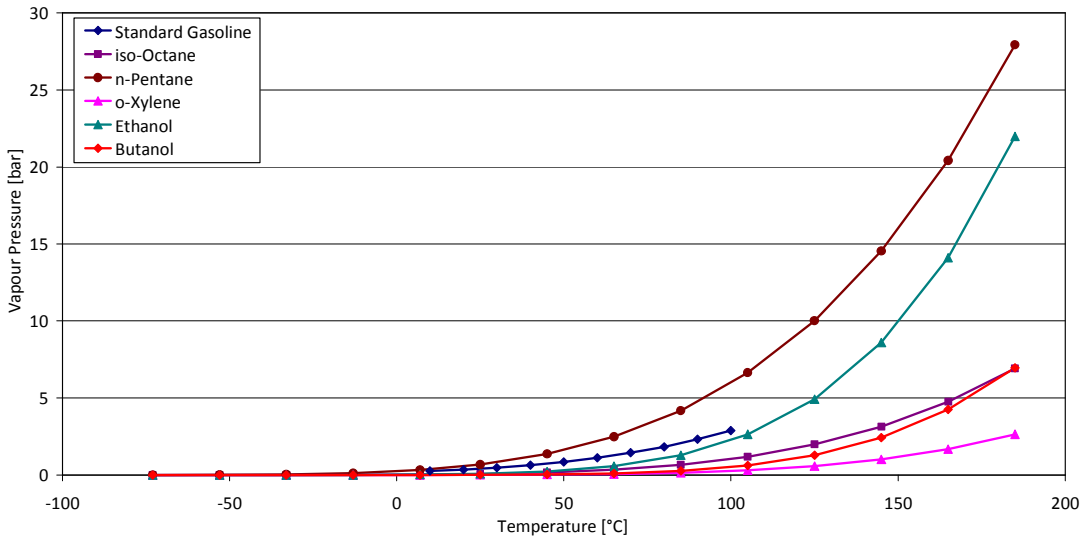

Figure 2-34 Fuel Vapour Pressures

To further indicate the temperature dependence of the fuel properties, bubble point and dew point pressures were calculated by Shell Global Solutions (UK) Ltd for each fuel at various temperatures using a Redlich-Kwong equation of state based on UNIFAC method coefficients for each species identified on the gas chromatograph of each of the fuels, as defined by Redlich and Kwong [1949]. The values calculated for the multi component fuels and the non-oxygenated fuels are listed in Table 2-3 and illustrated graphically in Figure 2-35 and Figure 2-36 for the bubble and dew pressures respectively. The bubble point is indicative of conditions under which light ends begin to flash off in a fuel spray, whereas the dew point is indicative of the final evaporation of heavy ends from a droplet. It should be noted, however, that the bubble point and dew point are equilibrium concepts and during a transient process such as spray development heat and mass transfer effects will complicate the picture.

Fuel	Bubble Point Pressure [bar]					Dew Point Pressure [bar]				
	20°C	50°C	90°C	120°C	180°C	20°C	50°C	90°C	120°C	180°C
Standard Gasoline (without additive)	0.3	0.8	2.4	4.5	13.0	0.0	0.1	0.5	1.3	5.9
Heavy Gasoline	0.4	1.0	2.6	4.5	11.6	0.0	0.0	0.3	0.8	3.8
Model Fuel	0.5	1.2	3.0	5.4	13.8	0.0	0.1	0.4	1.1	5.1
iso-Octane	0.1	0.2	0.8	1.8	6.3	0.1	0.2	0.8	1.8	6.3
Standard Gasoline (with additive)	0.3	0.8	2.4	4.6	13.2	0.0	0.1	0.5	1.3	6.0
n-Pentane	0.6	1.6	4.7	9.1	26.4	0.6	1.6	4.7	9.1	26.4
Butanol	0.0	0.0	0.3	1.1	6.3	0.0	0.0	0.3	1.1	6.3
Ethanol	0.1	0.3	1.6	4.3	20.7	0.1	0.3	1.6	4.3	20.7

Table 2-3 Fuel Boiling Characteristics

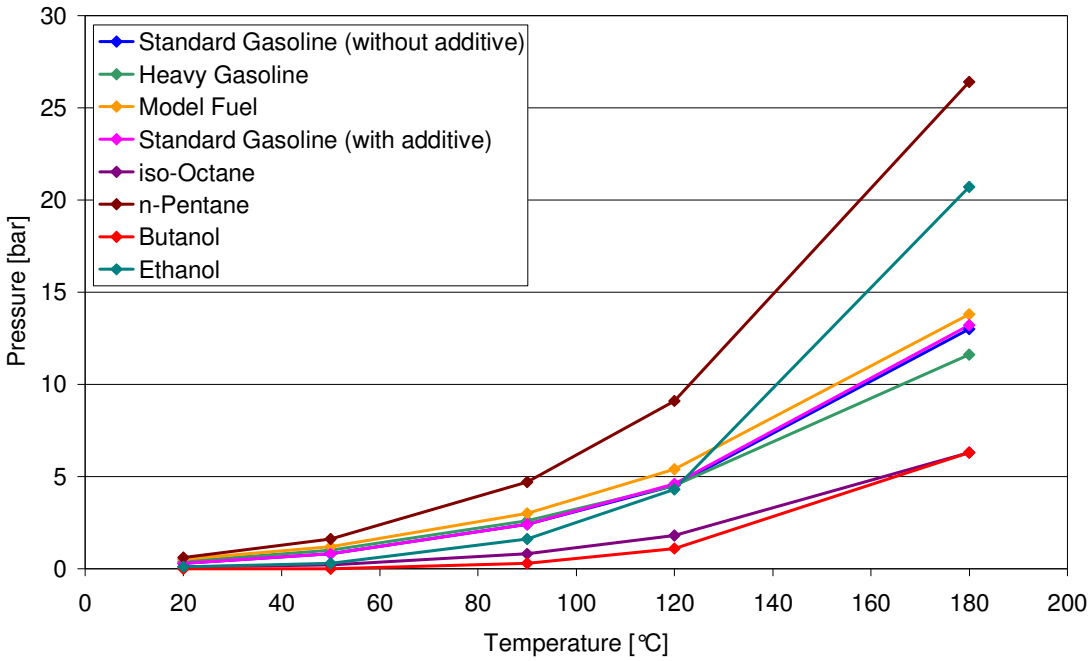

Figure 2-35 Graph of Bubble Point Pressures for Fuels

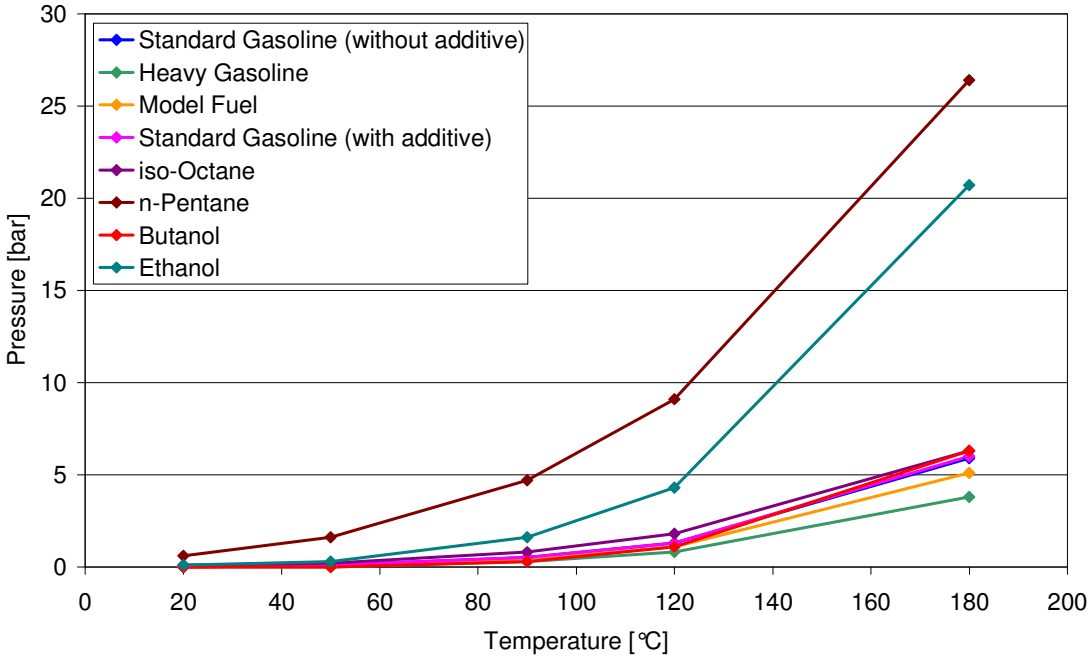

Figure 2-36 Graph of Dew Point Pressures for Fuels

2.6 Spray Characterisation Techniques

To achieve the aims of this work, the spray emanating from the injector was measured, analysed and characterised using a number of techniques to determine the physical phenomena at work during spray development and collapse, and the interaction between the injector operating conditions and these phenomena. The main spray analysis technique employed was visual spray imaging and subsequent image analysis. A number of imaging techniques were employed using both high magnification, focussed on specific regions in the spray, and the global visualisation of the spray development. Optical non-intrusive droplet sizing techniques were also used at various locations within the spray to link the observable phenomena to the physical properties of the spray, as described below.

2.6.1 Shadowgraph Imaging

Both single shot and high speed video digital imaging of the spray emanating from the injector was carried out to characterise the spray development and subsequent break-up. Both these techniques were in essence shadowgraphs as the lighting was provided by a uniform source directly behind the spray, the light source used being dependent on the imaging technique. In a shadowgraph, the detected light intensity at a given location in the image is a function of the light scattering by the second spatial derivative of the refractive index. For this work, the illuminating light was diffused through a pair of semi-opaque Perspex sheets to provide a uniform background to the spray. In a shadowgraph the light refraction responds to the second spatial derivative, Settles [2006]. For low refractive index gradients such as those produced by the presence of a vapour in a gas, this second derivative is small and hence the sensitivity of the technique to these gradients is very low, making the technique particularly suitable to imaging the liquid phase and its break-up in relation to spray formation.

2.6.2 Schlieren Imaging

The Schlieren backlighting technique was developed by August Toepler in 1864 in the study of supersonic motion, Settles [2006]. In the Schlieren technique a light source is focused on the region of interest, where the light is diffracted by density gradients and hence these can be imaged by focusing the detected image on the camera lens. Hence, Schlieren images are sensitive to the first spatial derivative of light diffraction, and hence are much more sensitive to low refractive index gradients

and suitable to the imaging of the vapour surrounding the liquid spray. The layout of light source, lenses and camera as well as the border of the light path for the Schlieren technique is shown in Figure 2-37. Note that a pin-hole was used instead of the more common knife-edge at the detector (high speed camera) to block part of the refracted light, causing a detected amplitude difference, and hence the Schlieren image.

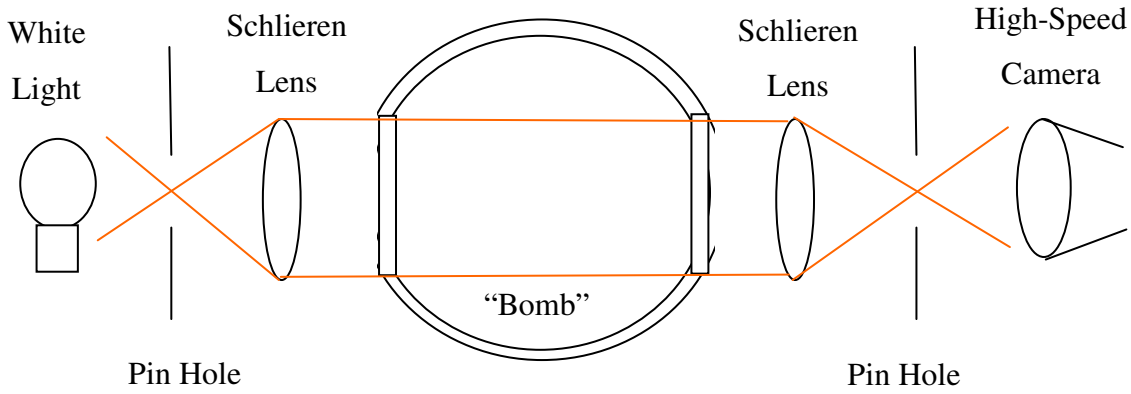

Figure 2-37 Schematic of Schlieren Imaging Technique

For this work, Schlieren imaging of the spray was carried out in the Leeds University combustion bomb. For a full discussion of the relative merits of these backlit imaging techniques, their history, optical set-ups and application the reader is guided to Settles [2006].

2.6.3 Mie Scattering Imaging

Mie Scattering as an imaging technique refers to the scatter of an incident light source by particles. In the case of spray imaging the light source is usually a laser sheet along the spray axis and the particles are the spray droplets. In this work, laser sheet illumination of the spray was carried out in the Leeds University combustion bomb using a copper vapour laser synchronised to the camera frame rate. A series of mirrors and sheet forming optics aligned the beam vertically with the centre of the spray along the y-axis. As such, the sheet did not pass through any of the plumes directly under normal spray formation. The bomb was filled with a fine mist of olive oil prior to injection, which was illuminated using the laser sheet. Upon combustion of the injected fuel the seed mist is also combusted, leaving a scattering "void" showing the location of the flame and the volume consumed by it.

Spray and combustion imaging was carried out in the Leeds bomb using a pair of high speed cameras. A mirror was placed at an angle of 45 ° to the imaging window to allow simultaneous recording. A dichroic filter, which blocked light at the laser wavelength of 510.6 nm, was placed over the lens of the Schlieren imaging camera to avoid saturation by the laser light during the simultaneous application of imaging techniques.

2.6.4 High Speed Imaging

High speed imaging of the fuel sprays using both the Shadowgraph and Schlieren techniques was carried out using a CMOS Photron APX high speed digital video camera. A number of optical lenses were used in conjunction with the high speed camera in this work to capture different aspects of spray development and break-up. For the majority of images, lighting was provided for the duration of the injection event by a Multiblitz Variolite 500 flash-gun, which provided a light pulse of ~2.5 ms duration, over which the spray event was imaged. Triggering for the high speed camera and flash lamp, as well as to the injector driver unit, was provided by an AVL 327 Timing Unit. The imaging and lighting hardware is shown in Figure 2-38.

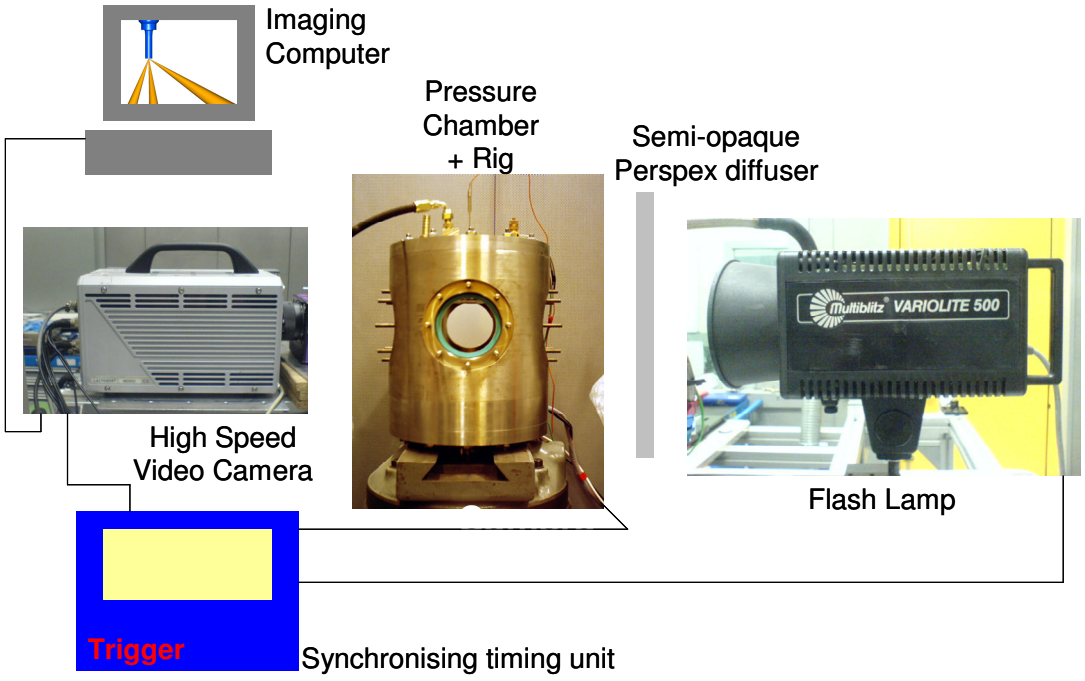

Figure 2-38 Schematic of High Speed Imaging Equipment

Global Spray Imaging

The majority of work here presented is based on the global spray development. To capture this development with a high temporal resolution, the high speed camera was set to a frame fate of 9000 frames/second to coincide with 1 frame every crank and degree (CAD) for an engine running at 1500 rpm, a standard research engine operating speed based on the World Wide Mapping Point. For clarity of images the camera shutter speed was set to 1 μs, the shutter opening occurring at the same interval in every frame. To capture the entire spray development viewable through the camber optical windows, a Nikon AF Micro Nikkor 60mm 1:2.8D lens was used at an f-stop of 2.8. These settings provided a maximum resolution of 640 x 480 pixels. A total of 20 frames were recorded for each injection event, with 120 injection events recorded for the majority of test points along with 10 background events (no injection). These events were subsequently scrutinised for adequate lighting or other imaging or triggering deficiencies to produce a set of 100 injection events and 1 background set for every imaged test point.

Zoomed Imaging

For the high-magnification, high-speed recording of the spray emanating from the injector nozzle, an Infinity Optics K2 long distance microscope lens was attached to the camera. This lens is made from a number of interchangeable modules, and for this section of the work was configured to give a magnification of 1.6, using a “standard” objective lens at a working distance of 560 mm. According the K2 manual, these settings equate to a depth of field of 0.47 mm. However, in practice the use of a fully open aperture and frame rate limited light intensity was found to give good resolution of the nozzle and spray. To capture the spray emanating from the nozzle and its initial development, the frame rate was set to 50,000 frames per second with a constantly open shutter, equating to 20 μs per exposure. Lighting was provided by the flash lamp located behind the spray as per the global spray imaging.

High Magnification Imaging

To capture the individual features of the spray as it emerged from the injector nozzle, the K2 microscope lens used for the zoomed imaging was reconfigured to increase its magnification. A Kenko doubler lens was inserted between the camera and lens, a 2x magnification extension tube was inserted between the objective and focusing lenses,

a CF3 objective lens was used in conjunction with the K2 lens. Furthermore, a magnification filter (additional thin lens) was attached to the front of the lens to further increase the magnification. These modifications increased the magnification to approximately 10x, giving a field of view of 3 mm by 3mm. Further additions to the optical system were found to visibly reduce optical clarity.

Due to the small field of view, the light intensity in that field to enable the diffracted light to be captured was required to be substantially increased. To achieve the required light intensity, a NewWave Pegasus Nd:YLF (Neodymium: Yttrium Lithium Fluoride) laser firing at 527 nm wavelength was used at a power of 20 Watts. A light sheet forming lens was attached to the laser, giving a planar illumination sheet onto which the optical arrangement could be focused. The laser was synchronised to the camera frame capture rate of 9000 frames/second, the exposure being limited by the laser light pulse duration of ~ 180 ns.

2.6.5 Image processing

A number of macroscopic spray parameters were measured from both the single shot and high-speed images of the spray. Image processing and measurement of the pertinent parameters was automated for speed and convenience through the creation of macro routines in the image processing software Image Pro. For the single shot images, the preliminary binarisation of the images was performed by hand due to the small number of images. The very large number of images acquired using the high speed techniques required the automation of all steps in image processing and measurement.

The Photron software used to record the majority of the spray events saved the entire test run consisting of all spray events in sequential files, with each file name containing the number of that file in the overall sequence. The Phantom camera software used to record the Schlieren lit sprays in the Leeds combustion bomb saved files in a similar manner to the Photron software, except that these had to be extrapolated from the proprietary format cine files as a prerequisite step.

The first task required was to correctly sequence the images in batches relating to the injection event number, and the image number in that event sequence. This was

achieved by identifying the file number in the saved sequence and dividing this number by the number of images recorded for each spray event. The integer of the result was then used as the sequence identifier, and the decimal used to order the sequence. Each file was then renamed and saved with the format [injection event number]_[sequence number] in a file the name of which contained the information of the test parameters.

Once all images were identified, the appropriate background image (same test conditions but without injection event) was subtracted from each spray image to normalise the background pixels. This was found necessary to compensate fro the decaying light intensity from the single-pulse flash gun used as the illumination source. 3 background pixels, selected to be near the nozzle but in an area where spray was not detected for any condition, were then sampled and the average of these used to determine the threshold value at which the image would be binarised into either white pixels to indicate the presence of spray, or black pixels for the background. To determine the optimum threshold value for each image, sensitivity analysis on the penetration calculated from the spray images based on different threshold levels was carried out on images of the spray produced by the standard pump gasoline, as this fuel had average volatility compared to the other fuels tested in this work, and would therefore show an average sensitivity based on the visibility of fuels droplets at the spray tip.

For the sensitivity analysis one frame was thresholded to different levels and the penetration length of plume pair 1/6 (as labelled in Figure 2-2), measured using the automated routine detailed above. The plume measurements recorded for the different threshold values are compared below in Figure 2-39. For each image in the sequence, there is an increase in measured spray length with increasing threshold value. The increase level is greatest at the lower and higher ends of the threshold scales, shown by the steeper gradient for each plume penetration curve. At the centre of the graph the curves for each sequence number plateau to some extent, showing the least sensitivity of plume penetration to threshold value over this threshold range.

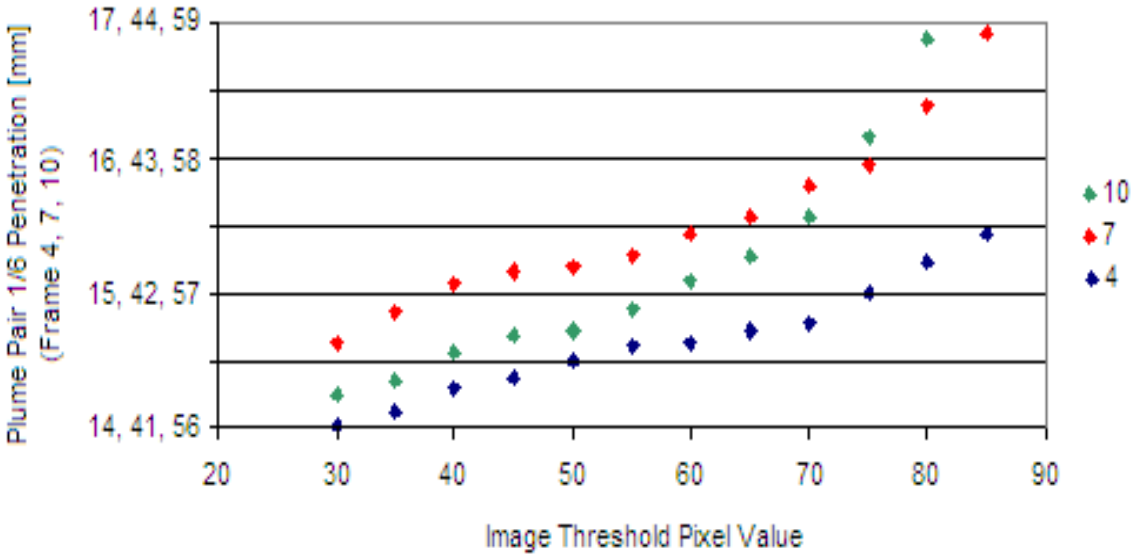

Figure 2-39 Plume Penetration Length Measurement Variation with Threshold Value

This effect is further illustrated by normalising each of the plume penetration curves shown in Figure 2-39 by the penetration measured at the pixel threshold value of 55, as shown in Figure 2-40. Any sensitivity relative to the measured plume length at a threshold value of 55 is shown by deviation from the normalised value of 1. As can be seen, for all threshold values the deviation is less the 6%. The least sensitivity is seen below threshold values of 60 for frames 7 and 10, although the sensitivity of frame 4 is larger for this pixel range.

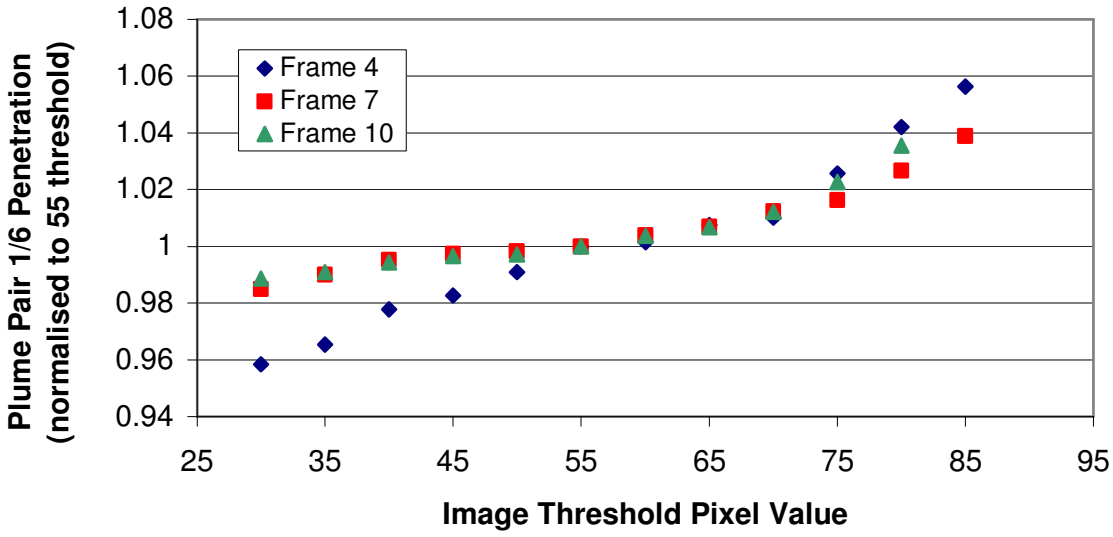

Figure 2-40 Normalised Plume Penetration Variation with Threshold Value

The sensitivity analysis showed that for all plume pairs throughout the spray development, the least sensitivity of the measured spray plume length to threshold value was observed for a threshold value of around and just above 55 for the lighting conditions for the images over which the sensitivity analysis was carried out. During image processing, it was found that some very early and later spray images had reduced lighting intensity due the flash lamp duration and gradual intensity reduction, although these images do not form the basis of in-depth analysis in this work. However, to successfully process these reduced intensity images, the greyscale value at which these images were thresholded was reduced, as tabulated below in Table 2-4. Note that for the majority of images the average background value was in the range of 95 – 255, the threshold value therefore being 56 to minimise the measurement sensitivity to the lighting intensity.

Average background pixel value range	Threshold
0 – 19	0
20 – 29	4
30 – 39	8
40 – 49	16
50 – 59	24
60 – 69	32
70 – 79	40
80 – 89	48
90 – 255	56

Table 2-4 Threshold Values for Average Background Pixel Intensity

Due to the very large number of images collected and analysed throughout this work (~ 300,000), a number of image analysis macro routines were written for the software programme ImagePro. The macros include routines to rename each captured image file so as to identify the spray number and the sequential order of the image, as well as the test conditions used for the experiment. Further routines thresholded the image to the appropriate value, and carried out a range of pixel value based measurements. All values were written to specific image name related cells in appropriately titled Excel worksheets for subsequent analysis. The overall automated spray analysis principles are as follows:

Due to the variety of angles at which the plumes emanate from the injector, and the different projections of these angles for each spray view, each thresholded image was rotated by the manually measured plume angle for that test condition, to align each spray plume in turn to the vertical axis. The rotated image was then scanned along each row of pixels from the bottom of the image upwards. As each row of pixels was scanned, the sum of the greyscale value of 2 adjacent pixels calculated. When this sum was equivalent to 2 white pixels (a white pixel being the detection of spray), the row number was stored. The condition of 2 adjacent spray pixels was used to avoid any measurement errors which may occur due to the detection of single white pixels whether due to detected spray droplets (but not the main plume), or due to small dark

spots in the original image background. Testing of the routine with the criteria set to 3 or more adjacent white pixels was not found to affect the sensitivity of the measurement. The pre-determined row number of the injector tip, and hence top of the plume, was then subtracted from the detected spray tip row number to give a spray length in pixel rows. A scale measured for each test batch determined from a graduated ruler imaged in the chamber then allowed the conversion of the detected spray length to an axial spray measurement. The steps taken in the spray detection and measurement routine are shown below in Figure 2-41. The individual plume length measurements were then stored and written to separate Excel worksheet cells based on the spray event number and the image sequence in that event. This process was repeated for each plume pair seen in the side view in turn (*i.e.* plumes 1 & 6, plumes 2 & 5 and plumes 3 & 4), for each image (*i.e.* each spray event at every time interval).

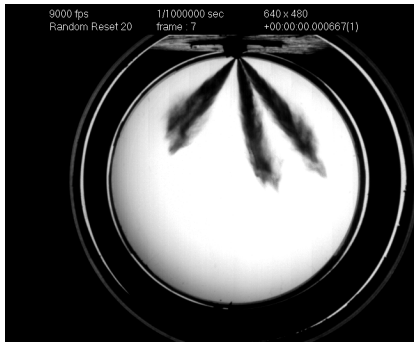

Raw Image

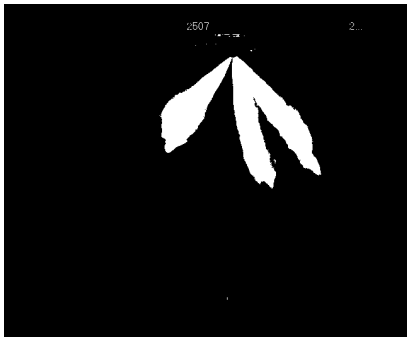

Background Removed and Thresholded Image

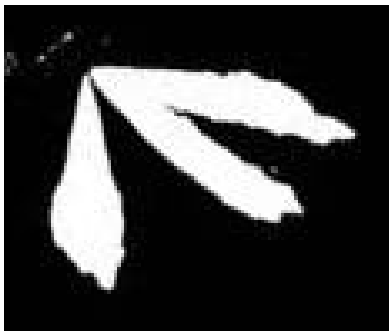

Image rotated to align spray plumes vertical image axis and scanned along rows from bottom of image to detect spray tip. For detection of cone angels, image not rotated and scanned at pre-determined row numbers.

In this example (20 °C, 1.0 bar Standard Gasoline, 7777 µs ASOI), image rotated through 320° to align plumes 1/6.

Figure 2-41 Spray Detection and Measurement Methodology

Spray plume angles were measured in the same routine by scanning along pre-determined pixel rows from the edge of the image until the plume boundary was detected from each side. A trigonometry routine was then used to determine the plume angle. This was also written to a templated Excel worksheet along with a combined overall spray angle calculated in a similar way. The image processing and measurement routines employed were checked against manual measurements of the parameters under investigation and were found to be robust in operation with little susceptibility against small droplets at the tip, or at the spray periphery when measuring the cone angles. The large number of spray events over which each of the measurements were aggregated further aided to reduce the influence of individual measurements on the average, trend indicating values.

At the end of each measurement routine one Excel workbook was produced for each test condition with separate worksheets for each plume penetration length, plume cone angle and overall combined spray cone angle. Each spray event was written in individual columns, and each sequence number was written in a separate row in that column. A number of aggregation calculations such as averaging over all the events for each sequence number were carried out to produce the graphs and figures presented in subsequent chapters of this Thesis.

2.6.6 Droplet Sizing

The instantaneous droplet size at a given location in a spray is both a function of the rate of break-up of the spray as well as the initial drop size. The rate of the droplet size change and potential break-up is determined by the fuel properties in relation to the prevailing operating conditions. Hence, for complete characterisation of a spray, information on the droplet size as well as the global spray formation and break-up is required to be known. Both Laser Diffraction and Phase Doppler Anemometry (PDA) were used to characterise the spray droplet size distribution.

Laser Diffraction

Laser diffraction is a relatively simple technique used to measure droplet size distributions within a spray. The technique measures the angle of diffraction of a light beam passing through a transparent particle caused by the curvature of the particle

boundary. The curvature of a particle, or droplet, is directly and inversely proportional to its size; a small droplet will have a surface with high curvature whilst a bigger droplet will have lower surface curvature, as illustrated in Figure 2-42.

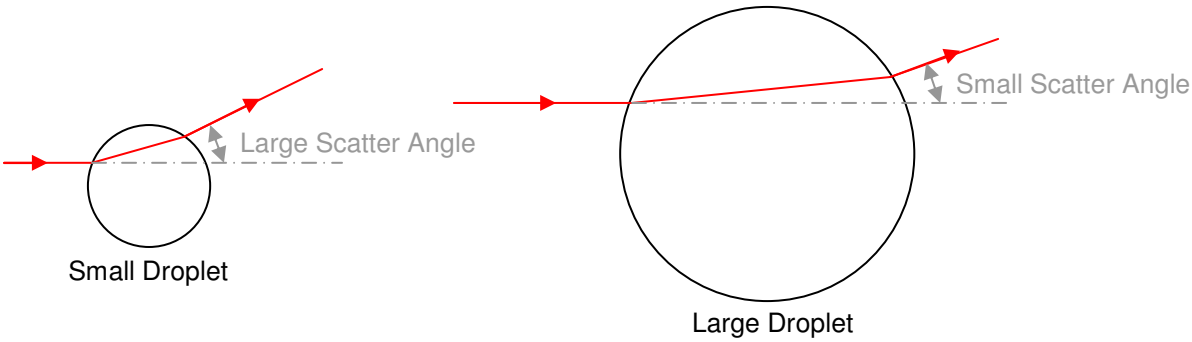

Figure 2-42 Effect of Droplet Size on Scattering Angle

In light diffraction droplet sizing hardware a monochromatic light beam of constant and known intensity is provided by a diode laser and the refracted beam is measured on a series of concentric annular photo-sensors, each relating to a discrete droplet size based on a series of calibration coefficients input into the calculation algorithm, relating to the hardware and material being analysed [e.g. refractive index of droplets and suspension]. The light intensity measured by each photo-sensor relative to the un-scattered light intensity measured at the sensor central location is used to calculate the number of droplets at that droplet size, and hence a droplet size distribution is calculated based on the light intensity collected on all the rings. Measurements are only valid if sufficient intensity is detected on both the inner target and the annular rings and hence the technique is limited to the measurement of sprays of low optical obscuration over the line of sight. The hardware used in this work to carry out laser diffraction droplet sizing was a Malvern Spraytec. The measurable droplet size range claimed by Malvern is from 0.1 µm to 900 µm (with the 300 mm lens as used), over a 36 element (log spaced) detector array.

Williams [1994] used an earlier model of droplet sizer based on the same principles (Malvern 2600c) to measure droplet sizes and distributions for a pintle type Port Fuel Injection (PFI) injector. However, it was found that towards the end of injection the number of large droplets was overestimated due to “beam steering” through small

angles of the incident light beam by evaporated fuel vapour. To this end a post-processing routine was developed whereby the user was presented with the raw scattering data and input the ring numbers over which they had confidence in the results. The light intensity data for the non-trusted rings was then interpolated from the trusted data and the propriety algorithm used to re-calculate the droplets sizes based on the modified data, effectively "removing" the beam steering effect from the calculated data. Due to the volatile nature of some of the fuels used in this work, a similar phenomena and hence measurement inaccuracy may have been expected to occur for the sprays analysed. However, the Malvern Spraytec used for this work had a much higher data rate than the Malvern 2600c used by Williams. The Spraytec records and analyses 250 records for each 2 ms injection event (125 kHz). To produce statistically valid results at least 100 events were recorded for each test condition, giving a minimum of 25,000 records for each condition. Such a number of records is obviously too high to manually interrogate and correct for the effect of beam steering. In addition, the variability in the internal trigger delay of the Spraytec computer meant that the record number related to a slightly different timing in each spray; for example in one spray the start of injection might be detected in record 20 whilst in the following spray the internal Spraytec delay was slightly longer and the start of injection was detected in record number 17. As such, it was not feasible to overlay the injection event data based on record number to produce an average temporal droplet size development for each test condition, from which the beam steering could then be removed. The only combination or averaging function available within the RTSizer software which controls the Spraytec is to average all the sprays over their entire record length. Initial droplet sizing experiments to align the apparatus with the spray revealed that the measured droplet size distribution changed little over the spray duration, until beam steering effects were evident toward the end, and after, the injection of heated fuel. To utilise the limited features of RTSizer and avoid invalid measurements due to beam steering, advantage was made of the stability of the droplet size distribution and the Spraytec measurement interval was limited to the early stages of spray development only for all test conditions.

Ipp *et al.* [1999] observed that late injection, high gas pressure sprays become so dense due to the entrainment of small droplets in the centre of the spray that laser-based drop size techniques could not be used. Due to the asymmetric nature of the

spray being analysed and the high plume liquid density, it was found necessary to isolate plumes under certain conditions to achieve the required optical transparency, and it was also found not to be possible to take measurements using the laser diffraction technique close to the injector nozzle. To enable droplet size measurements to be taken using this technique, a spray plume separator was designed and manufactured. This device was installed in the chamber just below the injector nozzle, and captured the plumes from 5 of the 6 nozzle holes whilst allowing the plume to be measured to pass through an opening. By allowing all the sprays to exit the nozzle, the internal injector flow rate and characteristics were not affected. The captured fuel was led away from the measurement beam through gullies, so as to avoid the erroneous measurement of the run-off fuel. A schematic of the plume separator is shown in Figure 2-43.

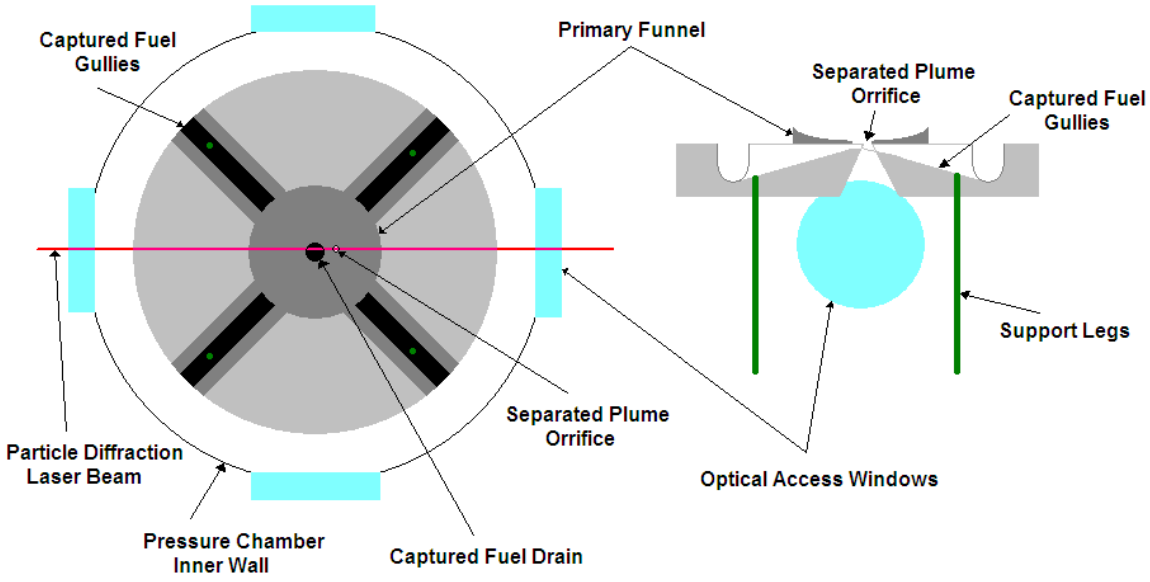

Figure 2-43 Spray Separator

Phase Doppler Anemometry

Phase Doppler Anemometry (PDA) refers to the measurement of flow or particle properties through detection of the scattering effect of the particle on non intrusive optical laser light. As such, a typical PDA set-up consists of a laser, a light frequency phase shifter, a transmitting optical unit, a receiving unit and a signal processor. The measurement volume of a PDA system is formed by the intersection of two laser

beams. The focused laser beams intersect and form an ellipsoid shaped pattern of bright and dark "stripes," known as fringes. The spacing of these fringes is determined by the light wavelength and the angle between the two beams which is set by the transmitting optics. The initial laser beam features a multicolour wavelength that ranges from 420 to 520 nm. For a two component system, a laser beam splitter separates the output beam into green (514 nm) and blue (488 nm) wavelengths. Both of these laser beams are further split into two beams by another set of beam splitters. The majority of PDA systems feature a frequency shift between the two laser beams of the same wavelengths generated by means of a Bragg-cell which imparts a constant velocity on the fringe pattern in the measurement volume. When a particle or droplet passes through this measurement volume, it scatters the light in all directions with a frequency dependant on the droplet velocity and phase dependant on its size. A stagnant particle in the control volume will generate a signal with the same frequency as the shift frequency. Particles moving at positive or negative velocities (directionally relative to the fringe velocity) will generate positive or negative signal frequencies (respectively) relative to the shift frequency.

To detect the scattered light, a receiver is placed at an off-axis location and contains optics which focuses the scattered light falling on its lens onto photo detectors. Whilst droplet velocity measurements may be obtained from a single photo detector, for size information further photo-detectors, located a known distance apart, are required. As the droplet passes through the measurement volume each photo-detector captures the same burst signal at a frequency proportional to the droplet velocity; due to their relative positions, a phase shift proportional to the droplet diameter is acquired at each detector. In the case of two photo-detectors, droplet size measurement may be achieved by measuring the time delay of the scattered light signal that is captured by the first detector at time (t) and the second detector at time (t + Δt).

Eq. 2.1 $$\Delta\varphi = 2\pi\frac{\Delta t}{T}$$

Where $\Delta\varphi$ is the phase difference, and T is the period of one cycle of the signal. A larger particle will have a lower refraction angle, increasing Δt, and so the phase difference detected between the two photo-detectors increases with increasing particle

size. However, since phase is a modulo 2π function, this value cannot be exceeded. Therefore, if a particle is large enough and causes the phase to go to, or beyond, a value 2π, a two-detector PDA system would not be able to discriminate between this large and a much smaller particle causing the same phase shift. Hence, a system of three photo-detectors is used, where two individual phase differences are obtained from two detector pairs having different relative positions.

To enable the selection of a suitable droplet measurement set-up, the light scattering mechanisms of a spherical droplet should be considered. As illustrated in Figure 2-44, the incident light beam is partially reflected at the surface and partially refracted into the particle. Upon exiting the particle without any further internal reflection, the scattered beam is known as the 1st order refraction. Higher order refraction (2nd order and above) also arises after internal reflections and subsequent refraction out of the droplet into the surrounding medium.

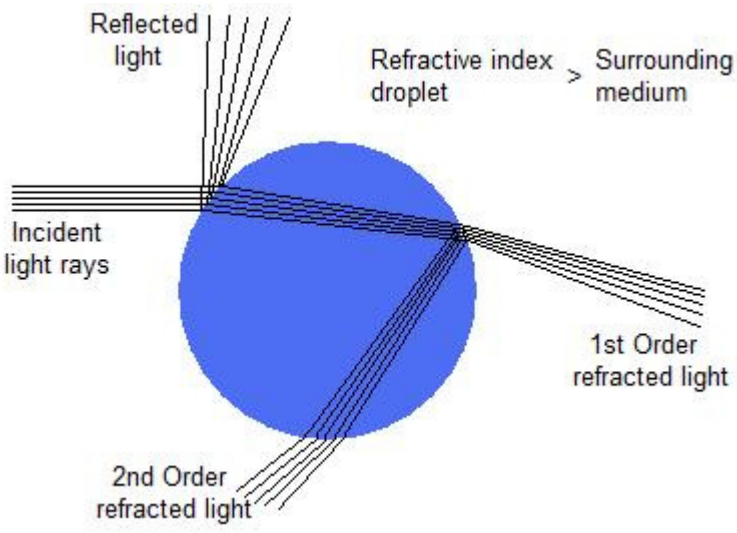

Figure 2-44 Schematic Representation of Light Reflection and Refraction of a Spherical Droplet

The intensity of reflected and refracted light varies with the angle of detection relative to the incident beam. For Phase Doppler measurements of high refractive index droplets relative to the surrounding medium (as is the case for gasoline sprays), the relatively steady intensity of first order refracted light over a range of forward scattering angles makes this the most suitable for detection, Albrecht *et al*. [2002].

Although the detection of any reflected light can be avoided at a forward detection angle of ~74° (dependant on the liquid refractive index; the "Brewster Angle"), the higher amplitude of refracted light than that of reflected light at forward detection angles up to 75° means that meaningful measurements can be obtained at any forward angle less than this value.

For this work, a 2 component TSI PDPA (Phase Doppler Particle Analyzer) system was used to allow simultaneous measurement of two components of a droplet's velocity as well as its size. The system used comprised of:

- Coherent Innova Argon Ion Laser 70c (S/No: 04059742)
- TSI Fiberlight multicolour beam separator and Bragg-cell; Aerometrics 450200 (S/No: 70515183)
- TSI Transmitter: TMx50 400 mm focal length (S/No: 70516053)
- TSI receiver: RVx070 300 mm focal length (S/No: 70517349)
- TSI Photomultiplier: PDM1000-2P (S/No: 70517173)
- TSI Signal Processor: FSA4000-2P (S/No: 70516120)

The focussing optics mounted on the transmitting probe formed an ellipsoid intersecting volume of the 2 pairs of laser beams of with major and minor axis of approximately 2.863 and 0.092 mm for the green and 2.716 and 0.088 mm for the blue beams respectively. The PDA receiver unit was fitted with a 300 mm focal length lens and 3 photo detectors. Using an opto-isolator to inhibit detection during non-trigger periods and resetting the measurement time interval with every trigger signal, the measurement period was defined by the measurement system trigger duration for each test case, which was 3.5 ms for all conditions to fully cover the injection duration of 2.0 ms as well as the post injection droplets resulting from the pintle closing event. The high spray density and the chaotic nature of break-up resulted in variable valid measurement rates for different injection events. The total number of samples collected for each injection event was of the order of 25 samples per millisecond for each of the 100 measurement injections, resulting in around 5000 valid droplet size and velocity measurements over the duration of the injection event for each test condition. A similar number of droplet measurements at each

measurement location was used by van der Wege and Hochgreb [2000, a] to characterise a pressure swirl injector and was found to give a good correlation to the expectant theoretical droplet size trends in relation to the fuel temperature and in-cylinder pressure conditions.

For the PDA system, the receiving optics were mounted at 40° to the transmitting beams to capture high intensity refracted light within the confines of the available optical access to the pressure chamber. To process the data collected for this work the measurement period was divided into narrow time windows of 0.1 ms for droplet velocity and size information relative to start of the measurement event. Post processing was performed using the proprietary TSI Flowsizer software using the following settings:

- Software Coincidence: On (to ensure measurements are from single individual droplets by setting a pre-defined measurement interval related to the estimated droplet size and velocity)
- Software Subrange: On
- Intensity Validation: On (To ensure only droplets with a detected beam intensity corresponding to its calculated size from the phase data were measured)
    - The slope of the upper intensity validation curve was set to 9.00 mV/µm*µm, with an intercept of 45.00 with a lower to upper intensity ratio of 0.1
    - The resulting measurable valid droplet size range was from 0 µm to 30 µm
- Probe volume correction: Off

	Channel 1	Channel 2
PMT Voltage (V)	400	420
Burst Threshold (mV)	700	700
Band Pass Filter (Hz)	10 – 65 M	10 – 65 M
Downmix Frequency (MHz)	0	0
	Minimum	Maximum

Diameter (μm)	0	30
Intensity (mV)	0	1000

Table 2-5 TSI PDA System Settings

The values measured by any PDA set-up are highly dependant on the experimental arrangement and equipment settings, Albrecht [2002]. As such, care should be taken not only in comparing measurements from different sources, but also in interpretation of the values. As is the case for this work as much as other published measurements, values should be taken to be comparative to those from the same data sets where similar experimental settings and assumptions are used.

2.6.7 Refractive Index

The refractive index of a material is a measure of the propensity for an electromagnetic wave (light) to propagate through the material. The electromagnetic conductivity of a material is dependant on its molecular density, and hence varies with material temperature. The refractive indices for the majority of the fuels used in this work are presented in Table 2-6 for fuel temperatures of 25 °C and 70 °C. Pitcher *et al*. [1990] carried out extensive sensitivity analysis of the refractive index of a liquid on PDA measurements and noted that the phase-droplet size relationship based on the geometric optics of first-order refraction for refractive indices from 1.45 to 1.29 were comparable with those obtained from Mie theory for refractive indices between 1.45 and 1.22. The analyses were restricted to droplets up to 30 μm in diameter, *i.e.* the upper size limit for the fuel spray droplets. The geometric analyses show virtually no dependence of the phase on the variation of the refractive index for forward scattering angles between 30 and 70 °. However, whilst validating the use of a single assumed value which limits the inaccuracy of the drop size measurement to +/- 5 %, Pitcher *et al*. also note that drop sizes at high temperatures will be overestimated if a “cold” (higher) refractive index is assumed.

Fuel	Source	Refractive index	
		25 °C	70 °C
Gasoline (unspecified)	Zigan *et al*. [2009]	1.427	1.410
iso-Octane	Zigan *et al*. [2009]	1.393	1.370
Ethanol	Speight [2005]	1.362	1.339
Butanol	Speight [2005]	1.395	
n-Pentane	Speight [2005]	1.358	

Table 2-6 Refractive Index Values for Fuels

Despite these limitations, a lack of information on the refractive index variability of the fuels used with temperature required the use of a single value for the refractive index. This value was selected as 1.4 for all PDA measurements to cover the range of refractive indices to 1 decimal place for the majority of the experimental conditions as the exact fuel temperature and hence refractive index was not known for all of the fuels at tested temperatures.

2.6.8 Comparison of Drop Size Measurements Obtained with Different Techniques

Prior to the commencement of measuring the spray droplet sizes in the chamber, a rig was set-up to validate the simultaneous spray measurement using both the Malvern Spraytec and the TSI PDA system. A spray paint atomiser was filled with water and held open to provide a continuous, near uniform source of droplets. This was directed at a large funnel connected to the vacuum pump system described above to prevent the build-up of water puddles. The assembled rig with the water droplet spray is shown in Figure 2-45.

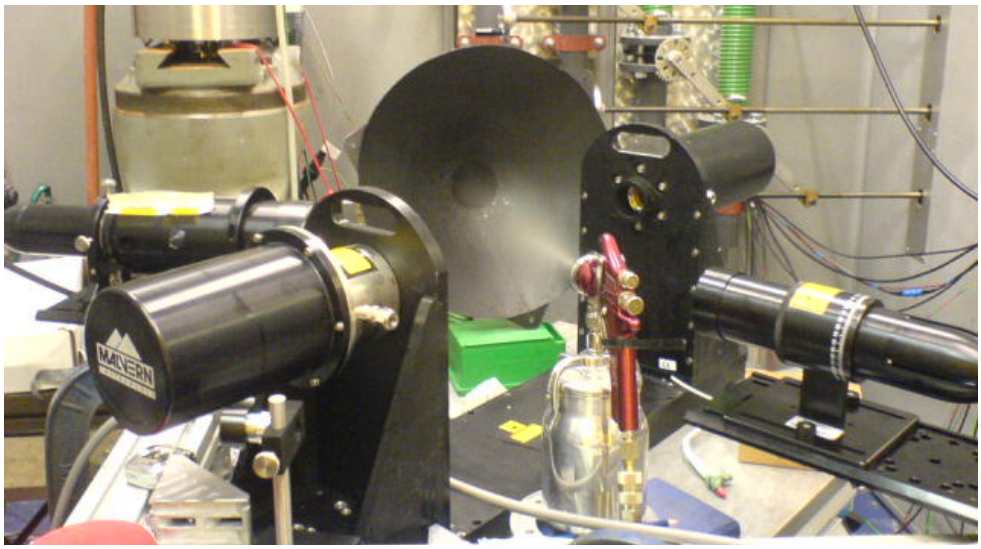

Figure 2-45 Droplet Size Measurement Validation Rig

As discussed above, the two droplet sizing techniques employed operate on different principles and take measurements of different properties of spray; the Malvern Spraytec measures the droplet size along its measurement beam (spatial measurement) whilst the TSI PDA system is a point measurement (temporal measurement). As such, these measurements are not directly equivalent, with different factors affecting each measurement, as discussed in detail by, for example, Hirleman *et al.* [1990]. The measurements obtained from this rig are recorded below in Table 2-7 in terms of the Sauter Mean Diameter (SMD, D[3,2]). The Sauter Mean Diameter is the diameter of a theoretical droplet which would have the same volume to surface area ratio as for the droplet size distribution measured, and is widely used in fuel spray analysis due to its indication of the vaporisation characteristics of the spray. The measured SMD is larger for the PDA system as this was aligned to measure the droplets in the centre of the spray, whilst the Spraytec system also accounts for the fine droplets in the "mist" surrounding the main core of the spray.

µm	Malvern Spraytec	TSI PDA	Difference
D[3,2]	24.45	29.35	16.5 %

Table 2-7 Comparison of Droplet Measurements

Appendix A

Nozzle Orifice Images

Injector 004

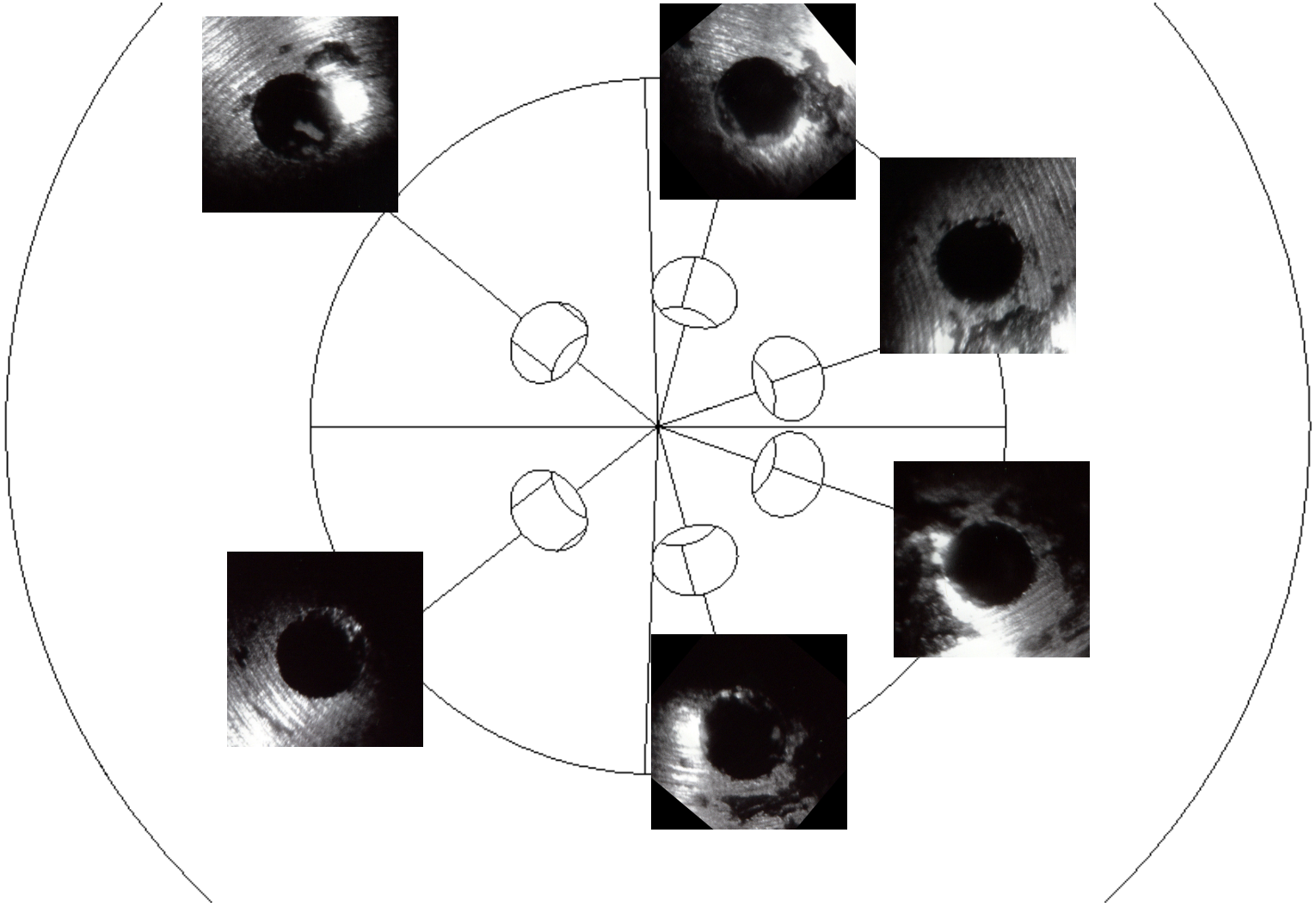

Appendix B

Octagonal Chamber Design Calculations

To calculate the required wall thickness, as a first order approximation the octagonal chamber was considered to be a cylindrical thin walled pressure vessel. A thin walled pressure vessel is one where the internal radius larger than 5 times its wall thickness. The highest stress in a thin wall pressure vessel is the hoop (circumferential) stress, which is that in the material to resist the pressure multiplied by the cross sectional area over which it acts, and hence the hoop stress can be calculated from the expression:

$$\sigma_h = \frac{pr}{t}$$

Where σ_h is the hoop stress, p is the maximum or minimum (if negative) gauge pressure to be contained (or resisted if external pressures), r is the internal radius of the vessel and t is the wall thickness. The hoop stress is twice the value of the longitudinal stress, and so in general if the wall thickness is sufficient to contain the hoop stress, the longitudinal stress can also be resisted. However, this does not account for mechanical fixings which may be stressed longitudinally, such as those which hold the lid and base to the chamber body. The material selected for manufacture was Grade 303 Stainless Steel (also designated as Euronorm 1.4305) for its strength and machineability. This grade of stainless steel has a tensile strength of 500 MPa, translating to a proof strength (0.2 % elongation) of 190 MPa. The maximum pressure to be contained by the chamber was 10 bar gauge, which equates to 1 MPa. The chamber diameter was limited by the transmission range of the Laser Diffraction drop sizing hardware ("Malvern" in Figure 2-23) to 400 mm between opposing flats. On the approximation of the octagonal chamber to a cylindrical pressure vessel, this equates to an internal radius of 200 mm, or 0.2 meters. The height of the chamber was designed to be 300 mm along the sides, to mirror the previous cylindrical chamber and minimise the required modifications to the existing instrumentation and services as regards cabling and plumbing etc. Within these dimensional constraints, each octagonal side was calculated to have a maximum width of approximately 163 mm. Based on the value of the internal "radius", the minimum wall thickness required to resist the pressure was:

$$t = \frac{1 \cdot 0.2}{190} = 1.05 \times 10^{3} m = 1.05 mm$$

Whilst such an approximation may be used to calculate the required wall thickness, the "flats and corners" arrangement of an octagonal chamber also bring about the possibility of additional stresses in these areas. The total force on each flat area is the multiple of the pressure and its surface area, resulting in a force of 48.9 x 10^3 N. The sides of the new chamber were designed to be jointed using a tongue and groove arrangement (see Figure 2-23) to lock the sides together under pressurisation and to present a small gap which could be filled with a sealant to maintain air-tightness. The highest material stress would occur at these tongues, where the forces on two adjoining sides would act. In reality, the force on the side plate would act over the two joining tongues as well as the lid and base. However, to enable the required thickness for each tongue to be calculated, it was assumed for the entire force to be withstood by a single tongue. The force divided by the proof strength of the material yields a required material surface area of 0.000257 m^2 at the base of the tongue, equivalent to 257.36 mm^2. Given the height of the chamber as the tongue length, the minimum required thickness was calculated to be 0.857 mm. These calculated minimum values were incorporated into the design process, where in most cases the material thickness as determined by practical considerations was far greater than that calculated to be required. The plate thickness used throughout the chamber design was 20 mm (approx 20 times required thickness), and the tongue thickness was 5.8 mm (approx 6.5 times required thickness). Using these values, the maximum plate deflection based on the force acting as a point load on a supported side plate was calculated using an on-line calculator to be 0.12 mm. Given that the optically accessed plates would be further supported by the window securing rings, and that the experiments for this work would be carried out a maximum of half the design pressure, such a deflection was deemed to be acceptable, and the above used values were used in the manufacture of the chamber.

The main other parameter important in the design of the chamber was the number of bolts required to secure the base and lid to the chamber sides. The total maximum force on the base on lid was calculated to be 123.8 x 10^3 N. For high tensile studding adhering to DIN standard 975, the proof stress is 340 MN/m^2. This gives a required studding cross sectional area of 364 x 10^{-3} m^2. For an M8 stud, with a diameter of 8mm, this

requirement would be met by 7.28, or rounded up to 8 studded fixings. To ensure sufficient redundancy, 2 fixings per side were used, resulting in 16 fixings for each of the chamber base and lid.

Appendix C

Octagonal Chamber Engineering Drawings

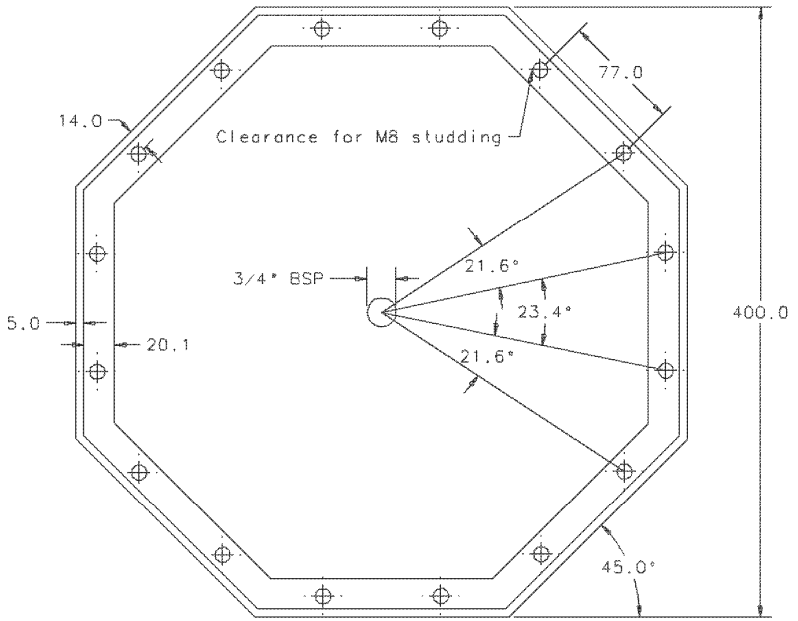

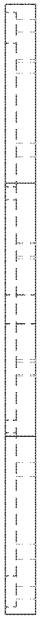

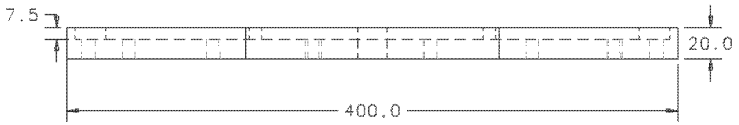

1 Off
Third Angle Projection

Chamber Base
Material: Stainless 303 All tolerances +/- 0.1mm
Drawn by: Zane van Romunde 17/02/06
All Dimensions in mm Do Not Scale

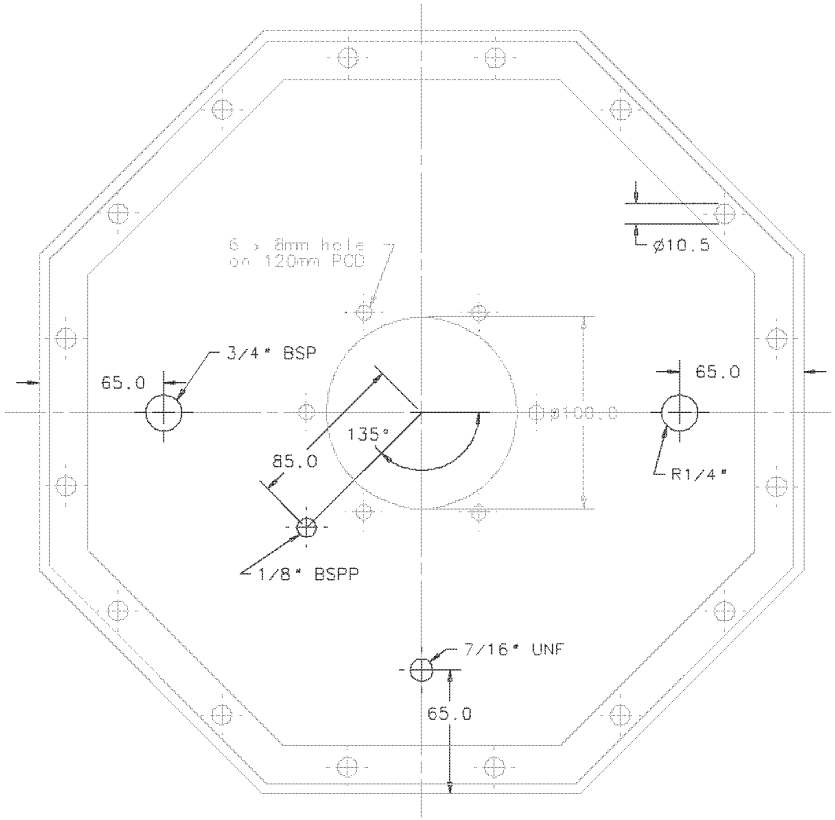

1 Off
Third Angle Projection

Dimensions same as
Base except central
features

Modifications shown
in RED

Modifications to
Chamber Lid

Material: Stainless 303
All tolerances +/- 0.1mm

Drawn by: Zane van Romunde
30/08/06

All Dimensions in mm
Do Not Scale

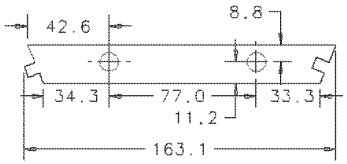

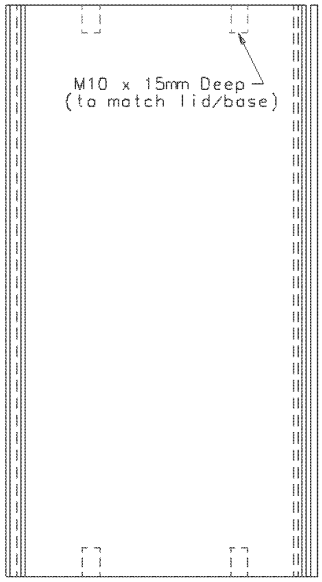

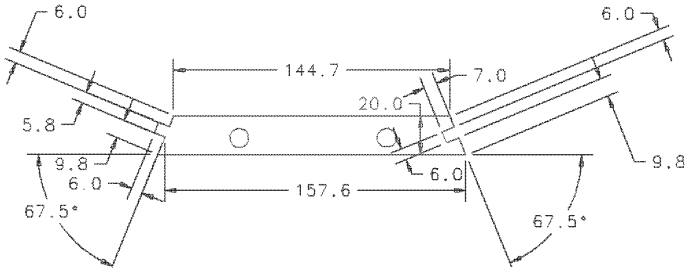

8 Off
Third Angle Projection

Blank Side
Material: Stainless 303 All tolerances +/- 0.1mm
Drawn by: Zane van Romunde 17/02/06
All Dimensions in mm Do Not Scale

2 Off
Third Angle Projection

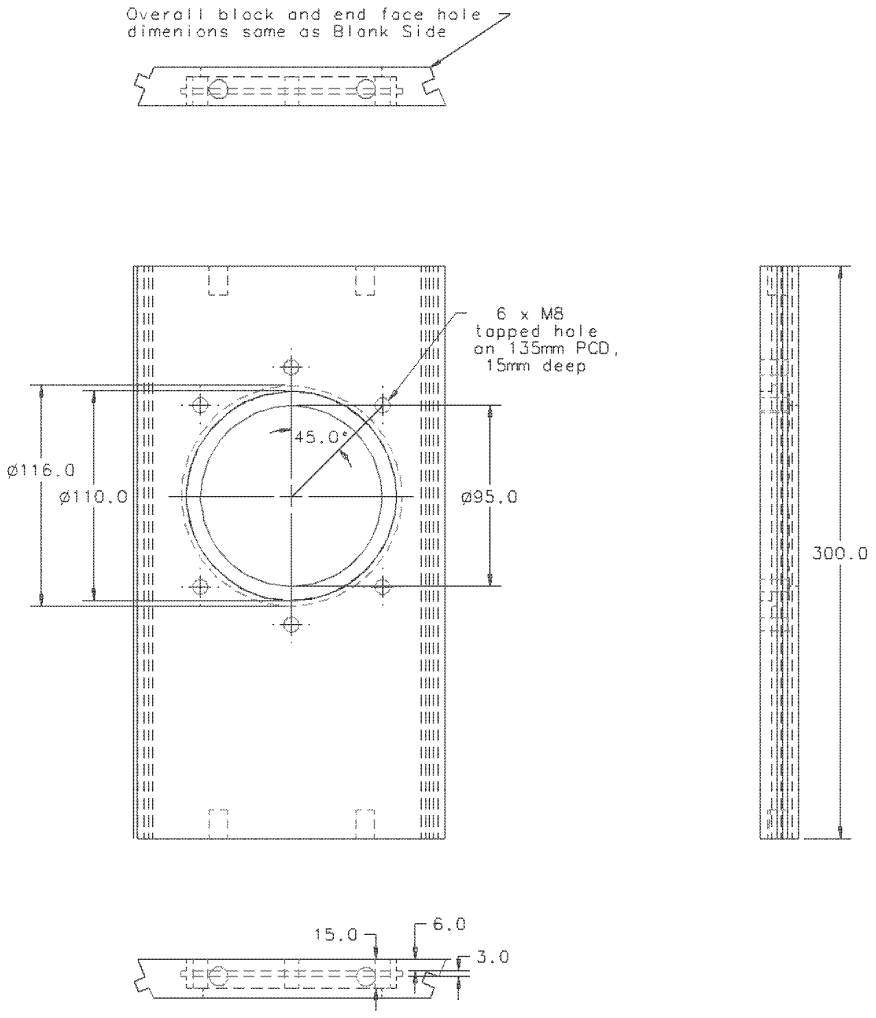

Small Window Side
Material: Stainless 303 All tolerances +/- 0.1mm
Drawn by: Zane van Romunde 17/02/06
All Dimensions in mm Do Not Scale

3 Off
Third Angle Projection

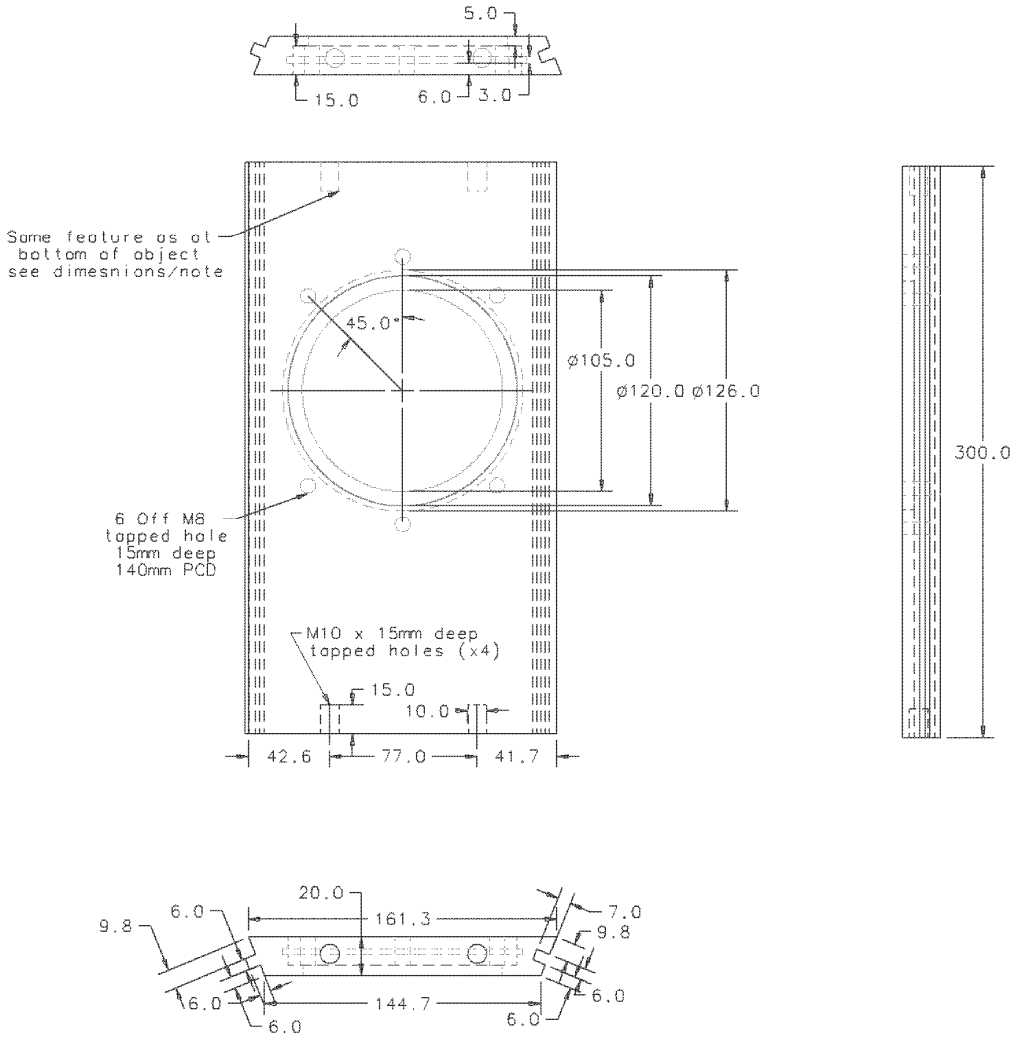

Large window Side
Material: Stainless 303 All tolerances +/- 0.1mm
Drawn by: Zane van Romunde 17/02/06
All Dimensions in mm Do Not Scale

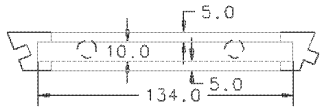

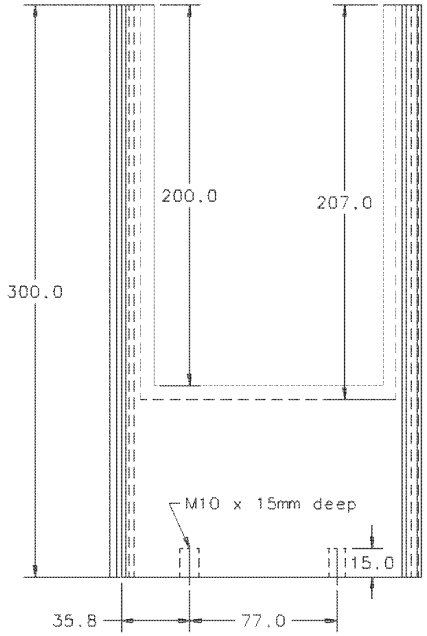

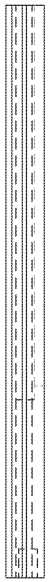

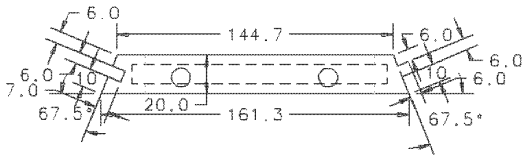

1 Off
Third Angle Projection

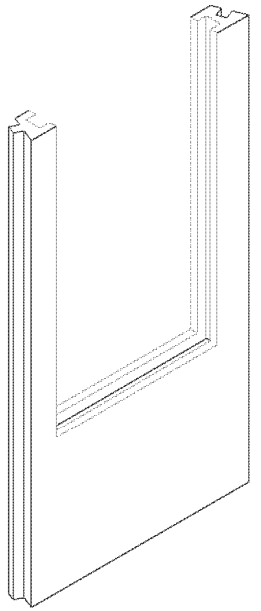

Plane Window Side
Material: Stainless 303 All tolerances +/- 0.1mm
Drawn by: Zane van Romunde 17/02/06
All Dimensions in mm Do Not Scale

1 Off
Third Angle Projection

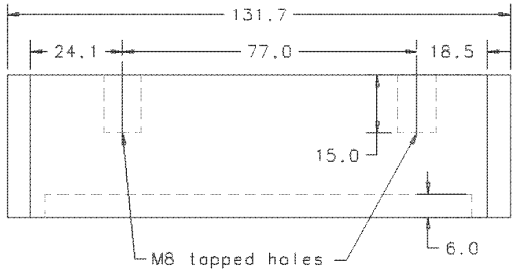

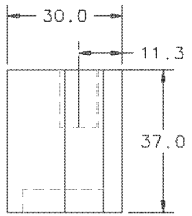

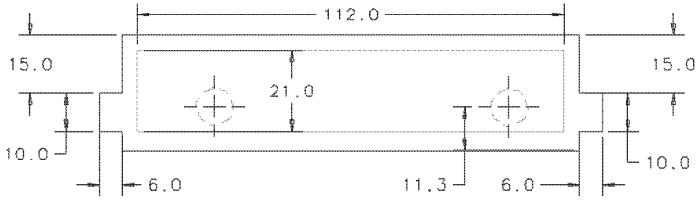

Upper Window Holder
Material: Stainless 303 All tolerances +/- 0.1mm
Drawn by: Zane van Romunde 17/02/06
All Dimensions in mm Do Not Scale

3 Spray Development

To examine the gas pressure and fuel temperature effects on the spray formation, initial spray development characterisation was carried out by high speed imaging of the spray from the injector from a variety of views, operating with the different fuels, injector body temperatures and chamber gas pressures. These global spray images are detailed in this chapter and the quantitative spray parameters determined from the processed images are discussed in relation to the images.

3.1 Experimental Conditions

3.1.1 Operating Conditions

To understand the physical mechanisms operating within the liquid flow and spray, the spray was imaged over a range of operating conditions. The parameters varied were the fuel temperature (by altering the injector body temperature) and the chamber gas pressure for a range of fuels with different single and multi-component properties as described in the previous chapter. To mimic engine in-cylinder pressure conditions for different direct injection strategies, the in-chamber gas pressure was set to a range of pressures from 5.0 to 0.3 bar absolute.

A high gas pressure of 5.0 bar was selected to represent late injection operation at around 25° before top dead centre (BTDC), although in an engine this would be accompanied by an increase in gas temperature, which could not be replicated for this work. 5.0 bar gas pressure at close to ambient gas temperature may also be considered as a test point to mimic highly-boosted operation during intake or early compression stroke, and acts as a comparable case to motoring optical engine running at similar conditions. 1.0 bar atmospheric conditions and 0.5 bar gas pressures were selected to be representative of early injection for homogeneous charge engine operation under high and low loads respectively. Low in-chamber gas pressures were observed to promote the alteration of spray characteristics and as such more in depth analysis was carried out at 0.5 bar than at the other pressure conditions; spray behaviour under extreme

conditions was investigated at a further reduction in gas pressure to 0.3 bar, the lowest pressure achievable in the chamber.

The fuel temperature was altered by the heating the injector body as previously described to replicate engine running conditions. To replicate conditions from ambient start to fully warm operation, the injector was heated to 20, 50 and 90 °C for the main test conditions. A further test temperature of 120 °C was included to replicate a heat sink scenario. An extreme temperature of 180 °C was also examined for scientific analysis to push the fuels to their limits of boiling and collapse and perhaps mimic extreme in-cylinder conditions such as those after a prolonged period of heat sink.

These experimental test points are shown in the matrix in Table 3-1 for clarity.

		Injector Body Temperature [°C]				
		20	50	90	120	180
Chamber Gas Pressure [bar]	0.3				Extreme	Extreme
	0.5	Main	Main	Main	Main	
	1.0	Main	Main	Main	Main	
	5.0	Main	Main	Main	Main	

Table 3-1 Test Matrix

3.1.2 Imaging

Imaging was initially carried out at the macro scale to capture the overall spray development and establishment into a quasi-steady, fully formed structure, labelled global spray development. Due to the asymmetric nature of the spray, imaging was carried out from a number of angles by rotating the injector mounting in the pressure chamber. These views and their orientation with respect to the injector are shown in Figure 2-2. It should be borne in mind that the injector is inclined at an angle of 19° (to the left in the "Side View" images captured for this work), and that in an engine the entire spray would be rotated clockwise through 19° as seen from the Side View. The images were then analysed to determine and quantify the effects of these operational parameters on the spray development characteristics. A more detailed investigation into the physical phenomena at work to bring about these effects was carried out using

higher resolution imaging of the spray at, and in, the injector nozzle and droplet sizing to correlate the observed characteristics with the physical properties of the spray.

Note that in the images presented in this work, “Base View” images are side-lit and hence are images of refracted and reflected light, and show white liquid against the dark background of the injector mounting. The other views are shadowgraphs of a dark liquid spray against a light background. As also detailed in the previous chapter, the side view is in the y-z plane and therefore directly overlays 2 spray plumes in each shadowgraph, whilst the end view is in the x-z plane and encompasses three plumes with near overlaying axis. In the angle and base views all 6 plumes can be differentiated. From all views, the spray represents the nominal form as supplied by the injector manufacturer and no major deviations were observed to occur over the temporal development of the spray. It should be noted that due to use of a single camera for this work, the presented spray temporal development images are for the same spray event at each condition for each view of the spray. However, sprays captured from different view angles are of different spray events. The images show a single, typical spray arbitrarily selected from the database of captured spray events at the presented condition. Variability analysis of the spray at a given condition was also carried out and is presented following the discussion of the typical spray development.

Due to the similarity in distillation curves of the Standard Gasoline with Additive and the Model Fuel to the Standard Gasoline (without Additive), and resultant similarity in spray reaction to changes in operating conditions, the spray images captured for these fuels are not presented here. However, these similarities should be borne in mind and for the purposes of the following discussion measurements and observations made in relation to Standard Gasoline may be taken to be directly applicable to Standard gasoline with Additive and the Model Fuel.

Images showing the temporal development of the spray for different fuels under a range of test conditions, as well as single time interval “summary” images are presented below to illustrate the observed spray development trends in relation to the fuel properties and test conditions. These images are followed in subsequent sections by further in-depth analysis of the development trends from a range of measurements derived from the images to further quantify the mechanisms affecting the spray form.

3.2 Global Spray Development

3.2.1 Standard Gasoline

Typical spray images captured using the high speed global spray imaging system are shown in Figure 3-1 for each of the imaging views. These images were captured using Standard Gasoline at an injector body temperature (and hence assumed fuel temperature) of 20 °C and at a gas pressure of 1.0 bar, therefore representing ambient conditions. Over the injection duration, the injection event could be described by three different stages with characteristics which are difficult to present in printed format. First, spray plume formation straight out of the nozzle when the flow field is still forming inside the nozzle and gradually. Second, a pseudo steady-state stage, where the spray is stable with defined cone angles, but noticeable periodicity within the inner core spray, with the air entrainment also being visible in the form of a vortex structure of fuel droplets surrounding the spray plume. In the final stage the spray undergoes significant distortion starting near the-nozzle, setting up large scale oscillations in the liquid plume. The time periods of each of these stages are not well defined, and vary between conditions, although these effects can be seen in the images as areas of darker spray which may indicate either regions of droplet clustering or ligaments, and was repeatable from shot-to-shot at all operating conditions. The reasons for this effect are not known but may arise from the hydrodynamic 'flapping' at flow separation locations inside the nozzle, including cavitation mechanisms that will be discussed later.

The development of the Standard Gasoline spray is shown with the same temporal resolution as for Figure 3-1 in Figure 3-2, Figure 3-3 and Figure 3-4 for an injector body temperature of 120 °C and gas pressures of 0.5 bar, 1.0 bar and 5.0 bar respectively. Note that the base view was not captured at the 5.0 bar gas pressure condition due the similarity of the spray form at this condition to the ambient spray form (Figure 3-1) at this gas pressure condition. Within the resolution of these images, the initial spray as captured at 333 μs ASOI appears quite similar for all conditions presented in Figure 3-2, Figure 3-3 and Figure 3-4. As the spray develops over time, however, the individual spray plumes converge at the 0.5 bar gas pressure condition and spread out to form individual jets at the higher pressures, with a closer spacing and more interaction of the jets at the 1.0 bar gas pressure condition relative to the 5.0 bar condition. The complete convergence of the closely spaced plumes (right hand plumes in Side View images) has been labelled "Spray Collapse" in this work as individual spray plumes and their features (spray tip *etc.*) are no longer identifiable in any of the image views.

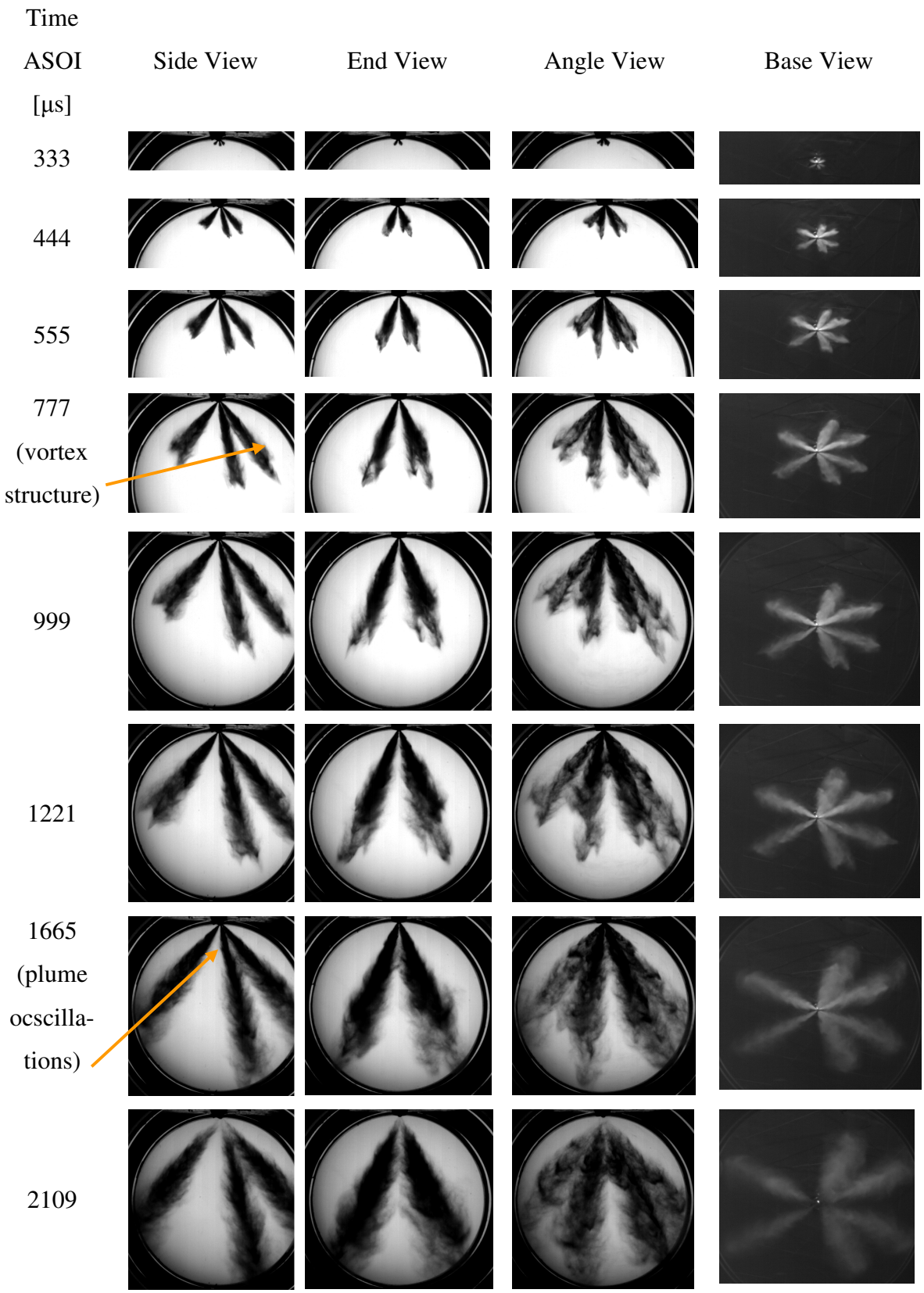

Figure 3-1 Spray Development Standard Gasoline 20 °C 1.0 bar

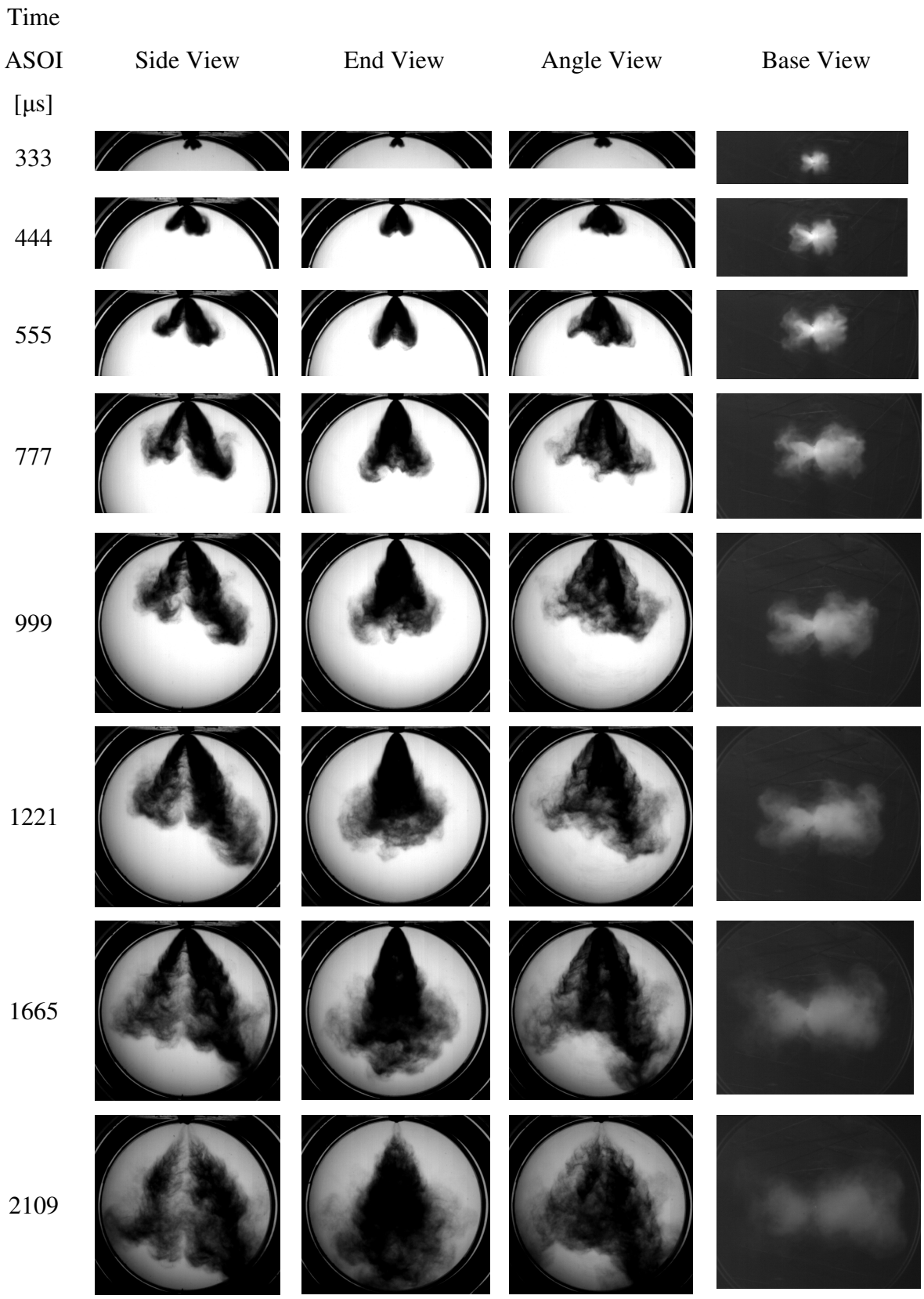

Figure 3-2 Spray Development Standard Gasoline 120 °C 0.5 bar

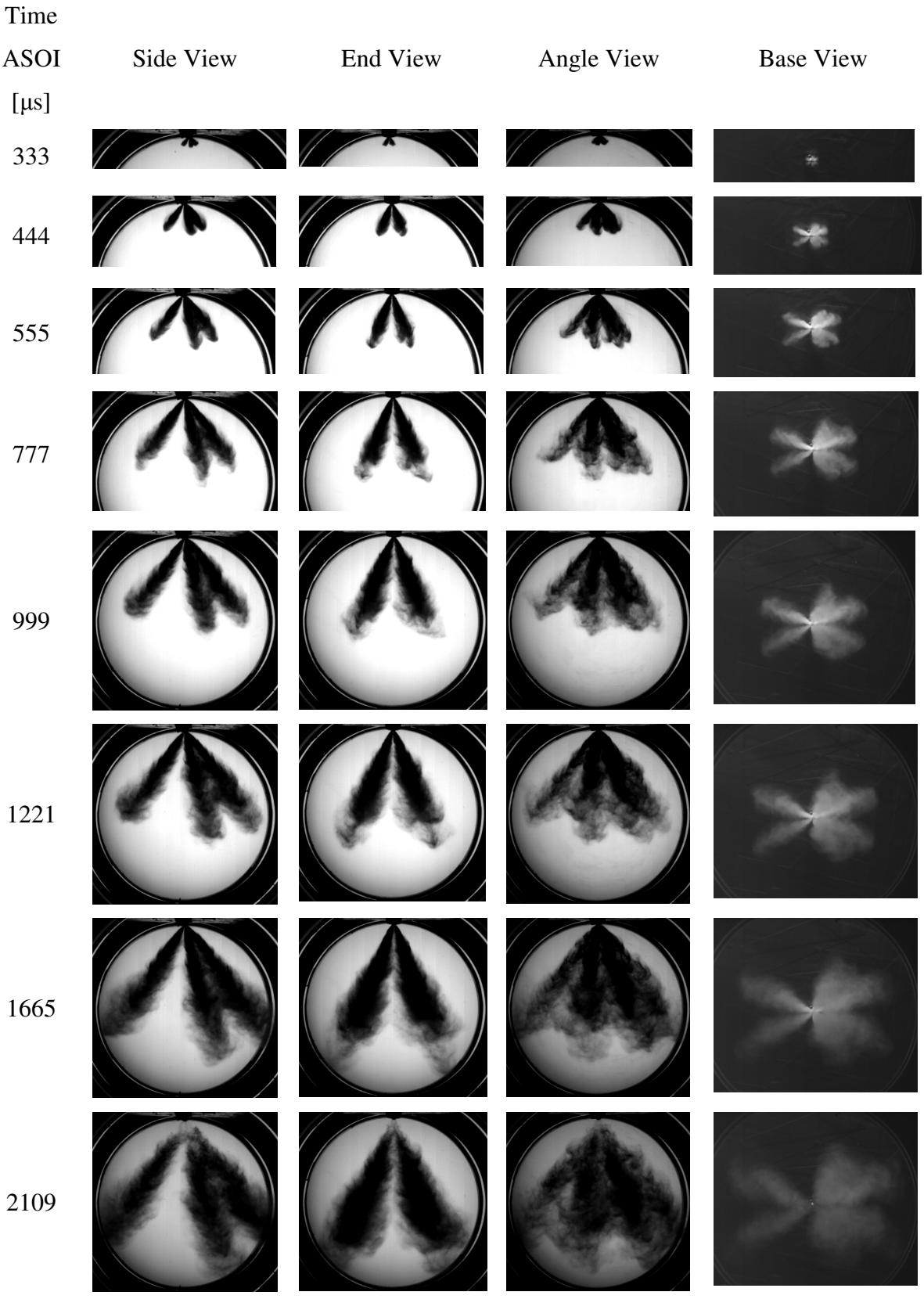

Figure 3-3 Spray Development Standard Gasoline 120 °C 1.0 bar

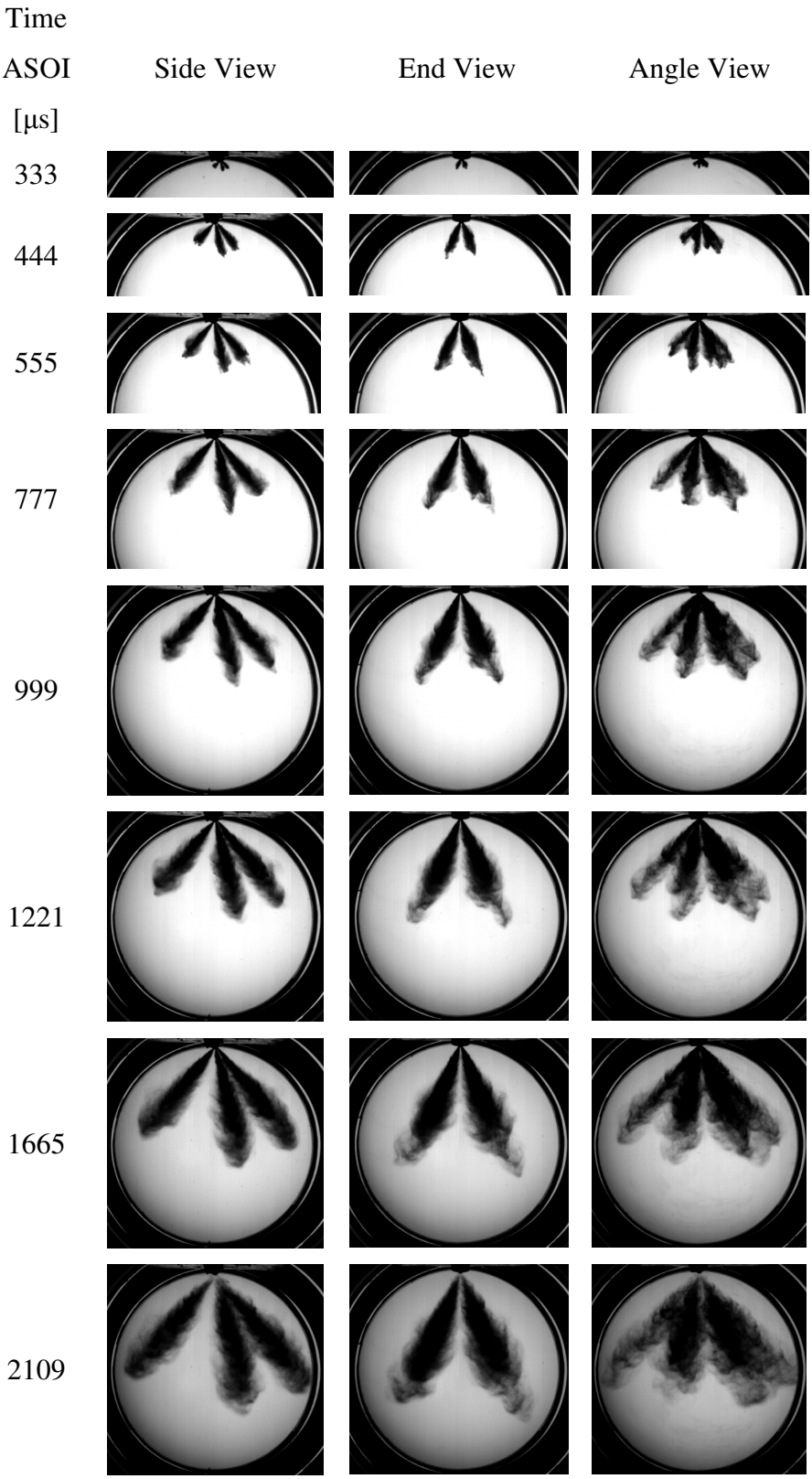

Figure 3-4 Spray Development Standard Gasoline 120 °C 5.0 bar

3.2.2 Spray Collapse

A direct comparison between the ambient, nominal spray form and the collapsed form is shown in Figure 3-5 from the side, end, angle and base views. The right hand column of Figure 3-5 shows Standard Gasoline at an injector body temperature of 120 °C and a gas pressure of 0.5 bar, at which the spray with this fuel may be observed to be collapsed. This condition is representative of an early, homogeneous charge injection strategy in an engine. In all views of the collapsed spray the individual plumes for the 4 closely spaced plumes are contracted into a single mass of fuel; the two further spaced plumes (left hand plume pair in side view image) also contract towards the spray axis, although the individual plume tips may still be distinguished in the base view. This is the typical 'collapsed' spray form which occurs due to 'flash-boiling'; as the fuel exits the nozzle it is rapidly depressurised to a pressure sufficiently below its saturated vapour pressure and the vapour generated is drawn towards the central low pressure regions, overcoming the radial momentum of the injected droplets. However, it is clear that pure 'flashing' does not occur from the high liquid volume imaged, and other mechanisms are involved with respect to transient heat and mass transfer phenomena and, most probably, phase change inside the nozzle (e.g. from cavitation) which also affect the spray shape outside the nozzle.

Spray convergence and collapse are observed here for conditions representative of those in an engine cylinder during early injection, homogenous charge operation (*i.e.* low gas pressure). Such a mixture formation strategy relies on the complete mixing and distribution of the fuel around the cylinder prior to ignition. However, the collapsed spray form appears to be denser in the regions where two or more plumes have combined and hence to oppose the promotion of mixing with the surrounding gas. Whilst collapse has been detailed in the literature by a number of authors in relation to pressure swirl sprays, no comparable analysis of this phenomenon can be found in the literature to date for multi-hole gasoline sprays. In contrast to the multihole injector and spray examined in this work, pressure swirl sprays have been observed to contract at high fuel temperature, *high* gas pressure conditions (*e.g.* Zhao [2002]) such as those found in an engine cylinder at late injection timing where a compact spray could aid spray direction (with the notable shortcoming that pressure swirl sprays are largely unsuitable for spray guided systems). At the collapsed condition in Figure 3-5 and detailed in Figure 3-2, a semi-vortex structure can be seen to be established on the side of the collapsed plume. A similar vortex has been observed by several researchers, (*e.g.*

[van der Wege and Hochgreb [2000], Davy *et al*. [2000] and Moon *et al.* [2005]), for pressure-swirl atomizers at spray-collapse conditions. The presence of this structure in the imaged sprays suggests that spray collapse for multihole sprays is bought on by the presence of fuel vapour, which is entrained into the air flow under motion due to shearing along the combined spray plume boundary.

To examine the gas pressure and injector body temperatures at which the spray collapses, full spray imaging was carried out over the test matrix listed in Table 3-1. For brevity these image sets are not shown in their entirety, but the Side View images captured at 777 μs ASOI are summarised in Figure 3-6 for the range of injector body temperatures and gas pressures tested. The convergence of the spray form at high injector body temperature, low gas pressure conditions is evident from the left hand column image in Figure 3-6. The onset of this convergence can be seen to be gradual with some convergence at 90 °C injector body temperature at 0.5 bar gas pressure, as well as a more pronounced degree of convergence at 120 °C injector body temperature and 1.0 bar gas pressure. As such, within the test condition resolution used for this work, there does not appear to be certain condition at which this convergence suddenly occurs and which acts as a "threshold" at which there is a sudden difference in observed spray form. The interaction of the gas pressure and injector body temperature (and hence assumed fuel temperature) in bringing about convergence and eventual collapse also illustrates a strong interaction with pressure and temperature dependant fuel properties as they alter over the test ranges.

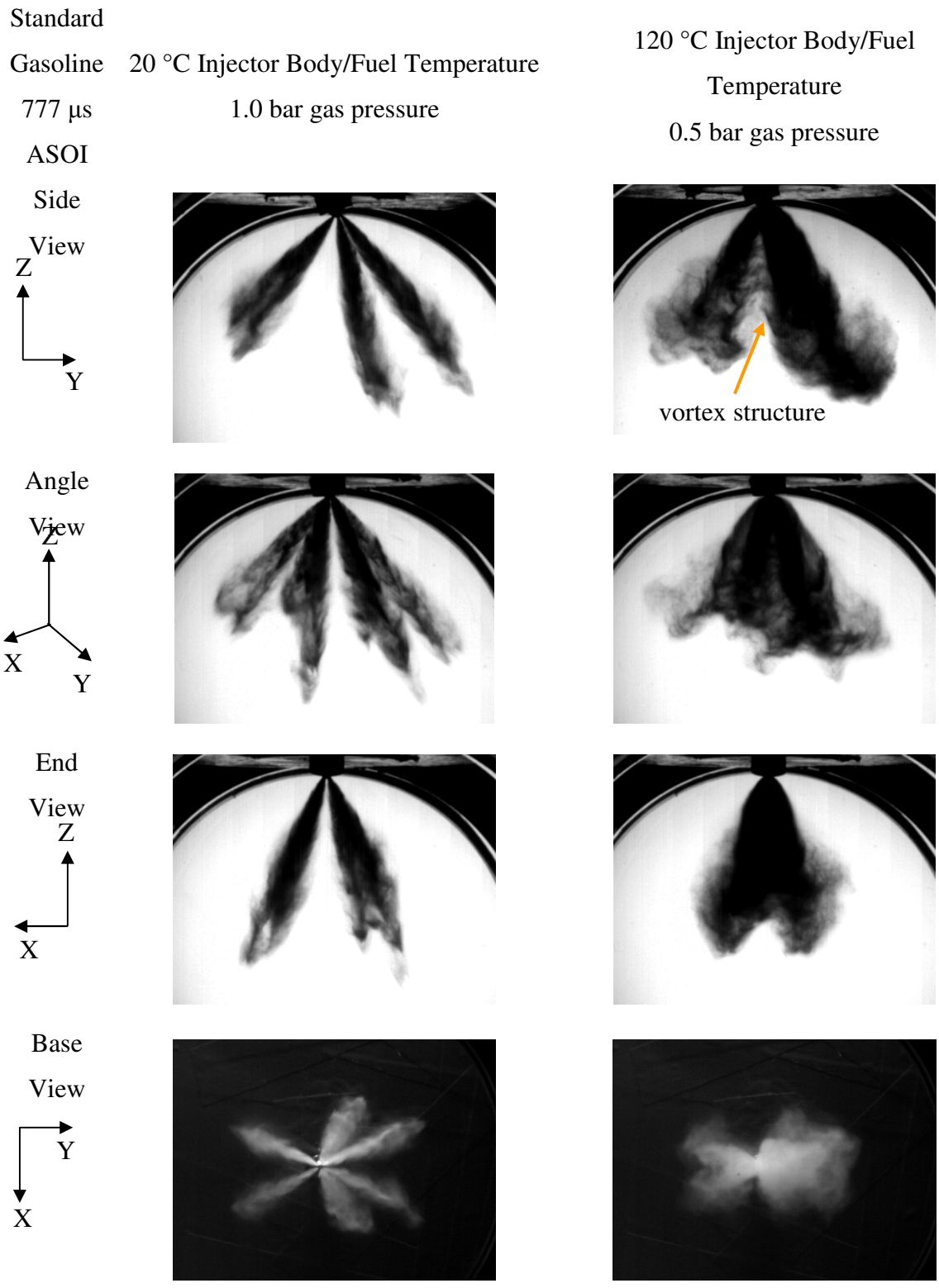

Figure 3-5 Different Views of Nominal and Collapsed Spray Form

Injector Body Temperature [° C]	Gas Pressure [bar] 0.5	1.0	5.0
20			
50			
90			
120	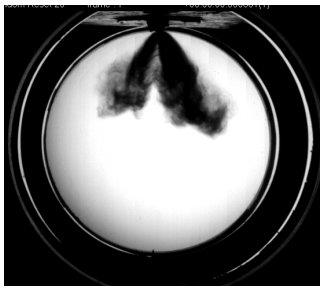		

Figure 3-6 Standard Gasoline, 777 μs ASOI

3.2.3 Heavy Gasoline

The ambient temporal spray development for the Heavy, multi-component Gasoline, which contains lower volatility components than the Standard Gasoline and hence has higher bubble point pressures and a lower vapour pressure than Standard Gasoline, is shown in Figure 3-7 whilst the spray development in relation to the range of test injector body temperatures and gas pressures is summarised in the side view images captured at 777 μs ASOI in Figure 3-10. These figures are followed by tables of images showing the temporal development of the spray at an injector body temperature of 120 °C and gas pressures of 0.5 bar and 1.0 bar in Figure 3-8 and Figure 3-9 respectively.

The images captured for spray development using the Heavy Gasoline show a similar reaction of the spray to injector body temperature and gas pressure conditions as for the Standard Gasoline. However, closer inspection of the images, especially those in the summary images in Figure 3-10, show a reduction in convergence of the spray plumes at the highest temperatures, lowest pressure condition relative to the Standard Gasoline spray in Figure 3-6. This is further illustrated by the spray images at an injector body temperature of 90 °C and 0.5 bar gas pressure, and at an injector body temperature of 120 °C and 1.0 bar gas pressure (*i.e.* those adjacent to the "spray collapse" condition), where plume separation can be clearly seen for the Heavy Gasoline sprays although not for the Standard Gasoline sprays. The spray development mechanisms behind these observations are discussed following the presentation of the spray development trends for the rest of the fuels.

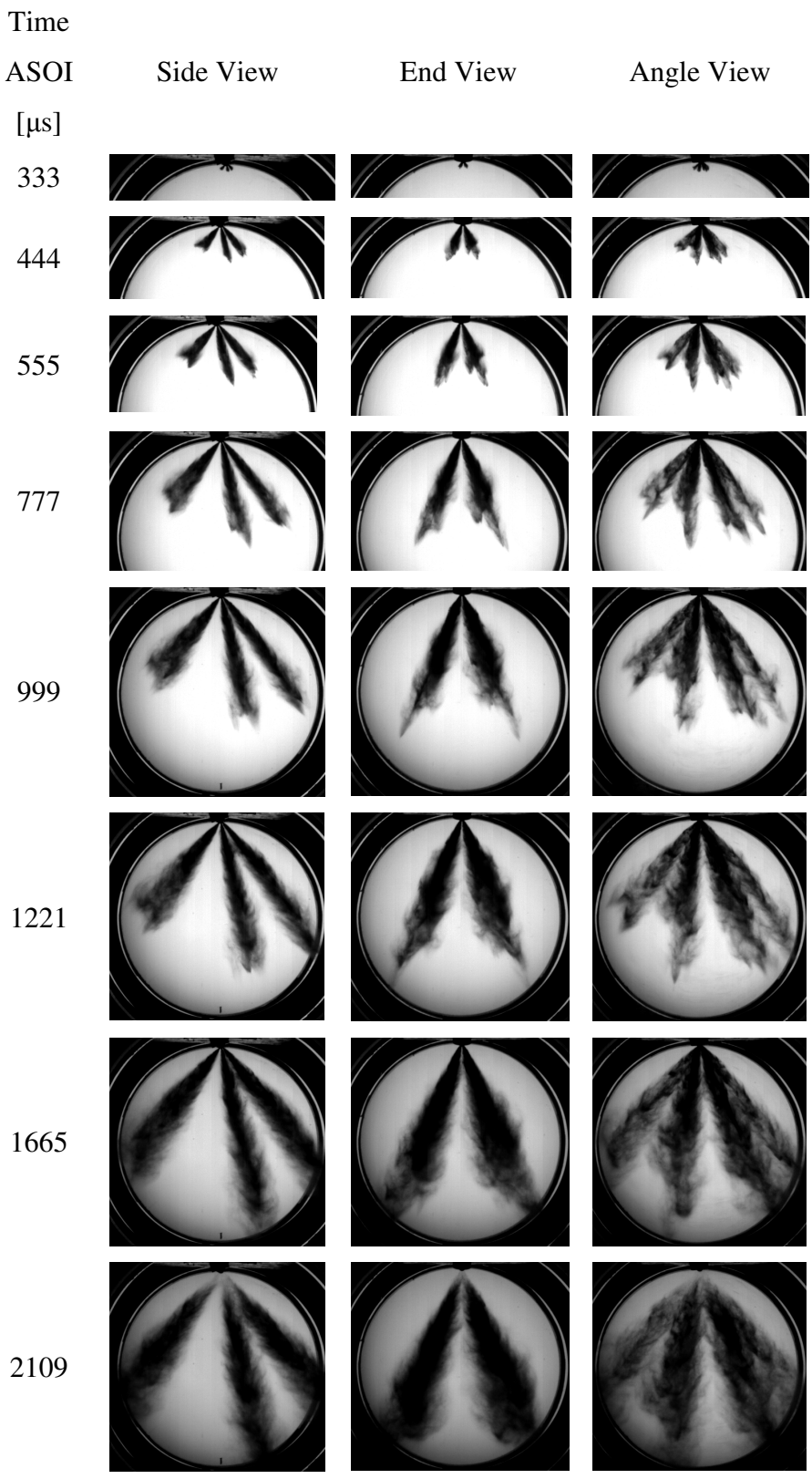

Figure 3-7 Spray Development Heavy Gasoline 20 °C 1.0 bar

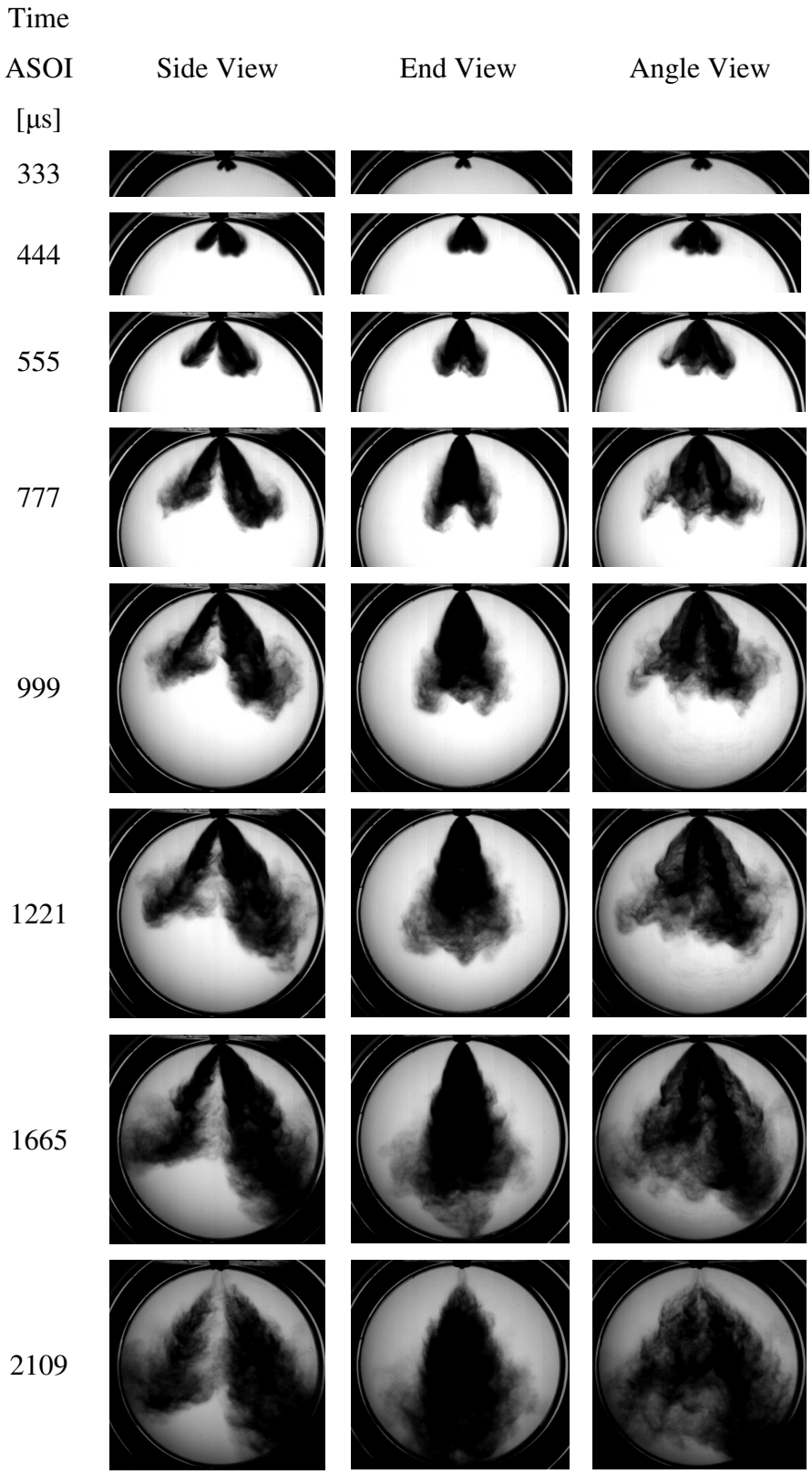

Figure 3-8 Spray Development Heavy Gasoline 120 °C 0.5 bar

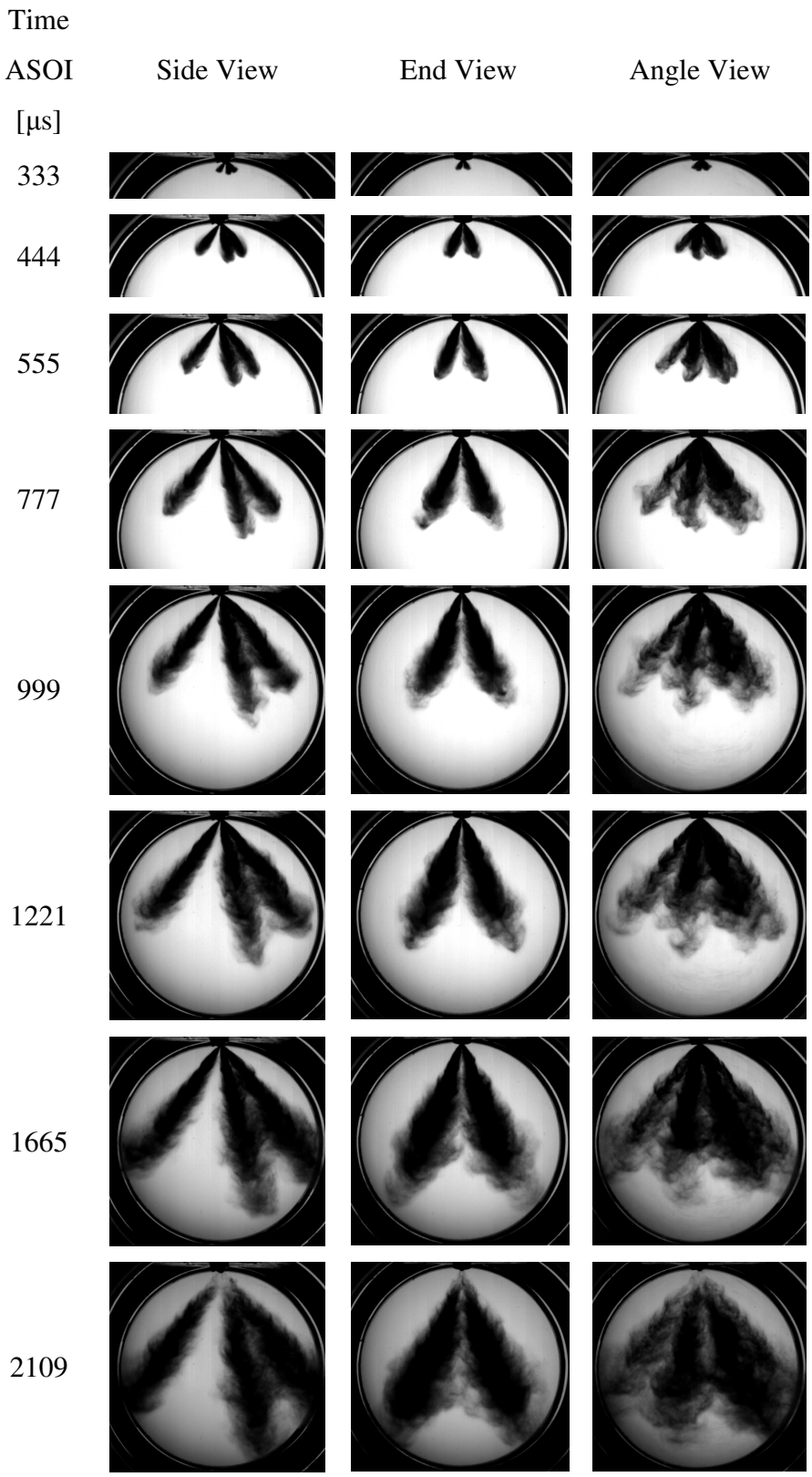

Figure 3-9 Spray Development Heavy Gasoline 120 °C 1.0 bar

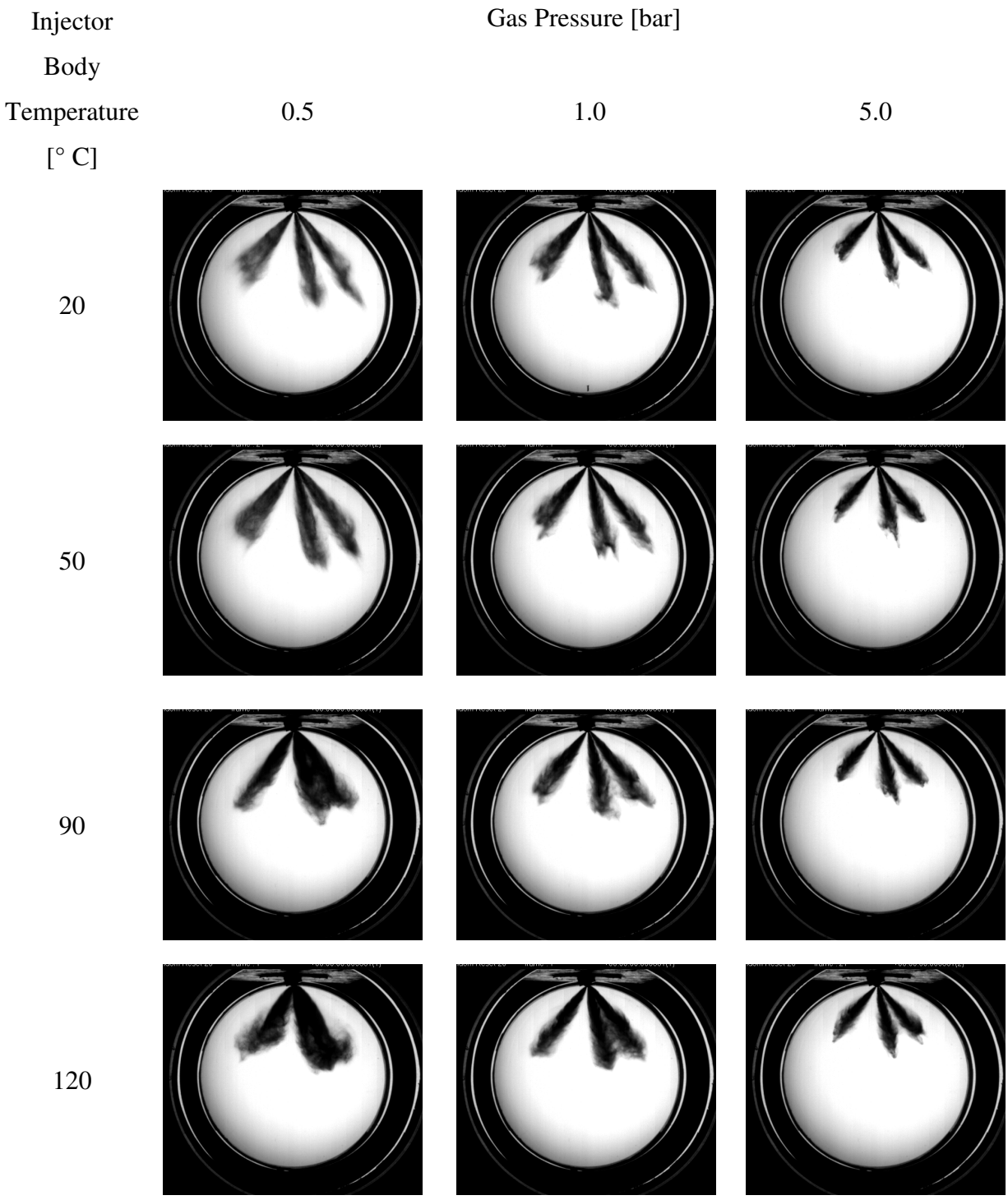

Figure 3-10 Heavy Gasoline, 777 μs ASOI

3.2.4 *iso*-Octane

iso-Octane is commonly used as a substitute fuel for gasoline in many engine research applications due to its single-component nature, which makes subsequent modelling of the spray development, evaporation and combustion a greatly simplified task relative to a multi-component fuel, Baumgarten [2006]. To investigate the representativeness of *iso*-Octane to gasoline, as well as to enable an interpretation of the results obtained from the gasoline spray development measurements, images of the *iso*-Octane spray were captured over the range of experimental conditions used for this work. Figure 3-11 shows the temporal development at an injector body temperature of 20 °C and gas pressure of 1.0 bar. These images are followed by further detailed temporal development sequences at an injector body temperature of 120 °C and gas pressures of 0.5 bar and 1.0 bar in Figure 3-12 and Figure 3-13 respectively, whilst a summary of the spray form at the main test conditions is given in Figure 3-14.

The images captured for the *iso*-Octane spray development, as summarised in Figure 3-14, show the nominal spray form at "ambient" conditions. At this condition, the plume boundaries can be seen to be better defined than those produced at the similar test condition using Standard Gasoline, particularly at early injection intervals ASOI (image rows 1-4). At the "spray collapse" condition (120 °C injector body temperature, 0.5 bar gas pressure, detailed in Figure 3-12), the *iso*-Octane spray, which has a higher initial boiling temperature (and correspondingly lowest Reid Vapour Pressure (RVP)) than the multi-component gasolines, shows some convergence, although the spray cannot be said to be collapsed, as each individual spray plume is clearly discernable, in contrast to the same condition with Standard Gasoline (Figure 3-2), where individual spray plumes are not distinguishable.

This variation in spray development at conditions relevant to early, homogeneous charge, injection strategies in an engine has important implications in the use of *iso*-Octane as a substitute for gasoline in engine test and simulation work. The effect of these differences on the physical geometry of the spray (spray plume penetration) is detailed in the following section of this work.

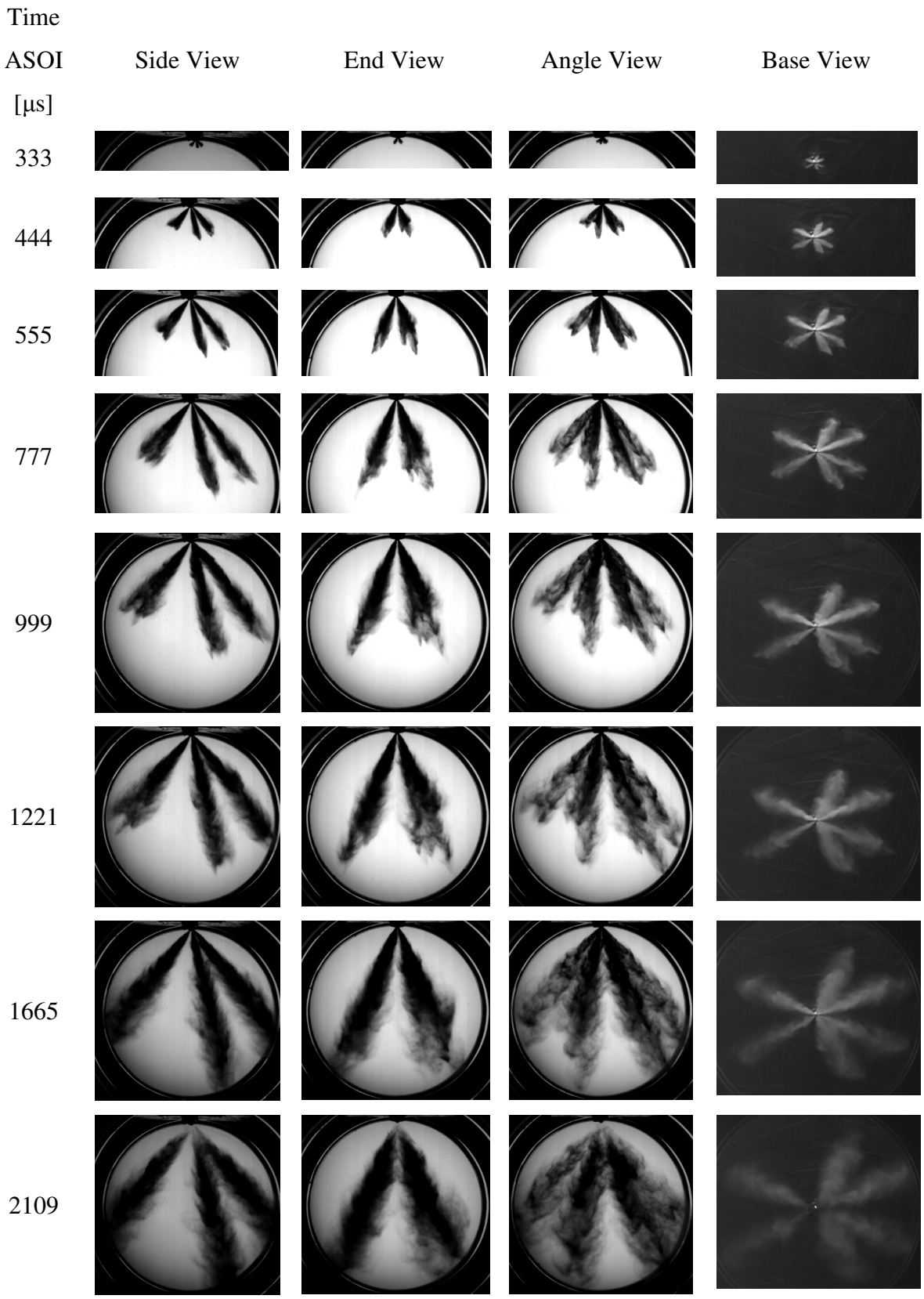

Figure 3-11 Spray Development *iso*-Octane 20 °C 1.0 bar

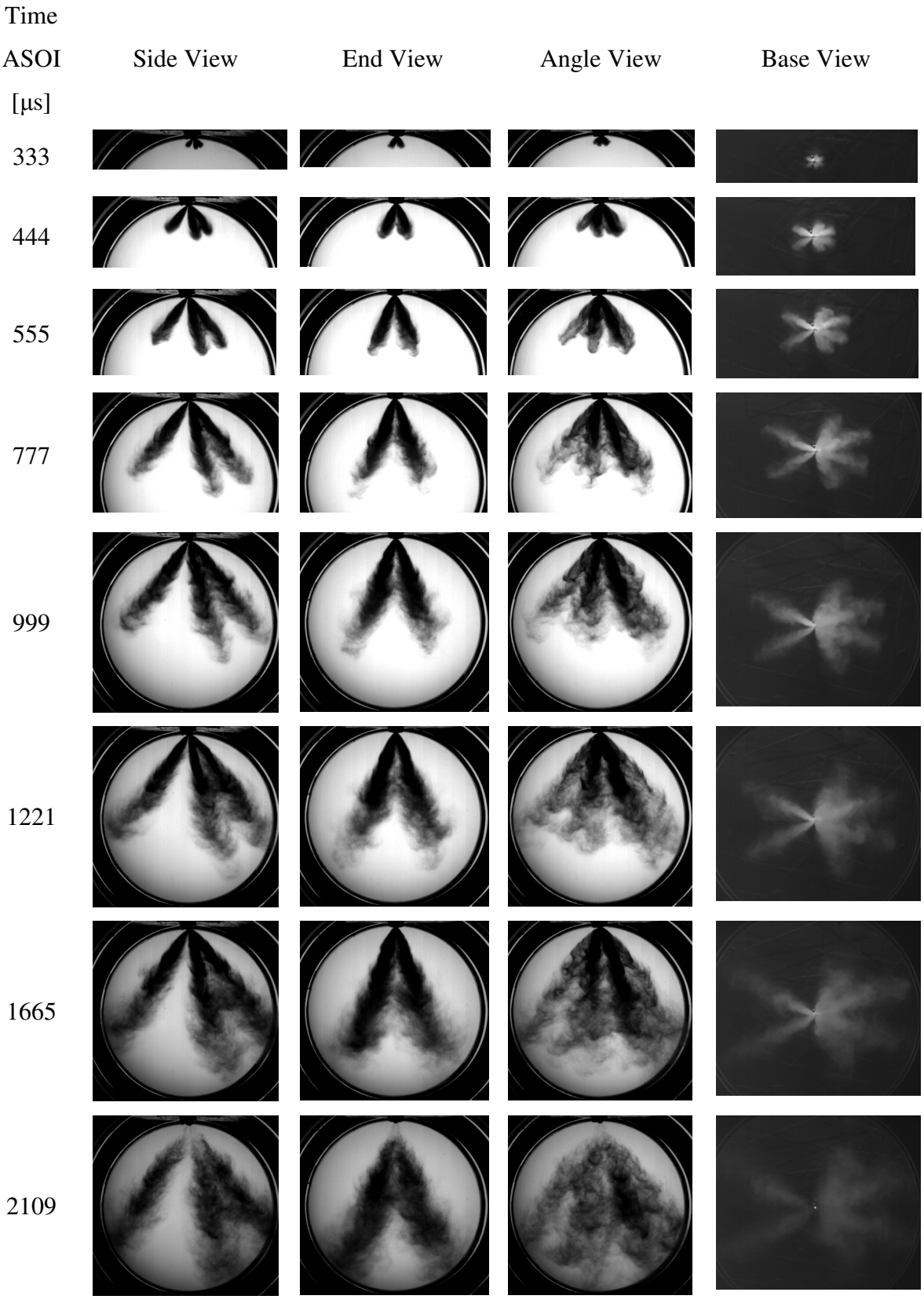

Figure 3-12 Spray Development *iso*-Octane 120 °C 0.5 bar

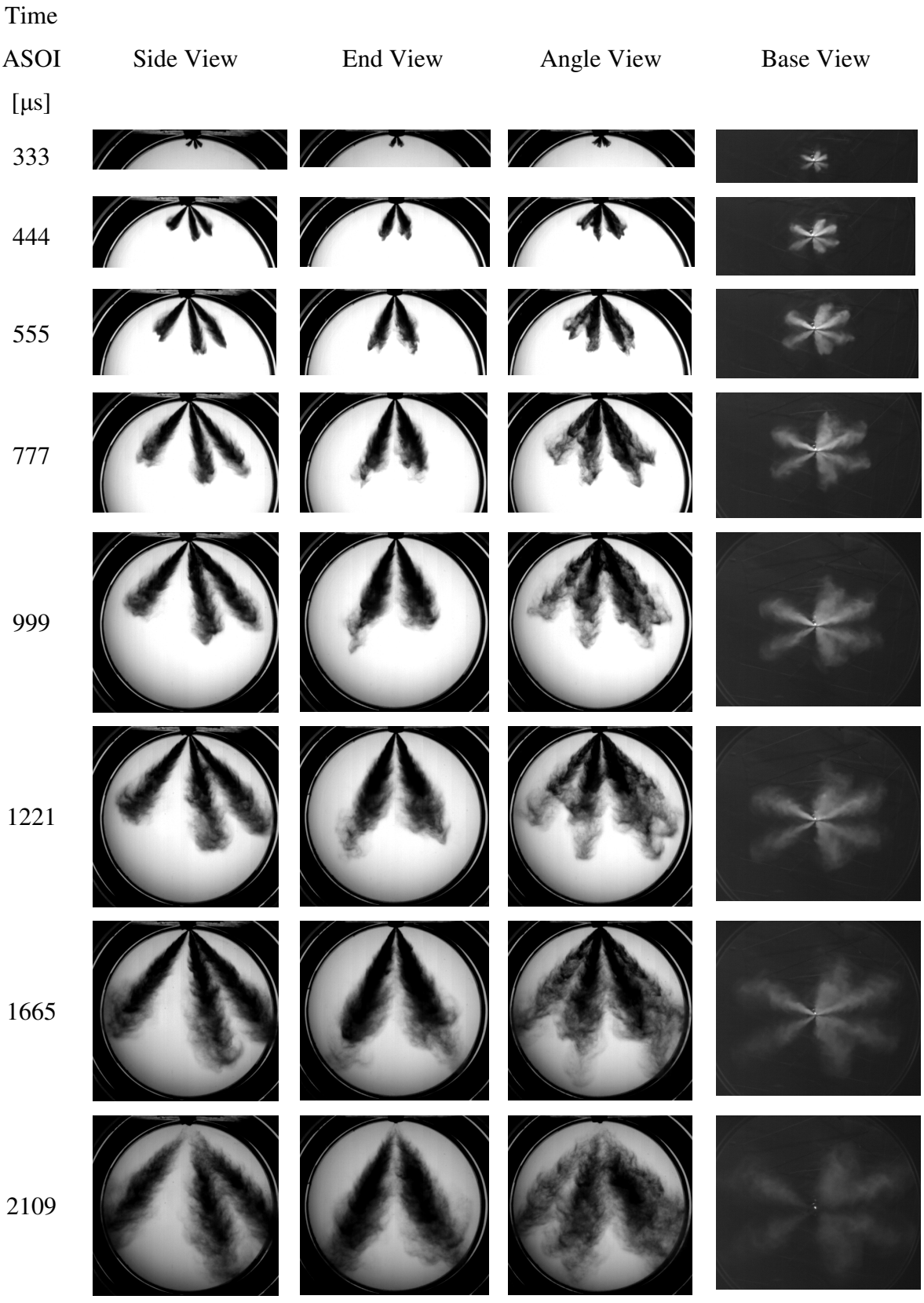

Figure 3-13 Spray Development *iso*-Octane 120 °C 1.0 bar

Injector Body Temperature [° C]	Gas Pressure [bar] 0.5	1.0	5.0
20			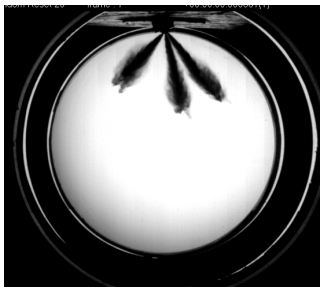
50			
90			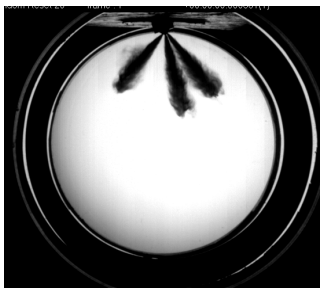
120	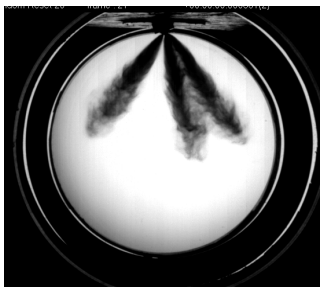	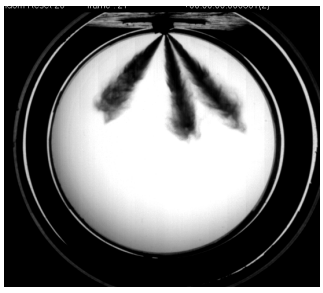	

Figure 3-14 *iso*-Octane, 777 μs ASOI

3.2.5 *n*-Pentane

To cover the range of volatility and boiling characteristics of the multi-component gasolines, further spray imaging was carried out using single component *n*-Pentane. The summary tables of images captured at 777 µs ASOI are presented in Figure 3-15, Note that the sprays for *n*-Pentane were only captured from the side view and at 0.5 and 1.0 bar due to little variation in spray form being observed at 5.0 bar relative to 1.0 bar

In the summary spray images for *n*-Pentane (Figure 3-15), The spray produced by *n*-Pentane, which has the lowest boiling point of the tested fuels at 36.1 °C, shows the greatest collapse. For this fuel, collapse can be observed to occur at 90 °C injector body temperature, and at 120 °C injector body temperature the left hand plume pair also show significant convergence towards the injector axis.

Injector Body Temperature [° C]	Gas Pressure [bar] 0.5	1.0
20	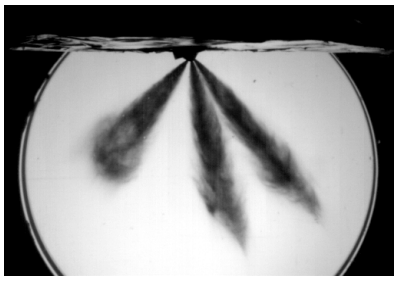	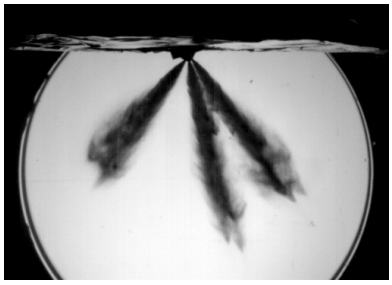
50	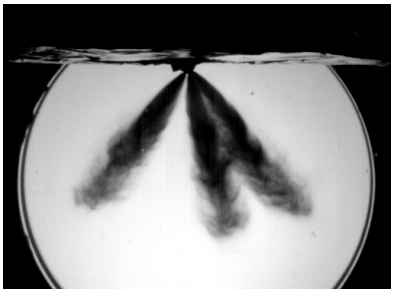	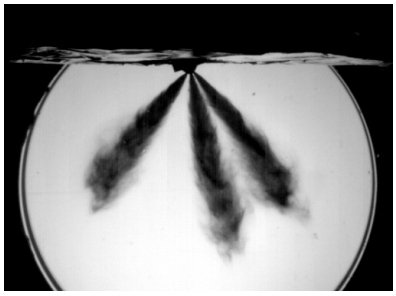
90	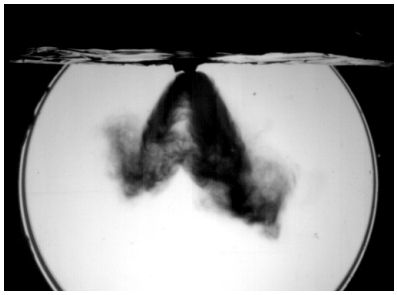	
120	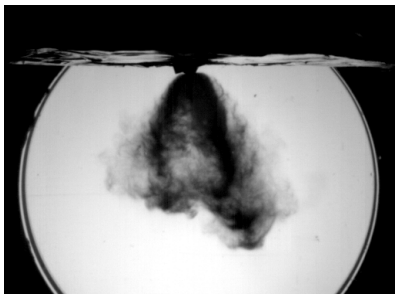	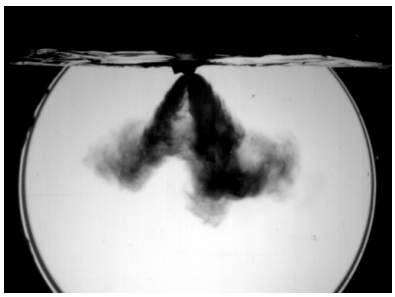

Figure 3-15 *n*-Pentane, 777 μs ASOI

3.2.6 Extreme Conditions

To examine whether the single component *iso*-Octane would follow a similar trend to the multi-component gasolines and gradually converge to collapse, or if for the single component fuels there was a certain threshold value at which the fuel flash boiled to bring about a sudden change in spray form, the gas pressure was further reduced to 0.3 bar and further images were captured at injector body temperatures of 120 °C and 180 °C. The temporal spray development at these conditions is shown in Figure 3-16 for Standard Gasoline, Figure 3-17 for *iso*-Octane and Figure 3-18 for *n*-Pentane.

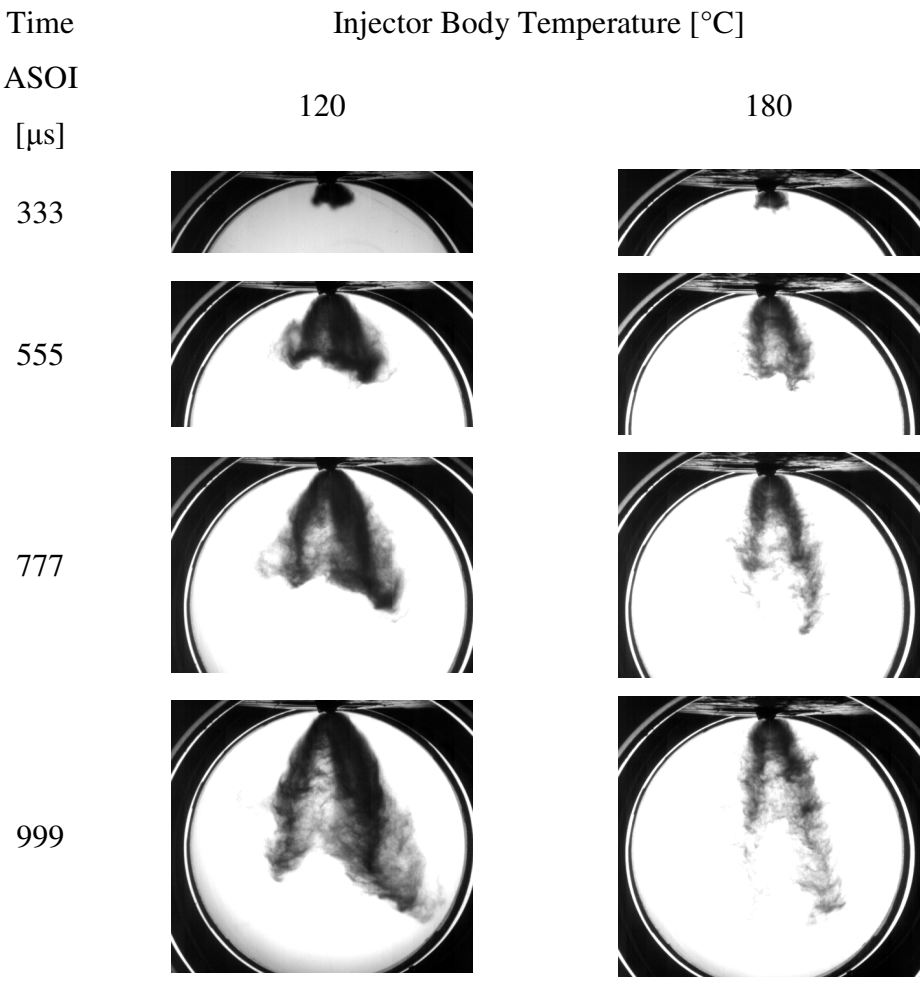

Figure 3-16 High Temperature Spray Development: Standard Gasoline, 0.3 bar

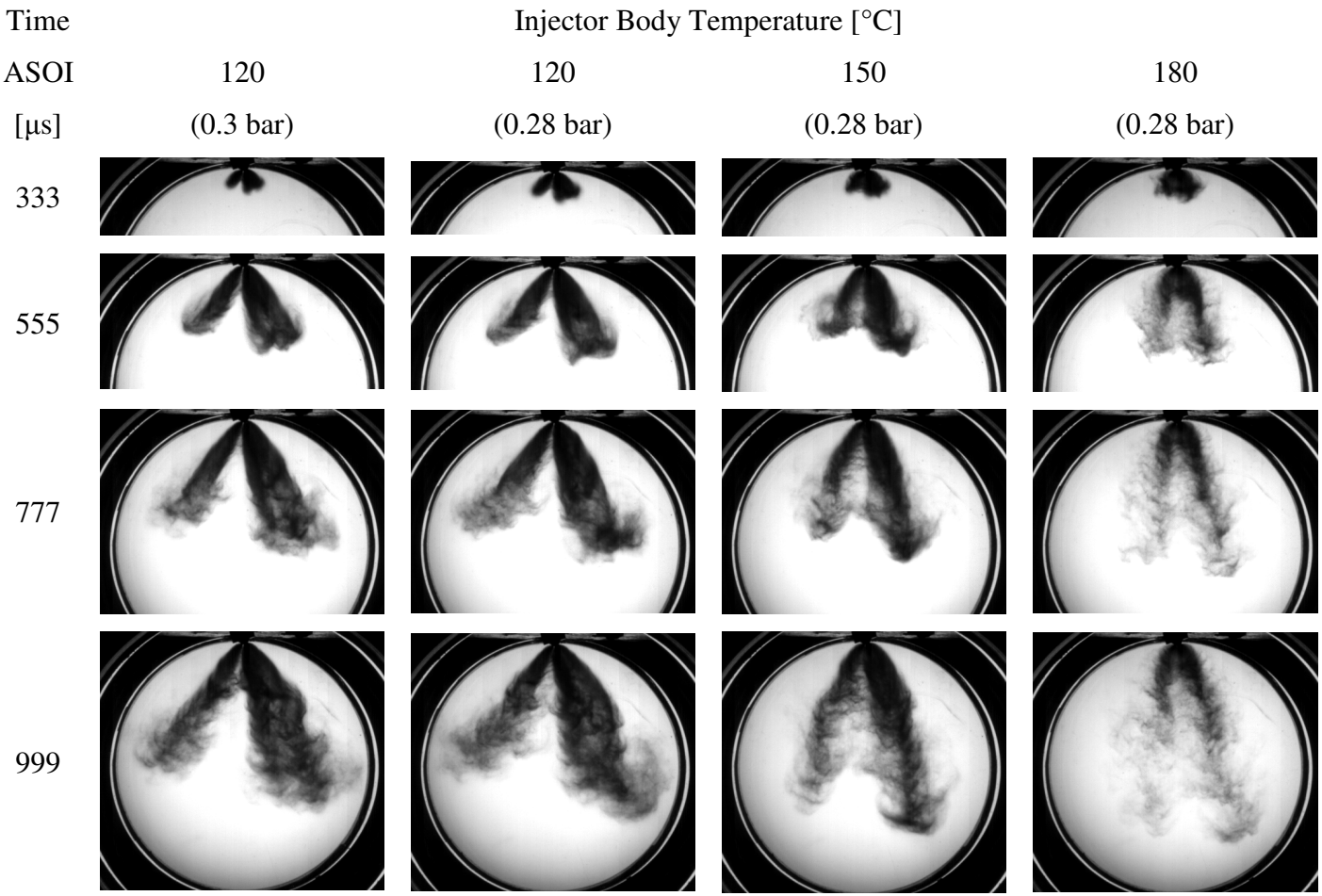

Figure 3-17 High Temperature Spray Development: *iso*-Octane, 0.3 bar

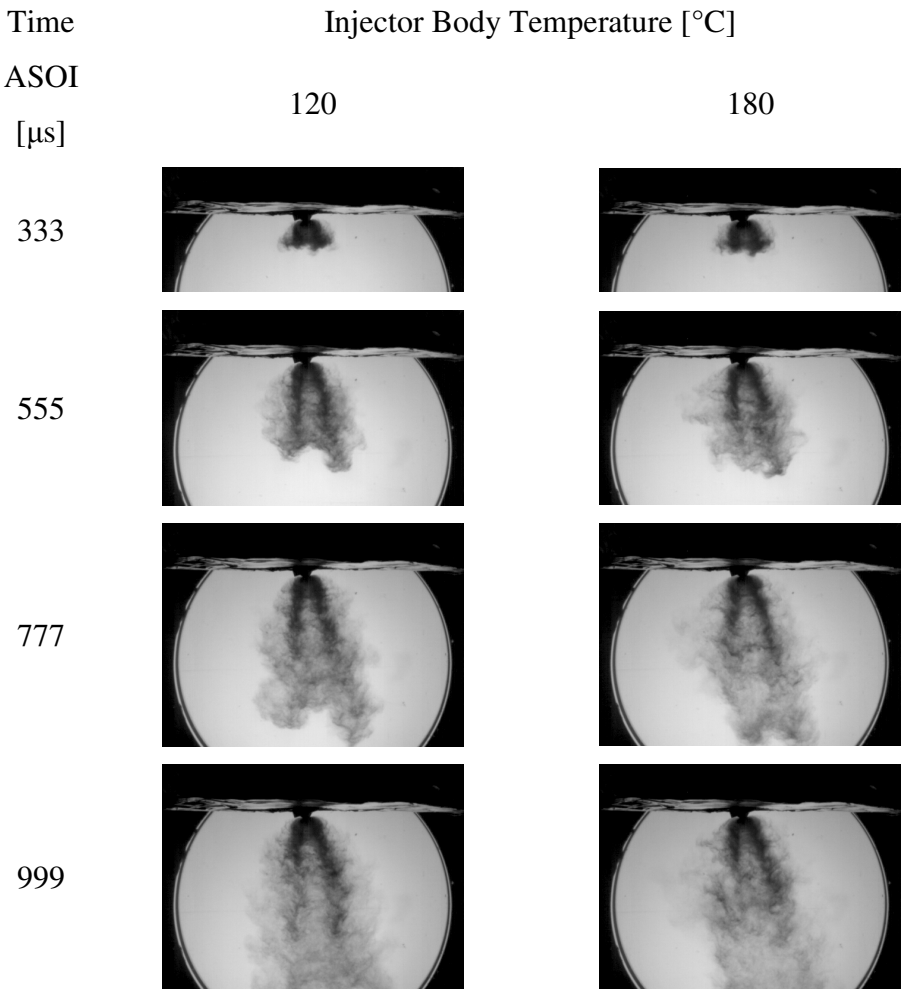

Figure 3-18 High Temperature Spray Development: *n*-Pentane, 0.3 bar

The spray development images for *iso*-Octane in Figure 3-17 at these "extreme" conditions (not likely to be encountered in an engine due to the high injector body/fuel temperature), show a gradual onset of collapse, as for the multi-component gasolines detailed earlier. A reduction in gas pressure to 0.3 bar at an injector body temperature of 120 °C (left hand image column in Figure 3-17) shows an increase in plume convergence relative to the same injector body temperature condition at 0.5 bar (Figure 3-12). Further increases in injector body temperature to 150 °C and 180 °C at 0.28 bar show a further convergence of the plumes until collapse occurs at 150 °C. At 180 °C increased liquid evaporation is evident from the reduced obscurance of the back light and "cloudy" structure of the plumes, especially further from the injector tip at longer plume lengths (later times ASOI). Note that the large scale oscillations of the plumes referred to earlier are evident at this condition (bottom right hand image in Figure 3-17) as the surrounding droplet cloud has evaporated and the wavy central, liquid dense,

region of the combined plumes remains, especially from the right hand plume set. Interestingly, it is the left hand plume pair (as shown) which appear to converge the most towards the injector axis (note that the injector is mounted at an angle of 19° to the image vertical axis). This may be due to the lower liquid mass and hence axial momentum contained within these plumes as these comprise the two plumes (plumes 1 and 6) as opposed to the right hand set of 4 combined plumes (plumes 2, 3, 4 and 5).

3.2.7 Spray Variability

The measurement of any spray parameter variability also includes any variability inherent in the timing of the injection hardware as well as the image capture equipment, which cannot be decoupled from the plume measurement variability. In particular, the assessment of the hardware variability detailed in Section 2.3.1 shows an inherent variability in the fuel delivery time of 4.0 μs, equivalent to approximately 0.24 mm at a plume velocity of 60 m/s. However, at a scale of 10 pixels per mm typical of the presented images, this would equate to an uncertainty of 2.4 pixels, which is not considered to be material to the measurements and observations made variability in the spray between individual injection events.

For all experimental conditions extensive spray tip penetration variability analysis was carried out over the 100 spray tip measurements at each time interval. The measurement of spray plume tip penetration showed little variation, with a standard deviation of the measurements of between 2.5% and 4.5 % of the measured plume length at each time interval. The amount of variability was also not found to vary with fuel or experimental condition.

The RMS (Root Mean Squared) and mean average images are shown for Standard Gasoline, *iso*-Octane and *n*-Pentane at the pertinent conditions in Figure 3-19 and Figure 3-20. The RMS was calculated for each pixel by overlaying 100 greyscale images (0 to 254 pixel value), and calculating the RMS of the variability in the value of each pixel. The scale has been normalized to the maximum value of RMS in these images. For the non-collapse conditions in Figure 3-19, similar levels of RMS around the plume tips can be observed for all fuels. The maximum value was of the order 20–30% of the mean and this gives a measure of the observed ‘variability’. For the collapse conditions in Figure 3-20 there is a similar level of maximum RMS about the plume tips for all fuels despite the large differences in spray formation. However, the regions of

non-zero RMS are wider for the collapse conditions, especially around the periphery of the plumes. The values of these levels of RMS though are quite low overall. In particular, for *n*-Pentane, it can be observed that the RMS image of the side view shows a wide area of RMS but with values very close to the bottom of the scale; the areas of high RMS are only localized close to the leading edge of the combined plume. The high volatility of this fuel would be expected to lend itself to high variability in the vaporisation regions, indicated by the width of the variability band.

At the high injector body temperature, low gas pressure condition shown in Figure 3-20, *iso*-Octane does not show full collapse and exhibits similar levels of maximum RMS to those at the ambient conditions in Figure 3-19. Additionally, the areas where variability is observed for *iso*-Octane do not seem to be much wider in Figure 3-20 than in Figure 3-19 due to the low volatility of this fuel. These observations seem to be somewhat in line with the findings of Kashdan *et al*. [2002] and Hung *et al*. [2003], who found the variation in the spray envelope to be independent of the pressure conditions for an *iso*-Octane pressure-swirl spray, although the fuel temperature was not varied. However, the levels of RMS are overall higher for the sprays presented in Figure 3-20, with a peak of approximately 28%. By comparison, using a nominally identical injector to that used for the presented work, installed in a firing engine, Williams *et al*. [2008] developed and used a Quantitative Planar Laser Induced Fluorescence (QPLIF) technique and showed a spatial variation in fuel distribution of up to 10 % at the time of ignition. Similarly, Hung *et al* [2003] note that for DI engine pulse-to-pulse variability in the spray structure, penetration and spray angle are the primary influences on the AFR local to the spark plug at the time of ignition. Using a similar injector in a single cylinder experimental engine was found to produce a coefficient of variance of 8% using iso-Octane and 6% for Standard Gasoline in the maximum in-cylinder pressure over 100 cycles using a single injection pulse strategy at a head coolant temperature (and hence presumed fuel temperature) of 90 °C. However, spatial variation was not observed to directly correlate to RMS, and overall increased variability between injection events was observed in the engine due to the variability of the air flow structures on a cycle to cycle basis.

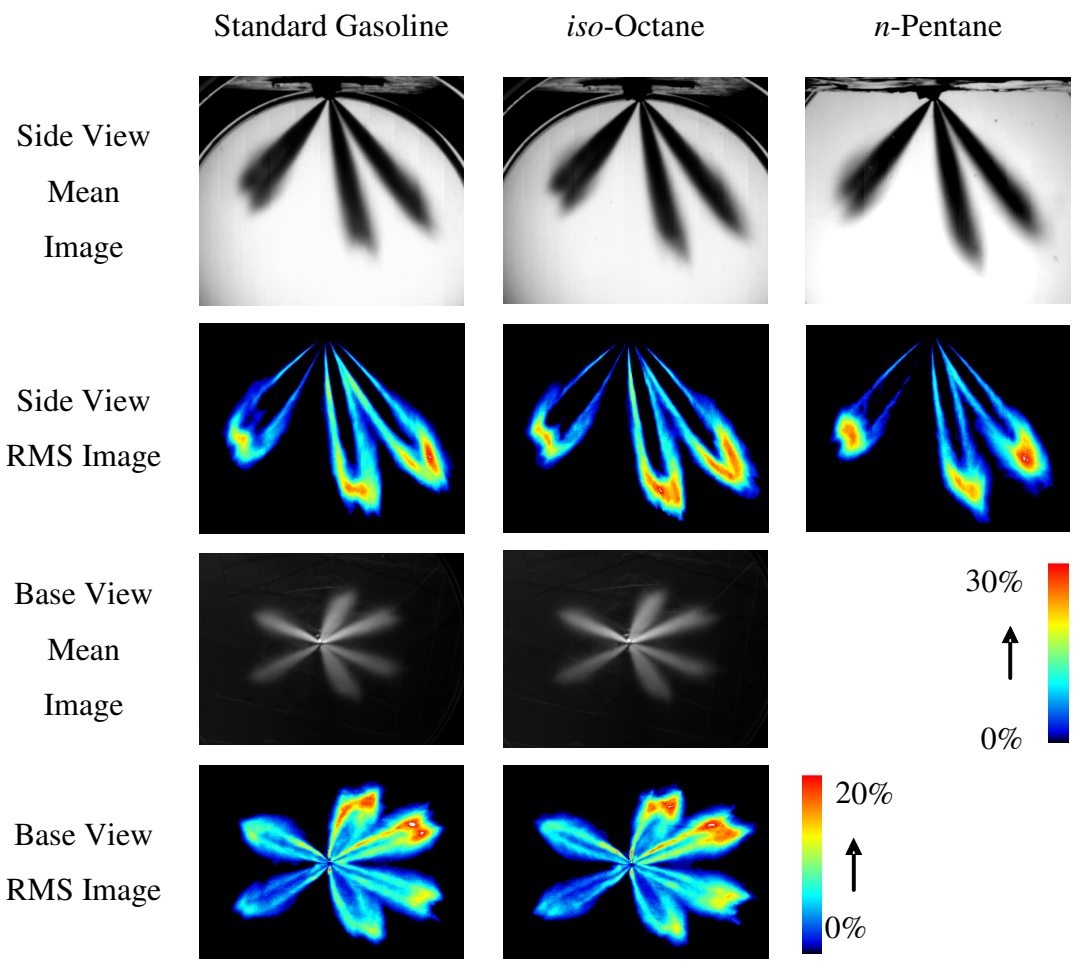

Figure 3-19 Mean and RMS Spray Images at 777 μs ASOI for 20 °C Fuel Temperature, 1.0 bar Gas Pressure

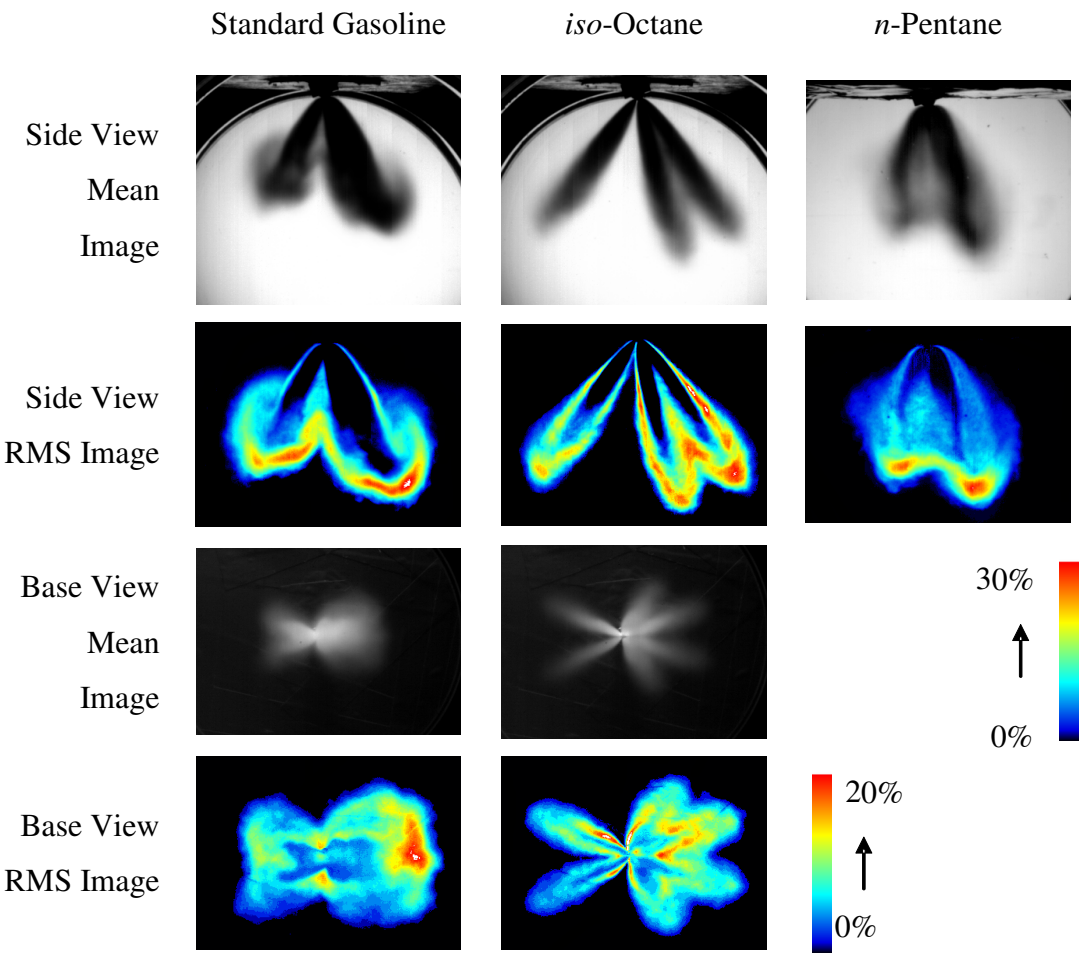

Figure 3-20 Mean and RMS Spray Images at 777 µs ASOI: 120 °C, 0.5 bar

3.2.8 Summary of Images Spray Development Trends

The spray images presented show the strong interaction of the fuel temperature and gas pressure in relation to the fuel's chemical and physical properties. By way of a summary, images captured at 777 µs ASOI for each fuel at each test temperature are presented in Figure 3-21 and Figure 3-22 for gas pressures of 1.0 bar and 0.5 bar respectively. A summary of the main spray development trends observed from these images is listed in the bullet points below:

- An increase gas pressure lead to a decrease in plume penetration
- The effect of decreasing plume penetration with increasing pressure was especially prominent at lower injector body (fuel) temperatures.
- An increase in gas pressure from 0.5 bar to 1.0 bar at both 20 °C and 50 °C acted to narrow the spray plumes, mainly by 'compacting' the droplet cloud at the

spray periphery towards the main spray plume, resulting in well defined spray plume boundaries.

- An increase in injector body temperature and decrease in gas pressure led to the convergence of the right hand plume pair (actually quartet). The extent of convergence for each test condition varies between fuels, suggesting an interaction between the prevailing conditions and the fuel properties.
- A general similarity between the sprays of Standard Gasoline and Heavy Gasoline for all condition, with a slightly lower convergence of the plumes for Heavy Gasoline (especially at 120 °C injector temperature), suggesting the effect of fuel volatility and evaporation in spray formation.
- A lesser extent of convergence of *iso*-Octane sprays is observed relative to Standard Gasoline sprays, even at high fuel temperature and low gas pressure conditions
- A greater extent of convergence of *n*-Pentane sprays is observed relative to Standard Gasoline sprays for all conditions where convergence was observed.
- The above observed trends indicate the interaction of the prevailing conditions with the fuel properties in determining the spray form, with spray convergence and collapse occurring where certain boiling characteristic parameters of the fuel have been surpassed.

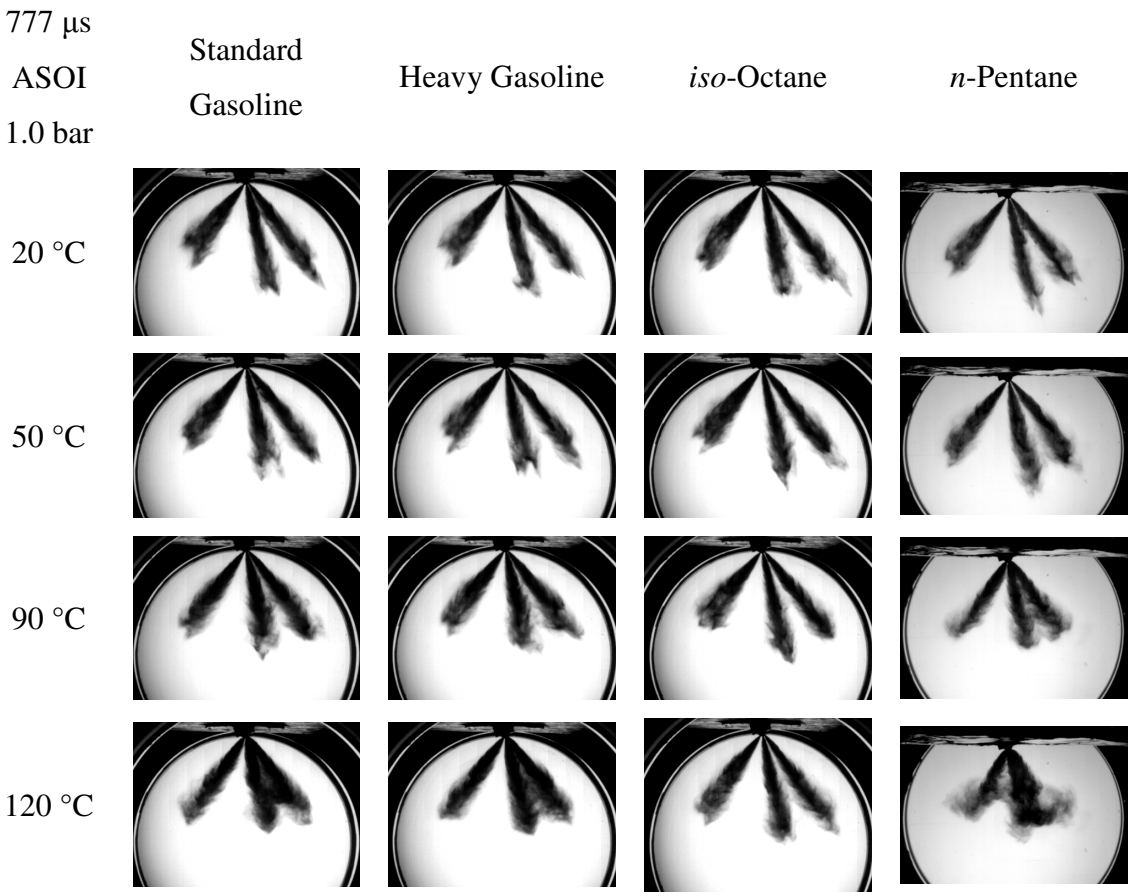

Figure 3-21 Global Spray Form for All Fuels – 1.0 bar Gas Pressure

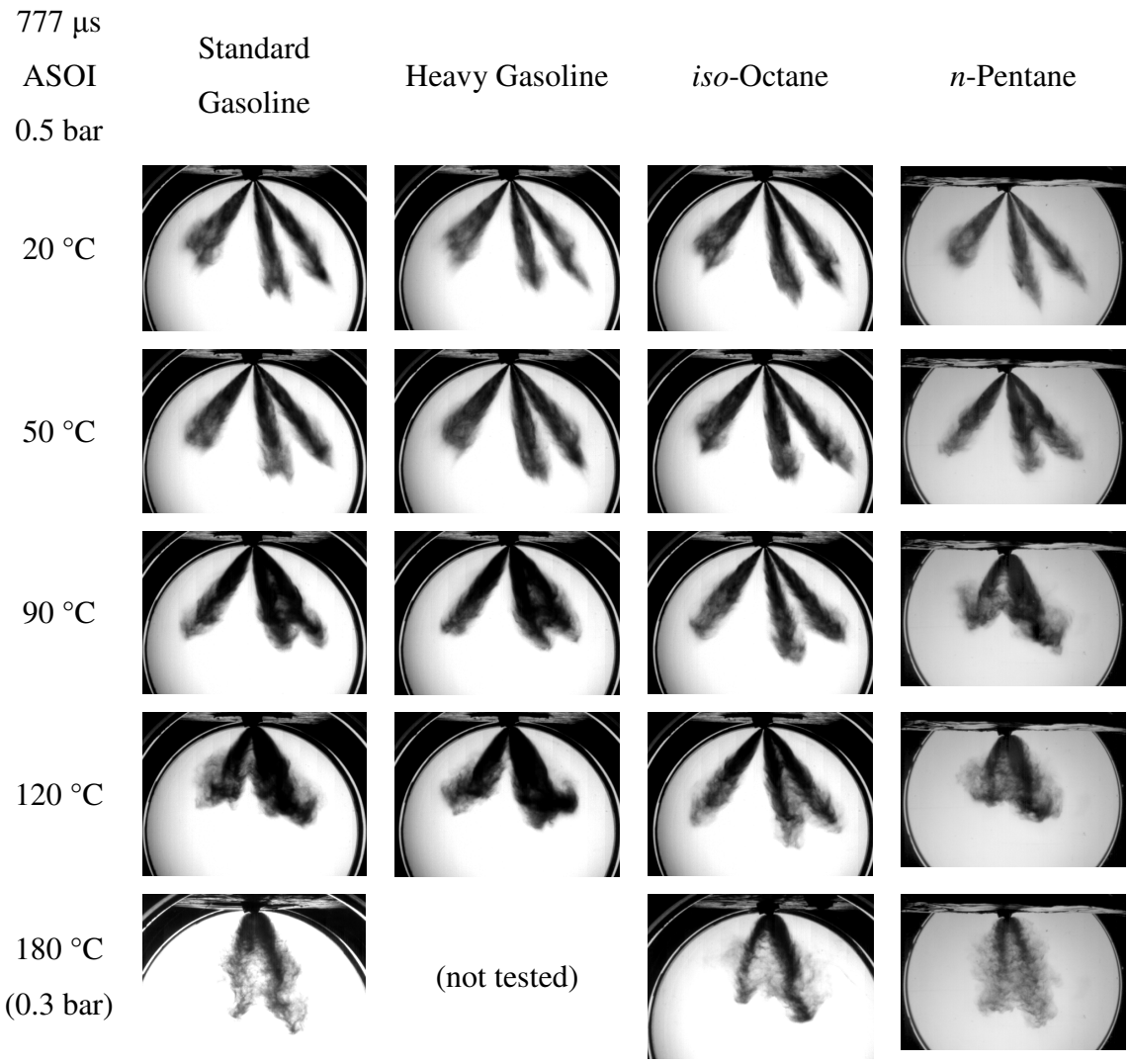

Figure 3-22 Global Spray Form for All Fuels – 0.5 bar Gas Pressure

4 Spray Parameter Measurement

To further quantify the extent of the trends observed, measurement of the principle spray parameters which were found to vary was carried out. These measurements include the automated measurement of certain characteristic spray envelope parameters from the spray images as well as the measurement of the diameters of the spray droplets at various locations downstream of the spray break-up. These quantitative measurements allow for the correlation of certain fuel properties and the experimental conditions to the physical spray parameters and fuel vaporisation rate, which have important implications for engine performance.

4.1 Spray Characteristic Parameter Measurement

For the quantitative comparison of sprays from different fuels at different test conditions, the spray-tip penetration and cone angles were measured from the captured images using automated image processing routines.

4.1.1 Spray Plume Penetration

To quantify the effect of the reduction in plume length with an increase in gas pressure at different fuel temperatures, the images were processed as previously described in Section 2.6.5. The plume lengths for spray plumes 1 and 6 (left hand plume pair in presented side view images) were automatically measured using a programmed measuring routine. At the baseline ambient conditions of 20 °C injector body (fuel) temperature, 1.0 bar gas pressure all tested fuels were measured (as averaged over the 100 spay event images recorded and assessed at each time interval) to have a similar spray plume penetration length for all captured time intervals After the Start of Injection (ASOI), as illustrated in Figure 4-1.

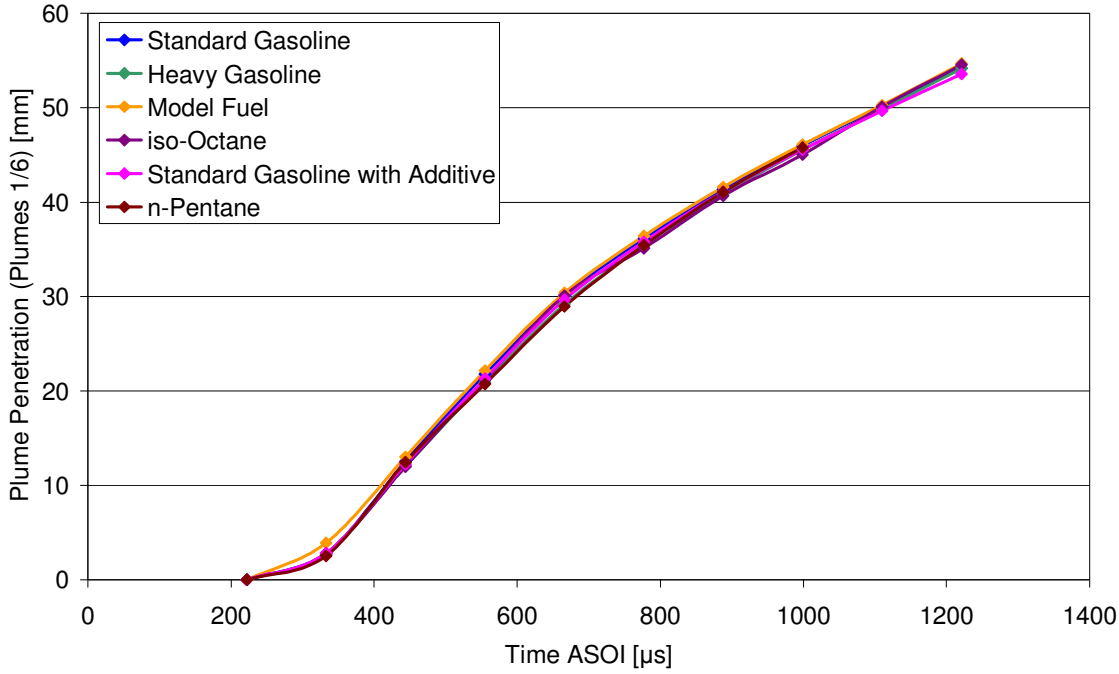

Figure 4-1 Spray Plume Penetration: 20 °C, 1.0 bar

As observed from the spray images, a decrease in gas pressure decreases the drag force on the liquid spray droplets and hence leads to an increase in measured plume penetration at any given time interval. This effect can be seen by comparing Figure 4-2 (0.5 bar gas pressure) to Figure 4-1 (1.0 bar gas pressure), which also shows the effect to be particularly evident after approximately 600 µs ASOI. After this time interval, the increase in penetration length is approximately 10% with a halving of the gas pressure from 1.0 bar to 0.5 bar, although at a constant injector body temperature there is little difference in the affect of the reduction in gas pressure for the different fuels. Prior to this time interval, the high spray momentum masks any measurable effect of gas drag on the plumes. For all fuel sprays at 20 °C, the effect of increasing gas pressure above atmospheric is to decrease spray plume penetration, as illustrated by the 20 % lower plume penetrations for all time intervals at 5.0 bar gas pressure (Figure 4-3) compared to the 1.0 bar gas pressure condition (Figure 4-1).

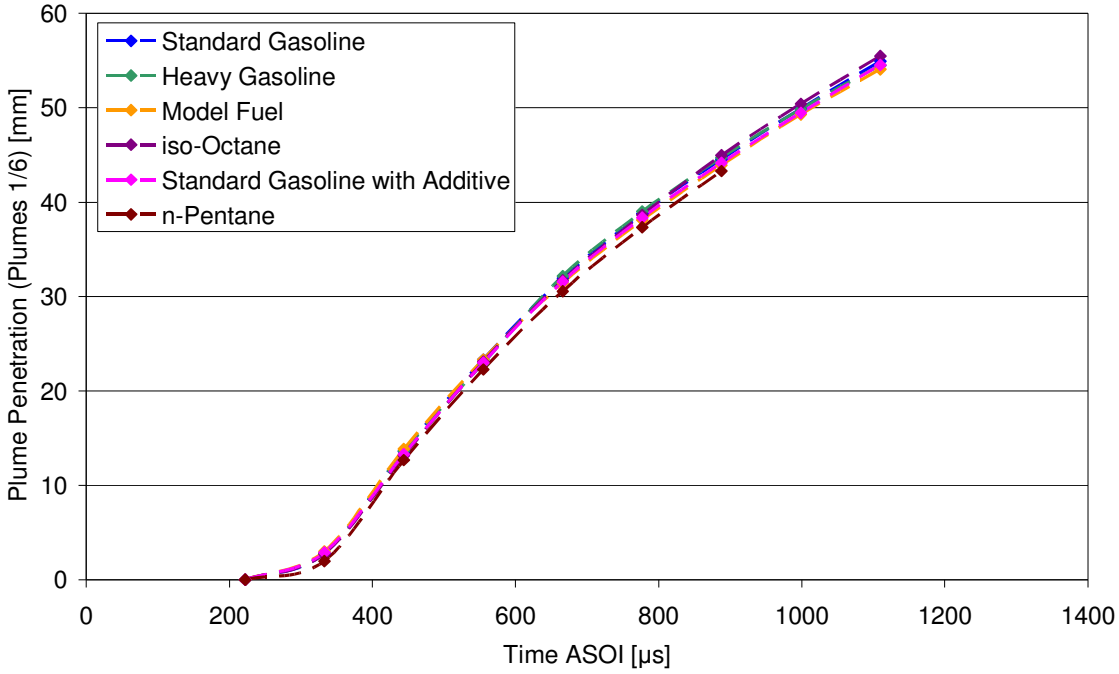

Figure 4-2 Spray Plume Penetration: 20 °C, 0.5 bar

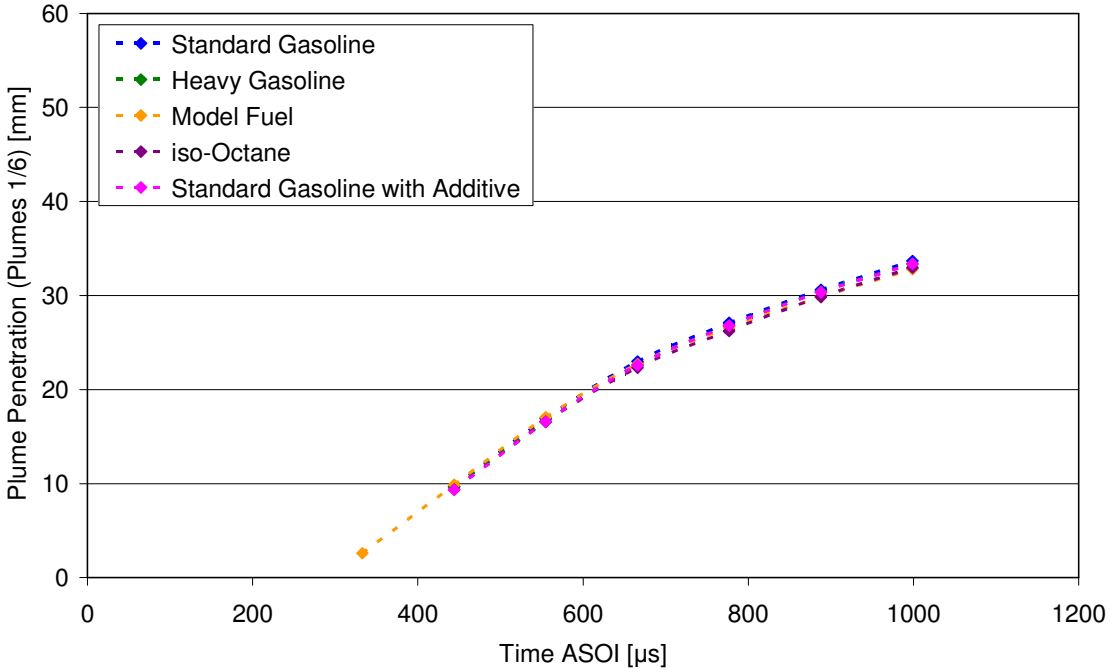

Figure 4-3 Spray Plume Penetration: 20 °C, 5.0 bar

Increasing the injector body temperature, and hence fuel temperature, appears to have only a small effect on plume penetration for a given gas pressure in the absence of spray collapse. This is illustrated in the plume penetration lengths being slightly longer at a gas pressure of 1.0 bar at 90 °C (Figure 4-4) than at 20 °C (Figure 4-1). This is likely to

be due to the increase in fuel temperature leading to a reduction in the liquid viscosity, decreasing the fuel flow drag inside the nozzle and hence increasing its outlet velocity. A parallel plausible explanation for this increase in measured plume length is an increase in vaporisation of the spray, which acts to cloud the spray tip and hence increase the plume length measurement, as can be seen at the spray tips at the appropriate condition in Figure 3-6.

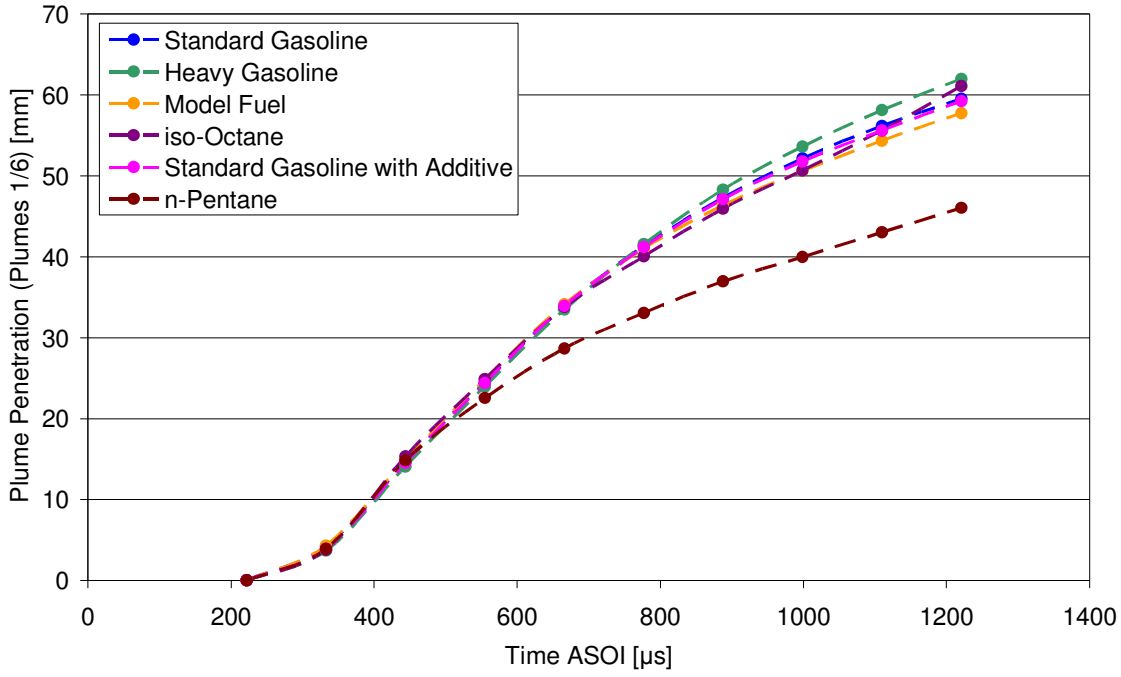

Figure 4-4 Spray Plume Penetration: 90°C, 1.0 bar

At an injector body temperature of 120 °C at 1.0 bar gas pressure, a further small increase in plume tip penetration may be observed in Figure 4-5 for the un-collapsed fuel sprays at this temperature. The *iso*-Octane spray shows the least increase in penetration with increasing fuel temperature as its boiling point has not been sufficiently exceeded to promote measurable vaporisation of the spray. The *n*-Pentane spray at an injector body temperature of 120 °C shows full collapse, even at the 1.0 bar gas pressure condition as illustrated in Figure 3-15. This is reflected in the much reduced plume tip penetration relative to the other, un-collapsed fuels due to the high liquid fuel evaporation rate from the plume tip, decreasing the measured plume axial length between the injector nozzle and the plume tip.

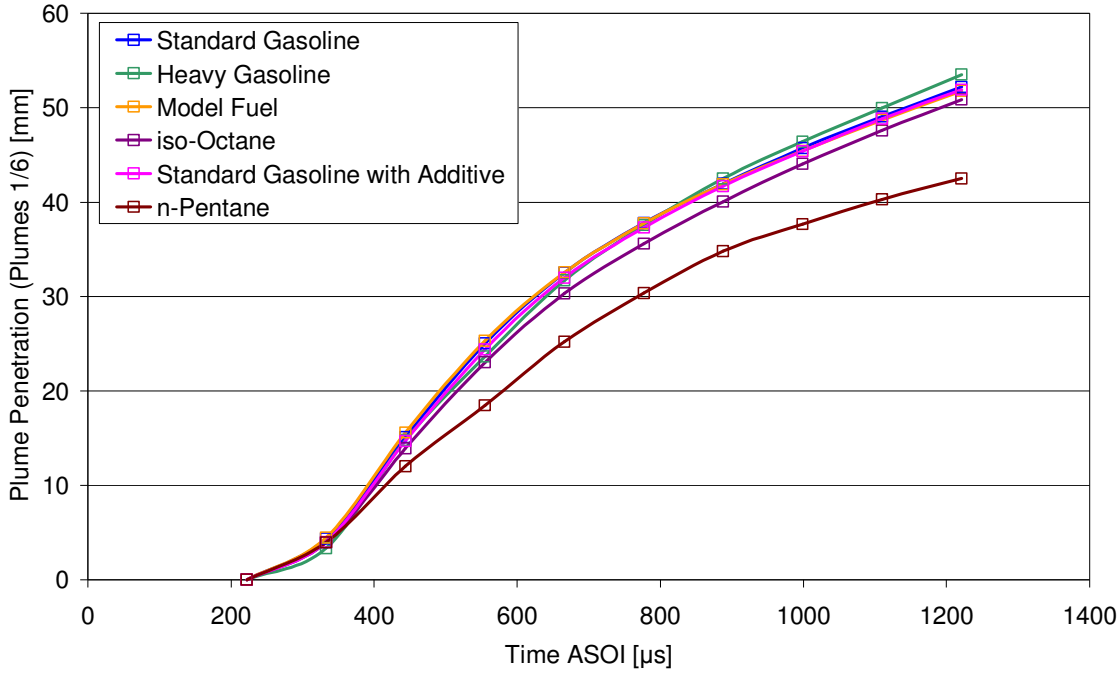

Figure 4-5 Spray Plume Penetration: 120°C, 1.0 bar

For an injector body temperature of 90 °C and gas pressure of 0.5 bar the global spray images show a spray form relatively similar to the nominal, atmospheric form for most fuels, with the exception of *n*-Pentane which is seen to be collapsed at this condition. In a similar fashion as for the 120 °C, 1.0 bar condition (Figure 4-5), Figure 4-6 shows similar plume tip penetrations for all fuels with the exception of the *n*-Pentane. The penetration of Heavy Gasoline is slightly higher than that of *iso*-Octane and the other multi-component fuels due to their low volatility components, which have the least degree of superheat.

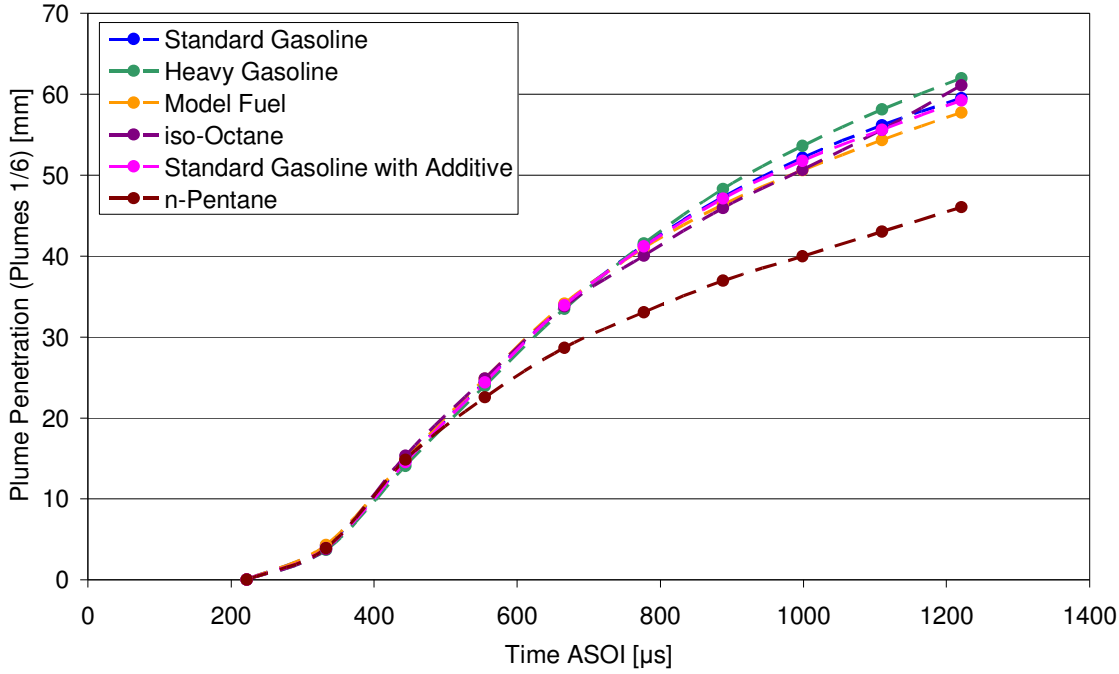

Figure 4-6 Spray Plume Penetration: 90 °C, 0.5 bar

At a higher injector body (fuel) temperature of 120 °C at 0.5 bar gas pressure, as may be encountered at the injector tip in a firing engine at early injection, the increased evaporation of the fuel can be seen to greatly affect the spray development in Figure 4-7, where the sprays produced by Standard Gasoline, Heavy Gasoline, Model Fuel and *n*-Pentane all show full spray collapse. For this condition a measurable difference in plume penetration lengths was observed between the tested fuels, as illustrated in Figure 4-7. For the fuels that are seen to collapse at this condition a similar penetration curve is observed. For the intermediate Heavy Fuel, the observed collapse is again less than that for the lighter fuels and this is manifested in a higher plume penetration rate (gradient of the curve) in Figure 4-7. *iso*-Octane, which has the highest boiling point, shows the least spray collapse and hence the highest penetration rate. At 120 °C, the penetration of *n*-Pentane was observed to be slightly higher than that of the Model Fuel, due to the extreme rate of evaporation of the *n*-Pentane and hence its reduction in droplet diameter, at this condition reducing the droplet drag to such an extent where the rate of plume tip penetration exceeds the rate of liquid fuel evaporation from the plume tip to cause a measurable increase in plume tip penetration over the collapsed sprays.

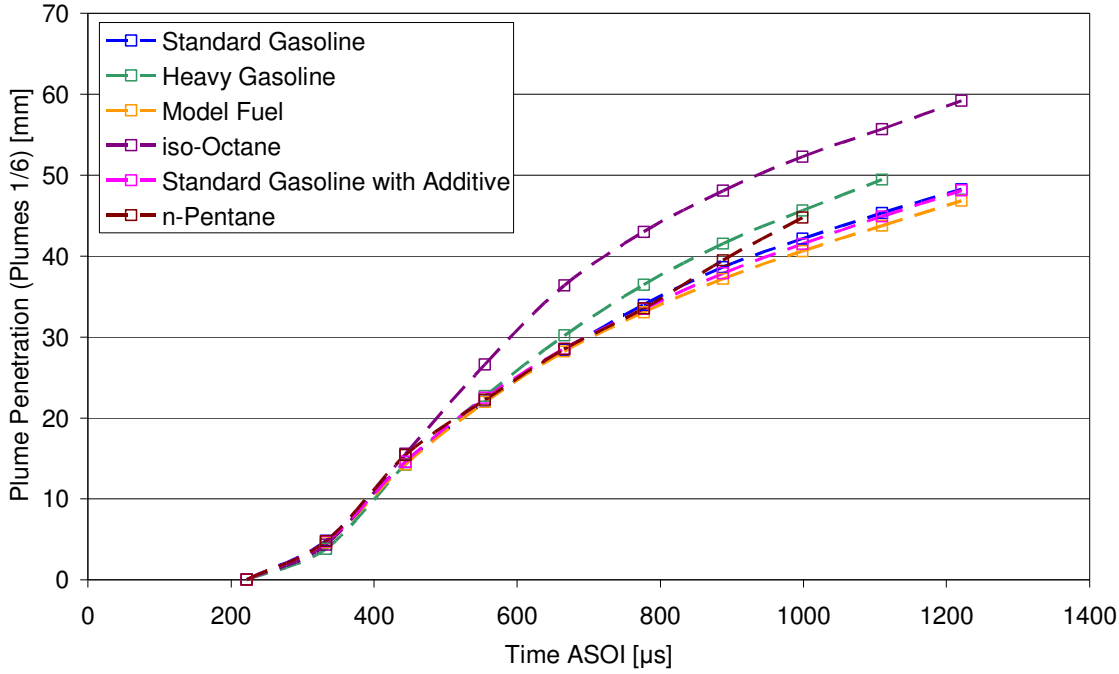

Figure 4-7 Spray Plume Penetration: 120 °C, 0.5 bar

Lastly, an increase in gas pressure at elevated fuel temperatures was found to reduce the measured plume tip penetration to similar values as those measurements made when increasing gas pressure at lower fuel temperatures. This is illustrated by comparing the plume tip penetrations at a gas pressure of 5.0 bar at an injector body temperature of 120 °C (Figure 4-8) to those at the same gas pressure at an injector body temperature of 20 °C (Figure 4-3). This is likely to be due to the high gas pressure acting to suppress the evaporation of the fuels even at high fuel temperatures.

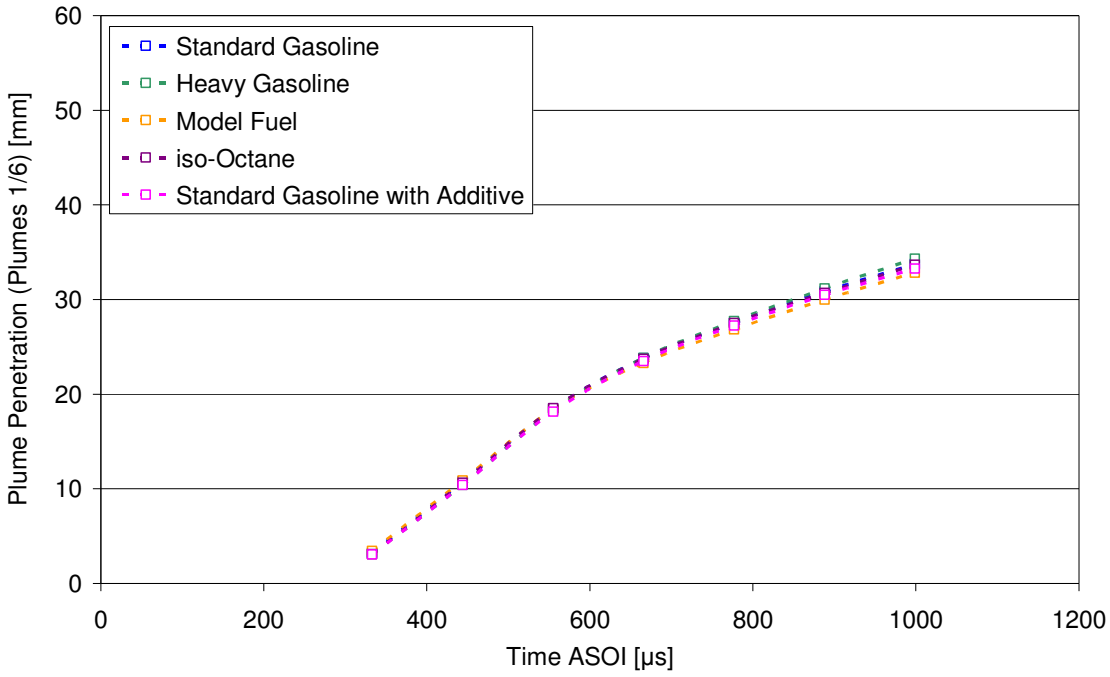

Figure 4-8 Spray Plume Penetration: 120 °C, 5.0 bar

The measurement of the spray plume lengths over the range of test conditions appears to validate the observations of the general behaviour trends visually derived from the images. An increase in fuel temperature initially leads to an increased measured plume penetration due to decreased flow drag and possibly an increase in fuel vaporisation at the plume tip. However, a further increase in fuel temperature leads to a reduction in measured plume length once a critical vaporisation rate is surpassed, and the vaporisation rate becomes high enough to visually "remove" the leading edge from the plume tip. These conflicting observations for a consistent trend are the possible reason that opposing views have been presented in the literature to date. For example, testing a multihole injector of undisclosed configuration using Indolene (a distillation gasoline substitute) at a fuel pressure of 110 bar and gas pressure of 2.5 bar, Zhao *et al* [2002] measured plume tip penetration at 1.0 ms ASOI along the injector axis. They report a measurement of 52 mm at an injector temperature of 20 ° C and 50 mm at 90 °C showing a decrease in penetration with an increase in fuel temperature. This suggests that despite the higher gas pressure, the rate of evaporation of the fuel at the plume tip at the elevated temperature was greater than the rate of plume tip penetration, relative to the lower temperature condition. For the same injector and fuel but at a lower gas pressure of 1.0 bar, the authors measured an increase in penetration with temperature

from 58 mm at 20 °C to 63 mm at 90 °C injector body temperature. This suggests that at the given gas pressure, the effect of evaporation in reducing droplet diameter and hence drag was greater than that of the vaporisation of the liquid, potentially due to the difference in evaporation characteristics between the low and high volatility components of the test fuel. Whilst these results offer some indication of the interaction of the effects of the fuel temperature and gas pressure in relation to the fuel properties in determining the spray development, it should be borne in mind that these interactions also result in geometric differences in the spray forms for different conditions. As such, whilst the possible causes of this increase in spray penetration are not detailed by Zhao *at al.* [2002], it is stated that complex spray behaviour under different gas pressure and fuel temperature conditions are related to "significant alterations in spray geometry."

4.1.2 Spray Velocity

Spray tip velocities were calculated from the plume penetration measurements using the central differencing technique. To calculate the penetration value in this way, the velocity at a given time interval ASOI was taken to be the difference between the plume penetration at the subsequent and previous intervals divided by the time difference between the measurement intervals. Measurements were based on spray plume pair 1 and 6, and are taken in the x-y plane only due to the nature of the shadowgraph imaging technique.

The calculated spray plume tip velocities for Standard Gasoline, *iso*-Octane and *n*-Pentane, for the nominally ambient conditions (20 °C injector body temperature, 1.0 bas gas pressure) are shown in Figure 4-9. The measurements show a similar initial plume tip velocity for all the fuels at this condition.

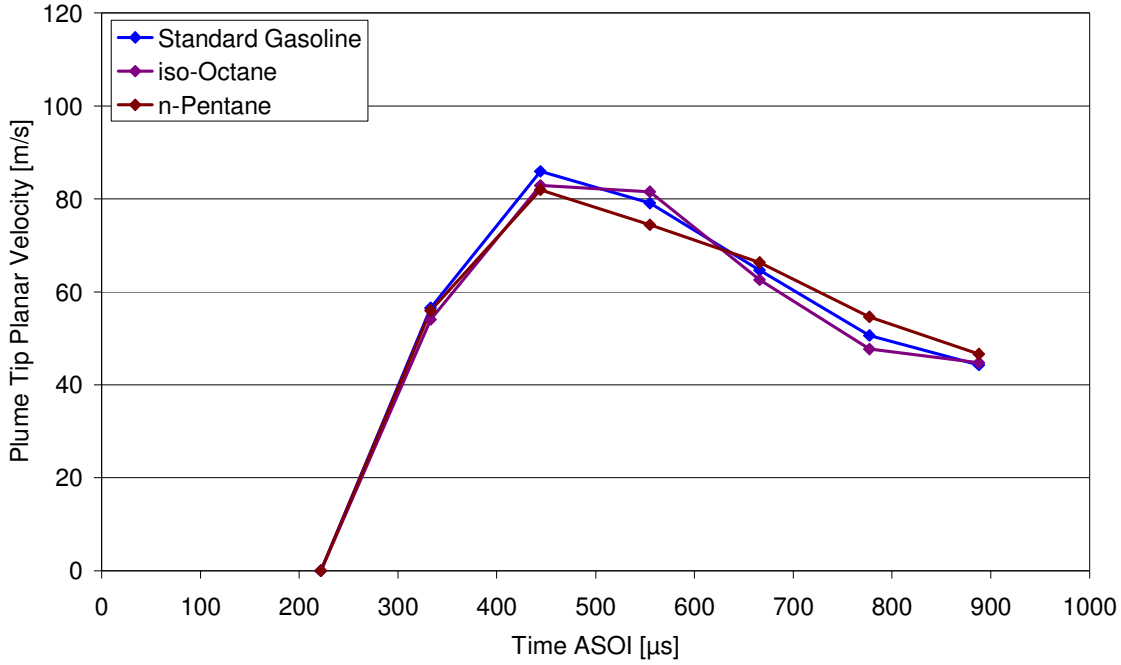

Figure 4-9 Spray Tip Velocity: 20 °C, 1.0 bar

At the spray collapse condition (120 °C injector body temperature, 0.5 bar gas pressure), as shown in Figure 4-10, an increased initial velocity is measured over the ambient condition, due to the reduction in gas pressure, increasing the accelerative force on the spray through the nozzle as well as reducing the aerodynamic drag. The *iso*-Octane spray, which does not show collapse at this condition, shows an increased measured spray tip velocity over the collapsed sprays showing the effect of evaporation for these fuels in reducing the plume length and hence measured spray tip velocity.

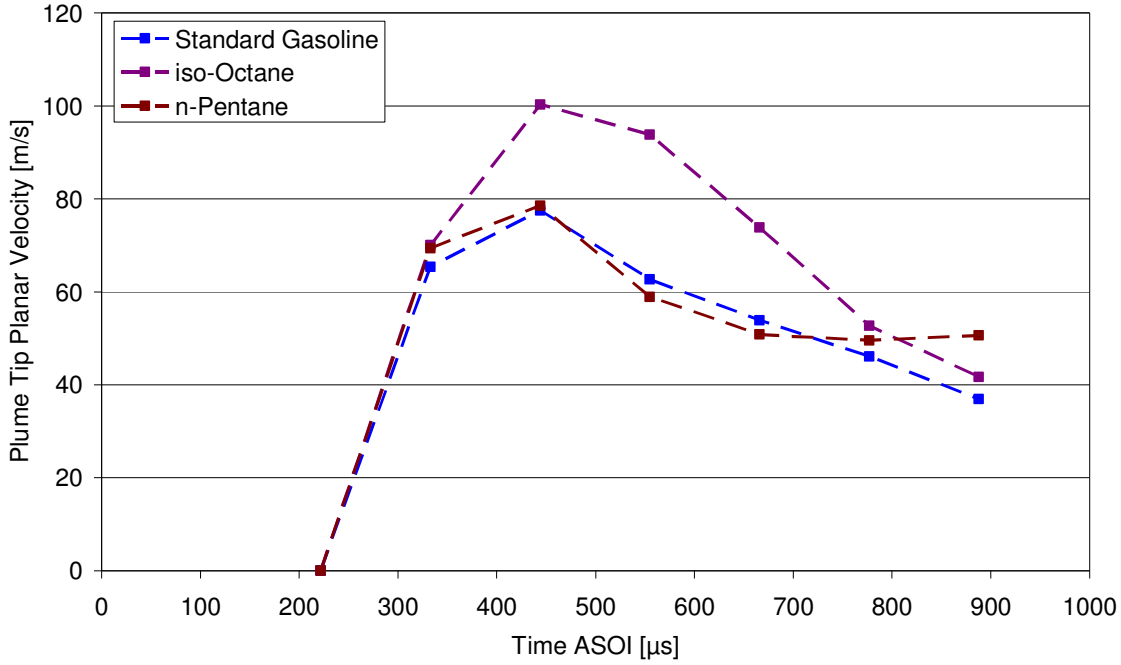

Figure 4-10 Spray Tip Velocity: 120 °C, 0.5 bar

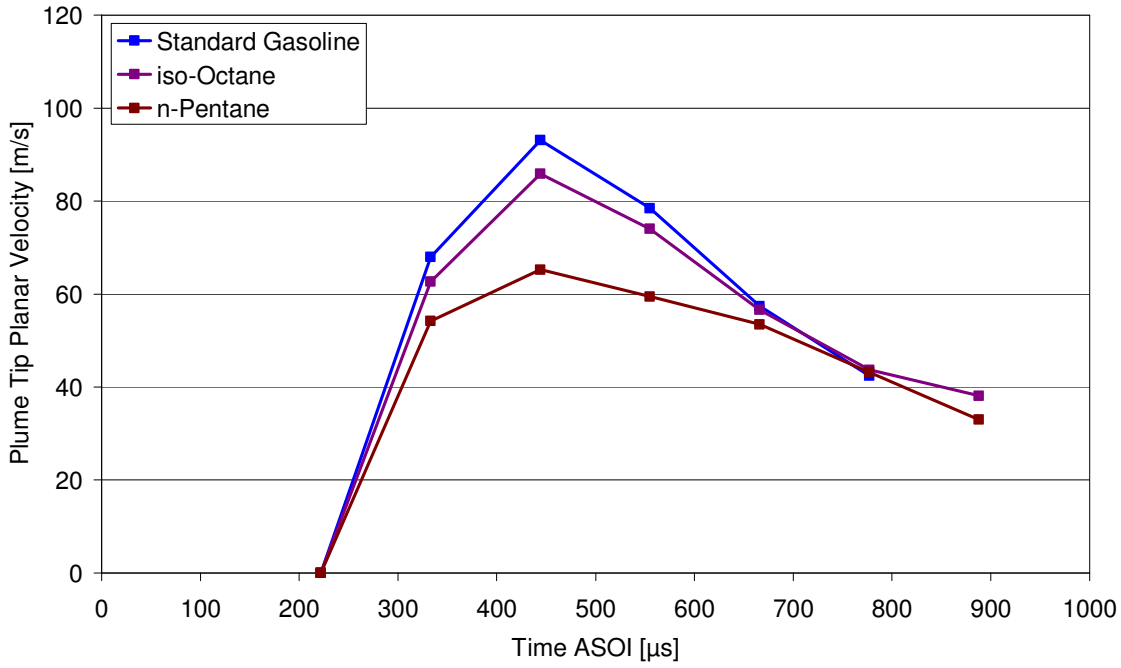

Figure 4-11 Spray Tip Velocity: 120 °C, 1.0 bar

Figure 4-11 shows the measured plume tip velocity at an injector body temperature of 120 °C and gas pressure of 1.0 bar, at which only the very low boiling point *n*-Pentane is seen to fully collapse from the spray images. As can be seen from Figure 4-11, a higher initial spray velocity is measured than at 20 °C for the same gas pressure, due to

reduced viscosity with increased temperature, except for *n*-Pentane which shows rapid evaporation even at this condition and hence shorter measurable liquid plume lengths. The un-collapsed sprays show a similar pattern to the un-collapsed sprays in Figure 4-10, but with reduced plume velocity due to the higher gas pressure.

Whilst the previous figures showed the effect of the test conditions on spray plume tip velocity for different fuels and hence their properties, the effect of the test conditions on the velocity for a single fuel is shown in Figure 4-12 and Figure 4-13 for Standard Gasoline and *iso*-Octane respectively. These graphs also show the measured plume tip penetration for an injector body (and hence fuel) temperature of 90 °C for gas pressures of 0.5 bar and 1.0 bar to illustrate the transition between the nominal and collapsed spray forms. Note that in Figure 4-12 and Figure 4-13 only one fuel is represented in each graph (Standard Gasoline and *iso*-Octane respectively) for clarification between the different test conditions and different shades of their representative colours have been used in these graphs.

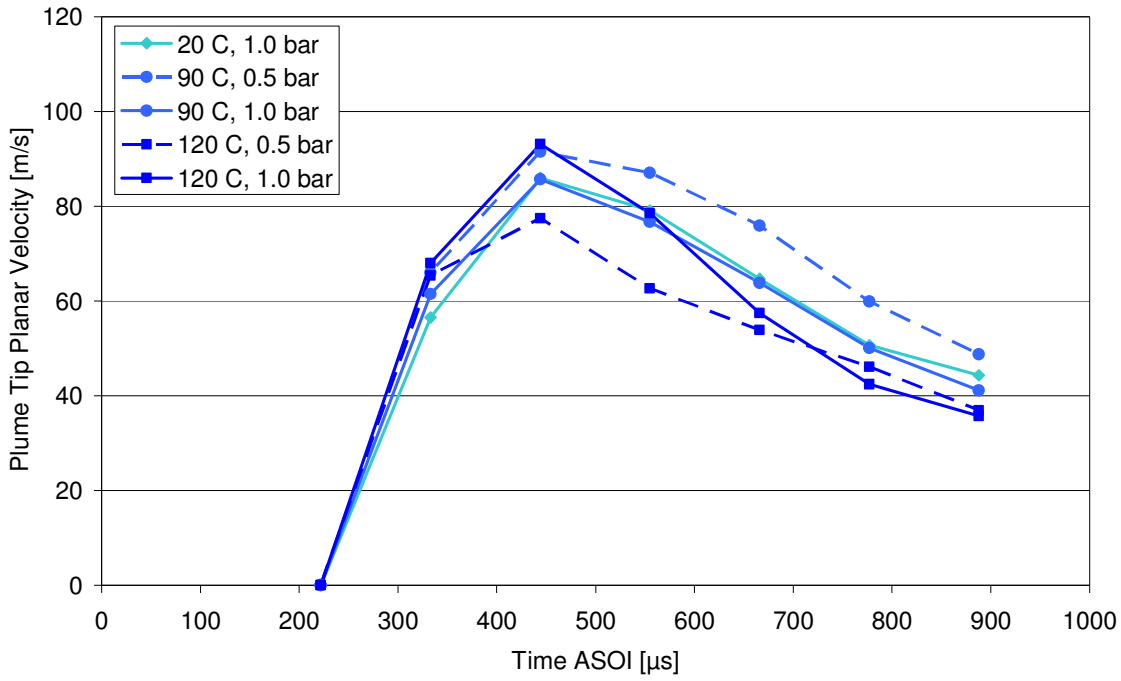

Figure 4-12 Spray Tip Velocity for Standard Gasoline

The spray tip velocities for Standard Gasoline in Figure 4-12 reflect the trends observed from the global spray images. At the nominal ambient condition (20 °C, 1.0 bar, palest blue line) an initial acceleration is observed to 444 µs ASOI due to the pressure acceleration of the fuel out of the nozzle, followed by a retardation due to the effects of

aerodynamic drag and fuel evaporation. An increase in injector body temperature to 90 °C (medium blue line) at the same gas pressure (1.0 bar) increases the initial velocity by a small amount, due to a reduction in liquid viscosity in the nozzle hole. The global spray images do not show the spray to be collapsed at this condition. A reduction in pressure at 90 °C injector body temperature to 0.5 bar (dashed middle blue) shows an increase in measured velocity at all time intervals ASOI due to a reduction in pressure having reduced the drag force. A further increase in injector body temperature to 120 °C at 1.0 bar gas pressure (solid darkest blue line) shows a similar high rate of initial penetration as for the 90 °C, 0.5 bar condition as the rate of evaporation in reducing the droplet size and hence drag is again evident. However, a rapid decrease in plume tip velocity is observed due to the evaporation of the fuel from the plume tip, shortening the measured penetration for these time intervals ASOI. For the collapsed condition of 120 °C injector body temperature, 0.5 bar gas pressure (dashed darkest blue line), a high initial velocity is measured followed by a rapid reduction in acceleration due to the effect of liquid fuel evaporation.

Similar trends to those observed for Standard Gasoline are observed for *iso*-Octane in Figure 4-13. However, the lack of collapse of this fuel spray is illustrated by a further increase in spray tip velocity at 120 °C injector body temperature at 0.5 bar gas pressure (dashed darkest violet line) over the lower temperature conditions, although a greater rate of decrease in velocity is observed for this condition relative to the other conditions at later time intervals ASOI as the liquid has had sufficient time post injection for the rate of evaporation to cause a measurable reduction in the penetration rate of the spray tip.

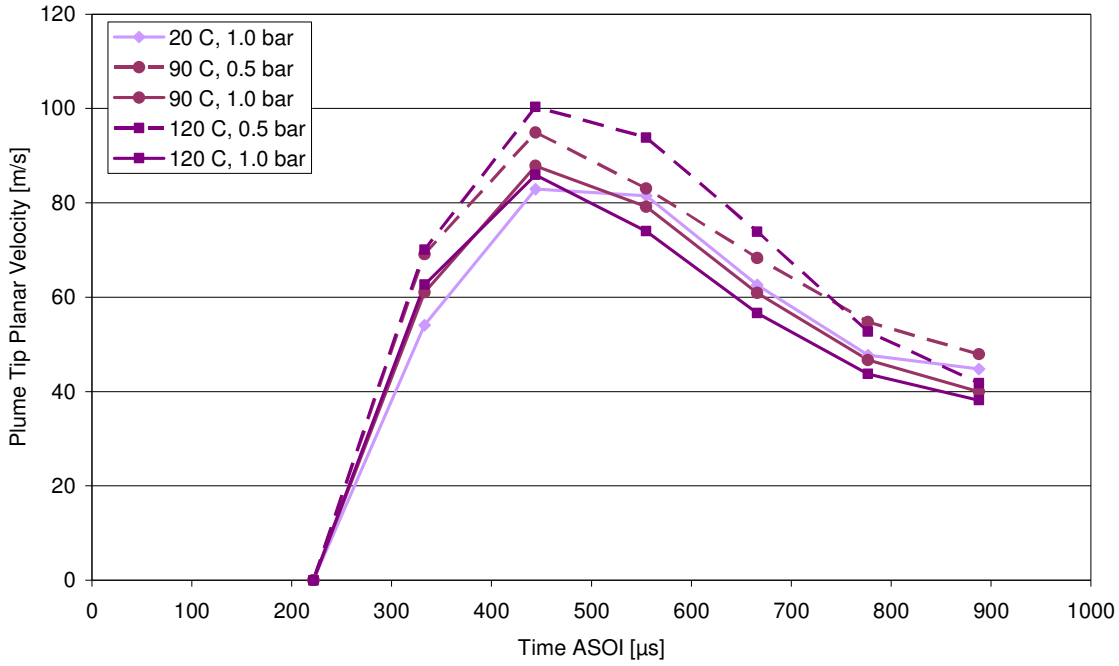

Figure 4-13 Spray Tip Velocity for *iso*-Octane

The spray plume tip velocity trends show the time dependence of the factors affecting these measurements. This applies to both the initial acceleration of the spray as well as to the factors affecting subsequent rates of reduction in measured velocity. The global spray images and plume penetration measurements, from which these velocity measurements are derived, show the rate of evaporation of the liquid fuel is a key factor in determining the spray penetration rate (velocity) and development form. This rate of evaporation appears to change with time, shown by the changes in rate of change of plume tip velocities, with collapse conditions being associated with greater rates of evaporation and hence greater rates of decrease in plume tip velocity.

4.1.3 PDA Velocity Measurement

The velocity as well as size of individual droplets in the spray plumes was measured using the Phase Doppler Anemometry Technique. The main considerations of the technique with respect to the measurements here presented are that a valid measurement can only be recorded if a single droplet is present in the measuring volume at any one time, and if sufficient light intensity is able to penetrate the spray and be detected from refractions at the measurement volume. Due to these limitations, this technique is best suited to taking a number of measurements at a suitable set location within the spray. To this point, the density of the spray is dependent on the location within the spray (*e.g.* the spray tip being more dense than the trailing plume), and the temporal variation of spray

density with respect to a set location as the phases of the spray pass the measurement location.

For comparison to the previously presented spray tip velocity measurements as measured from the image analysis relating to plumes 1 and 6, it was desired to measure the velocity of one of these plumes using the PDA technique. However, due to contracting nature of this plume for the majority of the fuels, only the non-collapsing *iso*-Octane spray could be analysed using the PDA technique at a fixed location within Plume 6 over the full range of experimental conditions. It should also be noted that these measurements were taken prior to the delivery of the oxygenated fuels, and unfortunately the PDA equipment was not available for subsequent experiments.

The droplet velocities presented in the figures below are calculated from the square root of the sum of the squares of the *y* and *z* axis measured velocity components of the droplets. The *x* axis, which has the smallest velocity component, could not be measured using the 2 beam PDA system employed for this work. Due to the two dimensional nature, on the same *y* and *z* axis, of the side view imaging of the spray from which the previously presented tip velocities were calculated, both of these spray velocity measurements are directly comparable in terms of their velocity vectors. By way of indication, the *y* axis component was measured to be typically around 25 m/s for the non collapsed conditions using the PDA technique.

The droplet velocity graph for plume 6 for the *iso*-Octane spray at nominally ambient conditions is shown in Figure 4-14. This graph shows an average droplet velocity (dark line) of approximately 50 m/s throughout the duration of the spray, although this is seen to reduce slightly towards the end of the measurement interval. The PDA point measurement measures any droplet which happens to pass through the measurement region, regardless of its location within the spray, and hence measures those that are slower than the leading edge, as well as those travelling at the same velocity as those droplets at the leading edge; the combined effect of these measurement is to measure a lower average velocity across all the droplets. Note that this measurement is spatially bound, and so is that of the droplets as they pass through the measurement location with a temporal dependence. This is in contrast the previously presented spray tip measurements which were spatially dynamic, in that the measurement was of the spray tip leading edge at all times, regardless of the spatial location of that leading edge.

Figure 4-14 shows a wider spread in droplet velocities early on in the spray, following a very narrow band of droplet velocities at the spray's leading edge (or the first droplets which could be measured). The well developed, steady state spray, measured from approximately 700 µs ASOI onwards (note that this time interval includes that required for the spray to travel the distance to the measurement location) is formed of droplets of a narrower band of velocities, with a slightly increased mean over those droplets measured prior to this period. This band of droplet velocities is then seen to tail off with a reduction in mean velocity, although some higher velocity droplets appear to have measured later in the spray. Note that the PDA measurement duration was limited to 1300 µs ASOI for this analysis due to greatly diminishing data rates following this time interval, and illustrates the reduction in spray density towards the end of injection (associated with pintle closing), diminishing the probability of droplets passing through the PDA measurement volume. This is likely to have prevented the measurement of velocities of droplets associated with the spray's actual trailing edge.

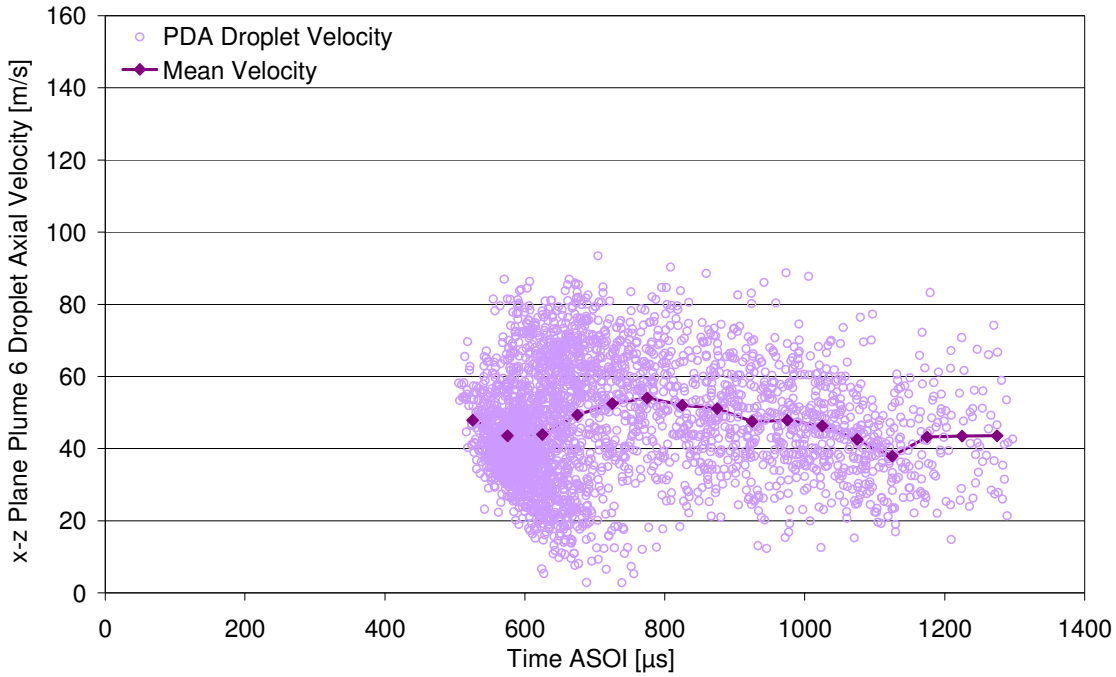

Figure 4-14 Plume 6 Droplet Velocity: *iso*-Octane 20 °C, 1.0 bar PDA

The graphs of *iso*-Octane spray droplet velocity plotted with respect to time at an injector body temperature of 20 °C and a gas pressure of 0.5 bar are presented in Figure 4-15. The droplet velocity profile in Figure 4-15 shows a more distinctive increase following the leading edge than for the ambient pressure (1.0 bar) condition, but with

the same trailing off in mean velocity, with the mean velocity being higher than for the 1.0 bar gas pressure condition due to reduced drag on the droplets.

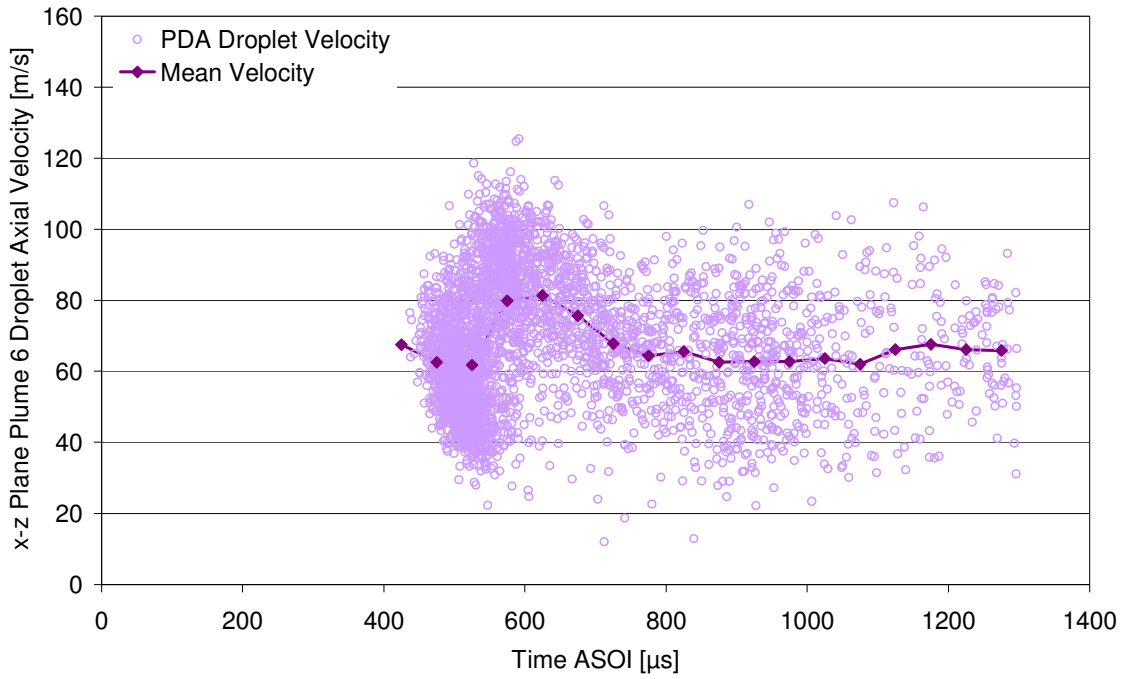

Figure 4-15 Plume 6 Droplet Velocity: *iso*-Octane 20 °C, 0.5 bar PDA

An increase in injector body (and hence fuel) temperature to 120 °C is seen to increase droplet velocities at a gas pressure of 1.0 bar in Figure 4-16 relative to Figure 4-14. The range of velocities of droplets following the initial spray also increases, with individual droplets having measured velocities over 120 m/s and the mean velocity being around 60 m/s throughout the spray duration. Although *iso*-Octane does not collapse at this condition, it is likely to be over or at its ambient boiling temperature whilst in residence in the injector at 120 °C, it being prevented from boiling by the pressure exerted upon it. Upon opening of the injector orifice, the liquid body expands, accelerating the initial volume out of the injector, resulting in the very high measure droplet velocities occurring early on in the spray.

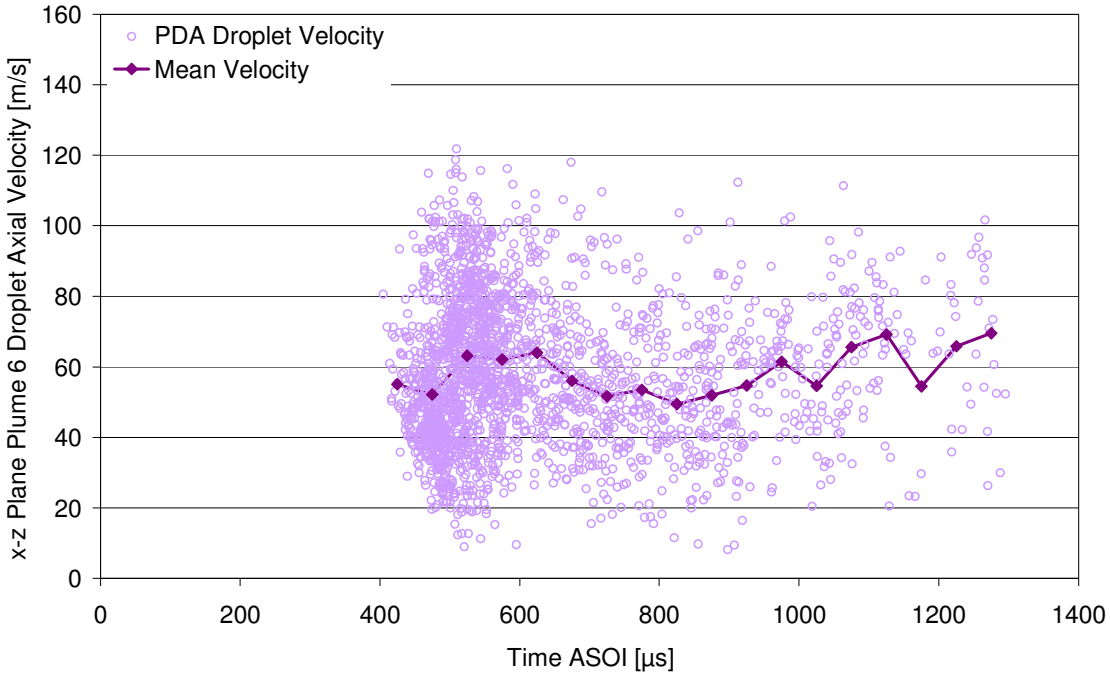

Figure 4-16 Plume 6 Droplet Velocity: *iso*-Octane 120 °C, 1.0 bar PDA

In Figure 4-17 there also does not appear to be a marked increase in measured velocity following the leading edge as for the previously presented conditions, presumably because of the high rate of evaporation for this condition relative to lower fuel temperatures and higher gas pressures. This would be expected to result in a less dense leading spray edge, and hence an increased droplet number during this time, including a number of distinct, high velocity droplets which were not measured for the previously presented conditions due to these droplets being masked by the dense volume of droplets. This is also shown by the increase in droplet velocity as the spray develops, with extremely high droplet velocities in excess of 140 m/s being measured for droplets during the steady state phase of the spray.

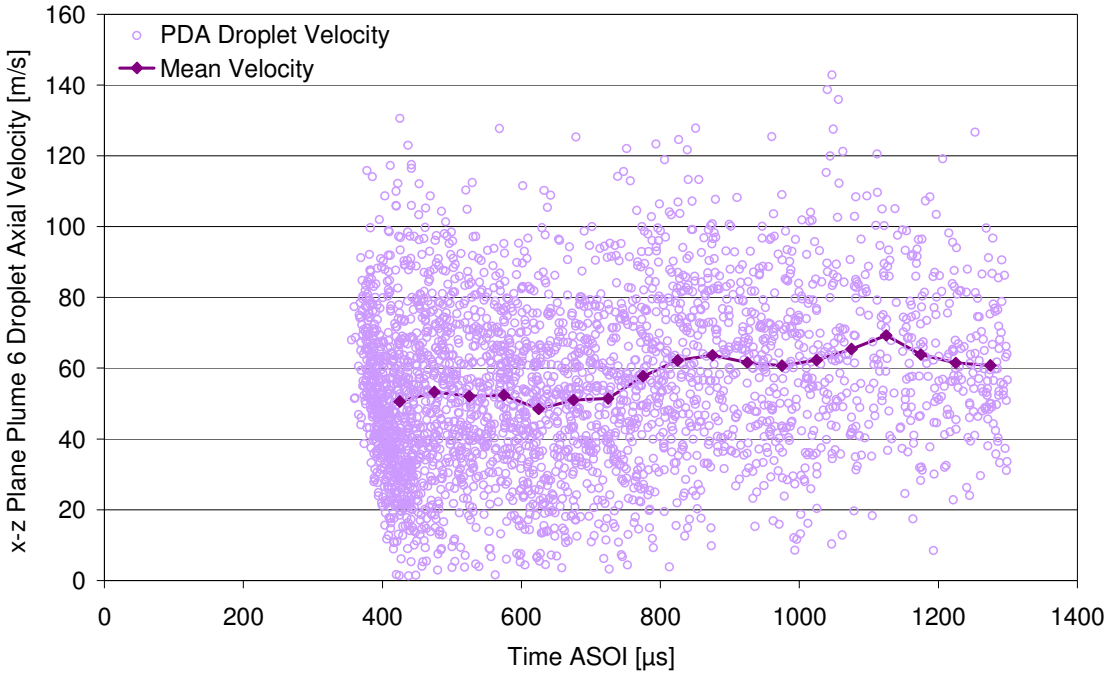

Figure 4-17 Plume 6 Droplet Velocity: *iso*-Octane 120 °C, 0.5 bar PDA

The PDA measurement location was 25 mm below the injector tip. Such a distance would be expected to lead to a start droplet size measurement at approximately 300 µs after the start of injection (ASOI). However the droplet size measurements show that initial droplet size measurements are made at approximately 400 – 500 µs ASOI. This additional delay is likely to be due to the leading edge of the spray being too dense to enable measurement, either for enough scattered light intensity to be detected or to ensure the presence of only one droplet within the measurement volume.

4.1.4 Spray Cone Angle

The main feature exhibited by a collapsed spray can be seen to be the convergence of the plumes, and hence a measure of this convergence can be seen to provide a measure of the extent of spray convergence and collapse. This measure can be provided by the value of the inclusive external spray cone angle. The external spray cone angle also has an important relevance to engine operation in that it indicates the position and area of the spray wetted footprint, and hence potentially un-burned hydrocarbons emissions from contact with the cylinder boundaries. However, the relationship between the overall spray cone angle and the wetted footprint is not straight forward. As the spray contracts, the cone angle decreases, which results in a smaller spray footprint. However, whilst the plume centre lines may contract, an increased swelling of the plumes could also result in a larger measured cone angle. Whilst each individual plume may be seen

to expand at the injector nozzle for spray-collapse conditions, the overall angle subtended by the extreme left and right-hand plume pairs, as imaged from the side, may actually be seen to decrease. This overall spray cone angle is of greater significance than the individual plume cone angles in relation to engine operation as it marks the outer boundary of the liquid spray and hence the rich air/fuel ratio area in the combustion chamber.

Although an often used measure of spray convergence, there is no set definition of the measurement locations used to determine the spray cone angle. Furthermore, the parabolic nature of the spray near the nozzle (as shown in Figure 4-18), can lead to marked differences in measured angle values, even of the same spray, for different measurement locations. Zhao [2002] investigated the effect of measurement location on measured cone angle for a typical pressure swirl spray, and ultimately concluded that the most appropriate location was purely dependant on the spray form and each investigator's preferences and requirements. In this respect, great care should be taken when comparing cone angle values from different sources. For multihole injectors, another important consideration when comparing overall spray cone angles is the nozzle hole diameter for individual plumes as well as the hole spacing and location on the injector tip. To this end, comparison may be made of the cone angles for individual plumes, although these are often impossible to measure for nozzles which produce more than one, closely spaced plumes, as was found to be the case for the injector used for this work. The measurement locations used in this work to define the spray cone angle (θ) are shown in Figure 4-18.

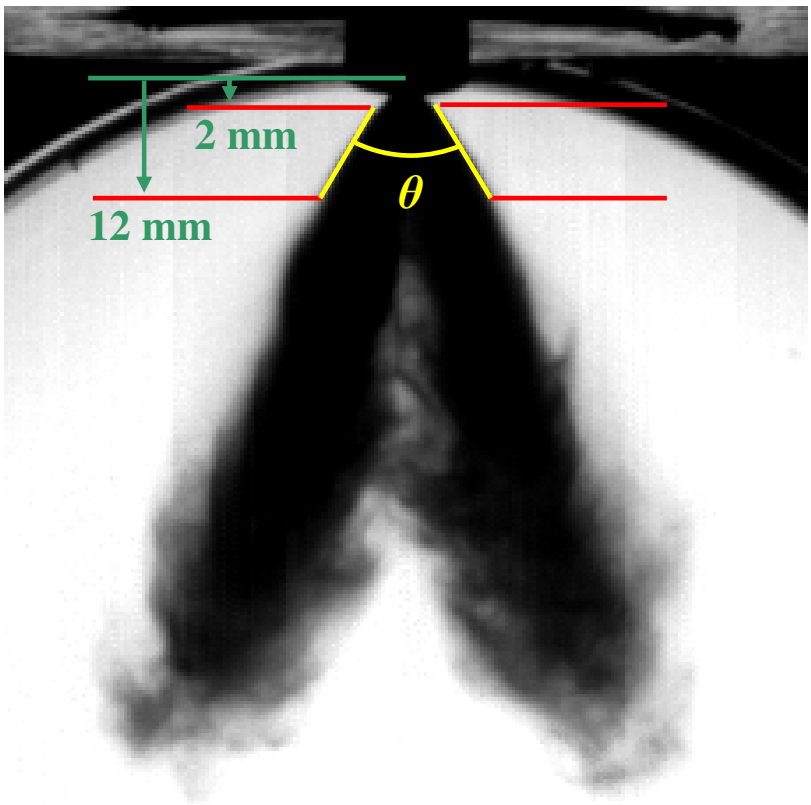

Figure 4-18 Measure of Spray Cone Angle (End View)

The near nozzle measurement location was selected to be 2 mm vertically downstream from the nozzle to avoid near nozzle spray development effects, whilst the downstream measurement location was selected to be 10 mm vertically downstream from the upper measurement location to avoid parabolic effects resulting from near nozzle spray expansion. The measured cone angle value was found to be constant over the duration of the fully developed spray for each experimental condition, and the results here presented are those measured from the images captured at 777 μs ASOI for all conditions.

The overall spray cone angles as measured from the captured end view spray images for each experimental condition are presented in Figure 4-19.

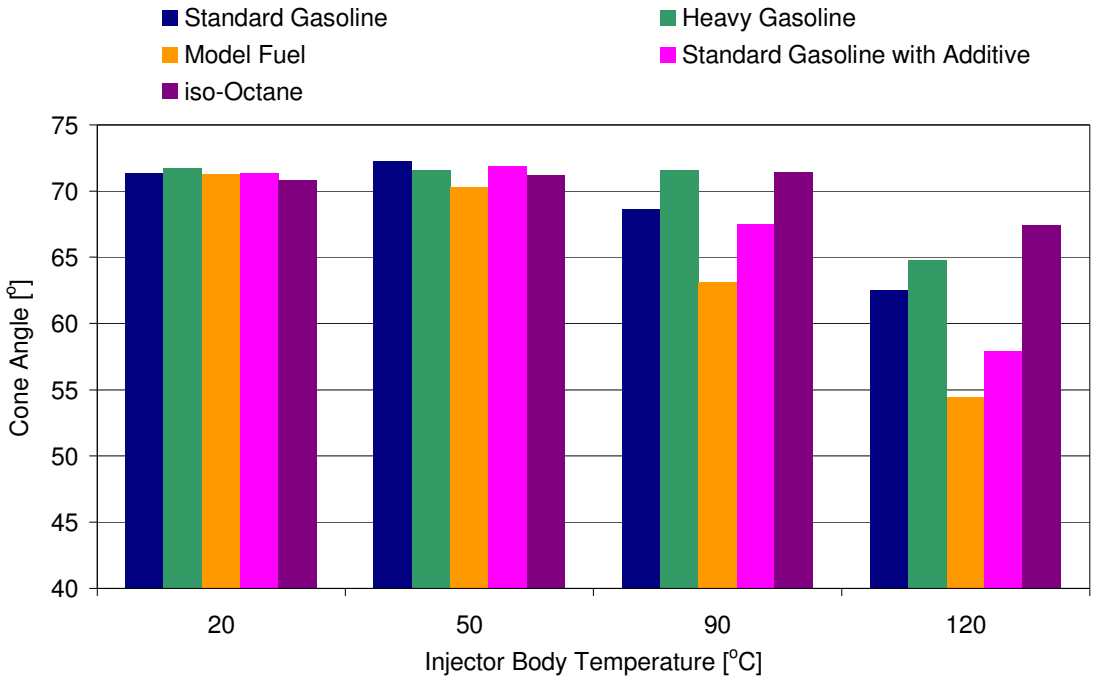

Figure 4-19 Overall Spray Cone Angle: 0.5 bar Gas Pressure, End View

Figure 4-19 shows that at lower injector body (and hence fuel) temperatures (*i.e.* 20 °C and 50 °C), all fuels produce similar combined cone angles, which reflects the similar spray form seen for all sprays at this condition. For most fuels the measured spray cone angle is slightly larger for 50 °C than 10 °C injector body temperature, showing a slight increase in the evaporation of the fuel at this temperature. For the multi-component fuels in this study this is likely to be due to the fuel temperature being in excess of the boiling temperature of some of their high volatility components. At 90 °C injector body temperature the cone angle was measured to decrease for Standard Gasoline with and without Additive and the Model Fuel, as reflected in the images of the fuel sprays (Figure 3-22). It may also be seen that the Model Fuel is measured to collapse the greatest extent at this point, which may be expected as it has the highest Reid Vapour Pressure of any of the tested multi-component fuels. A further increase in injector body temperature to 120 °C shows a further reduction in the spray angle for all presented fuels. Compared to Standard Gasoline, this reduction is less for the medium volatility Heavy Fuel and even less for *iso*-Octane. Again the multi-component Model Fuel is seen to collapse the most at this condition. In this respect, the trend in the reduction of spray cone angle directly reflects that in the extent of spray convergence with respect to injector body temperature and gas pressure for each fuel.

The cone angle measurements presented in Figure 4-19 clearly shows a reduction in inclusive cone angle for the spray as the plumes converge at increased fuel temperature, reduced gas pressure conditions. By comparing the global spray images in Figure 3-22 to the measured values and defining spray collapse in the case of this spray when the right hand plume pairs completely converge so as that individual spray tips are no longer discernable at the spray leading edge, it can be deduced that the spray can be said to be fully collapsed when the spray cone angle has reduced by at least 20 % from its nominal value (nominally atmospheric conditions) for the injector used for this work.

4.1.5 Base View Spray Areas

To illustrate the effect of the spray cone angle on the physical dimensions of the spray, the area of the liquid spray as seen from the base view in the octagonal pressure chamber was measured using an automated routine. This view is similar to that which would be seen from the piston crown in a running engine and so to put these dimensions into the context of an engine, the total liquid spray area has been normalised to the bore diameter of 89 mm of the engine for which this injector had originally been designed, by dividing the detected spray area by the area of the piston bore. The measured area was also trigonometrically corrected to account for the 19° injector mounting angle. A graph of the normalised spray area is presented in Figure 4-20 for Standard Gasoline and *iso*-Octane at a range of injector body temperatures, all at 0.5 bar gas pressure. Due to hardware availability, imaging and analysis of the spray through the base view was only carried out for these fuels. However, the general trends of how these fuels relate to the other fuels tested in these work are also applicable to this situation. Note that the usual graphical colour nomenclature used in this work has been altered for clarity in Figure 4-20, and that the lines for the 20 °C injector body condition have been shown in solid for ease of interpretation. Due to the image analysis technique employed, initial detection of the spray was not possible until the spray area was larger then that of the injector nozzle, and so the first detected spray is at a later time ASOI than for the side view spray assessments.

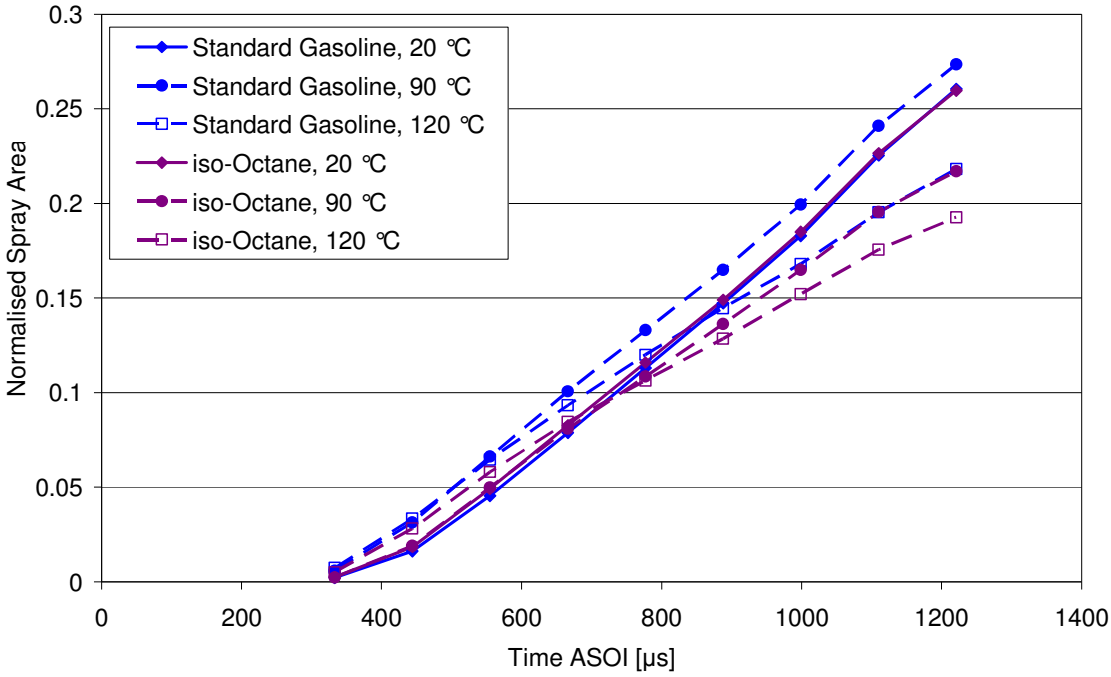

Figure 4-20 Base View Spray Area Normalised to Engine Bore

For both the Standard Gasoline and *iso*-Octane the measured spray areas are nearly identical at the ambient temperature (20 °C) condition. At a higher injector body temperature of 90 °C the effect is for a larger spray area to be detected for Standard Gasoline due to a widening of the spray plumes, whilst for *iso*-Octane at this temperature little effect on the detected spray area is measured at the beginning of the injection event and a reduction in area is seen from 800 µs ASOI, presumably due to a sharpening of the individual spray plume boundaries. A further increase in injector body temperature to 120 °C at this gas pressure of 0.5 bar leads to the onset of spray collapse for Standard Gasoline. This is evidenced by an initial increase in spray area over the ambient temperature condition, followed by a reduction in area to closely match that of *iso*-Octane at 90° at between 600 and 800 µs ASOI due to the combination of the closely spaced individual plume to a single central plume, which is individually larger than the normal single plumes, but smaller than their overall combined area. Lastly the contraction, but not collapse, of the *iso*-Octane spray seen at these conditions (120 °C, 0.5 bar) is manifest in a reduced total spray area as the plume are now more oblique to the angle of view and hence show a smaller footprint. In relation to an operating engine, the maximum spray footprint observed under typical high temperature, stratified charge operational conditions is equivalent to only approximately 1/4th of the total engine bore. For completeness, and for comparison with the in-cylinder imaging done using the same injector by Serras-Pereira *et al*. [2007b, 2008], it should to be noted that the diameter of

the optical piston-crown was ~64 mm, and that hence the ratio of the optically accessible bore area to the full cylinder bore area was ~0.52, so that 25% of the full bore area (upper measurement in Figure 4-20) corresponds to ~55% of the engine's bore imaging area.

4.2 Droplet Sizing

In addition to the above assessed parameters, the size of the droplets at various locations within the spray may be used to infer information about the break-up rate of the spray, as well as the fuel vaporisation rate. In order to investigate further the link between spray development and the atomisation and vaporisation rates, droplet sizing of the spray under a variety of conditions was carried out in both the cylindrical and octagonal chambers using both the Phase Doppler Anemometry (PDA) and Laser Diffraction techniques.

4.2.1 Phase Doppler Anemometry

The majority of droplet size measurements for this work were carried out using the Phase Doppler Anemometry (PDA) method. As described previously, the PDA technique is based on the analysis of droplets as they pass through a fixed measurement region, where this region is small in comparison to the spray plume diameter.

Previous work on both pressure swirl (*e.g.* van der Wege *et al*. [2000c] and Wigley *et al*. [2004]) and multi-hole injectors (*e.g.* Zigan *et al*. [2009]) has shown a considerable variation in droplet size across the diameter of spray plumes. The global spray images also illustrated plume convergence with increasing fuel temperature and decreasing gas pressure. To compensate for this convergence, and hence to ensure that the droplets at the same axial radius were measured for all conditions, the location of the PDA measurement region was altered for each condition in line with the expected degree of plume convergence. For all conditions, the measurement location was maintained at 25 mm downstream from the injector nozzle, with the adjustments being made in the *x*-*y* plane. To provide adequate optical access to the spray for the incident and refracted beams, the PDA technique was applied to plume 2 of the spray, as illustrated in Figure 4-21. By carrying out the PDA analysis of the spray in this plume, the spray plumes were not required to be separated near the injector nozzle, although due to hardware limitations, the PDA technique could only be applied further than 25 mm below the injector nozzle.

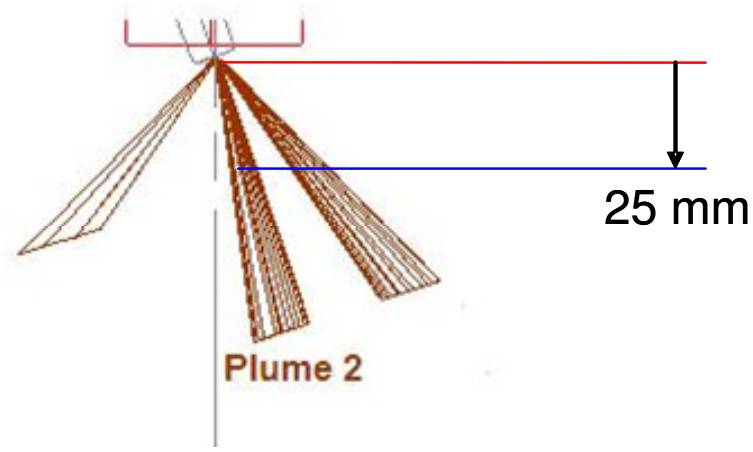

Figure 4-21 PDA Droplet Measurement Location

The anatomy of 100 overlaid injection events in terms of the droplets detected and measured is shown in Figure 4-22, where each blue diamond represents a single droplet. The diagram has also been annotated to show the main injection features and their temporal relations. A high number of droplets are detected in the initial spray as it passes the detection area. However, due to the high liquid density during the course of the main part (*i.e.* not pintle opening or closing periods) of the injection event, the detection rate reduces during the spray event. Towards the end of the injection event the number of detected droplets increases again as the closing of the injector pintle reduces the liquid volume flow rate. Lastly, a number of droplets entrained in the plume wake are detected following the injection event. For all PDA measurements, the droplet velocity and size were measured simultaneously. As detailed in Chapter 2, these measurements comprised of around 5000 valid detected droplets, and several tests were carried out to ensure repeatability of results for each condition.

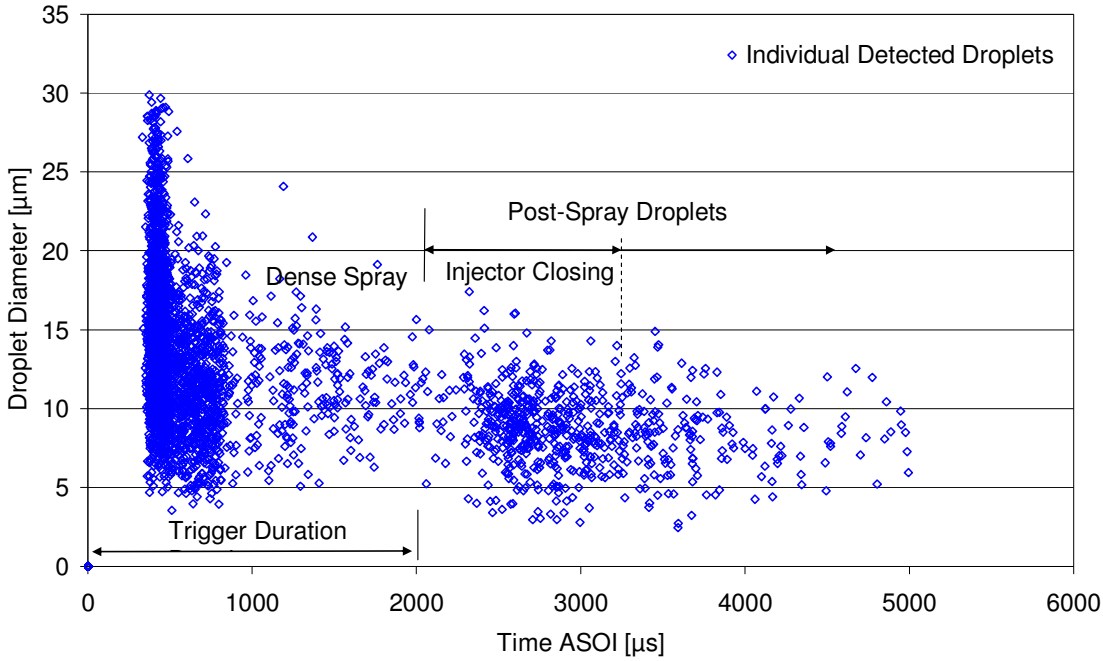

Figure 4-22 PDA Drop Size Characteristics (Standard Gasoline, 20 °C, 1.0 bar)

In the following graphs, the mean of the measured droplets over 100 µs intervals over the injection duration has been overlaid onto the individual droplet measurements, and hence these charts show both the mean and distribution of droplets over the injection duration. Unfortunately the mean trend lines are somewhat clouded behind the individual droplet points, despite every endeavour being made to bring the mean lines to the front of the images. However, the plot points and trend in the mean are clearly visible. As the means are calculated based on the droplet measurements over discrete time intervals, each mean point will be calculated based on a different number of individual droplet measurements, depending on the data rate over the averaging interval. As such, the low data rate sections in the middle of the spray events are subject to a greater skewing by individual measurements. The colour nomenclature used throughout this work has been retained in the mean trend analysis, although lighter shades of the fuel colours have been used for the droplets to clarify the graphs.

The measured droplet size trend for Standard Gasoline at the nominally ambient conditions is shown in Figure 4-23. The initial mean droplet diameter is around 15 µm, and is seen to diminish over the injection duration, and is around 11 – 12 µm over the main injection event. Increasing the injector body temperature to 120 °C, as presented in Figure 4-24, results in fewer large droplets being detected at the start of the injection event with the initial mean reduced to around 10 µm and the mid-injection mean being

centred on around 9.5 µm. The global spray images at this condition (Figure 3-3) show some convergence of the spray plumes but not a complete collapse of the spray form. Reducing the pressure at an injector body temperature of 120 °C to 0.5 bar induces the spray collapse condition for Standard Gasoline (Figure 3-2), and results in a further reduction in measured droplet diameter over the course of the injection event as illustrated in Figure 4-25. At this collapse condition the initial mean droplet diameter is around 9 µm and the mid injection mean is around 7 µm.

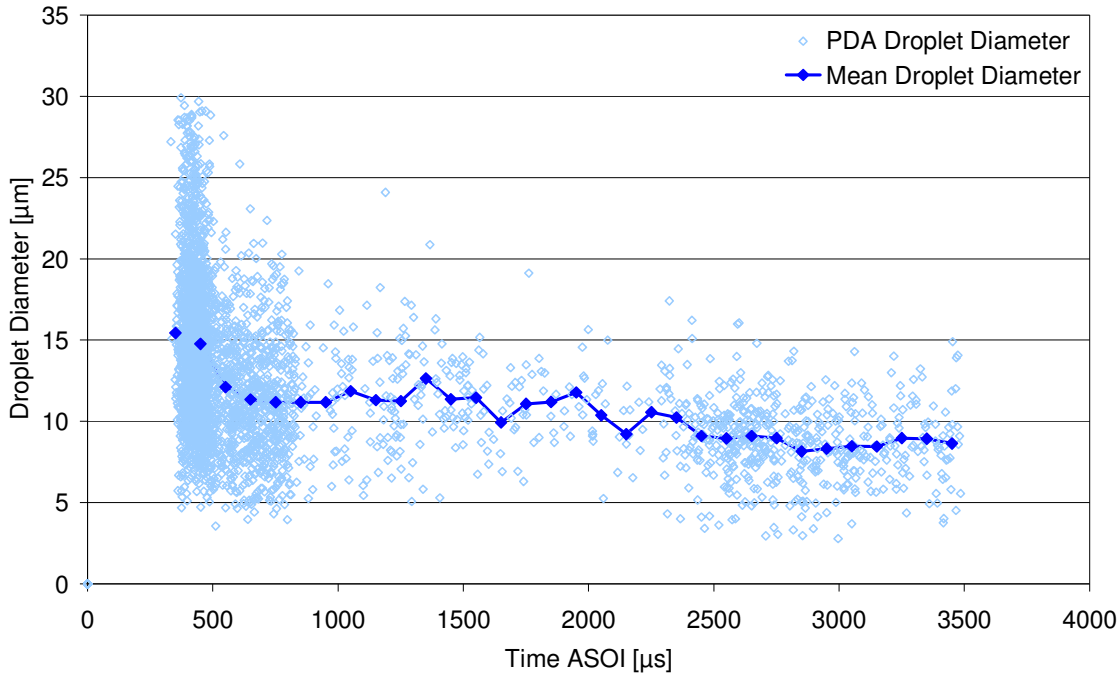

Figure 4-23 PDA Droplet Sizes with Instantaneous Mean over Injection Duration (Standard Gasoline, 20 °C, 1.0 bar)

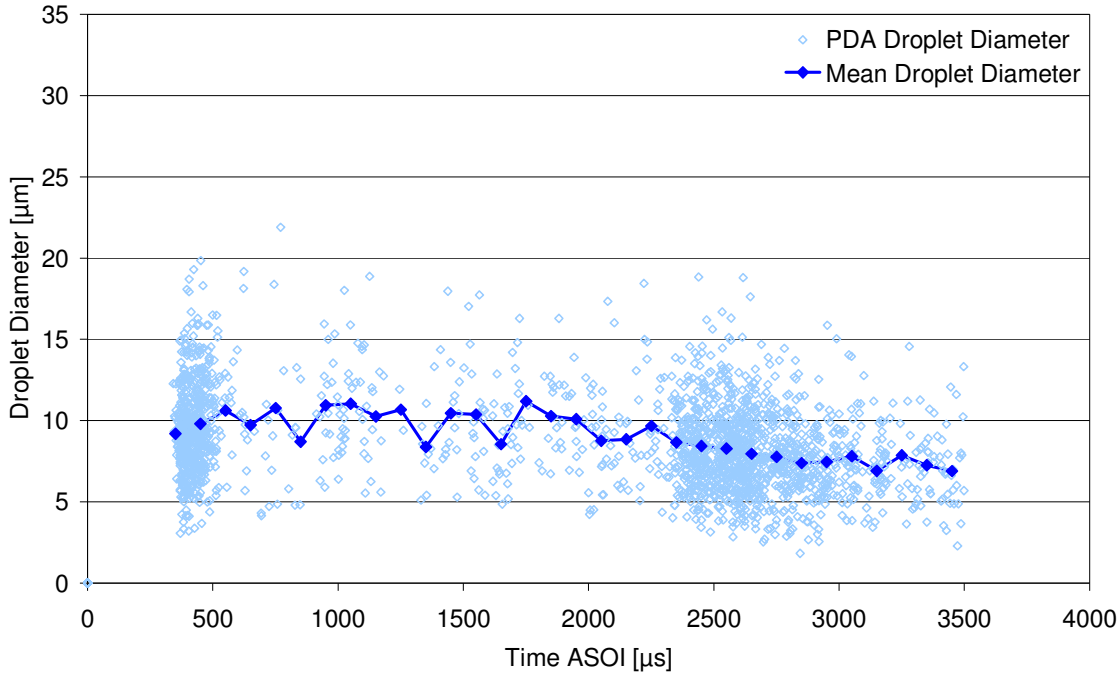

Figure 4-24 PDA Droplet Sizes with Instantaneous Mean over Injection Duration (Standard Gasoline, 120 °C, 1.0 bar)

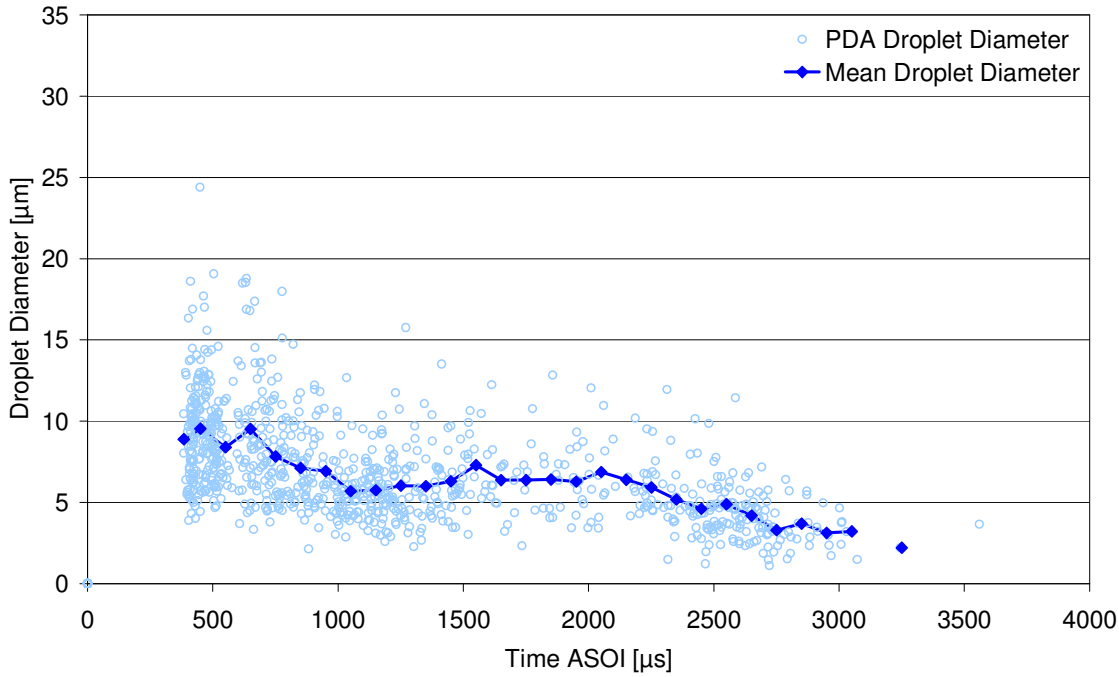

Figure 4-25 PDA Droplet Sizes with Instantaneous Mean over Injection Duration (Standard Gasoline, 120 °C, 0.5 bar)

The initial and mid-injection droplet size mean values and distributions for *iso*-Octane in Figure 4-26 are similar to those measured for Standard Gasoline at the nominally

ambient condition. Figure 4-27 shows a reduction in the initial mean droplet size with an increase in the injector body temperature to 120 °C at 1.0 bar gas pressure, although the decrease in initial droplet size for *iso*-Octane is not as great as for Standard Gasoline. Dense mid-injection spray prevented meaningful measurements being obtained over this region, although the post injection droplets are of a more constant, and smaller, size than those measured at the ambient condition for *iso*-Octane and are similar in size to those measured with Standard Gasoline at this condition. Decreasing the gas pressure to 0.5 bar at an injector body temperature of 120 °C resulted in a small decrease in initial mean droplet size from 12 to 10 µm as shown in Figure 4-28.

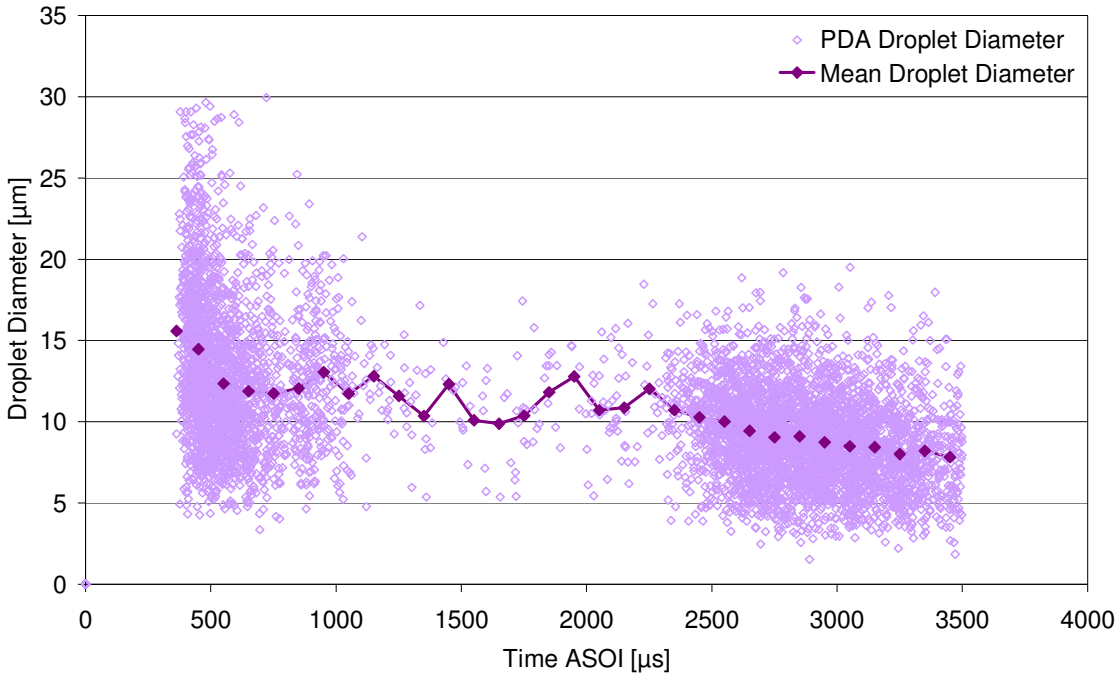

Figure 4-26 PDA Droplet Sizes with Instantaneous Mean over Injection Duration (*iso*-Octane, 20 °C, 1.0 bar)

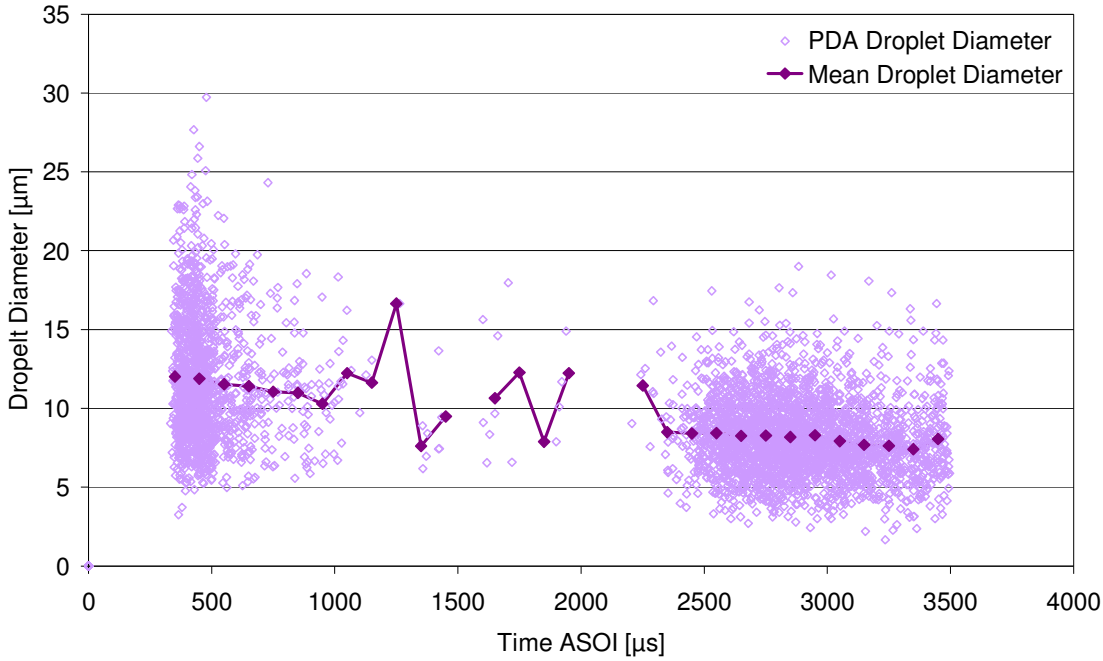

Figure 4-27 PDA Droplet Sizes with Instantaneous Mean over Injection Duration (*iso*-Octane, 120 °C, 1.0 bar)

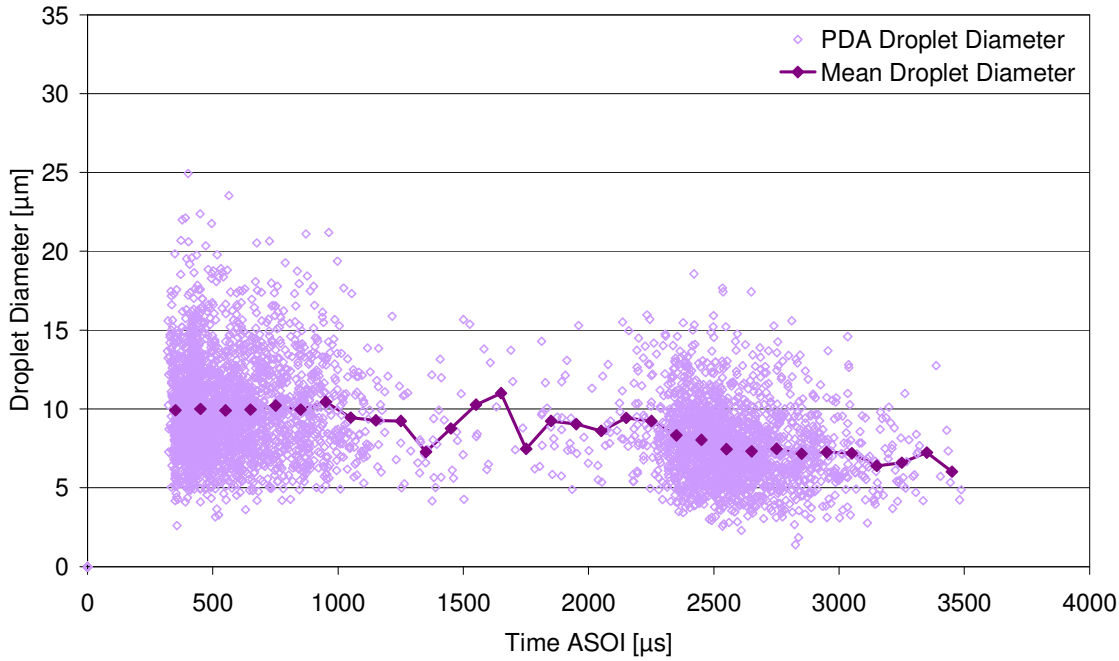

Figure 4-28 PDA Droplet Sizes with Instantaneous Mean over Injection Duration (*iso*-Octane, 120 °C, 0.5 bar)

At ambient conditions the mean initial droplet size measured using *n*-Pentane, as shown in Figure 4-29, is around 14 µm, and hence slightly lower than that measured for

Standard Gasoline or *iso*-Octane. The mid-injection mean droplet size is also slightly lower than for the other fuels at 10 µm, as would be excepted based on the high volatility and low boiling point of *n*-Pentane relative to *iso*-Octane and the majority of components in Standard Gasoline, illustrated by the fuels' distillation curves in Figure 2-33. An increase in injector body temperature to 120 °C leads to spray collapse for this high volatility fuel, shown in the bottom right hand image in Figure 3-15. This is reflected in a reduction in both the initial and mid-injection mean droplet sizes in Figure 4-30 to 8 µm. A decrease in gas pressure to 0.5 bar at an injector body temperature of 120 °C (Figure 4-31) leads to the a small further reduction in initial and mid-injection mean droplet size to around 7 µm. For both collapsed conditions using *n*-Pentane, high data rates and no post spray droplets were captured during the mid-injection periods, suggesting relatively low spray densities compared to the other tested fuels due to the high vaporisation rate of *n*-Pentane.

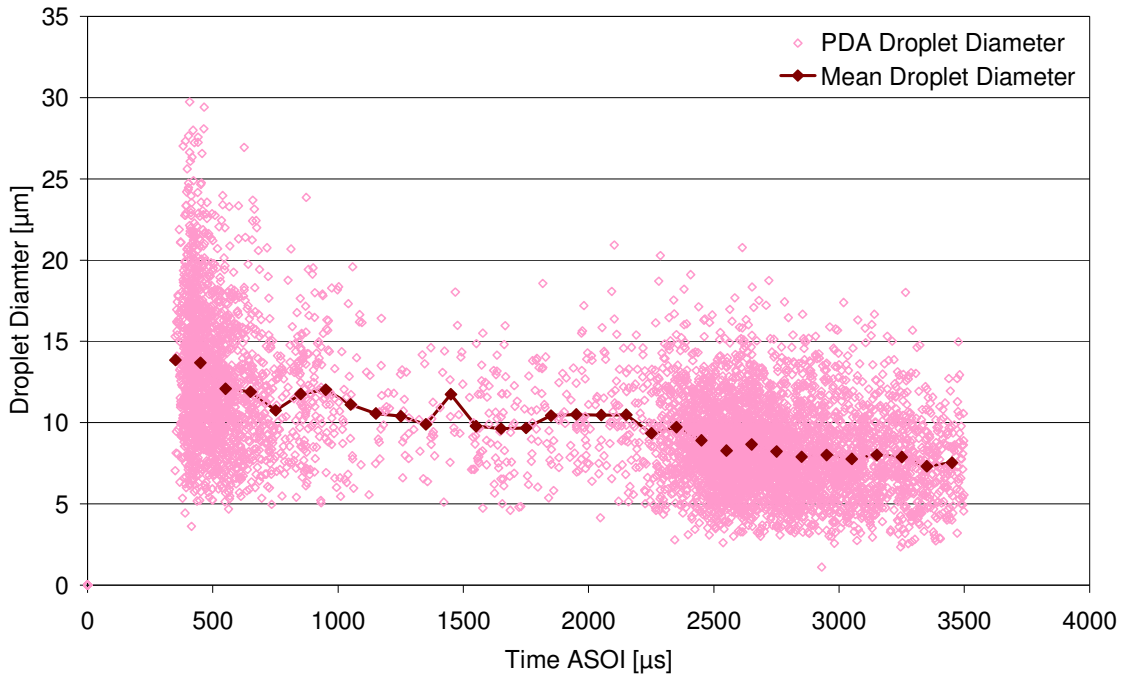

Figure 4-29 PDA Droplet Sizes with Instantaneous Mean over Injection Duration (*n*-Pentane, 20 °C, 1.0 bar)

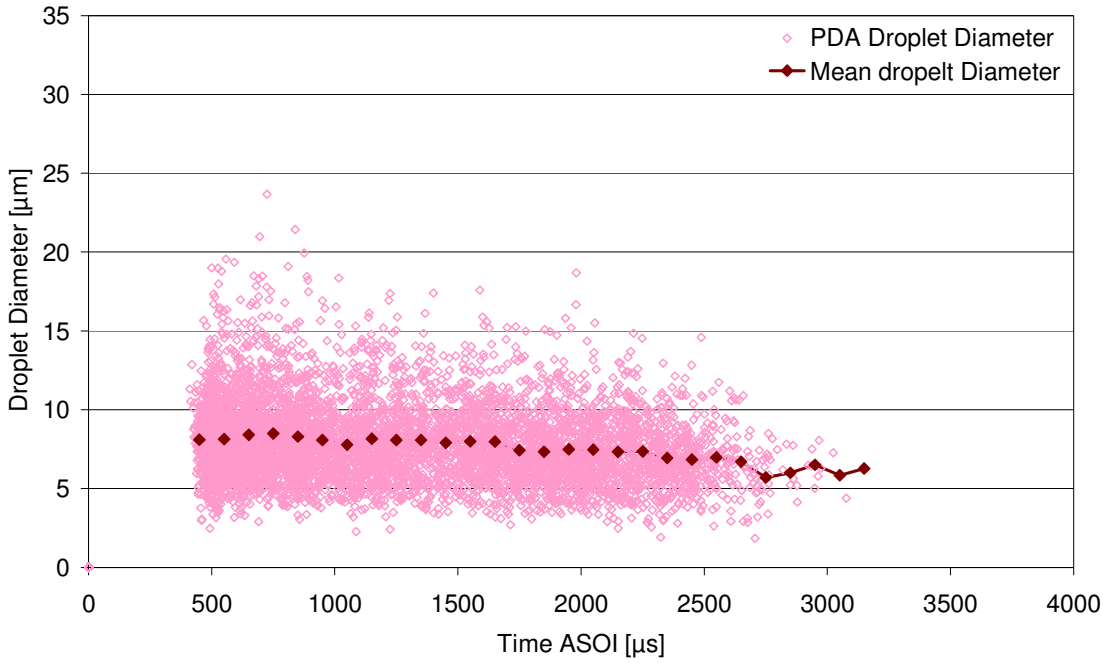

Figure 4-30 PDA Droplet Sizes with Instantaneous Mean over Injection Duration (*n*-Pentane, 120 °C, 1.0 bar)

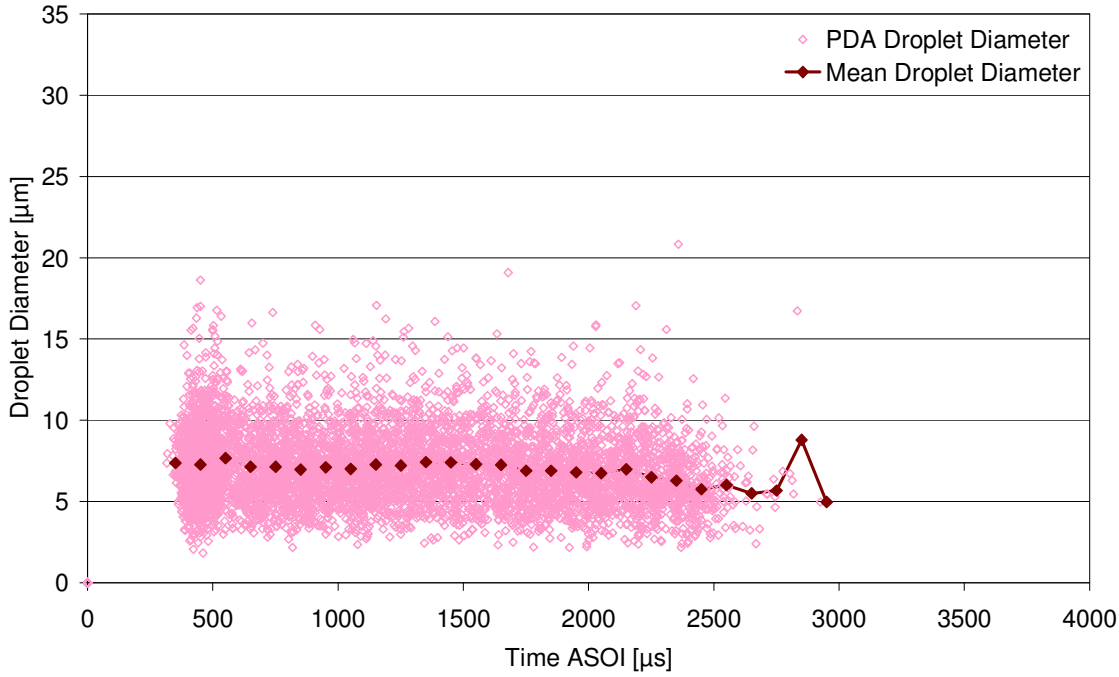

Figure 4-31 PDA Droplet Sizes with Instantaneous Mean over Injection Duration (*n*-Pentane, 120 °C, 0.5 bar)

The mean droplet size trend lines for Standard Gasoline, *iso*-Octane and *n*-Pentane are collated in Figure 4-32. For nominally ambient conditions (solid lines), a similar trend in drop size over the spray duration may be seen for all fuels. At this condition, relatively large droplets are measured at the spray tip (leading edge), with an ensuing reduction in mean droplet size during the remainder of the spray until a mean droplet size of approximately 11.5 µm is reached. The droplets at the leading edge of the *n*-Pentane spray are slightly smaller than for Standard Gasoline and *iso*-Octane, indicating a more rapid initial break-up for the *n*-Pentane spray. At the elevated fuel temperature, reduced gas pressure condition (120°C injector body temperature, 0.5 bas gas pressure - dashed lines) the droplet size trends again reflect the different break-up rates of the sprays for each fuel. For all sprays at this condition, the measured droplet size is relatively stable over the entire spray duration, including its leading edge. Variations in measured droplet size over the steady state period are due to low data rates (dense sprays) as previously described. The mean droplet diameter is lower than for the nominally ambient conditions for all fuels, though is highest for the *iso*-Octane spray indicating the lowest rate of spray break-up for the fuels tested for this section of the work. The spray produced by *n*-Pentane, which can be seen to be the most collapsed at this condition in the global spray images, also has the lowest mean droplet size of the tested fuels. The spray produced by Standard Gasoline is measured to have a small mean droplet size at its leading edge, which then gets larger over the spray duration. This similarity in small droplet size at the leading edge of the Standard Gasoline spray to that of *n*-Pentane may be an indication of the initial rapid break-up of the Standard Gasoline spray, driven by its high volatility components and resulting in spray collapse under these conditions.

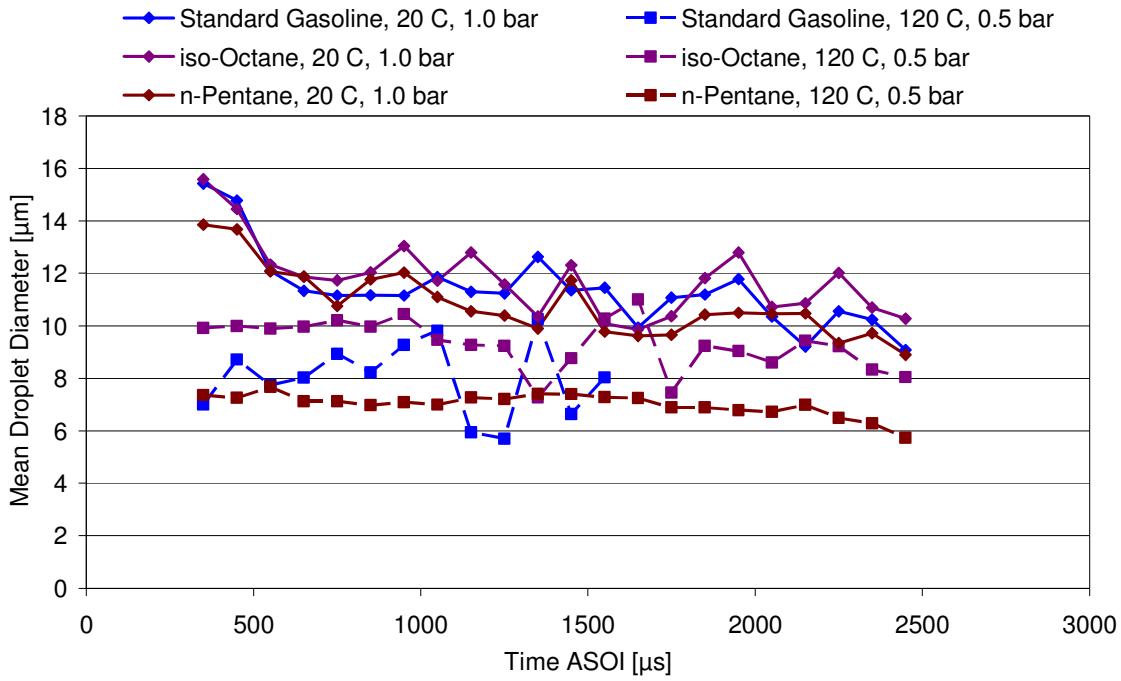

Figure 4-32 Collated Mean Trend Lines for PDA droplet sizing over Injection Duration for Range of Experimental Conditions

The trends in droplets size shown in Figure 4-32 show a consistency between the mean droplet diameter and break-up rate in relation to the global spray development images. Droplet sizing along the spray plume axis, as described below, was also carried out to indicate the rate of spray equalisation with gas conditions and hence the rate of secondary spray break-up.

4.2.2 Laser Diffraction Droplet Sizing

For laser diffraction droplet sizing individual plumes were required to be isolated to achieve enough optical transparency through the spray for measurements to be taken. Plume isolation was achieved by using a spray separator downstream from the nozzle itself to maintain the same internal flow within the nozzle for all conditions. Previous images of the spray development under a range of conditions have shown that the closely spaced right hand plume pair (Side View images, representing plumes 2, 3, 4 and 5) show the greatest convergence under spray collapse condition, leading to the convergence of these plumes into a single dense spray plume. As these plumes showed the greatest development variation, plume 3 was selected as the separated plume for which the droplet size was to be measured and the separator plate was so designed as to allow only plume 3 to pass through the plate under all spray development formations, including spray collapse. Due to instrumentation limitations, imaging to determine the

extent of plume deviation relative to the nominal spray form under plume separated conditions could not be carried out.

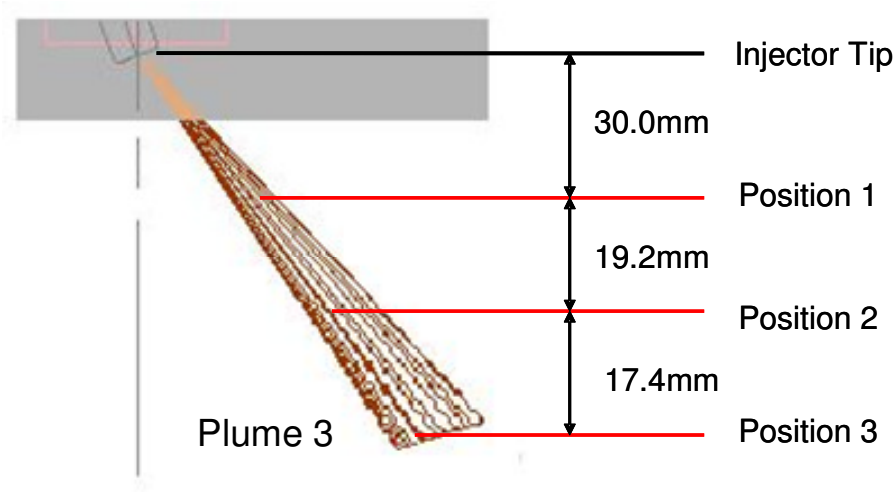

Figure 4-33 Laser Diffraction Technique Spray Droplet Size Measurement Locations

As can be seen from the graphs showing the trend in mean measured droplet diameter in Figure 4-34 and Figure 4-35, moving downstream from Position 1 (Z = 30 mm, blue line) to Position 2 (z = 49.2 mm, red line) and then to Position 3 (z = 66.6 mm, green line) can bring about both larger and smaller measured droplet sizes for the same injector body temperature and gas pressure conditions.

At 1.0 bar gas pressure (Figure 4-34), at the lowest injector body temperatures (20 °C and 50 °C), the droplet size is measured to increase moving downstream from Position 1 to 2, and then decrease again at Position 3, although not back to its original size as measured as Position 1. At 90 °C the measured droplet size at 1.0 bar gas pressure decreases slightly from Position 1 to 2 and is then roughly constant from Position 2 to 3. At the highest injector body temperature (120 °C), the measured droplet size is approximately equal at all measurement positions at a gas pressure of 1.0 bar.

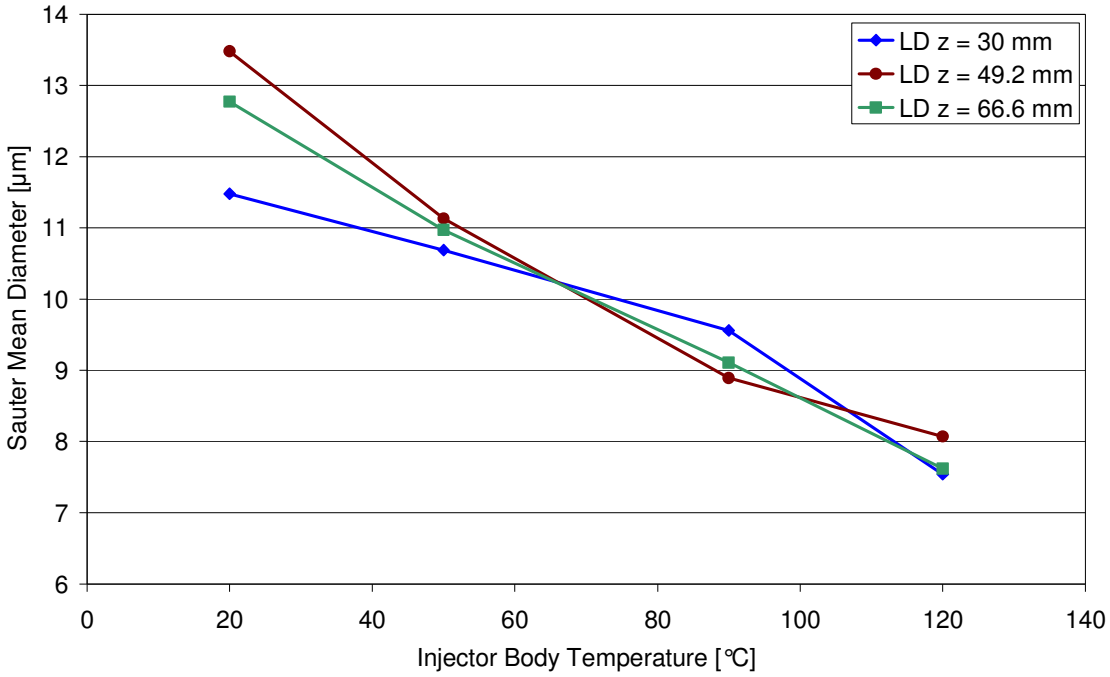

Figure 4-34 Laser Diffraction Droplet Size Measurements at Different Locations (1.0 bar Gas Pressure)

At 0.5 bar gas pressure (Figure 4-35), the measured droplet size shows only small amounts of variation between the measurement positions at injector body temperatures of 20 °C and 90 °C. At 50 °C, the measured droplet size increases from Position 1 (blue line) to 2 (red line) and then decreases as the measurement moves downstream to Position 3 (green line). At an injector body temperature of 120 °C, the measured droplet size increases steadily going downstream.

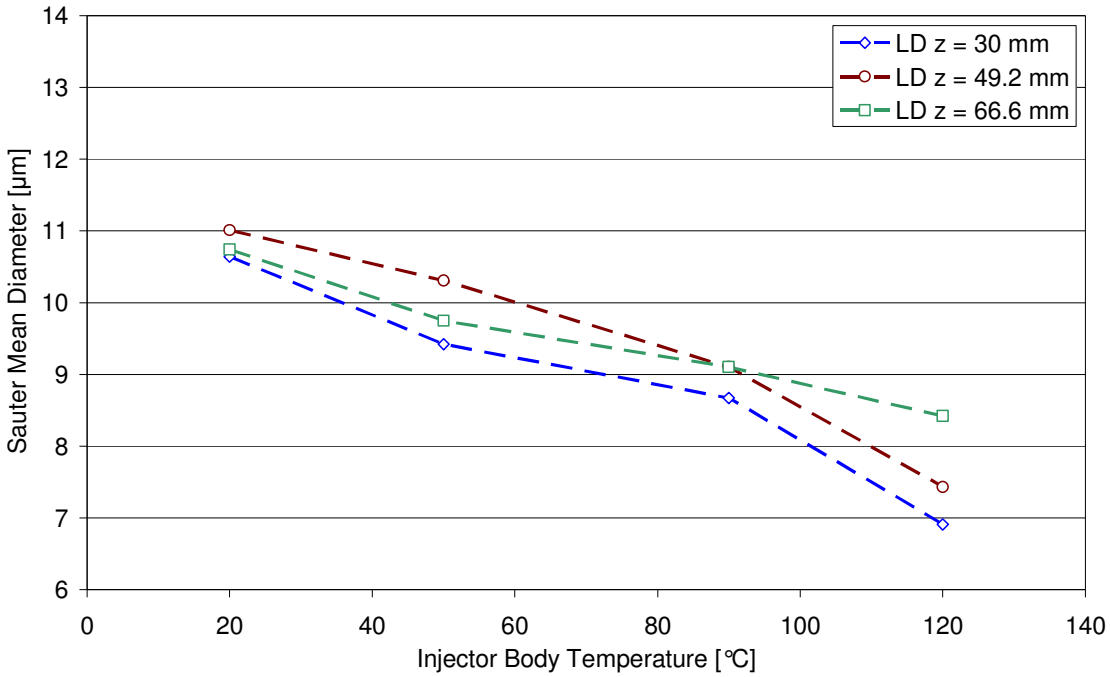

Figure 4-35 Laser Diffraction Droplet Size Measurements at Different Locations (0.5 bar Gas Pressure)

The trends detailed above are such that at Positions 2 and 3 the measured droplet size at an injector body temperature of 90 °C at a gas pressure of 1.0 bar is the same, or less than, that measured at 0.5 bar gas pressure. Similarly, this is also the case at Position 3 at an injector body temperature of 120 °C. The rational for these conflicting and often counter-intuitive trends remains unexplained, and may be a facet of the measurement technique employed, or its position with the spray.

For all measurements the trend is for a reduction in droplet size with increasing injector body temperature. A similar trend may be observed in relation to the gas pressure, where the graphs show that a reduction in gas pressure leads to reduction in measure droplet size for a given injector body temperature. At the highest tested injector body temperature (120 °C), the measured droplet size at 5.0 bar gas pressure is only marginally lower that that at 90 °C, showing that the rate of change of volatility with temperature is no longer linear, as indicated by the top bend on the "S" of the fuel's distillation curve in Figure 2-33.

4.2.3 Comparison of Results from Droplet Size Measurement Techniques

The SMD droplet diameter as measured with both the Laser Diffraction and PDA techniques are presented Figure 4-36, Figure 4-37 and Figure 4-38 for Standard Gasoline, iso-Octane and *n*-Pentane respectively. As for the previous results, the PDA results were acquired at a point source 25 mm along the *z*-axis below the injector nozzle in the centre of Plume 2 whilst those for the PDA measurements in these graphs are across the diameter of Plume 3, 19.2 mm along the *z*-axis below the injector tip. However, due to the similarity in these plumes' reactions to the experimental conditions, and the measurement location, qualitative comparisons of the trends obtained by these techniques at these locations are deemed to be valid if potential sources of variation between the measurements obtained with the different techniques are considered.

The measurements obtained with the Laser Diffraction and PDA systems vary by approximately 50 % of the Laser Diffraction measurements consistently. Although a nominal difference of 16 % in droplet sizes was measured between the systems during calibration, the larger difference in actual measurements may be attributed to a number of factors. A small portion of the difference may be due to the difference in distance from the injector tip at which the different techniques were applied. As has been measured, the average measured droplet size tends to reduce downstream for the injector tip due to droplet evaporation, and a small reduction in measured droplet size by the downstream Laser Diffraction technique may be attributed to this. The different plumes in which the measurements were taken will also have contributed to the difference in measured droplet size. In particular, as will be examined later in this work, the effect of the liquid flow through the nozzle interior geometry is likely to have contributed to the break-up of the liquid and hence the droplet diameters. To this end, the difference in interior turning angles of the nozzle holes for plume 2 (21.5°) and Plume 3 (24.2°) is likely to have played a role in the difference in measured droplet sizes. Consideration should also be paid to the difference in the nature of the techniques used, and in particular that the PDA is a point measurement whereas the LD technique acts along the line of sight of the measurement beam through the spray plume. The LD system therefore captures a higher number of smaller droplets along the beam, reducing the average measured droplet diameter. In addition, the Laser Diffraction technique is based on the number of measured spray events (100) whereas the PDA technique captures a set number of droplets to obtain the average drop size measurement (1000).

As such, the Laser Diffraction technique is likely to have captured a greater number of smaller droplets along the measurement beam, reducing the average droplet size. Lastly, there may also have been an effect of the presence of the spray separator plate in interfering with the spray break-up for the Laser Diffraction technique. Whilst every effort was made to ensure the separator did not interfere with the spray plume development, it was not possible to validate the effect of the separator plate as no comparative droplet size measurements could be obtained without the plate installed. Due to the difference in measured droplet size between the techniques care should be taken when comparing measurements. However, the droplet size trends measured with the different techniques in relation to the experimental conditions are highly consistent.

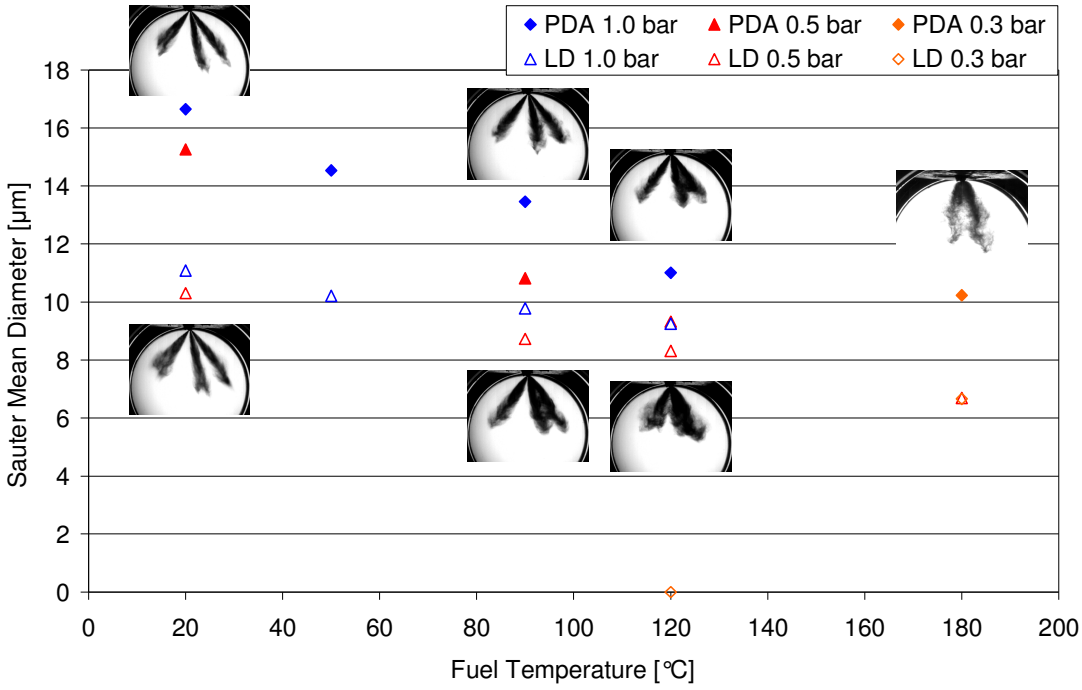

Figure 4-36 Sauter Mean Diameters - Standard Gasoline

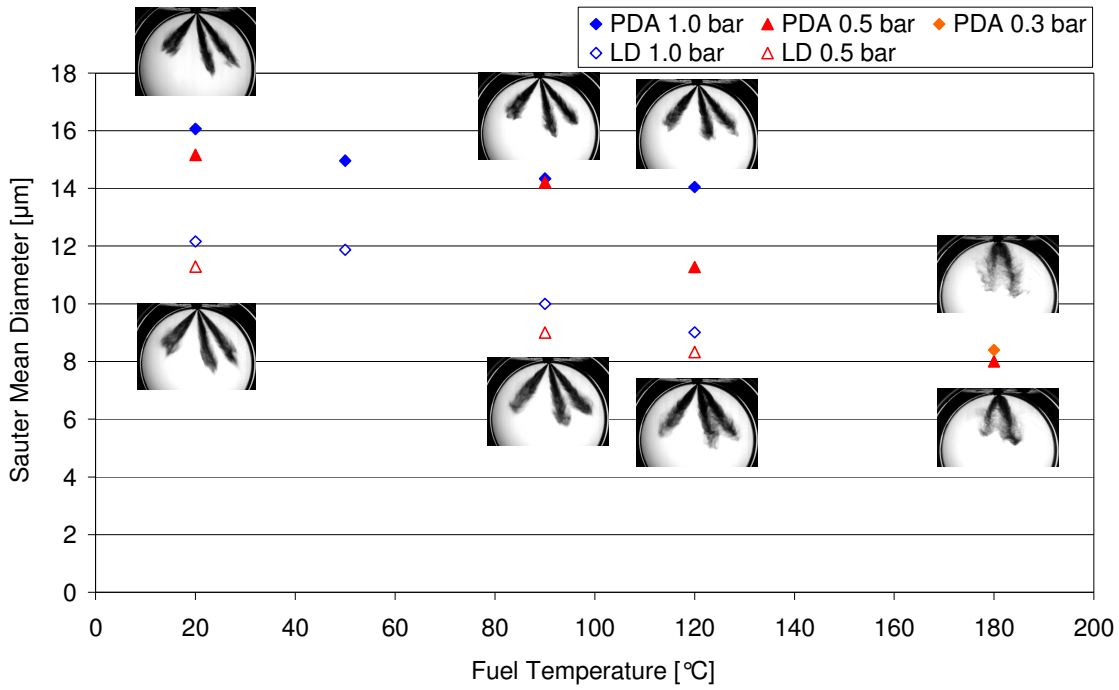

Figure 4-37 Sauter Mean Diameters - *iso*-Octane

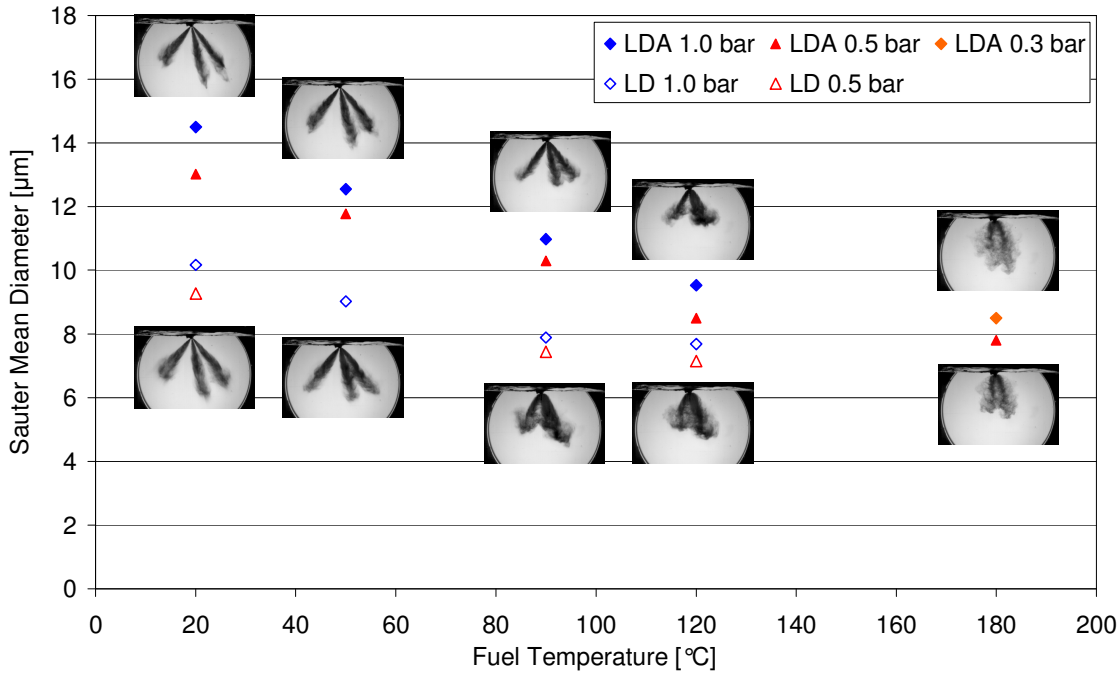

Figure 4-38 Sauter Mean Diameters - *n*-Pentane

4.2.4 Summary of Drop Size Measurements

In general, the measured values for the droplet sizes and their trends have been shown to be relatively consistent between the different measurement techniques employed. From

these measurements and trends, a number of conclusions can be drawn in relation to how spray development is affected by the break-up rate.

For the Standard Gasoline and *n*-Pentane, which both contain one or more component which have low boiling temperatures (below 50 °C), increasing the injector body/fuel temperature can be seen to steadily decrease the measured droplet size. For the Standard Gasoline (Figure 4-36), this reduction becomes more pronounced near the nozzle which shows a sharp reduction in droplet size as the spray collapse condition is approached. The droplet sizes measured for *iso*-Octane show little variation with increasing temperature until the highest test temperature of 120 °C is approached. This is reflected in the spray images which show little variation except some slight convergence at this highest test temperature, low pressure condition. The fact that this rapid reduction in measured droplet size occurs suggests that the rate of break-up and/or vaporisation increases once the boiling point of the liquid (98 °C for *iso*-Octane) has been exceeded. This would also be valid for *n*-Pentane (Figure 4-38), where its boiling temperature of 36 °C is exceeded between the lowest two test temperatures, and hence the sharp reduction is not observed due to the lack of temperature resolution.

A similar trend between droplet size and onset of collapse has been observed in the literature. Using a "multi-component petroleum product" at a fuel temperature of 90 °C van der Wege and Hochgreb [2000] measured an SMD of approximately 16–19 μm at 25 mm from the injector tip at the spray collapse condition for that injector. The work was carried out using a pressure swirl injector, and it should be borne in mind that pressure swirl sprays collapse under an increase in gas pressure at elevated fuel temperatures. They noted that the exact value of the SMD was a function of the radial distance from the injector axis. Although these droplets are slightly larger than those measured for the multi-hole injector investigated for this work, the increased fuel pressure and the alternative form of atomisation utilised would both lend themselves to the production of smaller droplets. The spray collapse condition was found to occur at an intake (gas) pressure of 0.6 bar and an injection pressure of 50 bar. Nonetheless, the similarity of relevant conditions and measured droplet sizes both suggest similar spray break up rates leading to spray collapse.

For the current work, initial convergence of the far right plume pair appears to occur when the measured SMD falls below ~12 μm from the images in Figure 4-36 overlaid

on the measured droplet sizes for Standard Gasoline. This suggests that there is a critical droplet size at which deviation from the nominal spray form occurs. In combination with the spray images previously presented, an increase in fuel temperature and/or decrease in gas pressure has been shown to lead to a gradual increase in break-up and droplet vaporisation rate. These operational parameters act in relation to the fuel properties to reduce the size of the droplets produced at any given location downstream of the injector nozzle. The droplet sizing work appears to show that once the droplets are below a certain critical diameter, possibly in relation to the liquid density, their momentum along the spray plume trajectory is diminished to the extent that they are drawn into the low pressure region in the centre of the spray, and their migration to this region acts to draw the plumes together. At another critical break-up rate value, both the rate of migration and the number of migrating droplets combined act to converge the spray plumes into the "collapsed" formation. The droplet velocity results and the "extreme condition" imaging results further suggest that any further increase in the break-up rate acts to accelerate the plumes along their collapsed central axis and increase the vaporisation rate further.

4.2.5 Correlation between Droplet Size and Velocity

In order to investigate the presence of a linkage between the measured droplets size and its velocity within the spray plume, correlations of these parameters over the course of injection events are presented below. These correlations could only be carried out for *iso*-Octane as this was the only fuel for which comparative results were captured, although the general trends in correlation are likely to hold for all fuels over the nominal spray form conditions due to linkage between these measured parameters. However, as spray collapse was not observed to occur with *iso*-Octane, unfortunately it is not possible to extrapolate these results to examine whether there exists a threshold value below which the momentum of the small droplets is sufficiently low that they are drawn into the central spray region (leading to spray collapse), as is postulated to be the case based on the droplet sizing results.

The linkage between droplet velocity and droplet size is seen to be only modest at the nominally ambient condition in Figure 4-39.

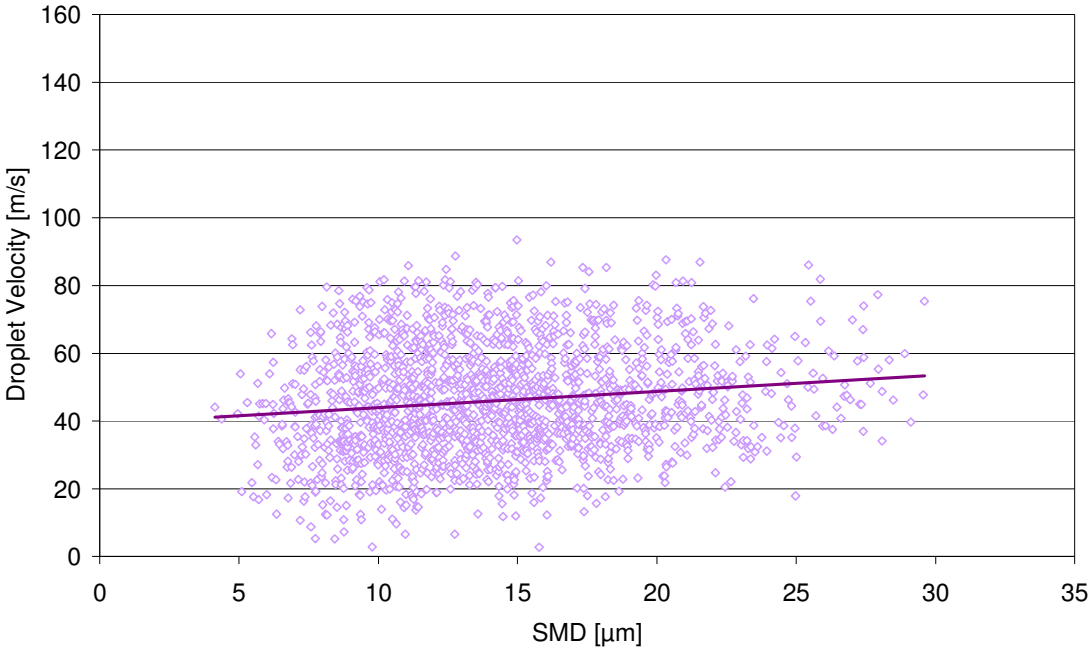

Figure 4-39 Droplet Velocity with Respect to Size: *iso*-Octane 20 °C, 1.0 bar

The gradient of the droplet velocity-size graph at an injector body temperature of 20 °C and gas pressure of 0.5 bar (Figure 4-40) is very similar to that at the 1.0 bar gas pressure condition (Figure 4-39), showing a similar, near-uniform velocity profile with respect to droplet sizes.

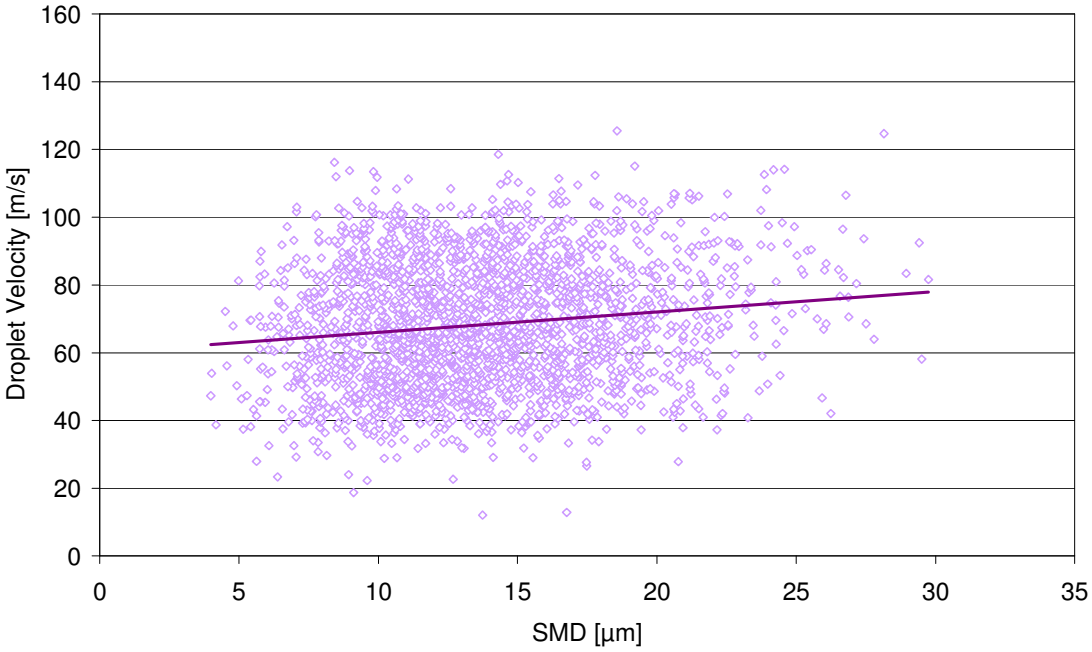

Figure 4-40 Droplet Velocity with Respect to Size: iso-Octane 20 °C, 0.5 bar

A stronger correlation between the droplet sizes and velocity is shown in Figure 4-41 (injector body temperature of 120 °C, 1.0 bar gas pressure), although it is interesting to note that some droplets towards the lower and middle of the size range indicate very high velocities, thought to be due to the heated nature of the fuel in the injector.

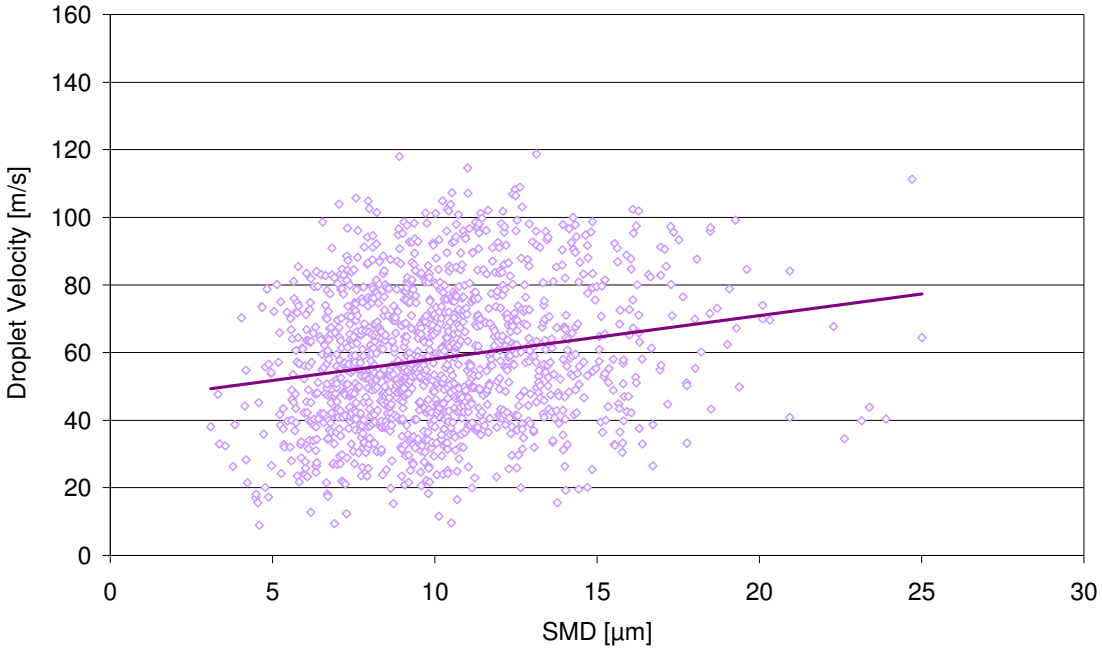

Figure 4-41 Droplet Velocity with Respect to Size: iso-Octane 120 °C, 1.0 bar

At the high injector body temperature of 120 °C, a reduction in gas pressure to 0.5 bar is seen to result in a wide spread of droplet velocities throughout the spray duration in Figure 4-17. This is the case even for *iso*-Octane, which does not appear to visibly collapse at this condition. In Figure 4-17 there also does not appear to be a marked increase in measured velocity following the leading edge as for the previously presented conditions, presumably because of the high rate of evaporation for this condition relative to lower fuel temperatures and higher gas pressures. This would be expected to result in a less dense leading spray edge, and hence an increased droplet number during this time, including a number of distinct, high velocity droplets which were not measured for the previously presented conditions due to these droplets being masked by the dense volume of droplets. This is shown by the greater number of small, high velocity droplets in Figure 4-42 than for the previously presented conditions.

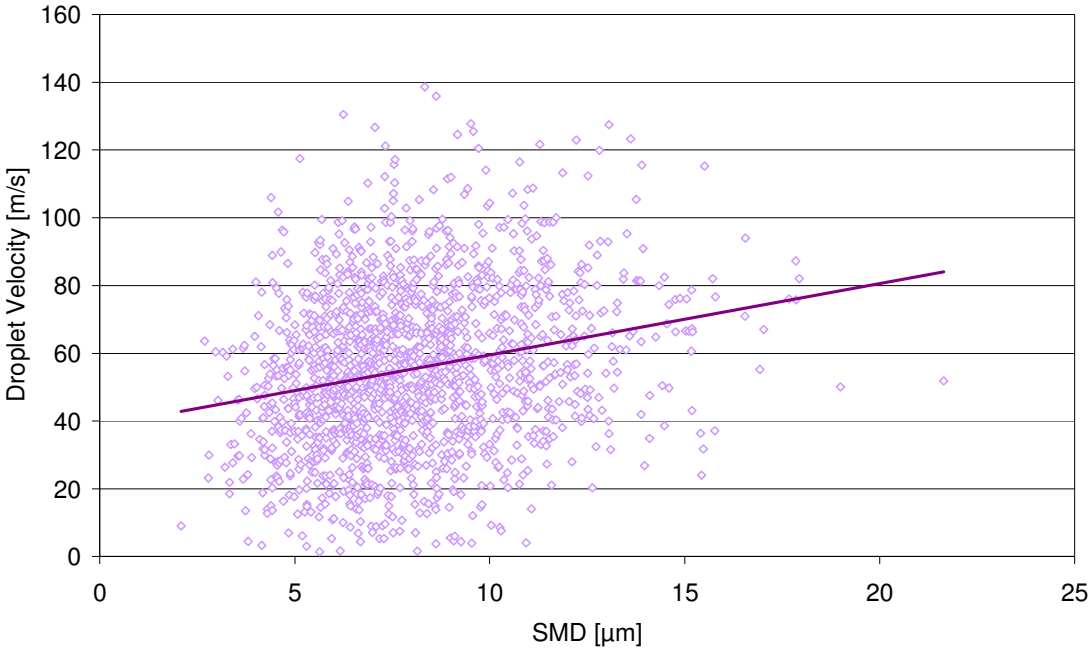

Figure 4-42 Droplet Velocity with Respect to Size: iso-Octane 120 °C, 0.5 bar

Comparison of the spray velocity values obtained from the two measurement techniques appear to show that the image-based velocity measurement only detects the fastest droplets in the spray as recorded by the PDA technique. This is illustrated by the spray tip velocity trend line roughly following the "horizon" (top) of the PDA velocity measurements. This trend may be expected as the droplets measured at this "horizon" are those that are the fastest at any given time interval, and hence these would be expected to reach, and become, the spray's leading edge.

4.2.6 Droplet Size Distribution Modelling

Despite being a fundamental consideration in the modelling of sprays, the difficulty in relating a representative droplet dimension to the prevailing conditions has prevented any such relationships being established for gasoline sprays at typical direct injection pressures. As with other aspects of gasoline direct injection, the most applicable research is that relating to diesel sprays. Hiroyasu *et al*. [1989] attempted to develop a quantitative relationship for the droplet size in terms of the SMD, based on the Laser Diffraction technique measurement of the droplet size distribution for a diesel spray injected at 900 bar into a gaseous atmosphere at 30 bar, and derived the relationship:

Eq. 4.1 $$SMD = d\,0.38\,\mathrm{Re}^{0.25}\,We_L^{-0.32}\left(\frac{\mu_L}{\mu_G}\right)^{0.37}\left(\frac{\rho_L}{\rho_G}\right)^{-0.47}$$

Where d is the nozzle diameter and all other nomenclature has its usual meaning. Due to its diesel spray origin, the relationship derived by Hiroyasu *et al*. does not make consideration for the effect of evaporation, and as such does not include a "measurement" location parameter in relation to the spray nozzle, which has been shown in this work to have a considerable influence on the measured diameter, especially at high fuel temperature, low gas pressure (*i.e.* high evaporation rate) conditions. Applying this relationship to the conditions used in this work yields the droplet size trends depicted in Figure 4-43, Figure 4-44 and Figure 4-45 for gas pressures of 0.5, 1.0 bad 5.0 bar respectively.

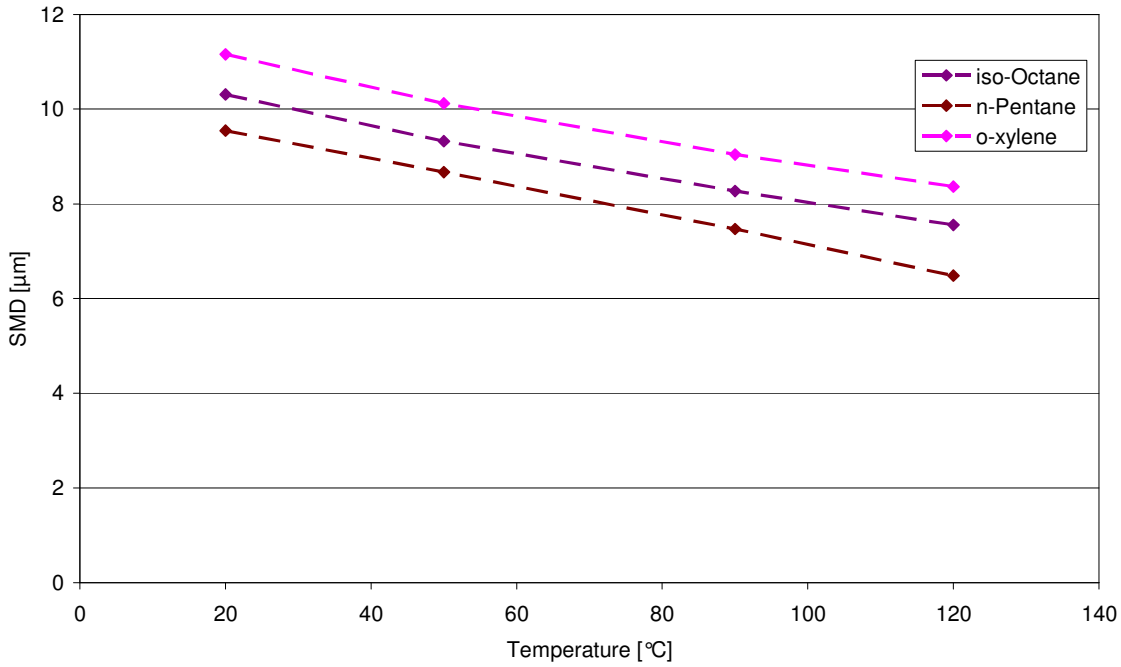

Figure 4-43 SMD Drop Sizes Calculated From Eq. 4.1, 0.5 bar Gas Pressure

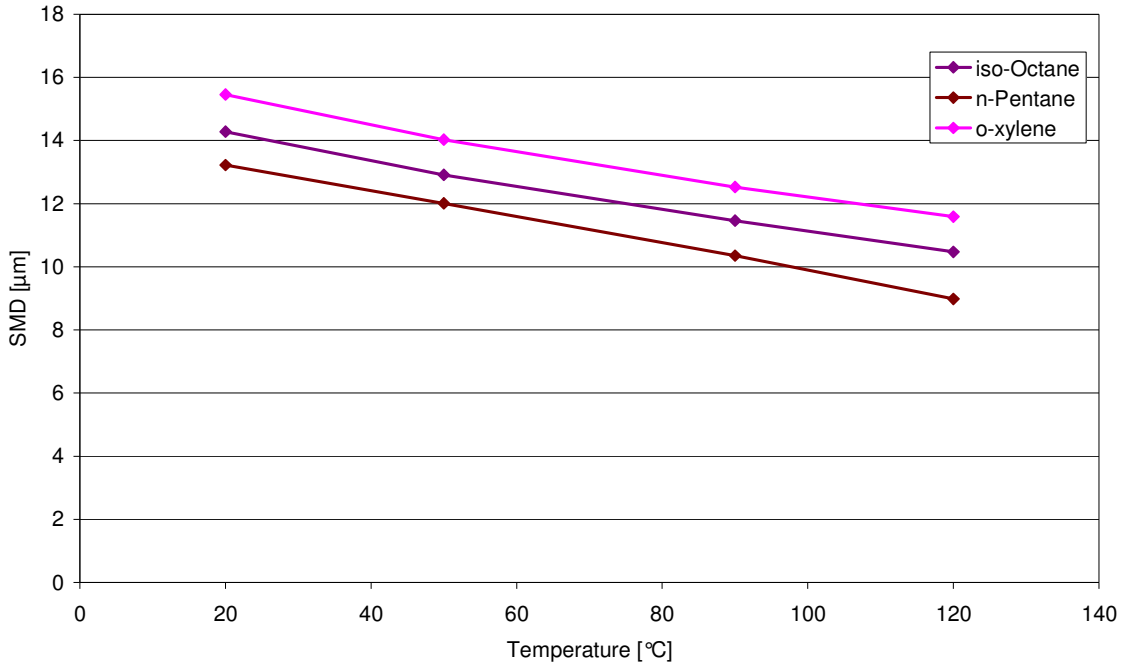

Figure 4-44 SMD Drop Sizes Calculated From Eq. 4.1, 1.0 bar Gas Pressure

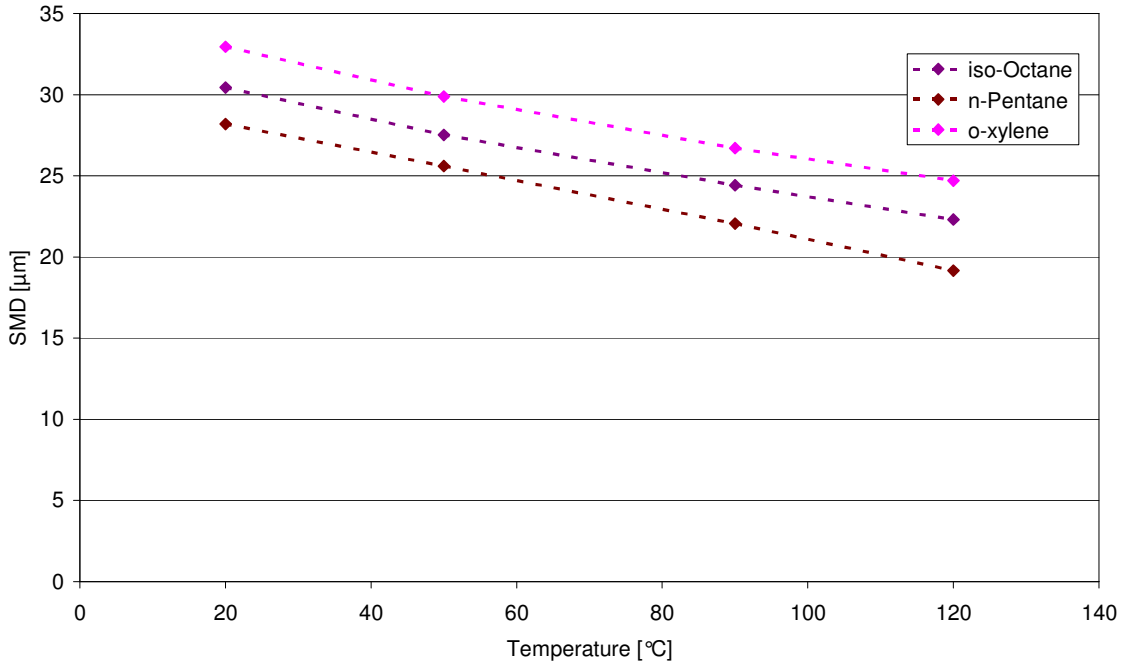

Figure 4-45 SMD Drop Sizes Calculated From Eq. 4.1, 5.0 bar Gas Pressure

In general, the relationship derived by Hiroyasu *et al.* appears to underestimate the droplet size by around 50%, as compared to the values measured during this work, despite not accounting for droplet size reduction due to fuel evaporation. However, the trend in droplet size reduction with increasing temperature and decreasing gas pressure,

as experimentally measured, is manifest in the relationship. It would therefore seem plausible that this relationship can be used to predict the "average" droplet size as a first approximation for a gasoline direct injection spray if the value of constants were further refined. A further investigation would be required to derive applicable values for the constants, whether as universal constants or as condition dependant variables.

4.3 Summary

The measurement and quantification of a number of physical spray parameters has allowed further analysis of the spray development trends observed from the images presented in the previous chapter.

Measurement of the plume penetration length over the temporal development of the sprays showed that an increase in fuel temperature initially leads to an increased measured plume penetration. This is likely to be due to the decreased flow drag, and possibly also due to an increase in fuel vaporisation at the plume tip, "swelling" the tip. However, further increases in fuel temperature were found to lead to a reduction in the measured plume length, once a critical vaporisation rate was surpassed. Beyond this point, the vaporisation rate was such to visually "remove" the leading edge from the plume tip, and hence reduce the measured length. These results suggest that the rate of evaporation of the liquid fuel is a key factor in determining the spray penetration rate (velocity) and development form. This rate of evaporation appears to change over the injection duration, further shown by the changes in rate of change of plume tip velocities, with collapse conditions being associated with greater rates of evaporation and hence greater rates of decrease in plume tip velocity.

The rate of spray break-up and fuel vaporisation was also found to affect the near nozzle cone angle, both due to the swelling of the spray and by altering the trajectories of the spray plumes. Although each injector nozzle configuration will have different cone angles, for the current work the spray was found to be fully collapsed when the spray cone angle has reduced by at least 20 % from its nominal value (nominally atmospheric conditions).

Comprehensive droplet sizing work confirmed the above observed effects of spray break-up and vaporisation rate in affecting the spray development and the measured parameters. The droplet sizing suggested that once the droplets are reduced to a size

below a certain critical diameter (nominally ~12 μm SMD for the injector used for this work), their momentum along the spray plume trajectory is diminished to the extent that they are drawn into the low pressure region in the centre of the spray, and their migration to this region acts to draw the plumes together. This effect increases up to the point where the spray becomes fully collapsed.

5 Spray Break-Up

The previous chapter presented the observed and measured trends of spray development for different fuels in relation to the fuel temperature and gas pressure when injected into a quiescent atmosphere. This chapter relates these trends to the spray break-up mechanisms, and to the physical fuel properties affecting the break-up. To characterise the break-up mechanisms leading to the different observed spray formations (*i.e.* spray plume convergence and collapse), further detailed analysis of the spray at break-up was carried out. Spray break-up was investigated by high magnification imaging of the spray in the near nozzle regions. High speed back-lit images show the emergent spray whilst laser sheet illumination provided high resolution visibility of the spray's leading edge and cone "surface".

5.1 Near Nozzle Imaging

In order to capture the first fuel seen from the injector nozzle and the ensuing spray development, the frame rate of the high speed camera used for the previously presented work was increased to 50 kHz, giving a time period between frames of 20 μs. In order to allow adequate light intensity to be captured for the shadowgraphs, the image integration period ("shutter speed") was over the duration of each image; i.e. 20 μs. Due to the fixed processing capacity of the camera, increasing the frame rate decreased its resolution to 256 by 128 pixels.

As detailed in the description of the injector nozzle, the injector nozzle used for this work is of a stepped design, with the smaller diameter orifice, which forms the fuel flow path, being recessed from the nozzle surface. This small orifice opens up to a larger diameter orifice, which is that seen at the nozzle surface. As such, the fuel imaged at the injector tip is actually 0.2 mm downstream from its actual injection location at the end of the small orifice and the plumes will have started to break-up due to effects upstream of where they can first be imaged.

5.1.1 Flash Bulb Illumination

Despite image lighting intensity limitations when using the photographic flash lighting unit as for the global spray images, backlit shadowgraph images of the spray were captured with sufficient spatial resolution to capture initial spray injection and development. Using the settings described above, the plume tip penetration at initial spray development was measured to be approximately 1.0 mm per frame interval (20 μs), equivalent to a tip velocity of 50 m/s, in line with the spray tip velocities measured from the global spray images. Images of the initial fuel injected and development are presented in Figure 5-1 alongside a typical fully developed global spray image for the same conditions.

As can be seen from Figure 5-1, the very first fuel as seen at the injector tip (left hand column) appears to be very similar for all test conditions. Each plume pair is clearly defined with a gap evident between each plume, including the closely spaced plume quartet on the right hand side of the image. For the high temperature conditions, the sprays are wider at the nozzle exit than for the ambient conditions, suggesting some widening and expansion of the spray plume between its injection location and the nozzle surface. However, combination of the plumes is not yet evident at this stage of spray development for any of the test conditions.

The second frame, captured 20 μs later than the frame showing first fuel, continues to show clearly defined plume pairs for the non-collapse condition for Standard Gasoline (top row of Figure 5-1). However, at this time interval after the start of injection, at an inject body temperature of 120 °C and a gas pressure of 0.5 bar (spray collapse condition for Standard Gasoline – middle row of Figure 5-1), the closely spaced plumes on the right hand of the image have combined and individual spray plumes are now more difficult to discern. In a similar reflection of the global spray form at this time interval, the *iso*-Octane spray shows some coming together but less widening of the plumes at the injector tip is evident than for Standard Gasoline and individual plume tips can still be easily made out with a clear gap between the plume tips.

The tables of images on the following pages (Figure 5-2, Figure 5-3, Figure 5-4 and Figure 5-5) illustrate these trends in near-nozzle spray development to be highly representative of the global spray form for all conditions from 20 μs after first fuel is seen at the injector tip.

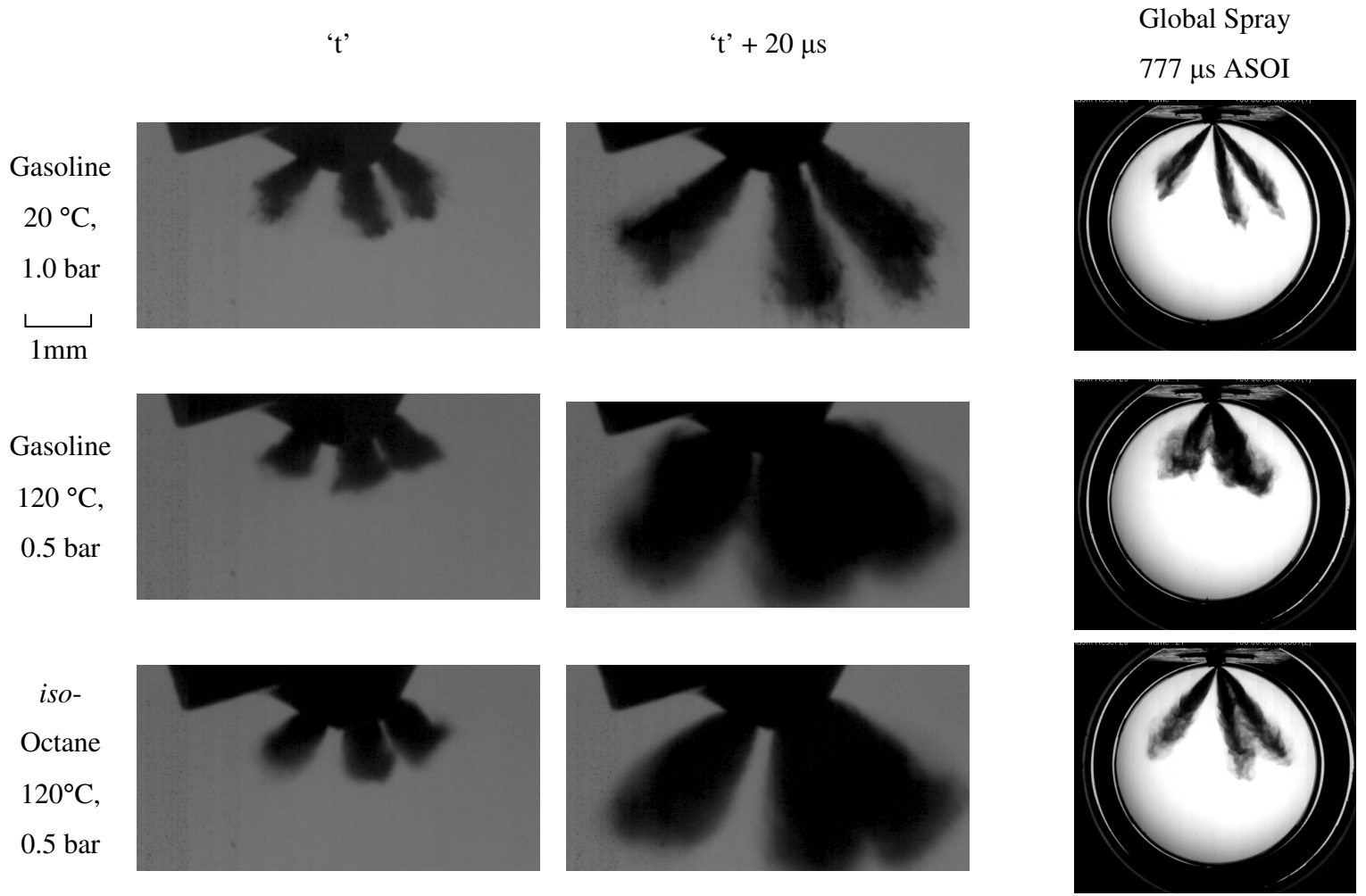

Figure 5-1 High Magnification Imaging of Very Early Spray Development

Images of the first fuel and initial spray development for the principle fuels and experimental conditions used for this work are presented in Figure 5-2, Figure 5-3, Figure 5-4 and Figure 5-5. These collections of spray images also show the steady state and injector closing spray form in the near-nozzle region. For all fuels the very early spray first seen at the nozzle (top row) is very similar for all conditions. This is the case also for those conditions at which spray convergence and collapse are observed in the global spray form, where individual plumes are clearly discernible in all conditions with clear separation between them, although some widening of the individual spray plumes may be observed.

Interestingly, the greatest spray plume width increase is seen at the higher gas pressure condition images at the highest injector body temperatures (1.0 bar), even though this condition does not lead to the same level of spray convergence as the low gas pressure condition. This is likely to be due to the higher gas pressure offering greater resistance to the spray plume progress, and the conservation of momentum forcing it to penetrate more radially to compensate for the inability to penetrate axially.

The second rows of Figure 5-2, Figure 5-3, Figure 5-4 and Figure 5-5 show the initial spray development 20 μs after the fuel is first seen at the tip. At this stage, the main characteristics of the global spray form are evident. For the conditions at which the global spray form shows plume convergence and collapse these characteristics are displayed by the plumes at this time interval after the start of injection. For some collapse conditions, individual plume tips can still be made out, although the trajectory of convergence of the plumes is highly evident (e.g. *n*-Pentane at 90 °C injector body temperature, 0.5 bas gas pressure in Figure 5-5).

As may be expected, the global spray form is reflected in the steady state sprays (row three) in the near nozzle region. At pintle closing (row four) the throttling action of the pintle at the nozzle orifice inlet reduces the extent of plume interaction and hence plume separation is once more evident for all conditions. This reduction in fuel flow and hence spray velocity and break-up energy can be seen to lead to the formation of large droplets. The size and low break-up rate of these droplets may be expected to adversely affect vaporisation and mixing, and hence affect engine out un-burned hydrocarbon emissions.

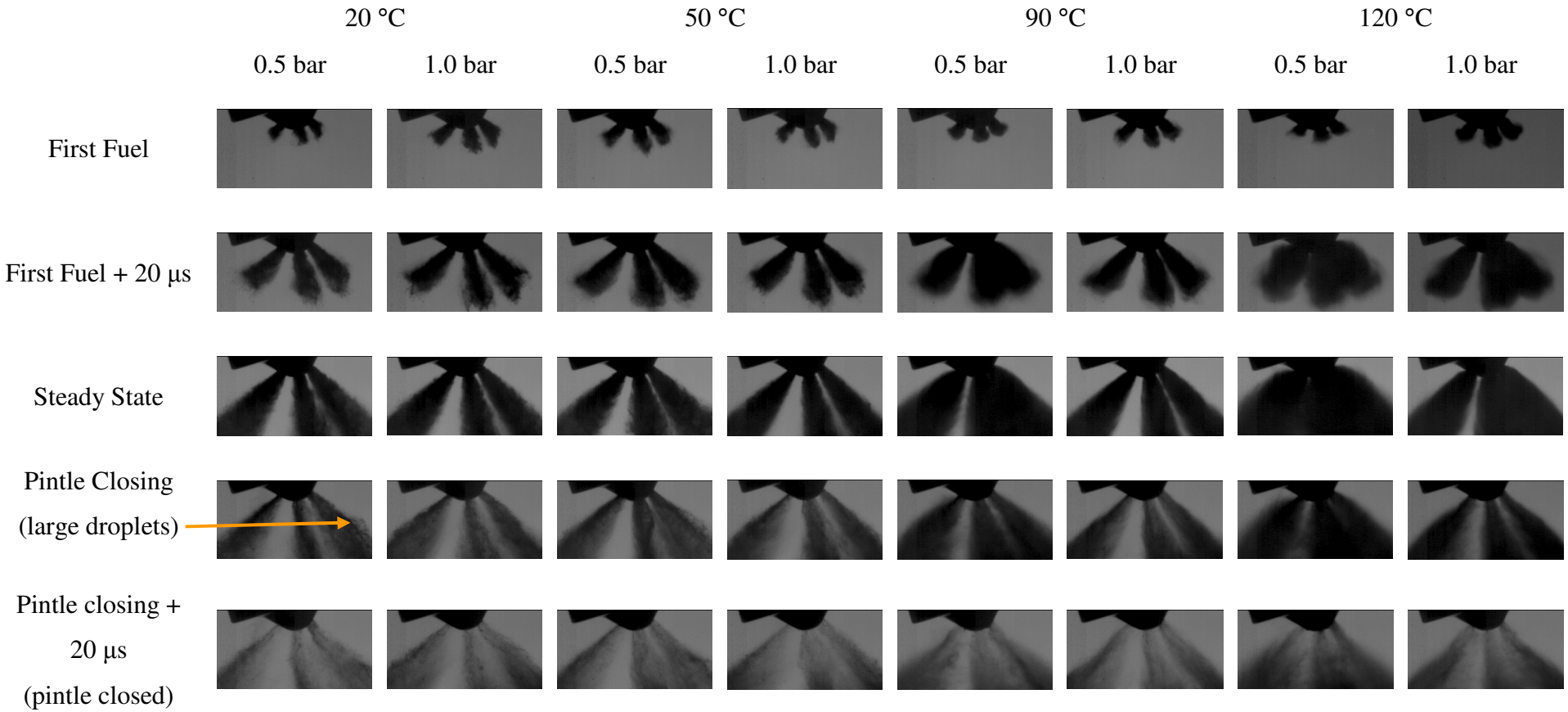

Figure 5-2 Standard Gasoline, High Speed, High Magnification Imaging

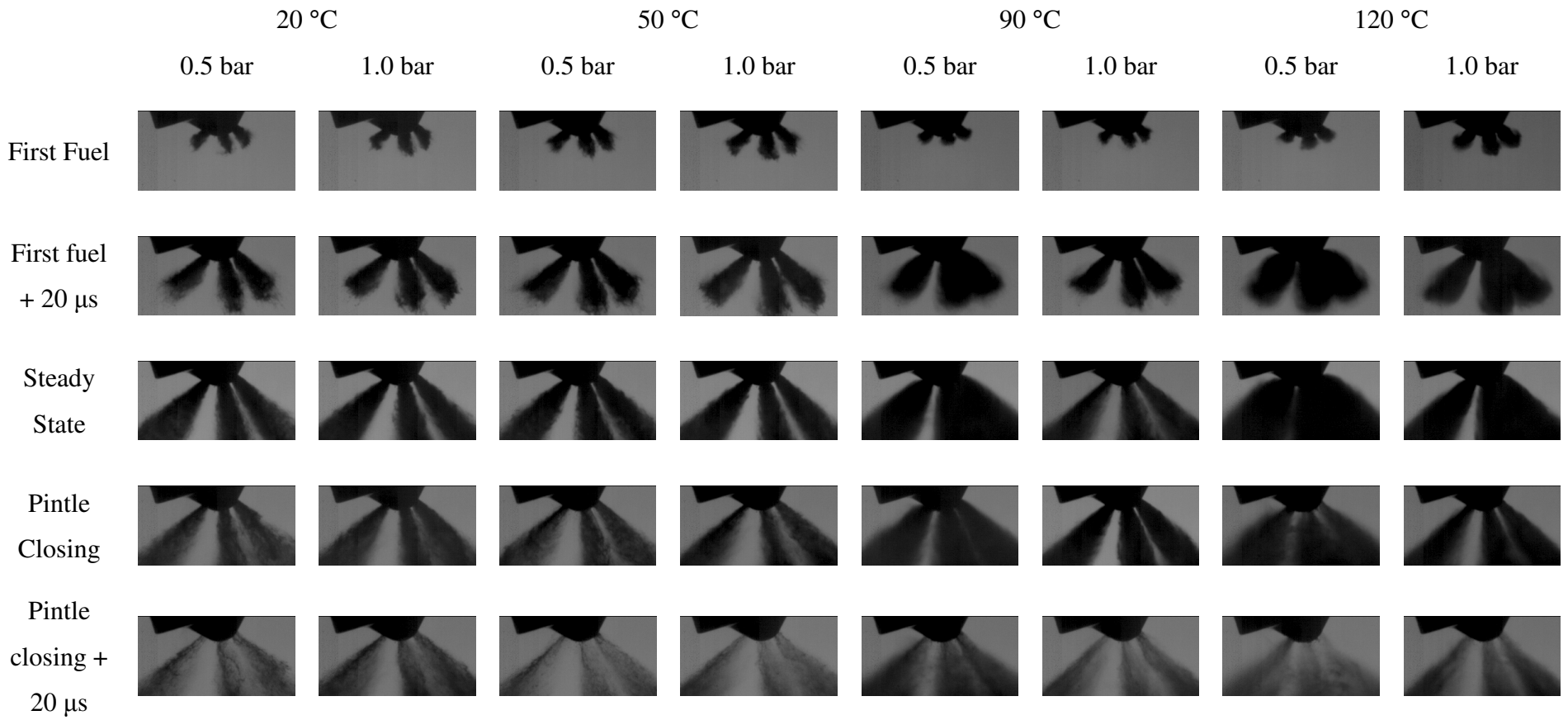

Figure 5-3 Heavy Gasoline, High Speed, High Magnification Imaging

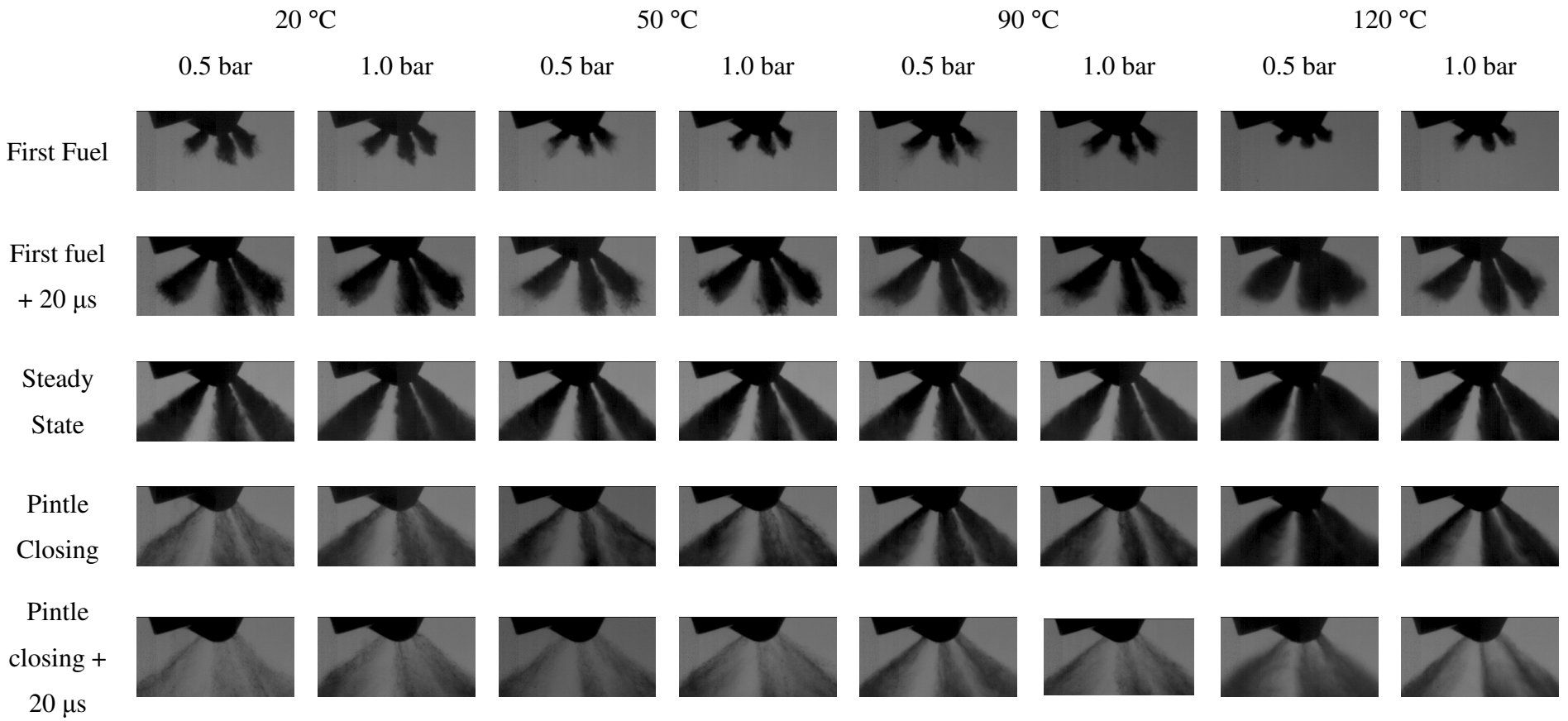

Figure 5-4 *iso*-Octane, High Speed, High Magnification Imaging

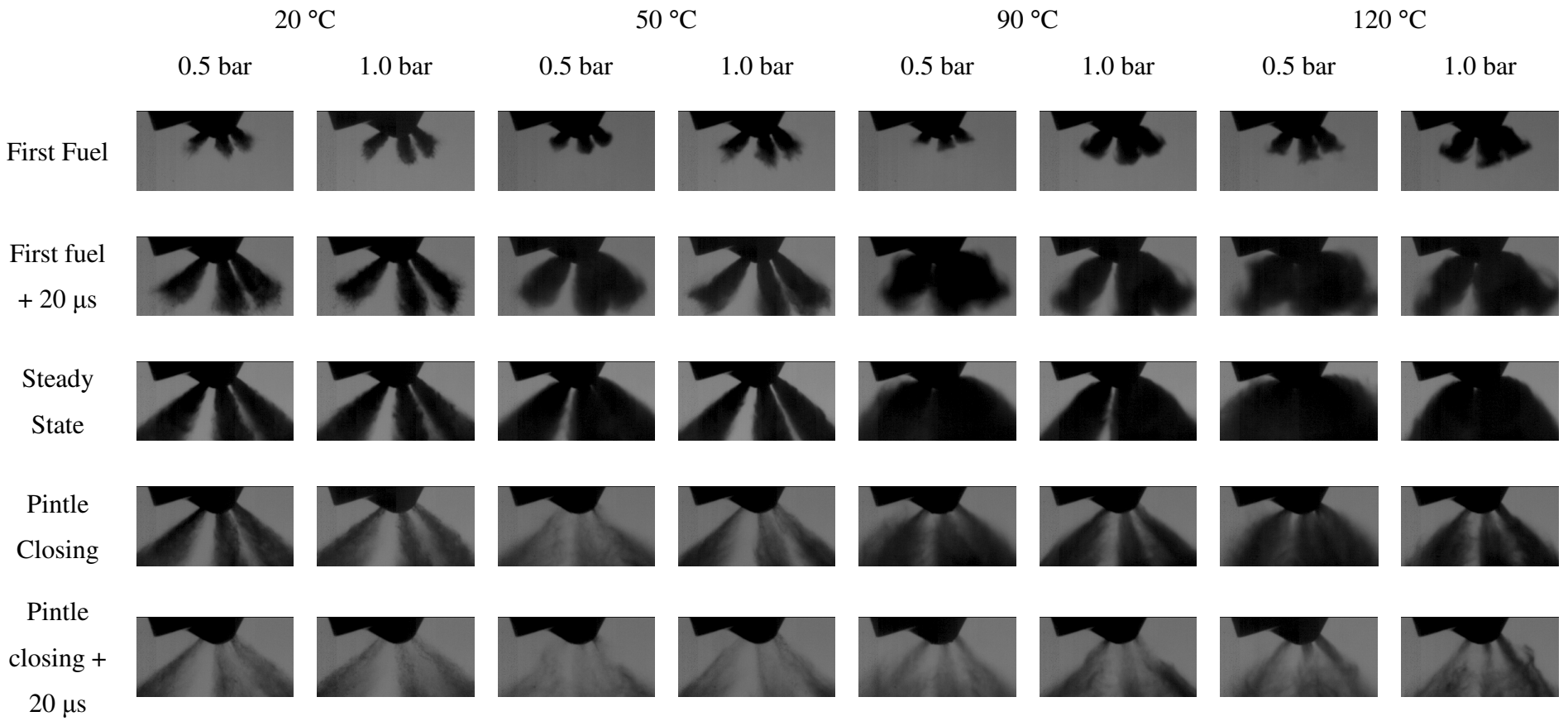

Figure 5-5 *n*-Pentane, High Speed, High Magnification Imaging

The time interval between the initial fuel and the plume tip width growth effect shows that a finite time is required for the rate of evaporation to increase to sufficient levels to cause the plume tip to expand in this manner, and that in nozzle boiling, resulting in instantaneous vaporisation of the liquid, or "flash boiling" does not occur under the conditions tested for this work. The fact that the fully developed spray characteristics are not displayed at the injector until 20 μs after the first fuel would appear to indicated that even at the most extreme vaporisation rates a timescale in the order of 20 μs is one of the determining factors in the development of equilibrium conditions between the liquid fuel and surrounding gas, leading to the existence of an external spray break-up length. Such time and length scales are also relevant to engine in-cylinder mixture formation strategies which are reliant on near spontaneous vaporisation under low in-cylinder pressures for homogenous charge establishment.

5.1.2 Laser Sheet Illumination

The resolution and clarity of the back-lit images presented above were limited by the light intensity available to the high speed camera over its interrogation area. To increase the visual resolution, high intensity laser illumination was used. The source light from a Nd:Yag laser was passed through a sheet forming lens to form a vertical light sheet, which was aligned to the spray plumes. In the first instance, an attempt was made to capture the entire spray in the near nozzle region using this illumination technique, as shown in Figure 5-6. However, as can be seen from Figure 5-6, due to the illumination form the left hand side of the image the right hand plume (plume 4) is poorly illuminated due to the obscuration of the light by the other plumes, and the nozzle itself.

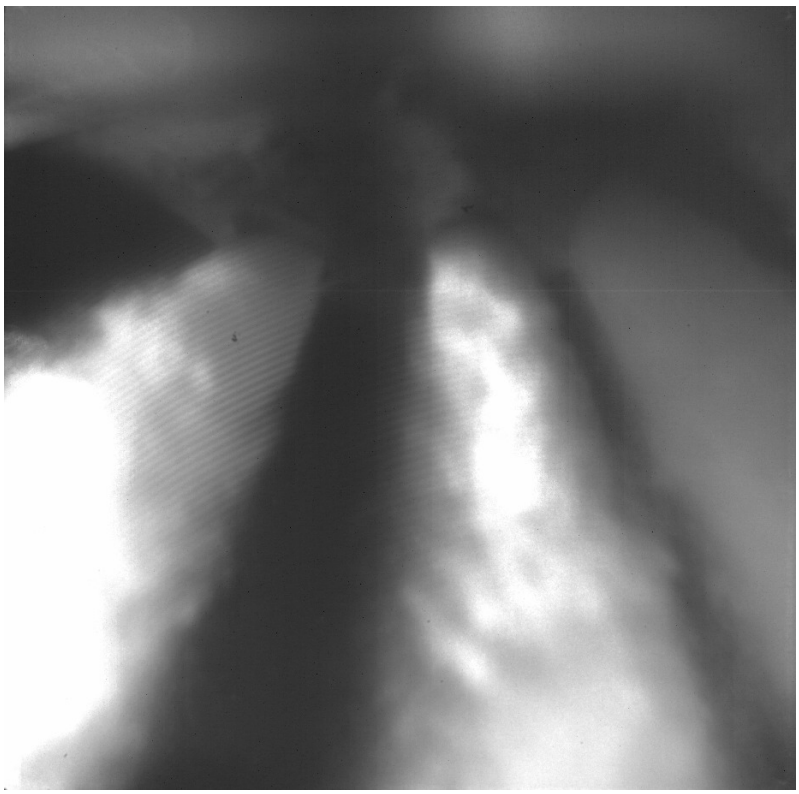

Figure 5-6 Spray at Injector Nozzle with Laser Sheet Illumination

As a second iteration, the camera was realigned to the left hand plume (plume 1) for the analytical images for this section of the work using the set-up illustrated in Figure 5-7. For these images, the laser was synchronised to the camera so as to provide a light pulse at the same frequency and timing as the camera shutter opening. The camera was operated at frame rate of 50 kHz, allowing the initial spray as well as the end of injection droplets to be captured as they passed through the illuminating laser light sheet. Due to the angular projection of the plumes and the fixed alignment of the sheet, it was only possible to visualise a small section of the spray at the nozzle orifice before the liquid spray in front of the sheet obscured the illuminated section of the plume.

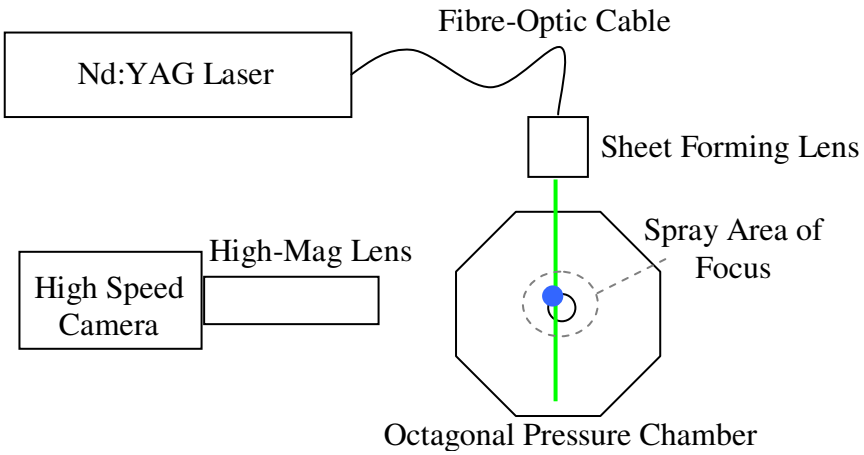

Figure 5-7 Schematic of Laser Sheet Illuminated High Magnification Imaging Set-Up

Laser sheet illuminated images of the left hand plume (plume 1) were captured at emergence from the injector nozzle (Initial Spray), at 800 µs ASOI (Steady State) and at 2000 µs ASOI (End of Injection) for Standard Gasoline, Heavy Gasoline and *iso*-Octane over the range of experimental conditions used for this work, as shown in Figure 5-8, Figure 5-9 and Figure 5-10 respectively.

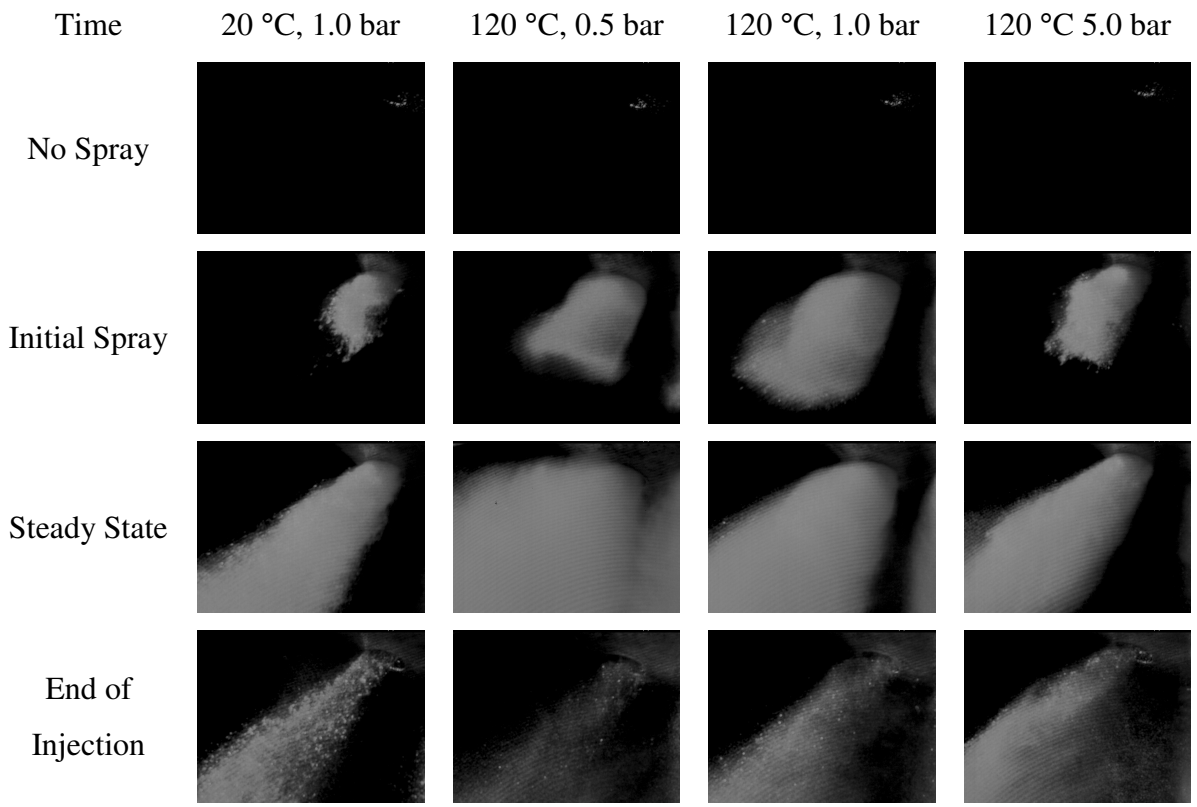

Figure 5-8 Laser Sheet Illumination, Standard Gasoline

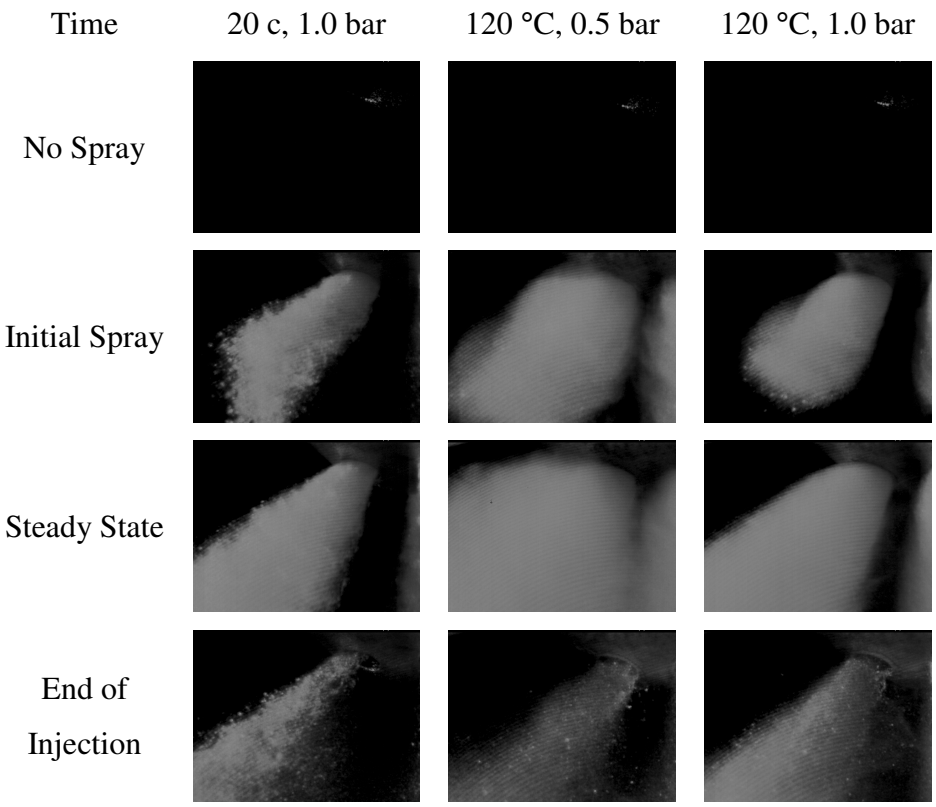

Figure 5-9 Laser Sheet Illumination, Heavy Gasoline

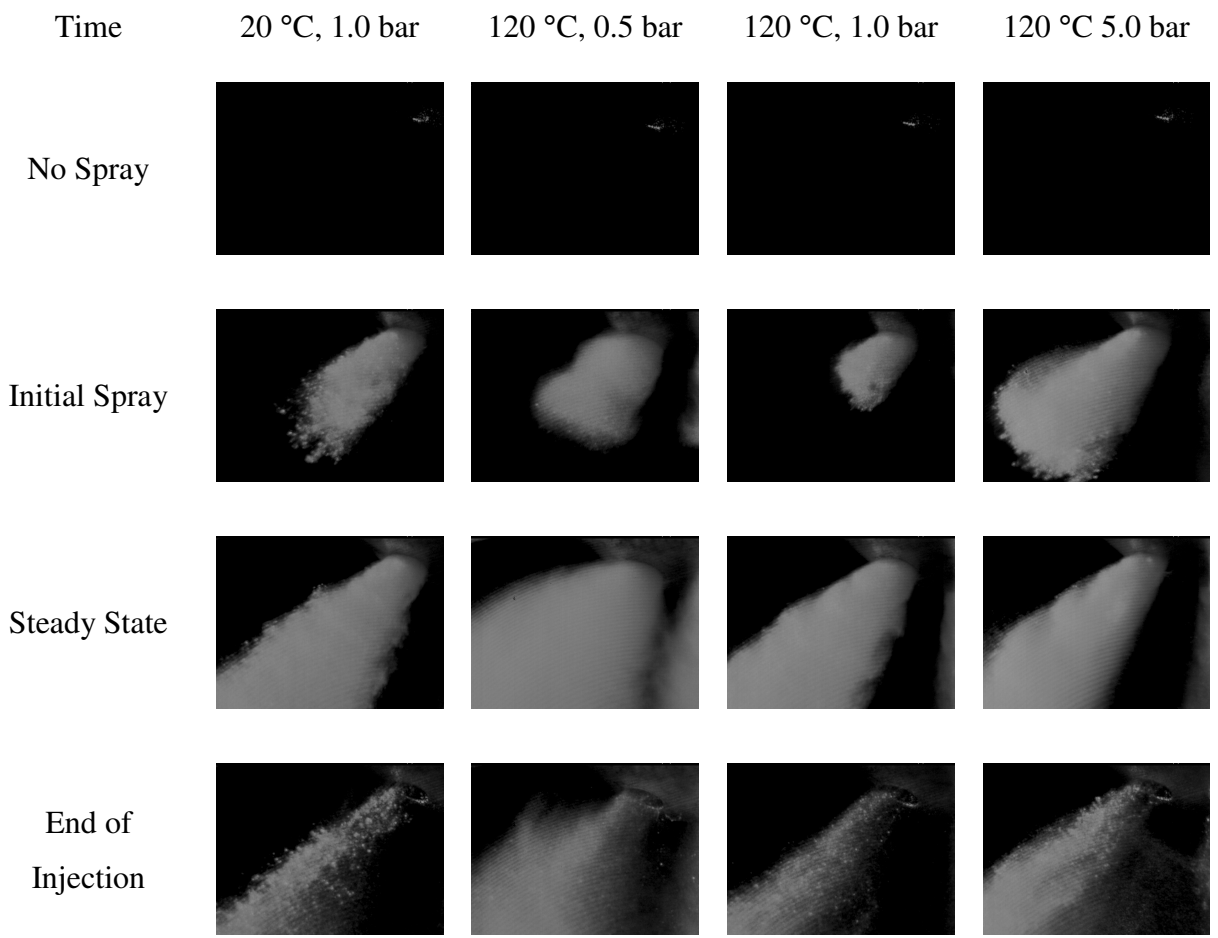

Figure 5-10 Laser Sheet Illumination, *iso*-Octane

In Figure 5-8 the initial Standard Gasoline spray at the nominally ambient conditions (20 °C injector body temperature, 1.0 bar gas pressure) shows clearly discernable individual liquid ligaments and droplets at and around the leading edge of the spray. These features are also evident in the initial spray images at the nominally ambient conditions for both the Heavy Gasoline and *iso*-Octane sprays in Figure 5-9 and Figure 5-10 respectively.

For all three fuels the Steady State spray plume has a well defined boundary and again individual features on the boundary and plume surface can be depicted. Likewise, the End of Injection image shows a number of larger droplets associated with the reduced break-up energy in the spray as the pintle closes at the end of the injection event. The clarity of these features suggests that they are in a steady state in relation to the image integration time interval of 20 μs, and hence that the effect of evaporation or other mechanism to bring about a flux in the spray over this time interval is small under these conditions.

At the spray collapse condition (120 °C injector body temperature, 0.5 bar gas pressure), the increased level of evaporation is evident in pictorial form. For the Standard Gasoline (Figure 5-8), the spray boundaries and leading edge are no longer clearly defined and there is a gradual reduction in pixel brightness between the white liquid spray and the surrounding black background. The imaged plume bulges as it exits the nozzle and the darker shading to the right of the plume suggests a “solid” cylindrical form to the plume. In both the Initial Spray and Steady State Spray images the adjacent plume can be seen in this image due to the increased girth of the plumes. At the End of Injection some large droplets are evident “suspended” in a hazy mist likely to be due to the small droplets which are present at the spray periphery, formed due to the evaporation of the spray as it exits the nozzle.

These general observations also relate to the near nozzle spray produced by Heavy Gasoline and *iso*-Octane, although the higher boiling temperature range of these fuels is reflected in their near nozzle spray behaviours. The spray produced by Heavy Gasoline shows a number of larger droplets within and around the spray, relating to a greater resistance to break-up than the Standard Gasoline and *n*-Pentane sprays. Likewise, the *iso*-Octane spray shows the greatest clarity of the presence of large droplets, and hence the lowest break-up rate of the fuels tested for this section of the work.

5.1.3 Spray Development Relationship to Fuel Properties

At elevated fuel temperatures, the difference between the fuel temperature and the boiling temperature of the fuel at the given gas pressure is different for each fuel. The extent of this difference is dependant on the fuel temperature and the fuels boiling temperature, as listed in Table 2-2, and is known as the superheat of the liquid, where the liquid pressure prevents bubble formation and vaporisation. For multi-component fuels, a range of superheat will be present in the fuel, although the driver for initial vaporisation will be the degree of superheat of the lowest volatility component. This degree of superheat of the lowest volatility component(s) appears to affect the rapidity of the vaporisation of the fuel as evidenced in the difference in global spray forms at the high fuel temperature, low gas pressure ("spray collapse") condition in the previous image sets.

The relative tendency for the tested fuels to collapse at the nominal "collapse condition" of 120 °C injector body temperature and 0.5 bar gas pressure may also be directly compared to the fuel bubble points as listed in Table 2-3. The bubble point is the absolute ambient pressure at which a liquid will boil at the stated temperature, where increasing ambient pressure suppresses boiling and the formation of bubbles by exerting a greater force on the liquid surface. At a temperature of 120 °C, comparison of the fuel bubble points shows that the highest boiling pressure is for *n*-Pentane, indicating that it is "the most willing to boil" of all the fuels (i.e. the greatest ambient pressure is required to prevent the formation of bubbles), which is illustrated by the extent of its collapse at elevated fuel temperatures. In reference to the fuel's bubble points listed in Table 2-3, it may be observed that the spray is collapsed when the chamber gas pressure is at or below $1/10^{th}$ of the fuel's bubble point pressure at the given fuel temperature. For example, Standard Gasoline is observed to collapse at 120 °C at 0.5 bar chamber gas pressure, which is approximately $1/10^{th}$ of its bubble point pressure at this temperature of 4.5 bar. Within the resolution of the temperature and gas pressure settings tested in this work, this trend appears to hold for all presented fuels, including those close to the transition values, such as at 90 °C injector body temperature and 0.5 gas pressure for Standard Gasoline. In all cases, the high rate of spray break up when system equilibration commences suggests that the in-nozzle flow regime affects the level of internal energy within the liquid volume, which further increases the imbalance in energy between the liquid and gaseous bodies.

To verify the trend of observed spray collapse for all fuels in relation to their bubble points, the injector body temperature was further increased for some investigative experiments to 180 °C at 0.5 bar gas pressure, as shown in Figure 3-22 alongside summary images of the sprays at lower fuel temperatures, all at 0.5 bar gas pressure (note that Heavy gasoline was not included in the 180 °C imaging investigation). This extremely high injector body temperature condition was included within this investigation for academic interest to investigate whether the likely drivers of spray convergence held at higher temperatures, and whether instantaneous "flash boiling" of fuels would occur when an extent of superheat threshold was surpassed, but this temperature condition is not thought to be likely to be representative of an engine operating under normal conditions.

At an injector body (fuel) temperature of 180 °C and gas pressure of 0.5 bar the spray produced by *iso*-Octane, which was not fully collapsed at 120 °C, was observed to fully collapse, indicating that the critical collapse threshold had been exceeded. At these test conditions the chamber gas pressure was below $1/10^{th}$ that of *iso*-Octane's bubble point pressure, showing the continuation of the trend for these fuels also. Due to experimental limitations, it was not possible to further validate this hypothesis through reductions in chamber pressure for lower injector body (fuel) temperatures although the consistence of the trend suggests that spray collapse could be observed at any given fuel temperature provided the ambient gas pressure into which the spray is injected is at least $1/10^{th}$ the bubble point pressure at that fuel temperature.

The relationship between spray form and fuel bubble point is not widely discussed in the literature. In the one identified correlation which seeks to validate the computational modelling of pressure swirl sprays, van der Wege and Hochgreb [2000] note that bubble point calculations suggest that superheat of 20 °C is sufficient to bring about flash boiling which is rigorous enough to alter the spray form for the pressure swirl sprays under investigation. For these pressure swirl sprays, spray collapse is thought to be brought about by vaporised fuel being drawn to the low pressure core of the spray between the closely spaced plumes when the momentum of the fuel vapour being drawn to the spray core is sufficiently large to overcome the relatively low radial momentum of the fuel droplets for the plume form examined, causing these plumes to deviate and drawing them together to form the collapsed spray observed. As such, the mechanism

for spray collapse in pressure swirl sprays is likely to be different for that for multihole sprays, and hence pressure swirl spray development appears to be more sensitive to the degree of fuel superheat than multihole spray development. Wigley *et al*. [2006] also noted that lower chain single component hydrocarbons, and in particular *n*-Heptane, appeared to be better than *iso*-Octane in simulating the volatility characteristics of multi-component gasoline.

5.1.4 Flash Boiling

Particularly for single-component fuels, if the gas pressure is below the bubble-point pressure at the given fuel temperature, it would be suggested that the fuel would spontaneously vaporize, i.e. 'flash boil'. Whilst a much collapsed spray form was observed under such experimental settings, no spontaneous and complete vaporization of the fuel spray was observed, even under extreme gas pressure and fuel temperature conditions. This is likely to be because that as 'flash boiling' starts to occur the evaporation process takes heat away from the liquid and cools it down, which in turn inhibits 'flash boiling' and brings about a form of equilibrium, or repetition of the process. This sequence also suggests the relevance of a timescale, and the hence vaporisation cannot be truly instantaneous. Therefore, it may be said that the level of superheat is important in two ways for the spray. Firstly it can influence the time taken for the spray to begin to rapidly vaporise, since it is a measure of the 'thermodynamic driving force' for moving the system towards equilibrium, and secondly that it influences the amount of vapour that is produced during the boiling process. Thermodynamic calculations performed by the fuel supplier Shell (by an unknown methodology) showed that for *iso*-Octane at 120 °C at its bubble-point pressure, a constant enthalpy flash until it reached 1.0 bar would lead to a vapour fraction of 0.198 mol/mol. By contrast, the same calculation for *n*-Pentane led to a vapour fraction of 0.61 mol/mol. For flash calculations at the same initial conditions to 0.5 bar, the vapour fractions were 0.38 and 0.71 for *iso*-Octane and *n*-Pentane, respectively. These numbers show that the amount of superheat can affect the amount of vapour given off during the spray break-up process and they also illustrate that without heat transfer into the spray there is not enough enthalpy in the system for the whole spray to evaporate. However, spray break-up behaviour is not fully explainable by equilibrium thermodynamics on the basis that the enthalpy of the spray is constant. Rapid heat and mass transfer can alter this picture dramatically. Furthermore, due to the multi-component nature of the

fuels and the dynamics of vaporisation, a complete and thorough analysis of spray behaviour on the basis of such equilibrium calculations is not possible.

5.2 Summary

High magnification imaging of the spray in the near-nozzle region was carried out over the duration of the spray cycle, including its initial emergence, development, steady state and disintegration. Even using very high speed imaging of the initial emerging spray, spontaneous and complete vaporization of the fuel spray was not observed for any gas pressure and fuel temperature conditions. This is likely to be because that as 'flash boiling' starts to occur the evaporation process takes heat away from the liquid and cools it down, which in turn inhibits 'flash boiling' and brings about a form of equilibrium, or repetition of the process. The high rate of spray break up when equilibration commences suggests that the in-nozzle flow regime affects the level of internal energy within the liquid volume, which further increases the imbalance in energy between the liquid and gaseous bodies. This sequence also suggested the relevance of a timescale, and that hence vaporisation cannot be truly instantaneous. This was further evidenced by the high speed imaging which showed an initial similar, well defined spray structure for all fuels under all conditions, even for those which in the subsequent frame showed the characteristics of a collapsed spray. For this work, a timescale in the order of 20 μs appears to be one of the determining factors in the development of equilibrium conditions between the liquid fuel and surrounding gas. For any spray, the time requirement for the establishment of equilibrium conditions would lead to the existence of an external spray break-up length.

The imbalance between the fuel's internal thermal energy and that of the gaseous body is the extent of superheat present within the fuel. Within the confines of the injector flow path, the liquid pressure prevents bubble formation and vaporisation, allowing large degrees of superheat to be contained in the fuel. For multi-component fuels, a range of superheat will be present in the fuel, although the driver for initial vaporisation appears to be the degree of superheat of the lowest volatility component. For the current work, the degree of superheat was sufficient to lead to spray collapse when the chamber gas pressure was at or below $1/10^{th}$ of the fuel's bubble point pressure at the given fuel temperature.

6 Oxygenated Fuels

Global concerns over the sustained use of fossil fuels are leading to an increased use of biogenically derived liquid fuels. The production of these fuels by the fermentation of glucose and cellulose results in liquids which have the general formula $C_nH_{2n+1}OH$, commonly known as "alcohols." The first four primary alcohols (in order of number of Carbon atoms) are Methanol, Ethanol, Propanol and Butanol. These are of interest as fuels for internal combustion engines due to their combustion properties and potential compatibility with the existing fuel distribution and filling infrastructure. In particular, as listed in Table 6-1, their higher activation energies lead to an increased resistance to engine knock, allowing for the use of higher compression ratios and hence higher engine thermal efficiencies. In addition, their higher heats of vaporisation leads to a charge cooling effect, increasing the charge density. For these reasons, the use of methanol and ethanol in racing engines has been wide-spread for some time. It should be noted that demand, and hence cost, for Propanol is driven by its use as a solvent, and that hence it is not commonly considered as fuel.

Fuel	Formula	Energy density [MJ/l]	Stoichiometric air/fuel ratio	Specific energy [MJ/kg air]	Heat of vaporisation [MJ/kg]	RON	MON
Gasoline (Typical)		32	14.6	2.9	0.36	95	85
Methanol	CH_3OH	16	6.4	3.1	1.2	106	92
Ethanol	C_2H_5OH	19.6	9.0	3.0	0.92	107	89
Butanol	C_4H_9OH	29.2	11.1	3.2	0.43	96	78

Table 6-1 Properties of Oxygenated (Alcohol) Fuels

An assessment of the life-cycle sustainability criteria of each of these fuels, their combustion characteristics or the extent of their compatibilities with existing infrastructure and engine hardware is beyond the scope of this work. However, in recognition of the growing use of these fuels, the spray development characteristics of these fuels were compared to those of gasoline to investigate whether their increasing use would align with the development of direct injection spark-ignition engines.

6.1 Fuel Selection

Following the investigation of the spray development of gasoline in relation of its constituent components, two alcohol fuels were selected for comparison. The alcohol currently most commonly used as an engine fuel is Ethanol, with worldwide ethanol fuel production in 2009 being 73.9 billion litres [Global Renewable Fuels Alliance]. Ethanol is widely used in Brazil and in the United States, with the use of 10% ethanol mixed with gasoline mandated in some U.S. states and cities. The longer hydrocarbon chain of Butanol causes it to be relatively non-polar, and hence less miscible in water and have a higher surface tension than the other alcohols. In this respect, Butanol is more similar to Gasoline than Ethanol, and hence was also selected for further examination.

6.2 Spray Development

To examine the reaction of oxygenated fuels to the test conditions, back-lit global spray imaging using the high speed video camera was carried out as for the Gasoline sprays. All other test conditions (fuel pressure, injection duration etc.) were also maintained constant, although these parameters could be altered in an engine to compensate for the different properties of these fuels. The Butanol and Ethanol spray images were captured from the side view and at 0.5 and 1.0 bar gas pressures only due to little variation in spray form being observed at 5.0 bar compared to at 1.0 bar. The spray images for Butanol and Ethanol are presented in Figure 6-1 and Figure 6-2 respectively.

Injector Body Temperature [° C]	Gas Pressure [bar] 0.5	1.0
20	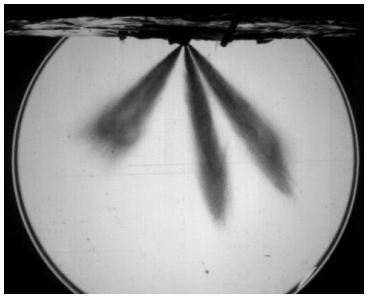	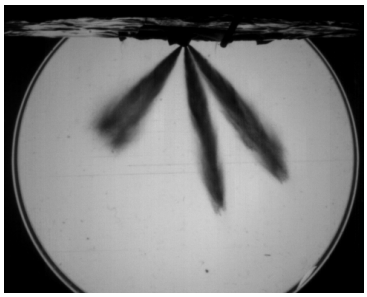
50	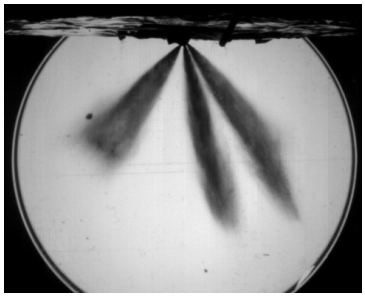	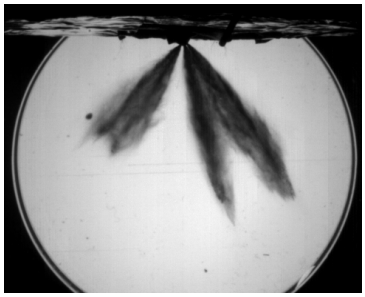
90	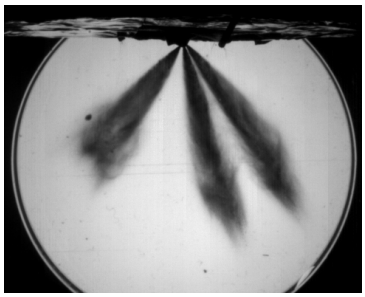	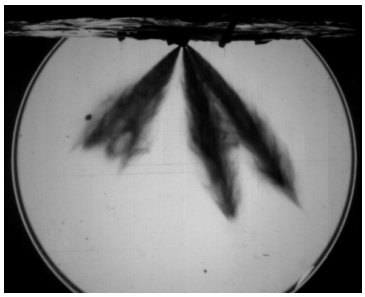
120	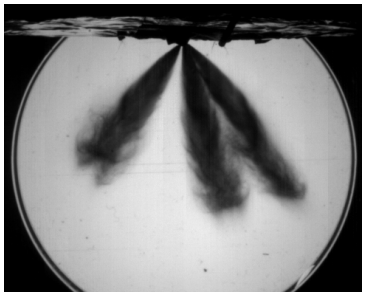	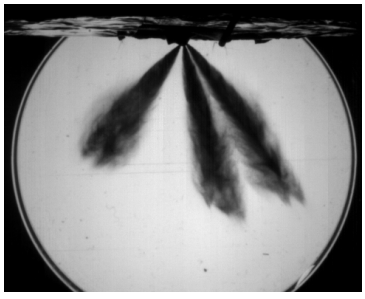

Figure 6-1 Butanol, 777 μs ASOI

Injector Body Temperature [° C]	Gas Pressure [bar] 0.5	1.0
20	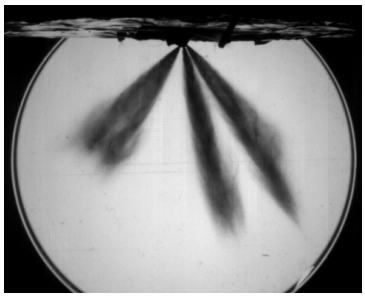	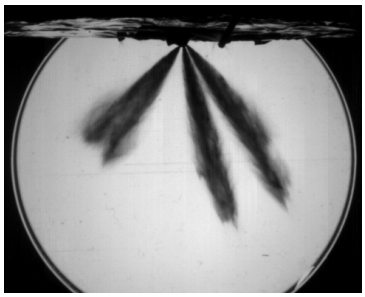
50	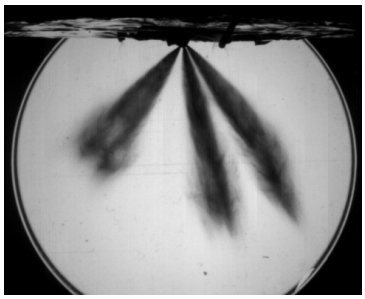	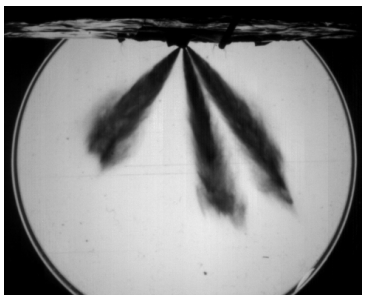
90	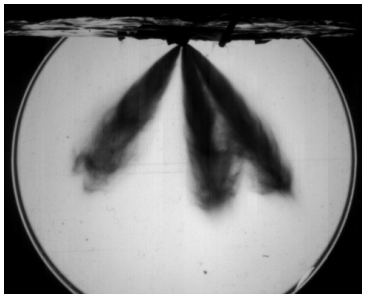	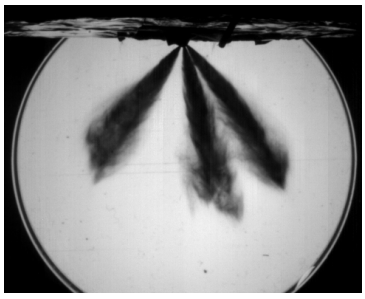
120	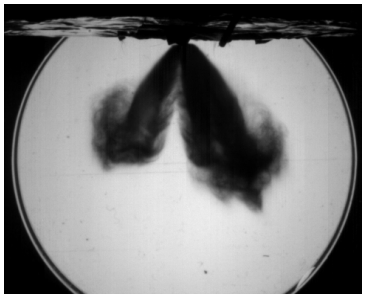	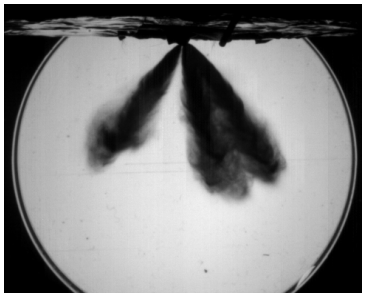

Figure 6-2 Ethanol, 777 μs ASOI

In general, Butanol (Figure 6-1) and Ethanol (Figure 6-2) show a similar spray form to the multi-component fuels and *iso*-Octane at the nominally ambient conditions. However, at the spray collapse condition (120 °C injector body temperature, 0.5 bar gas pressure), obvious differences in the spray form may be observed between the fuels. In general, the spray development behaviour of Butanol appears to be similar to *iso*-Octane over the range of experimental conditions. For Butanol, as for *iso*-Octane, full collapse is not observed at the "spray collapse" conditions, which may be expected from Butanol's high boiling temperature (117.2 °C). The Butanol sprays appear less well atomised than the *iso*-Octane sprays at injector body temperatures up to 90 °C, which is likely to be related the higher viscosity and surface tension of Butanol, which both resist break-up. Despite this, the Butanol spray can be seen to be somewhat converged at the spray collapse condition. This is somewhat unexpected given the considerably lower Reid Vapour Pressure of Butanol relative to the other fuels, although shows that the boiling temperature threshold has been surpassed at the given gas pressure.

For Ethanol, which has a boiling temperature of 78.5 °C, the observed spray development trend is similar as for the Standard Gasoline in that collapse is observed to be complete at the "spray collapse" condition. However, closer inspection of the plumes produced using Ethanol shows a clearer, more defined spray boundary than those of Standard Gasoline at equivalent conditions. In this respect, the sprays produced by Ethanol are more similar to those produced by *iso*-Octane at low injector body (fuel) temperatures.

6.3 Comparison of Spray Characteristics

The general form and observations of the spray development for Ethanol and Butanol appear to follow those for petroleum, non-oxygenated fuels. Further quantitative analysis was carried out from the images using the same techniques as for the petroleum fuels to further aid comparison of the sprays developed by these fuels.

6.3.1 Spray Penetration

The graphs of the penetration of plume tips 1 and 6 are shown in Figure 6-4 to Figure 6-7 for gas pressures of 0.5 and 1.0 and injector bogy temperatures of 20, 90 and 120 °C. These graphs show the penetrations measured from the sprays produced by Ethanol and Butanol in comparison to those produced by the Standard Gasoline and the main high and low volatility components *n*-Pentane and *iso*-Octane.

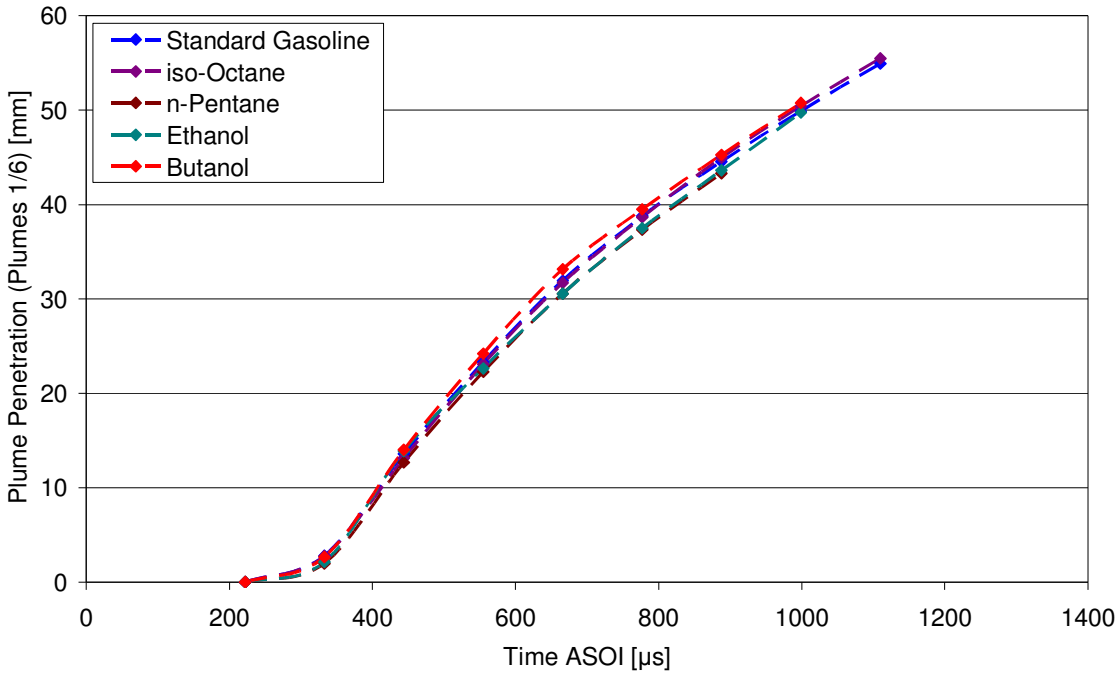

Figure 6-3 Oxygenated and Non-Oxygenated Fuels: Plume Penetration: 20 °C, 0.5 bar

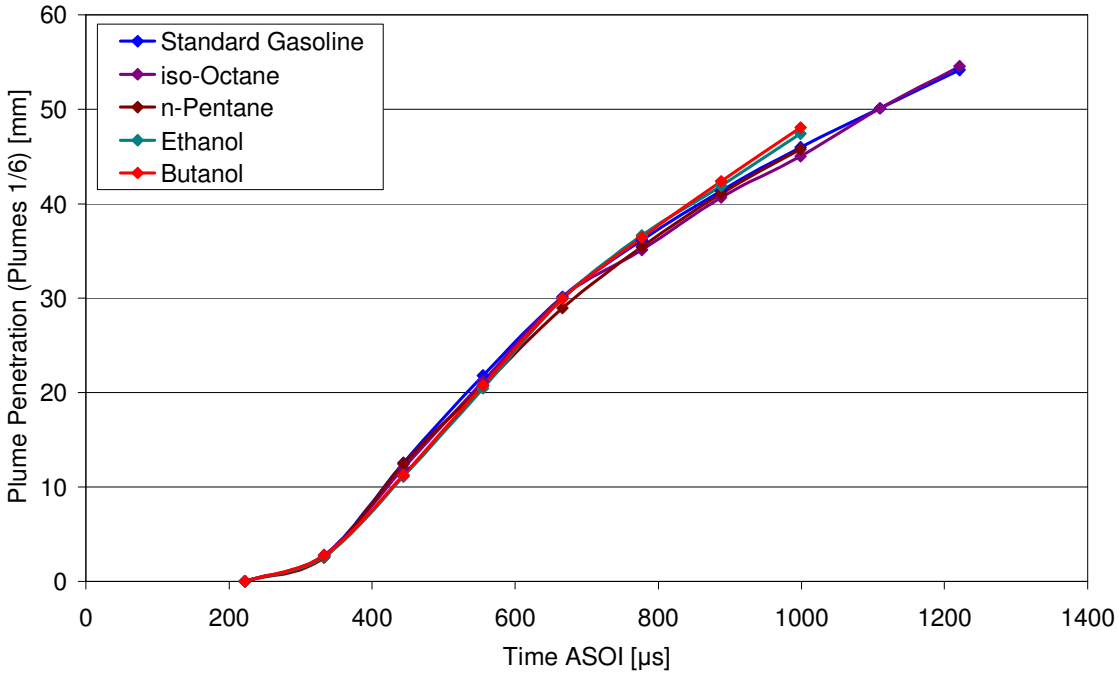

Figure 6-4 Oxygenated and Non-Oxygenated Fuels: Plume Penetration: 20 °C, 1.0 bar

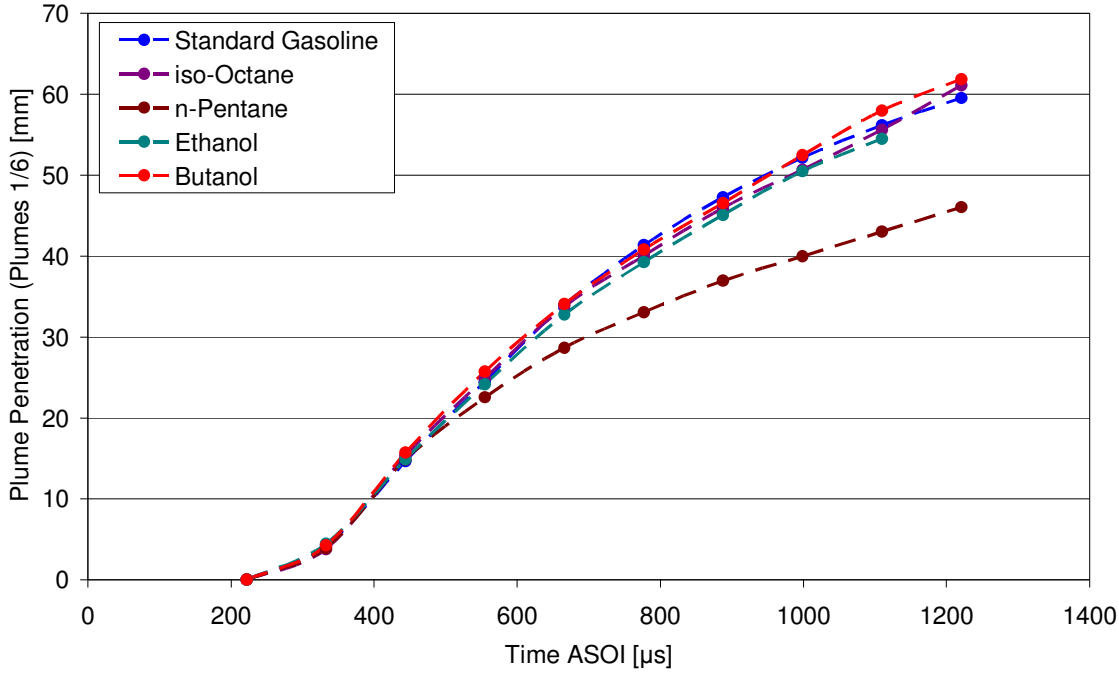

Figure 6-5 Oxygenated and Non-Oxygenated Fuels: Plume Penetration: 90 °C, 0.5 bar

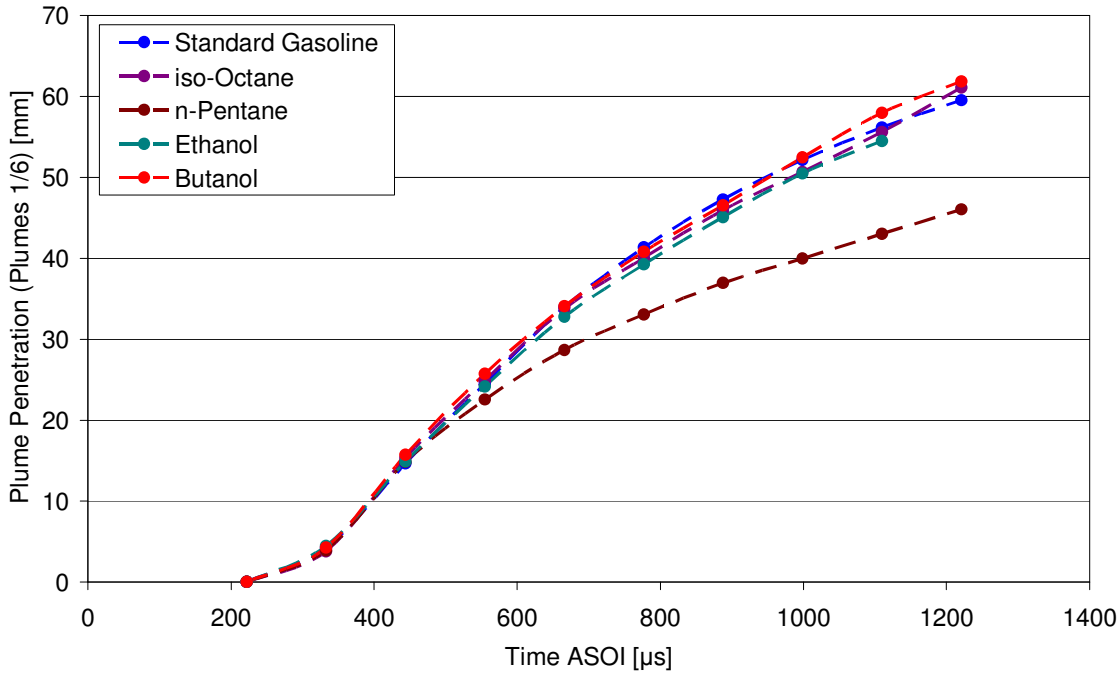

Figure 6-6 Oxygenated and Non-Oxygenated Fuels: Plume Penetration: 90°C, 1.0 bar

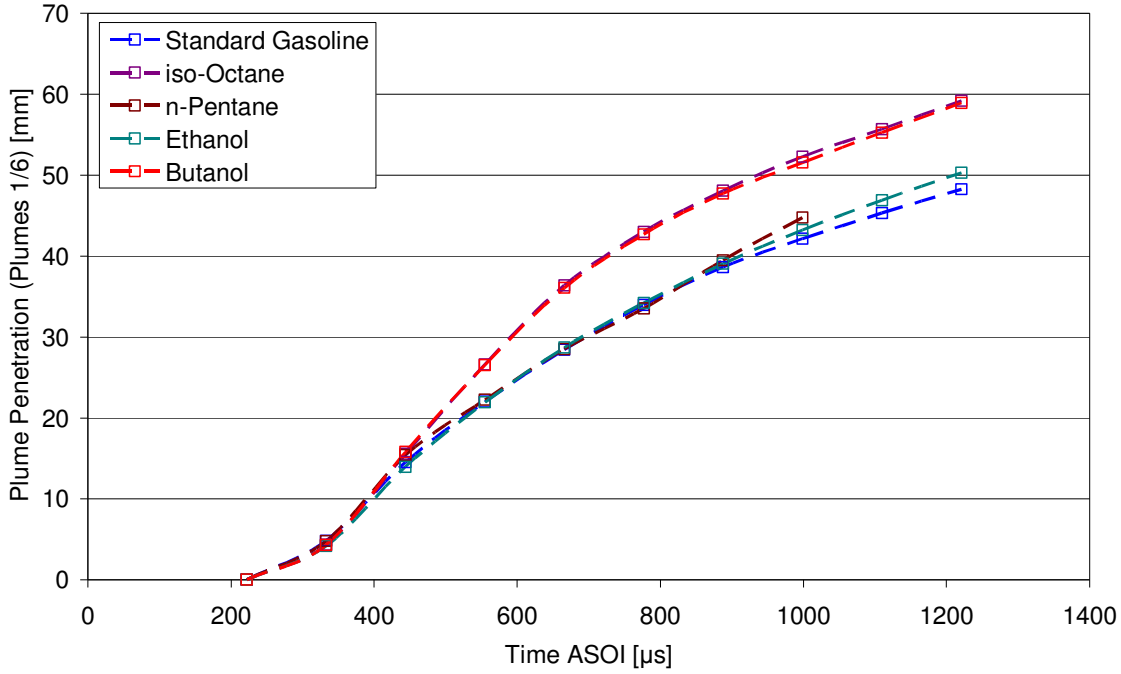

Figure 6-7 Oxygenated and Non-Oxygenated Fuels: Plume Penetration: 120 °C, 0.5 bar

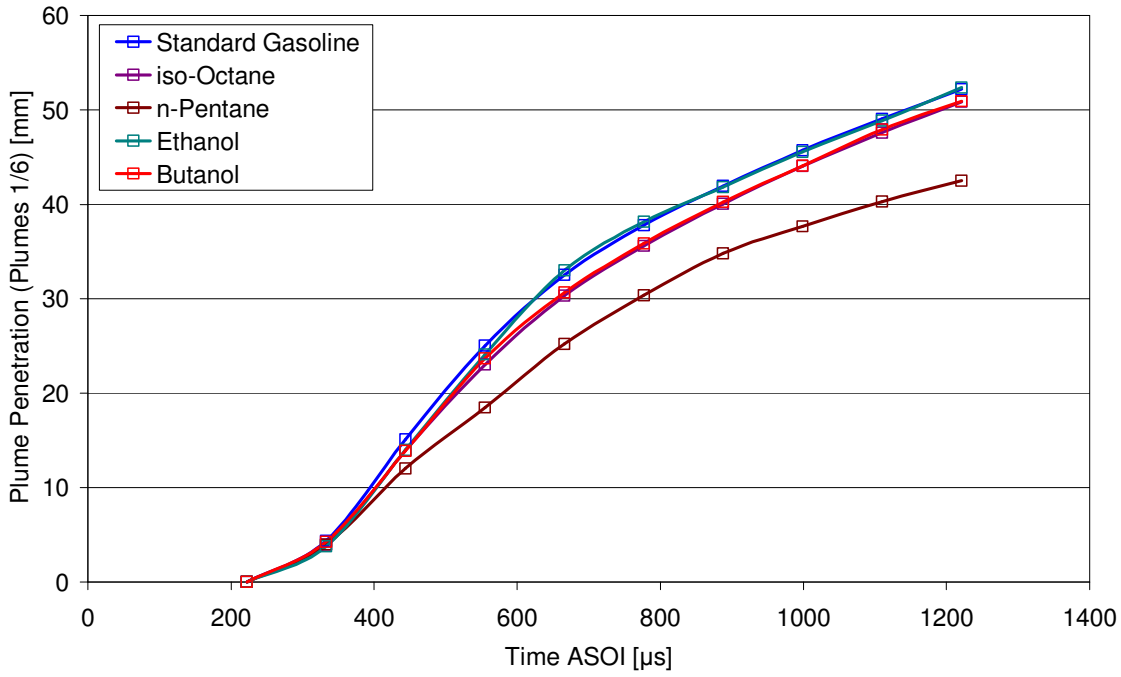

Figure 6-8 Oxygenated and Non-Oxygenated Fuels: Plume Penetration: 120°C, 1.0 bar

The overarching observation from the plume penetration graphs above is the striking similarity of penetration rate reaction to the conditions of Ethanol and Standard Gasoline and of Butanol and *iso*-Octane. This is especially evident from the graphs showing the spray plume penetrations at the elevated injector body temperature of 120

°C (Figure 6-7 and Figure 6-8), which is also the condition where the most difference between high and low volatility fuels is observed.

6.3.2 Spray Velocity

The calculated spray plume tip velocities for Standard gasoline, *iso*-Octane, *n*-Pentane, Butanol and Ethanol are shown in Figure 6-9, Figure 6-10 and Figure 6-11 for the nominally ambient condition and 0.5 and 1.0 bar gas pressures at an injector body temperature of 120 °C respectively.

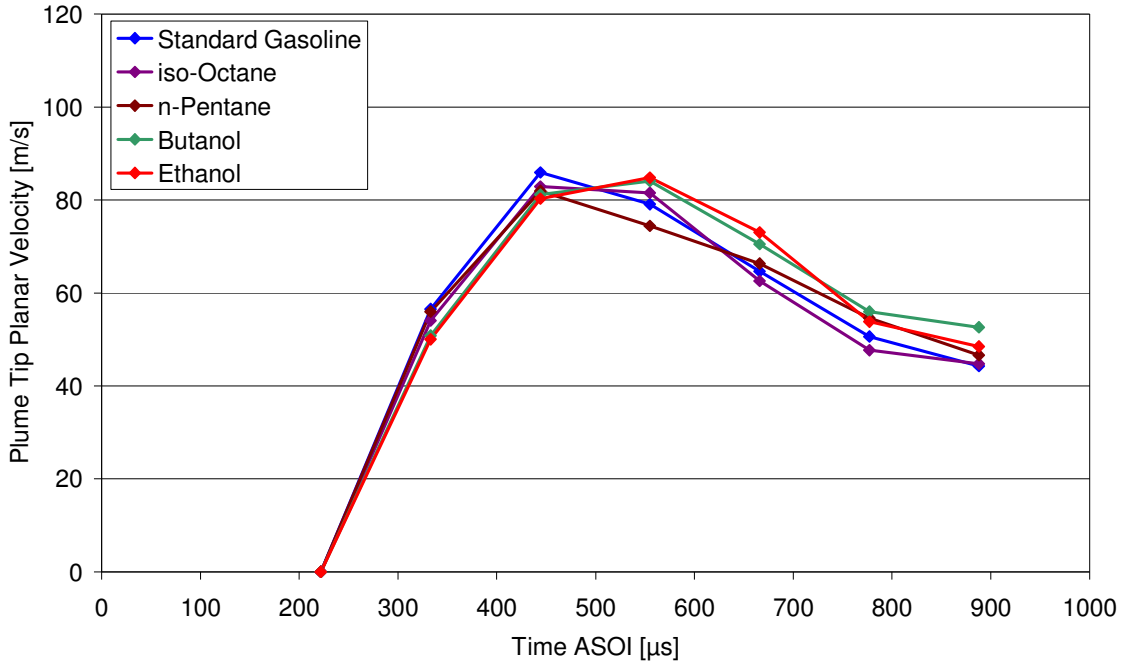

Figure 6-9 Spray Tip Velocity: 20 °C, 1.0 bar

At the ambient condition (Figure 6-9) the measurements show a slightly lower initial velocity measured for Butanol and Ethanol. These oxygenated fuels have approximately 2 to 6 times the viscosity of the other tested fuels (for Ethanol and Butanol respectively), and this reduction in their initial velocities may be due to increased in-nozzle friction drag. For this ambient condition, the Butanol and Ethanol sprays continue to accelerate and show an increased velocity over the other fuels at the subsequent measurement interval. The greater density of these oxygenated fuels over the other, non-oxygenated, fuels means their spray momentum is greater for a given droplet size, and hence the effect of aerodynamic drag on reducing the droplet velocity is diminished.

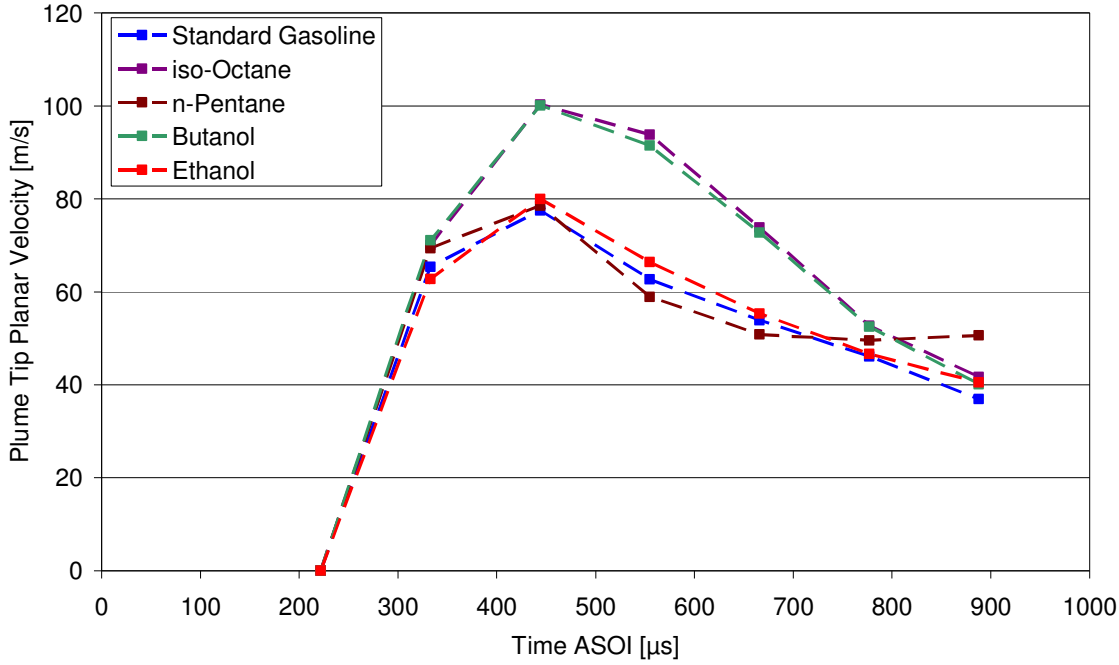

Figure 6-10 Spray Tip Velocity: 120 °C, 0.5 bar

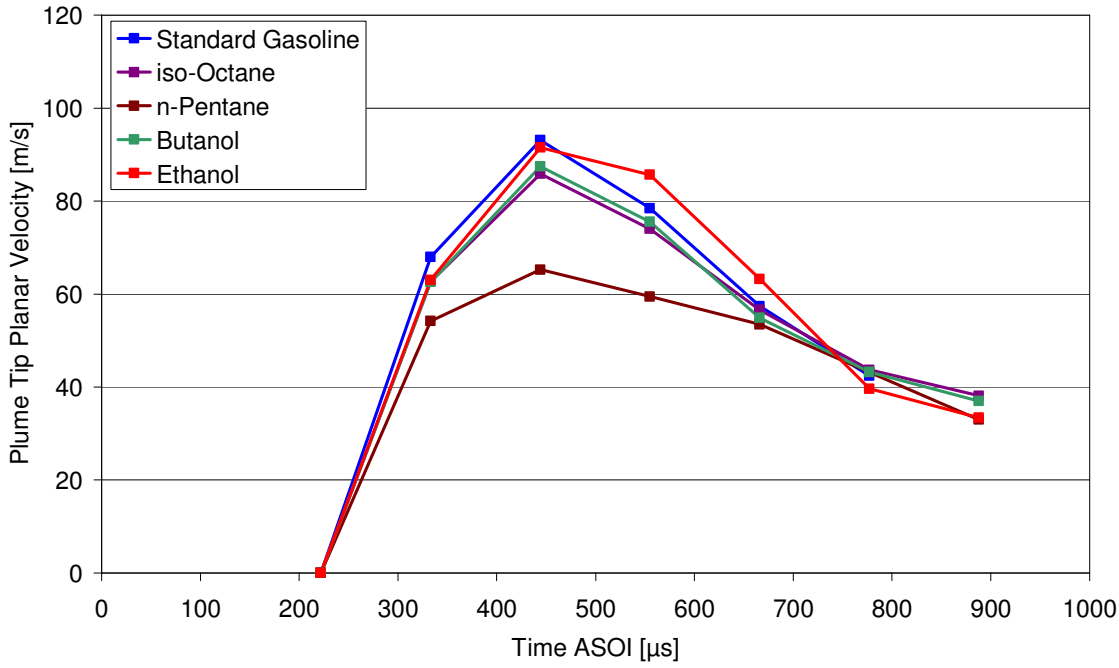

Figure 6-11 Spray Tip Velocity: 120 °C, 1.0 bar

The similarity of velocities between Ethanol and Standard Gasoline and Butanol and *iso*-Octane is again evident at the nominal spray collapse condition of 120 °C injector body temperature and 0.5 gas pressure (Figure 6-10). At an injector body temperature of 120 °C and a gas pressure of 1.0 bar (Figure 6-11), the spray tip velocity of the Butanol

spray again matches that of *iso*-Octane. The initial rate of penetration of Ethanol is slightly slower than that of Gasoline at this condition, and as for the same gas pressure at a lower fuel temperature (Figure 6-9) the Ethanol spray appears to maintain its velocity for a longer duration than the other fuels.

6.3.3 Spray Cone Angles

Due to fuel availability constraints, end view images were not captured for the oxygenated fuels Butanol and Ethanol. Observation of the images in Figure 3-22 shows that the side view spray cone angles for these fuels are similar to that of the other fuels, and the magnitude of these angles may be estimated from those fuels to which the sprays show a similar form for each test condition (e.g. *iso*-Octane for Butanol, Standard Gasoline for Ethanol) in Figure 4-19.

The spray cone angle as measured for both the oxygenated and principal non-oxygenated fuels over the range of test conditions are shown in Figure 6-12. The measurement location of these angles is the same as that for the end view cone angles previously presented, although measured from the side view images of the sprays. At 20 °C injector body temperature, 1.0 bar gas pressure (light blue bar) all fuels show a similar cone angle The small differences in cone angles between the fuels at this condition are likely to be due to the evaporation of the liquid fuel from the plume boundaries, where *iso*-Octane evaporates less than Standard gasoline to bring about a slightly smaller measured cone angle. Conversely, the high rate of peripheral spray evaporation (to where it is no longer detectable by the imaging technique) of *n*-Pentane also acts to produce a narrower cone angle than the Standard Gasoline. In addition, physical fuel properties such as viscosity may be affecting the flow regime inside the nozzle, leading to slight difference in spray development and hence measured cone angle.

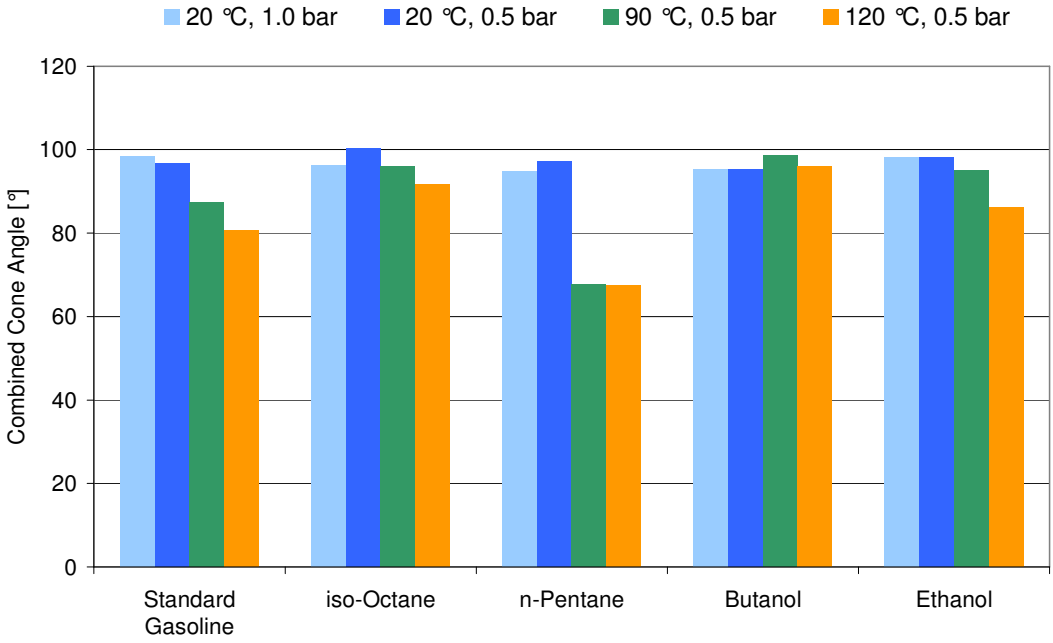

Figure 6-12 Overall Spray Cone Angles – Side View

This graph again illustrates the similarities in spray convergence behaviour between Ethanol and Standard Gasoline, in that both sprays show a clear reduction in cone angle with an increase fuel temperature. However, the inclusion of lower boiling temperature, high volatility components in Standard Gasoline is shown by a greater decrease in cone angle than for the single component Ethanol. By contrast, Butanol shows only a small increase in cone angle at 90 °C injector body temperature, as also seen for *iso*-Octane at 20 °C injector body temperature, 0.5 bar gas pressure, and no further reduction in cone angle below its nominal angle over the test conditions examined. The fact that Butanol has a higher boiling temperature than *iso*-Octane again indicates the effect that the vaporisation rate has on causing spray convergence.

6.4 Summary

The images captured of the sprays produced using Butanol and Ethanol show a general similar spray form as for the hydrocarbon fuels previously presented. This is also the case for the physical spray parameters such as the plume penetration length and cone angle, which appear to be little affected by any differences in physical properties bought about by the different chemical composition of these oxygenated fuels. At conditions away from those bringing about the nominal spray form, the spray development of these oxygenated fuels is again similar to that previously witnessed with the hydrocarbon fuels. However, the degree of reaction to increases in injector body temperature and gas

pressure differs between Butanol and Ethanol. In this regard, there is a striking similarity between the reaction of the sprays of Butanol to *iso*-Octane and Ethanol to Standard Gasoline.

In considering the drivers for spray convergence as examined in the previous chapters, these similarities in spray reaction appear to further evidence that it is the superheat within the fuel which drives its rate of break-up and vaporisation, which in turn affects the spray form. Comparing the bubble point pressures of the similar fuel pairs (*i.e.* Standard Gasoline and Ethanol, *iso*-Octane and Butanol) in Table 6-2 shows the similarities in their bubble point pressures over the tested fuel (injector body) temperature range. This is particularly the case for the temperatures at which they show spray collapse (*i.e.* 120 °C Standard Gasoline/Ethanol, 180 °C *iso*-Octane/Butanol). The similarity in these bubble point values show that each of these fuel pairs contains a similar amount of superheat at these conditions, which is above the critical value which leads to a rapid enough break-up to bring about spray collapse.

Fuel	Bubble Point Pressure [bar]				
	20°C	50°C	90°C	120°C	180°C
Standard Gasoline	0.3	0.8	2.4	4.5	13.0
Ethanol	0.1	0.3	1.6	4.3	20.7
iso-Octane	0.1	0.2	0.8	1.8	6.3
Butanol	0.0	0.0	0.3	1.1	6.3

Table 6-2 Fuel Boiling Characteristics

By way of a summary of the macroscopic spray forms for each of the fuels tested under the range of experimental injector body (and hence fuel) temperature and gas pressure conditions, spray images at 777 µs ASOI are presented in Figure 3-16.

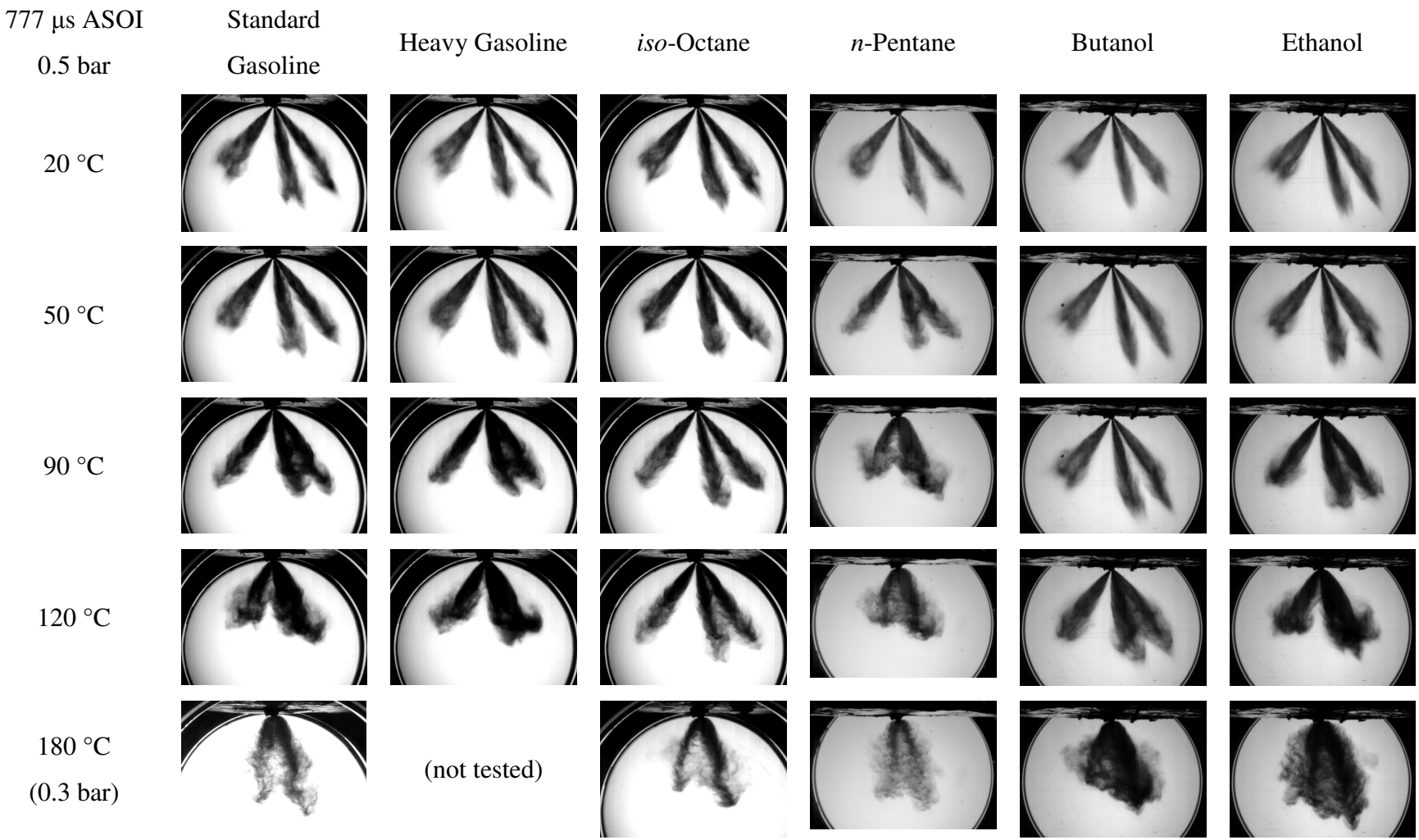

Figure 6-13 Summary of Fuel Sprays under Range of Test Conditions

7 Cavitation

The previous chapters examined the spray development and break-up downstream of the injector nozzle. The results and observations, especially in relation to the rate of break-up, suggest that the upstream, in-nozzle fuel flow has a significant bearing on the spray formation. In particular, the high rate of break-up suggests that upstream perturbances are acting to initiate the spray break-up earlier in the fuel flow path. The likely source of this perturbation is the presence of cavitation inside the nozzle. There is some evidence in the literature to suggest that cavitation occurs inside multihole gasoline direct injection nozzles, and in particular that the formation of bubbles due to cavitation provides nucleation sites for an increased rate of evaporation and hence break-up once released from the nozzle, for example by Gilles Birth *et al*. [2006]. However, only limited literature exists which examines the interaction of the fuel temperature on in-nozzle cavitation (Moon *et al.* [2007] in relation to pressure swirl injectors), and no existing literature could be found which examined these effects for a full cone spray. This chapter details the in-nozzle fuel flow using optical nozzles to investigate the extent of cavitation present in the injector nozzle, and to observe its impact on spray break-up.

7.1 Cavitation

Hydrodynamic cavitation occurs when the static pressure of a liquid fuel flow falls below its vapour pressure. This condition, which may be induced by a high liquid flow velocity or sharp turnings, causes the vapour to form bubbles in the liquid. The process of bubble formation, growth and collapse results in very high energy densities, leading to very high temperatures and pressures at the surface of the bubbles. However, the lifetime of these bubbles and their total volume are relatively small, and so the overall liquid medium remains at the global temperature and pressure. Sharp turning of the liquid may be caused at the injector nozzle inlet. If the corner at the inlet is sufficiently sharp, the flow separates from the nozzle wall and forms a *vena contracta* inside the nozzle. The contraction in the inlet effectively reduces the area through which the liquid

flows. This reduced area is accompanied by in increase in velocity, due to the conservation of mass flow. The conservation of momentum then means that the acceleration of the liquid through the *vena contracta* causes a reduction in static pressure and resulting in the formation of cavitation bubbles in the flowing liquid. The flow will be affected by any surface with which it makes contact, and so surface features, including the surface roughness, will affect whether cavitation occurs. In this regard, the extent of cavitation witnessed at any location in fuel flowing through an injector nozzle is extremely sensitive to the geometry of the nozzle inlet, with smoothed and/or conical nozzle inlets likely to result in lower levels of cavitation. Particularly for nozzles with sharp inlet geometries or other step feature, cavitation occurring at the nozzle entrance can extend along the length of the nozzle, causing the flow to become completely detached from the walls of the nozzle, known as "hydraulic flip." When this occurs, in effect all surface flow effects are removed and cavitation can no longer be triggered or supported in the liquid. As such, this results in a smooth, steady, liquid, stream exiting the nozzle. In all cases, cavitation is a transient, unsteady phenomena, and is not necessarily azimuthally symmetric in a nozzle due to the dependence on the instantaneous, local flow conditions.

7.1.1 Cavitation Number

The Reynolds and Weber numbers have been previously considered in this work as indicators of the in-nozzle flow and the break-up regime under which the spray operates. As such, these parameters may also provide an initial indication of the likelihood of a fuel undergoing cavitation in the nozzle. However since cavitation is a phase-change phenomenon, the vapour pressure p_v (and its temperature dependence), should also be considered as a critical parameter. At low temperatures, fuels with high vapour pressure (e.g. *n*-Pentane) will tend to induce cavitation more easily than those with lower vapour pressure (e.g. *iso*-Octane).

As detailed in the literature survey, the cavitation number for a flow can be taken as an indication of the likelihood of that flow cavitating, based on the ratio of the local static to vapour pressure. Care should be taken in comparing cavitation number values, as the physically correct definition, Ca, given in 5Eq.7.1 is not always that used in the literature.

Eq.7.1
$$Ca = \frac{p_\infty - p_v(T_\infty)}{\frac{1}{2}\rho_L u_\infty^2}$$

Using the definition of the cavitation number in Eq.7.1, increasing likelihood and magnitude of cavitation are indicated by reducing values of Ca. However, in the majority of published literature cavitation numbers are based on the popular definition of:

Eq.7.2
$$CN = \frac{(p_{inj} - p_g)}{(p_g - p_v)}$$

For this definition of the cavitation number, a higher value is indicative of a larger probability of the flow cavitating. Critical cavitation numbers, which indicate the onset of cavitation, based on CN have been quoted in the literature as in the range from 0.5 to 0.75 (Nouri *et al.* [2007]) and 1.5 to 10 (Bergwerk [1959]) with associated critical Reynolds Numbers of between 5,000 and 30,000.

The likelihood of cavitation in the injector under study in the current body of work was also examined by comparing nozzle flow rates with data presented by Gilles-Birth *et al.* [2006], who investigated the effect of in-nozzle fuel flow and cavitation on spray development for multi-hole-designed gasoline injectors. They used an injector body coupled to an optical nozzle with a single angled nozzle hole (0.2 mm in diameter). When flow rate was plotted against back pressure by the latter authors, the onset of cavitation was illustrated by the onset of a 'chocked' flow regime where there was no further increase in flow rate with reduction in back pressure. Specifically, their data showed that with a reduction in gas pressure from 16 bar to 10 bar, there was a linear increase in flow rate from approximately 3.5 mm^3 to 5.0 mm^3 per injection event for a pintle opening time of ~1.0 ms. Any further decrease in gas pressure maintained the flow rate between 5.2 mm^3 and 5.5 mm^3 per injection event. These results are presented in Figure 7-1 with the back pressure and flow rate for the real injector used for the global spray imaging in this work superimposed. For the multi-hole injector examined in the current study the flow rate per nozzle hole over 1 ms equates to ~5–5.2 mm^3 at 20 °C and 1 bar gas pressure. This value's proximity to the trends of Gilles-Birth *et al.* [2006] further suggests operation of the current nozzle very close to the onset or inside the cavitating regime. It can be seen that increasing the pressure drop across the nozzle

(i.e. reducing the gas pressure, p_g, or increasing the injection pressure, p_{inj}) would increase the severity of cavitation. Even accounting for variations in the transition regimes between nozzles with geometrical differences, these larger cavitation numbers compared to the values of 0.6 and 0.8 reported by Gilles-Birth *et al*. [2005] suggested from the outset that the real injector nozzle of the present study was operating well inside the cavitation regime at the conditions considered.

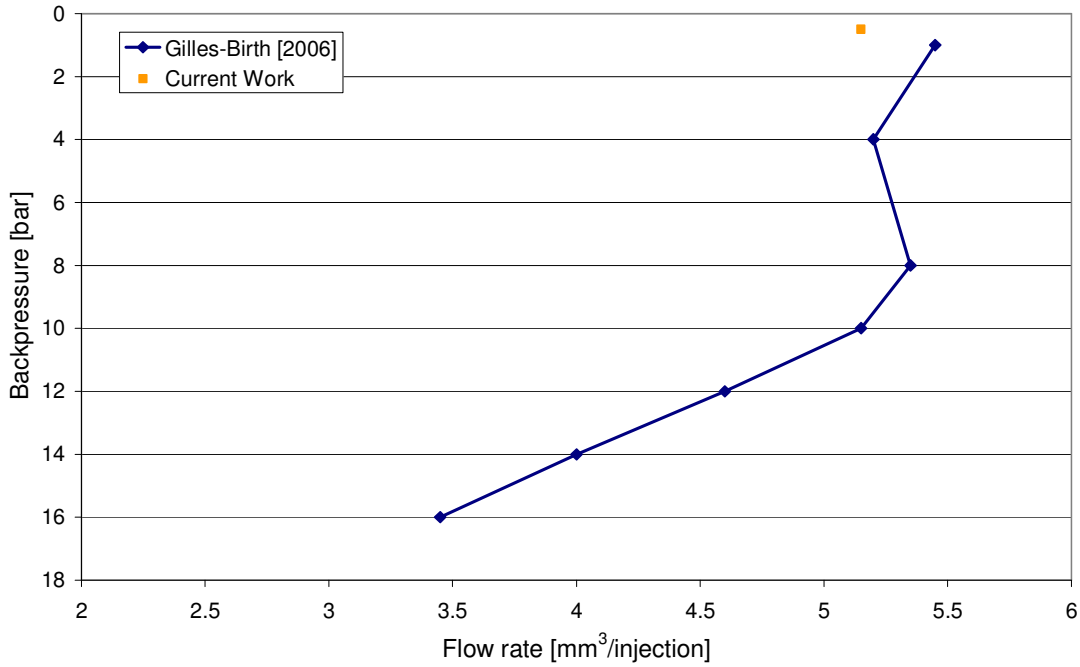

Figure 7-1 Graph of Flow Rate vs. Back Pressure (Gilles-Birth [2006]) with Current Work Super-Imposed

For early injection, warm engine conditions, represented in this work by a low chamber gas pressure injection and high injector body (and hence fuel) temperature, spray collapse has been observed to occur, with the extent of collapse being proportional to the volatility of the fuel. Under these spray collapse conditions, the plumes are drawn together under the injector tip, and the designed directionality of the spray is diminished. This phenomenon has been observed to occur as the result of fast disruptive evaporation of the fuel upon injection, due to the reduction of the fuel's boiling temperature caused by the low pressure environment into which it is injected. As evidenced by the above analysis, the examined spray is likely to be cavitating under all temperature conditions at reduced gas pressures, with the extent of cavitation increasing with increasing fuel pressure, especially once the fuel's boiling temperature is exceeded. Hence, it is very likely that over the spray collapse regime, in-nozzle phase-change

phenomena due to cavitation are directly coupled to phase-change phenomena arising from boiling, altering the spray formation in a complex manner. In order to better analyse this mechanism the fuel flow in real size optical nozzles was imaged.

7.2 In-Nozzle Flow Imaging

The majority of previous experiments of cavitation in injector nozzles, particularly of multi-hole design, have been conducted at fixed temperature and with fixed liquids. Several different liquids have been used for such investigations, including Diesel oils, calibration oils and various unspecified hydrocarbon mixtures such as white spirits and gasolines. All of these liquids have widely different transport properties such as surface tension (σ), viscosity (μ), density (ρ), boiling point and vapour pressure (p_v). In addition, many experiments have been carried out on large, scaled up models of injector nozzles. However, a major challenge in scaling is translating the data from a large scale nozzle and/or using a certain liquid to predict the onset of cavitation in a real size nozzle, possibly using another liquid. This implies that the cavitation and Reynolds numbers should be controlled as much as possible in cavitation experiments. The control of these parameters is not trivial, especially when considering modifications to a system for optical access which might involve some change in configuration or scale. For example attempts to match *Re* by changing the flow rate on a large-scale model may lead to effects on the residence time and the cavitation number. The liquid pressure may be altered to recover the cavitation number but changing the pressure would also impact the liquid density, and hence the nuclei density. Additionally, fluid transport properties have non-linear temperature and pressure dependencies. Therefore, a global transition regime map is extremely difficult to build from non-cavitating to cavitating flows. Fortunately, the above parameters are all much less sensitive when cavitation is already developed, justifying the continued use of *Re* and the cavitation number as the two most widely applicable non-dimensional parameters to control in comparing flow regimes.

7.2.1 In-Nozzle Flow Condition Matching

Flow rate measurements were conducted in order to match the Reynolds number *Re* of the real injector and the optical nozzle. The spray characteristics of injectors depend not only on the physics of atomisation of the liquid jet but also on the levels of turbulence generated by the internal flow upstream of the nozzle exit, as well as the extent to which cavitation occurs inside the nozzle passage. The effect of turbulence can be characterised by the Reynolds number; $Re = \rho u d/\mu$ where ρ and μ are the density and

dynamic viscosity of the liquid fuel, respectively, d is the nozzle hole diameter and *u* the flow velocity in the nozzle. The injector flow rate was measured while injecting at a constant working pressure of 150 bar. This was divided by the number of nozzle holes (six) so as to obtain the flow rate per nozzle. The flow rate of the real injector at 150 bar injection pressure was 16.68 g/s giving an approximate flow rate of 2.78 g/s per nozzle. Injection pressure was varied while injecting through the optical nozzle, and an injection pressure of 23 bar gave a flow rate of 2.81 g/s which closely approximated that of the real injector. Hence all injection events using optical Nozzle A were carried out at 23 bar. The jet velocity was obtained by dividing the nozzle mass flow rate by the product of the fuel density and the flow area using the Nozzle A diameter of 0.5 mm. This was calculated to be 22 m/s. Nozzle B has a hole diameter of 0.2 mm. An injection pressure of 40 bar was found to give the same Reynolds number to the real injector and Nozzle A. The velocity of the jet from Nozzle B was calculated to be 55 m/s.

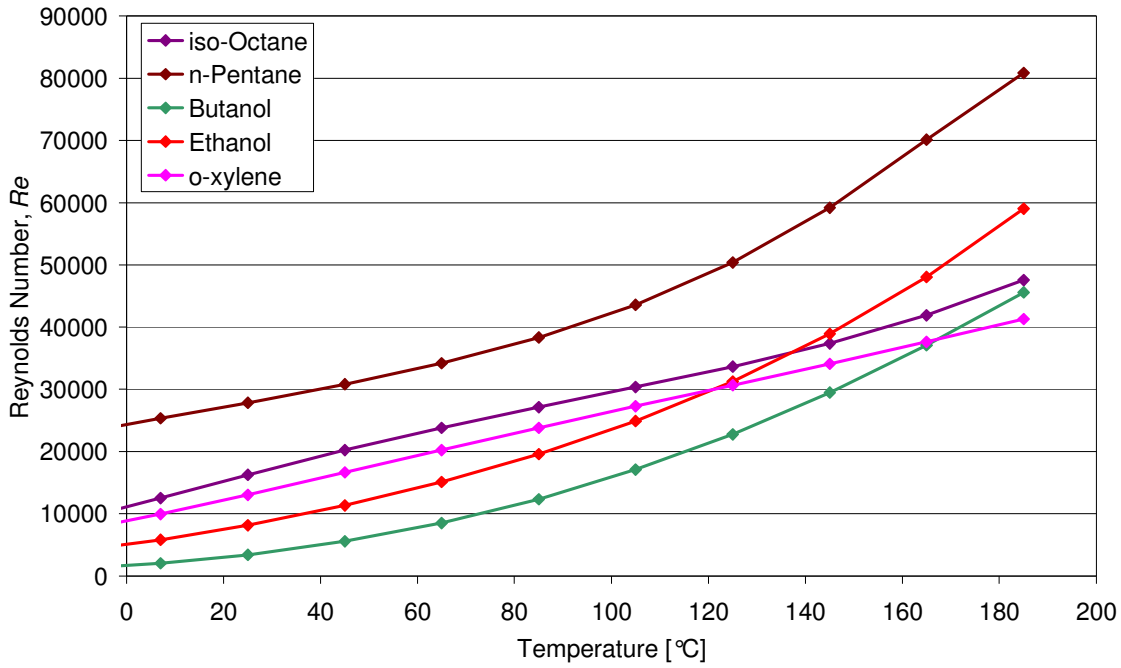

Figure 7-2 Flow Reynolds Numbers Optical Nozzles A and B

Figure 7-2 shows the *Re* plot for all single-component fuels tested with fluid properties of density and viscosity for varying temperatures along the liquid saturation curve. In the range 20–90 °C, the calculated *Re* numbers were 4,000–40,000; interestingly, Butanol's *Re* at 20 °C was the lowest, indicating flow potentially under laminar-turbulent transition conditions.

7.2.2 Cavitation Numbers of Experimental Nozzles

As detailed in Section 2.2 of this work, two transparent nozzles were designed and manufactured from Perspex to enable the fuel flow inside the nozzle to be visualised. Nozzle A had a nozzle diameter of 0.5 mm and a length of 2.5 mm (L/d=5). Nozzle B was a more faithful representation of the real (steel) nozzle, with a hole position closer to the bottom of the needle seat, and a nozzle diameter of 0.2 mm and length of 1.0 mm (also L/d=5).

Cavitation numbers were calculated for the main experimental conditions in terms of both Ca and CN at gas pressures of 0.5 and 1.0 bar (for CN), as illustrated in Figure 7-3 to Figure 7-5 for Nozzle A and Figure 7-6 to Figure 7-8 for Nozzle B. The values for cavitation numbers were calculated for Standard Gasoline and its light, medium and heavy representative constituents (*n*-Pentane, *iso*-Octane and *o*-Xylene respectively), as well as the oxygenated, alcohol fuels examined in the previous chapter. It can be observed that the cavitation numbers *Ca* obtained from Eq.7.1 (with p_∞ set to p_{inj} and U_∞ set to the flow velocity in the nozzle, u) are smaller in magnitude when compared to *CN* obtained from Eq.7.2. Also, there is an approximate constant increase in *Ca* with temperature against the continuous change in the slope of *CN*. The effect of temperature on *Ca* is relatively small, with *Ca* increasing by ~10% when temperature increases from 20 °C (293 K) to 90 °C (363 K). This increase comes from the effect of density in the denominator of Eq.7.1 because the numerator decreases drastically with temperature from the effect on the vapour pressure. However, upon reaching a critical value of vapour pressure (as a function of the temperature), the numerator rapidly decreases causing a drop-off in the value of Ca, as seen for *n*-Pentane and Ethanol within the temperature range plotted in Figure 7-3. Concerning *CN*, the effect of temperature on vapour pressure shows that the vapour pressure increases with temperature, therefore causing the denominator to approach a negative value, leading to negative values of *CN*. Hence only values up to the transition point from positive to negative CN have been plotted for clarity. It can further be observed by comparing Figure 7-4 to Figure 7-7 and Figure 7-5 to Figure 7-8 that *CN* values are considerably lower at the higher gas pressure. However, for all cases the calculated values of *CN* are above 10, the highest critical value of *CN* denoted in the published literature. This suggests the high likelihood of the examined flow undergoing cavitation inside the injector nozzle for all fuels and temperatures at gas pressures of 0.5 and 1.0 bar.

An important observation in the cavitation number, which was also highlighted from the global spray imaging, is that gasoline appears to be more temperature sensitive compared to *iso*-Octane. This is especially seen from the values of CN, which incorporates a term for the liquid's vapour pressure at the given temperature. Although *iso*-Octane is commonly used as a substitute for gasoline in many engine research applications these results show that higher volatility components, like *n*-Pentane, are better substitutes for gasoline when a single-component fuel is to be used as a surrogate for gasoline, especially at elevated temperature conditions.

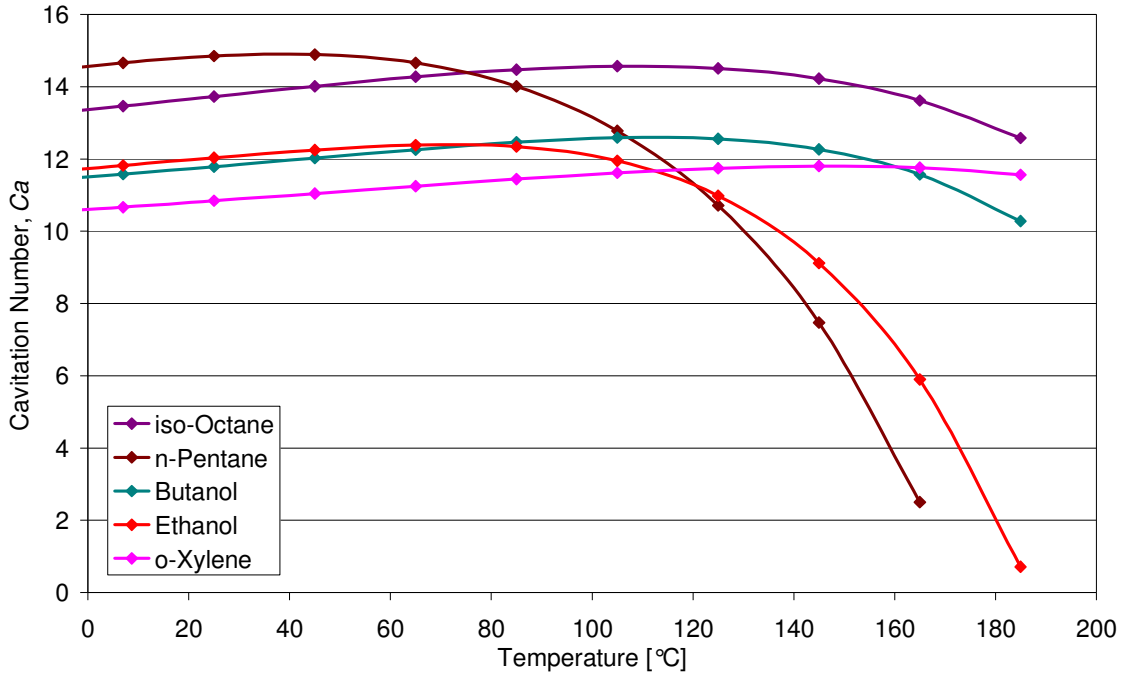

Figure 7-3 Experimental Cavitation Numbers (Ca Eq.7.1), Nozzle A

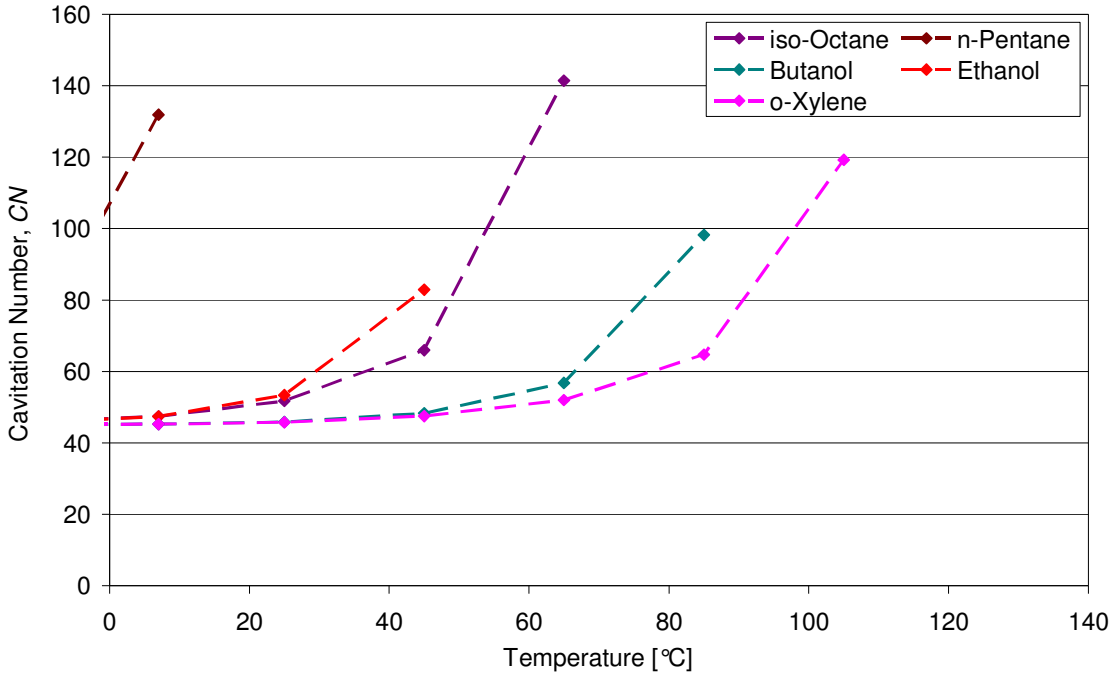

Figure 7-4 Experimental Cavitation Numbers (CN Eq.7.2), Nozzle A, 0.5 bar

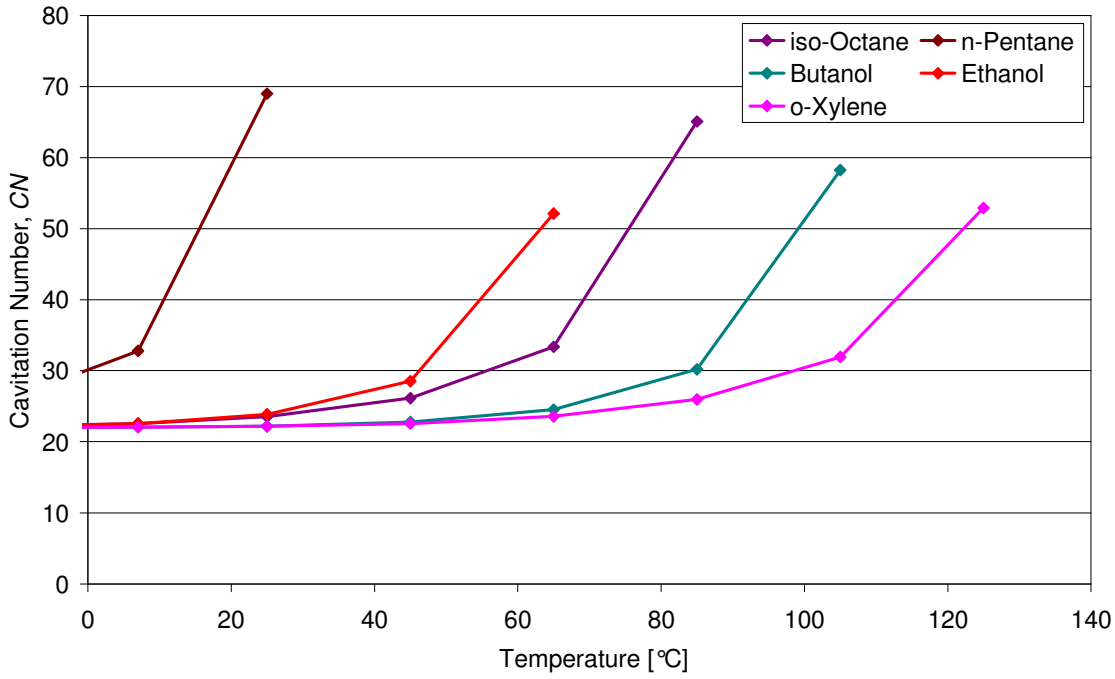

Figure 7-5 Experimental Cavitation Numbers (CN Eq.7.2), Nozzle A, 1.0 bar

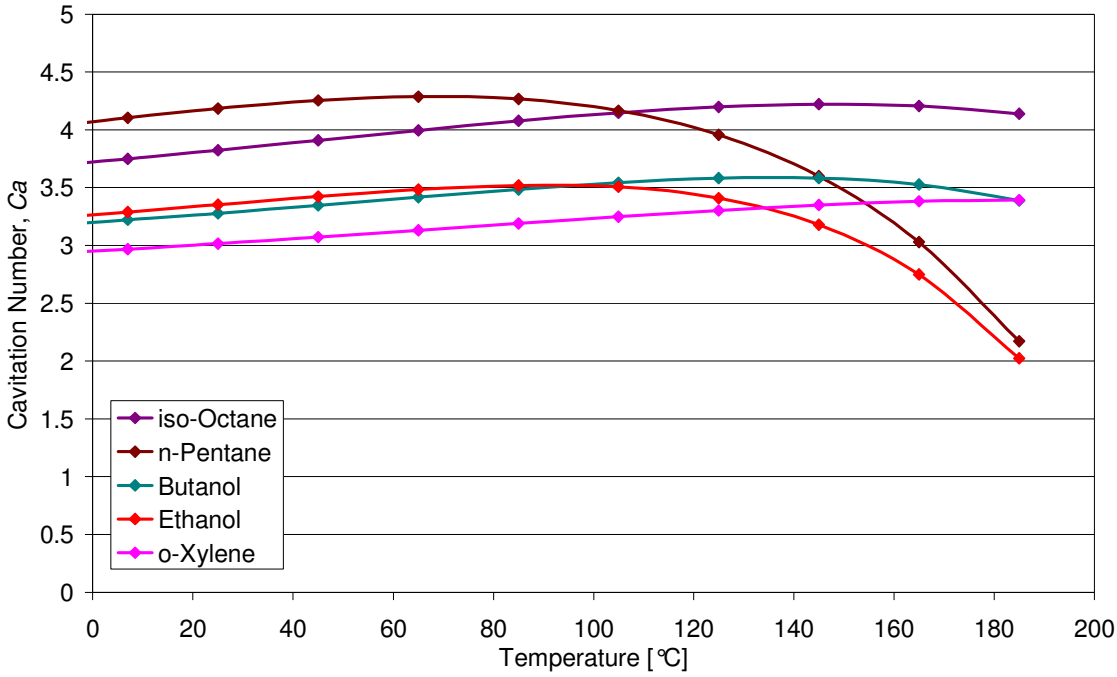

Figure 7-6 Experimental Cavitation Numbers (Ca Eq.7.1), Nozzle B

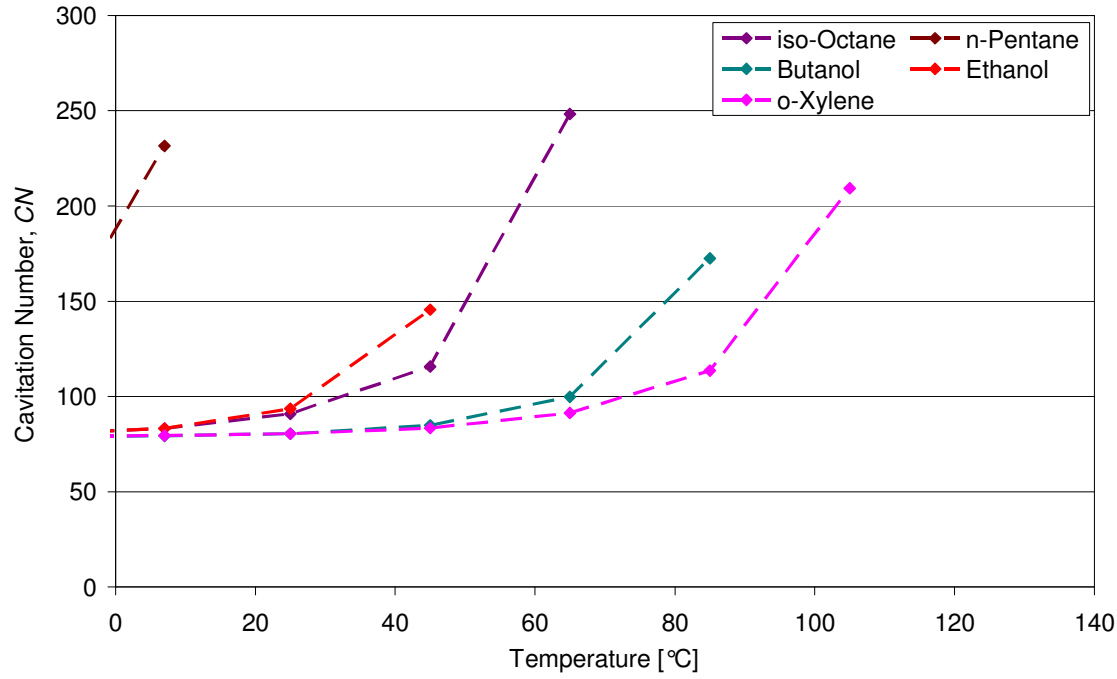

Figure 7-7 Experimental Cavitation Numbers (CN Eq.7.2), Nozzle B, 0.5 bar

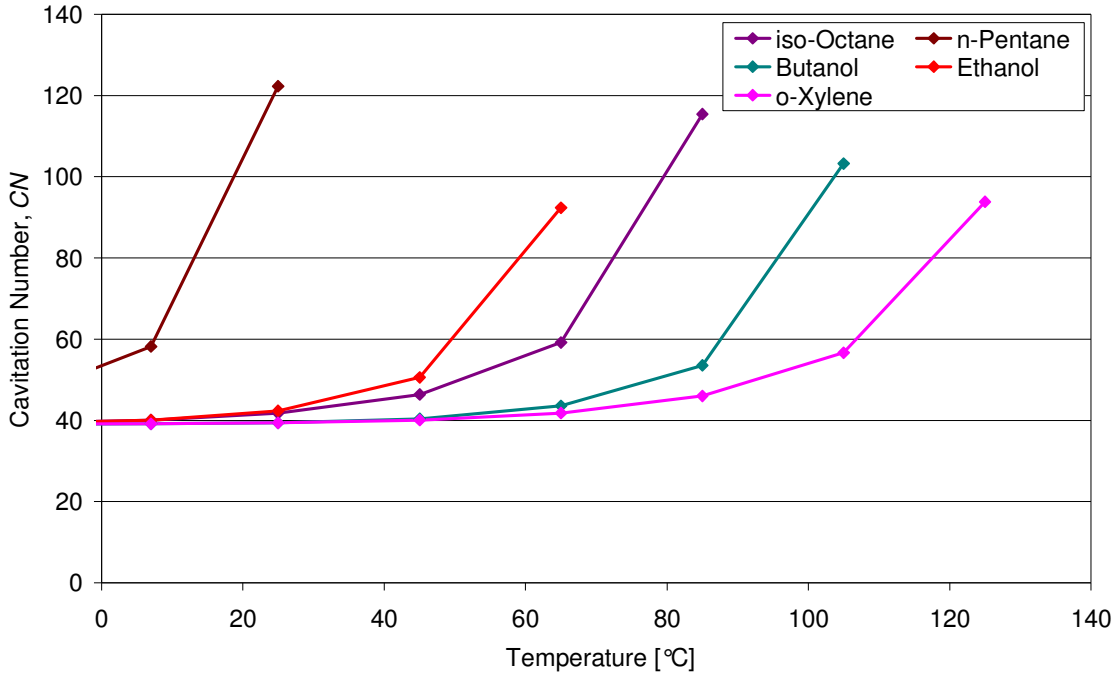

Figure 7-8 Experimental Cavitation Numbers (CN Eq.7.2), Nozzle B, 1.0 bar

Figure 7-9 to Figure 7-12 present the calculated *We* and *Oh* numbers for the single components selected and for the experimental temperature range of 20 °C (293 K) up to 120 °C (393 K) and for both nozzles. The Ohnesorge diagram is shown in Figure 7-13 for Nozzle A and in Figure 7-14 for Nozzle B for the same single component fuels, with the Reitz and Bracco [1982] defined break-up regimes superimposed. It is interesting to note that *n*-Pentane is generally in the atomisation regime when used with both nozzles but *iso*-Octane is solely in the atomisation regime with Nozzle B and crosses into the second wind induced regime when it is colder than ~70 °C (343 K) with Nozzle A. The heavy component of gasoline, *o*-Xylene, crosses into the second wind induced regime when it is colder than ~100 °C (373 K) and ~40 °C (313 K) with Nozzles A and B, respectively. The two alcohols lie mostly in the second wind induced regime and cross into the atomisation regime only when at quite high temperatures, which has potential implications for engine cold-start conditions. A similar observation can be drawn from the We_l diagrams in Figure 7-9 and Figure 7-10, where the values for Butanol and Ethanol lie well below the atomisation regime defined as $We_l > 30{,}000$ by Sallam *et al.* [2002].

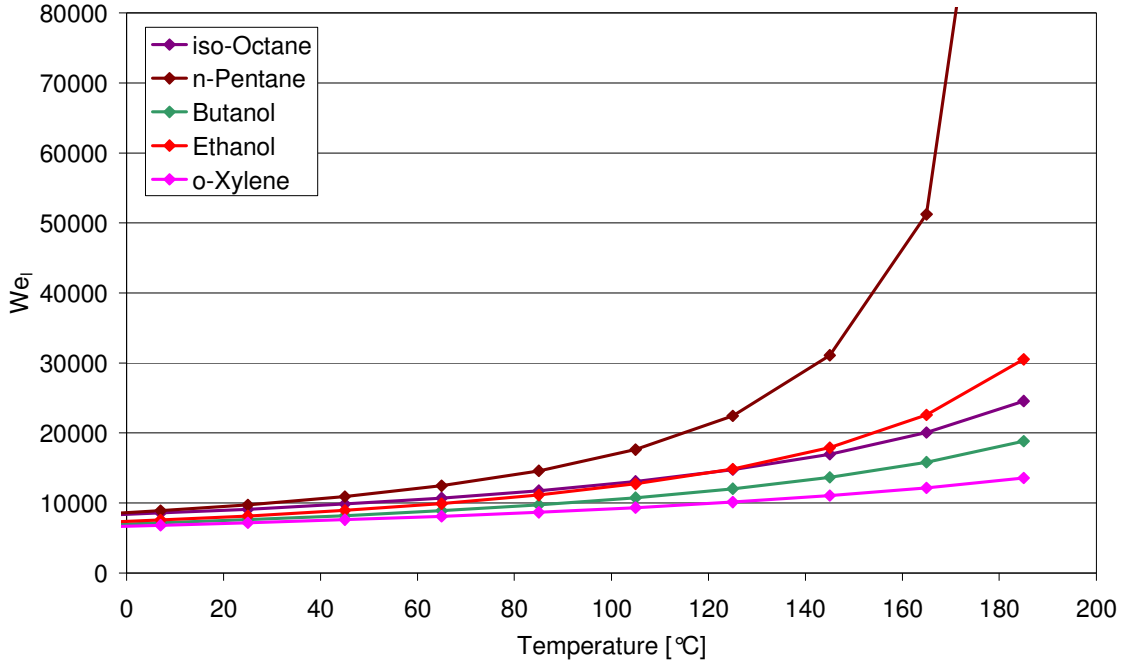

Figure 7-9 Weber Number (liquid) Nozzle A

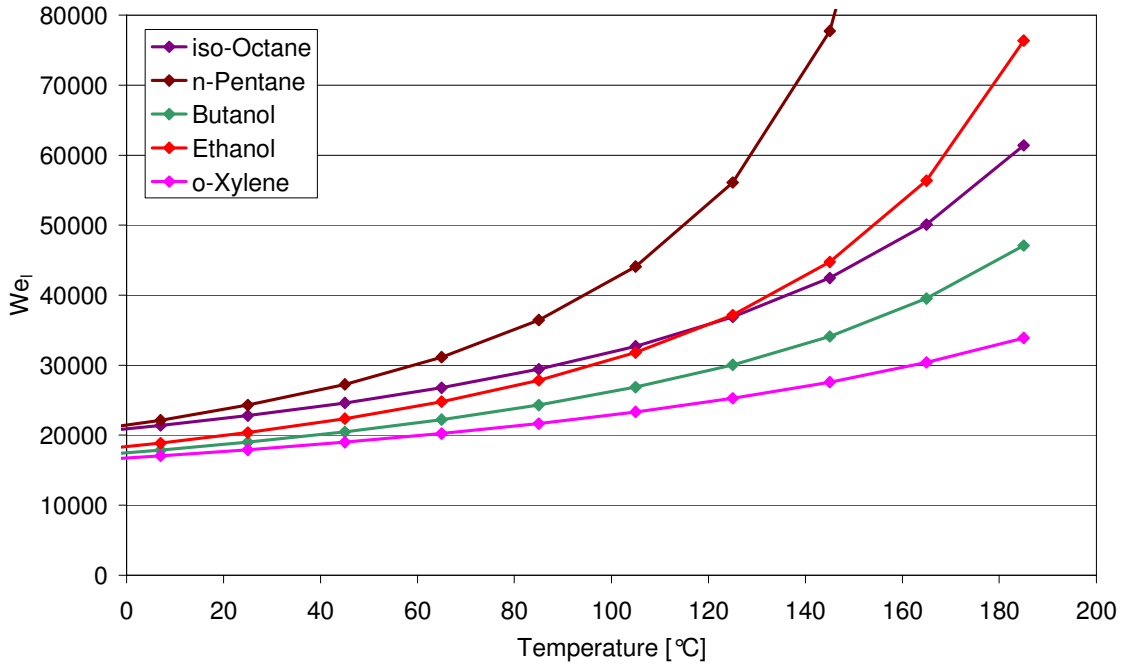

Figure 7-10 Weber Number (liquid) Nozzle B

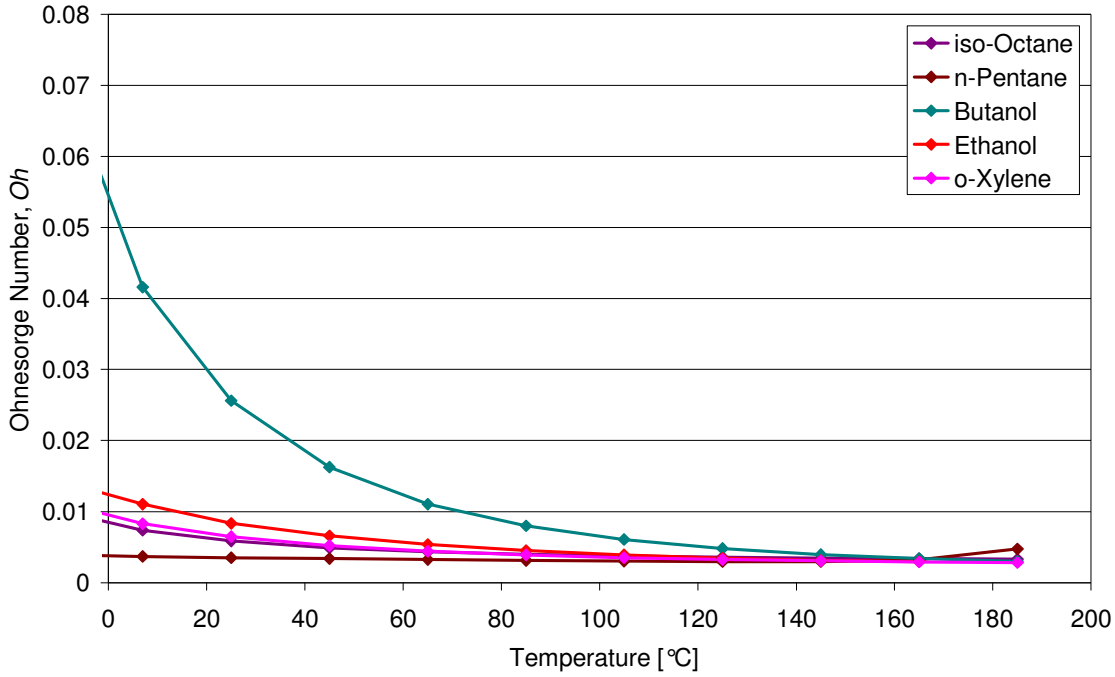

Figure 7-11 Ohnesorge Number Nozzle A

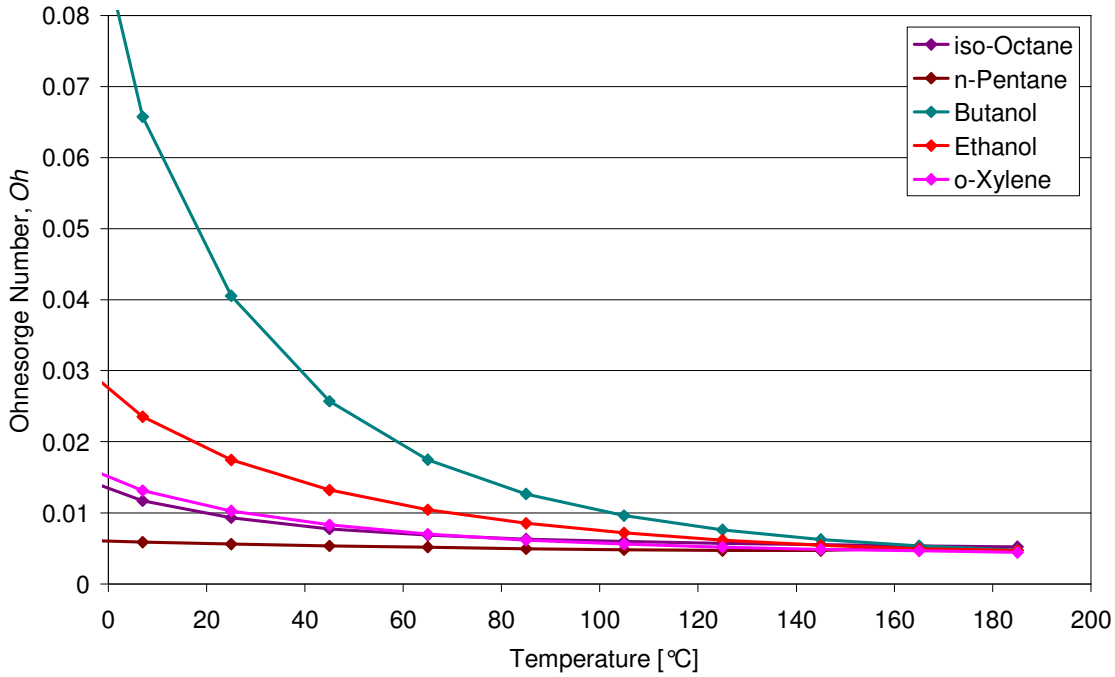

Figure 7-12 Ohnesorge Number Nozzle B

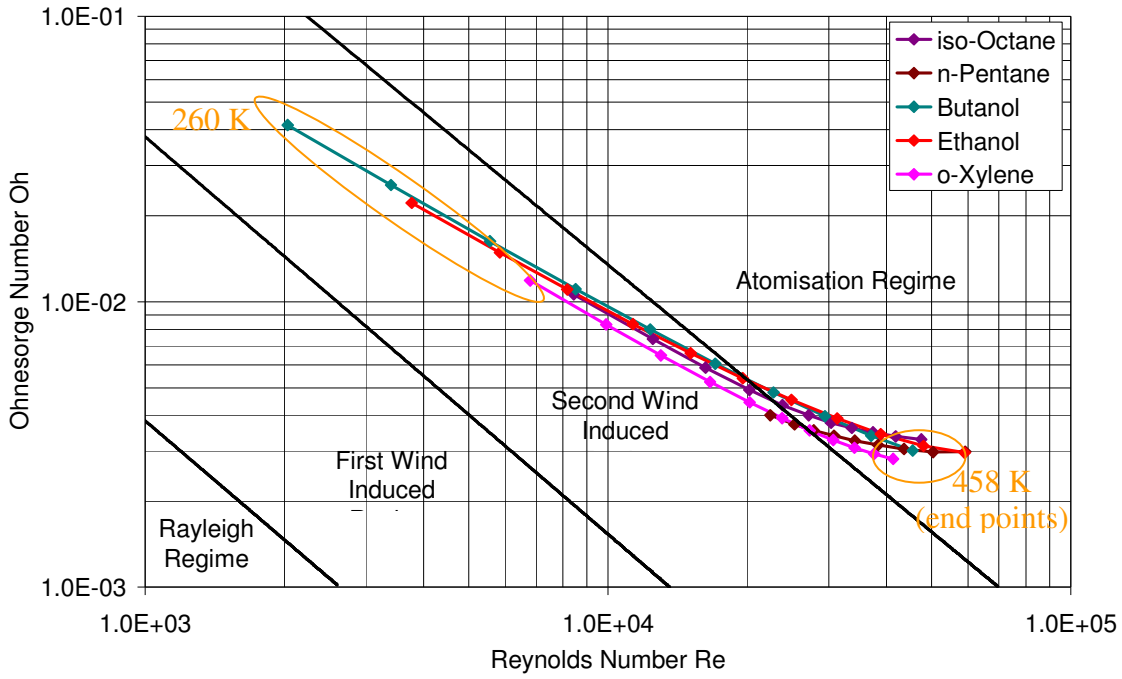

Figure 7-13 Ohnesorge Diagram Nozzle A

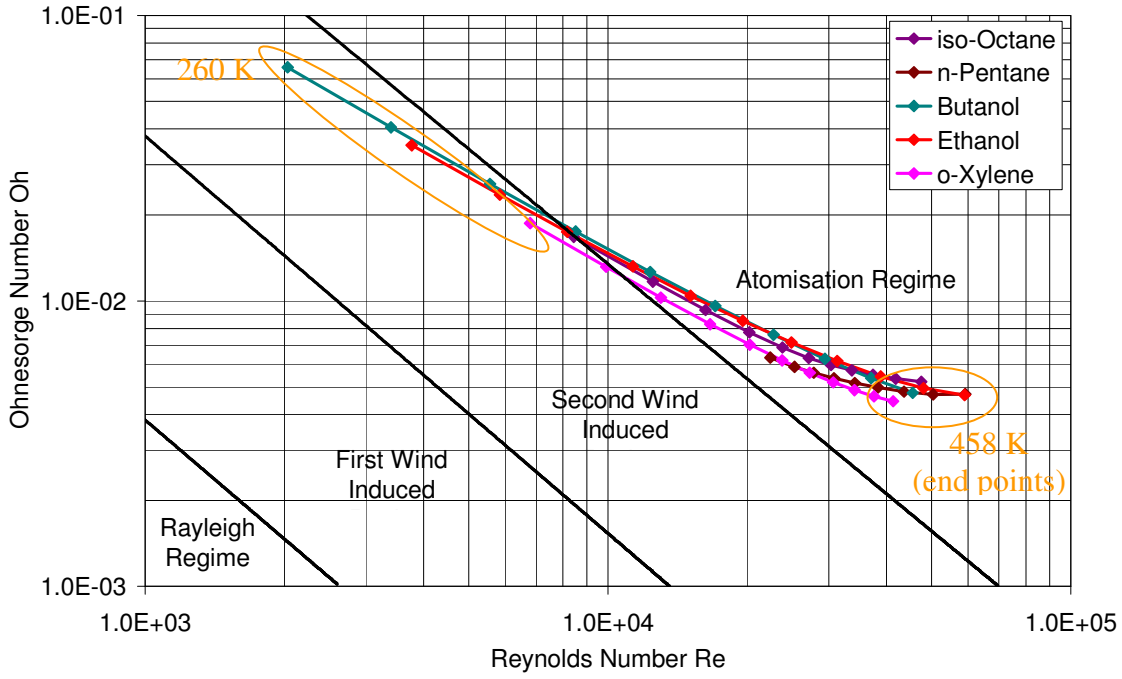

Figure 7-14 Ohnesorge Diagram Nozzle B

7.3 Imaging of Flow in Optical Nozzle

Initial experiments found that the pintle seat surface in the Perspex was too soft and was chipped away by each subsequent pintle closing event. It was therefore decided to operate the nozzle in a steady state, constantly open mode. The fuel flow was controlled

by an upstream quarter turn ball valve at the junction of the fuel line and injector mounting. Relatively short manually controlled injection periods in the order of 2-5 seconds combined with sufficient fuel availability ensured that fuel pressure was maintained by the pneumatic-hydraulic system at all times. The fuel pressure was calibrated against the air pressure supplying the pneumatic-hydraulic pump as measured by the pressure transducer mounted in the injector mounting clamp for the all-steel injector used for the majority of the imaging work. Independent control of the high-speed camera and flash trigger allowed for the capture of images. However, due to the constantly open nature of the injector, the high speed images were all very similar, capturing only the steady state flow in the optical nozzle. The delay between opening the upstream fuel flow valve and capturing the images was minimised. Due to the mounting of the thermocouple some distance upstream from the nozzle, and the steady state flow of the fuel through the nozzle, the exact fuel temperature at the time of imaging could not be known for Nozzle A. Hence the fuel conditions for the optical nozzle could only be split between "cold" (nominally 20 °C) and "hot" (nominally 120 °C). The addition of a solenoid controlled valve in the fuel flow line when using Nozzle B to control the fuel injection period allowed for a longer fuel residence time in the injector body, and hence for more precise control of the fuel temperature when using this nozzle.

Initial images of the main operating conditions of cold and hot fuels and 1.0 bar and 0.5 bar gas pressure are shown in Figure 7-15 for Nozzle A. Note that these images were captured using the bowl cut-out in the optical nozzle, and hence the spray at actual emergence from the nozzle is obscured. However, the spray form slightly downstream of the nozzle exit, as well as the flow in the nozzle channel, can be clearly seen. The similar refractive index of the optical material and the fuels, in combination with the back light illumination method, allows the observation of cavitation inside the nozzle. Specifically, there is a dark flow region along the top of the nozzle passage at all conditions, indicating cavitation initiation at the flow separation point just at the nozzle's inlet. When the nozzle hole is completely filled with liquid fuel and light rays are incident at the nozzle hole perpendicularly, the area of total reflection at the transition boundary surface from the optical material to the fuel is kept at minimum (Gilles Birth *et al.* [2005]). This was also observed in a number of "calibration" images captured for this work, where very low flow rates (valve open, but pump not activated – essentially leakage flow) were seen to produce images where the nozzle was defined by

thin black lines at the top and bottom boundaries of the hole (as per the lower boundary of the nozzle in Figure 7-15), with high light transmissivity occurring through the liquid filled nozzle. On the contrary, when cavitation occurs in the nozzle, the presence of bubbles whose surface boundaries disperse the light rays makes cavitation areas appear as dark structures.

20 °C Fuel Temperature, 1.0 bar Gas Pressure

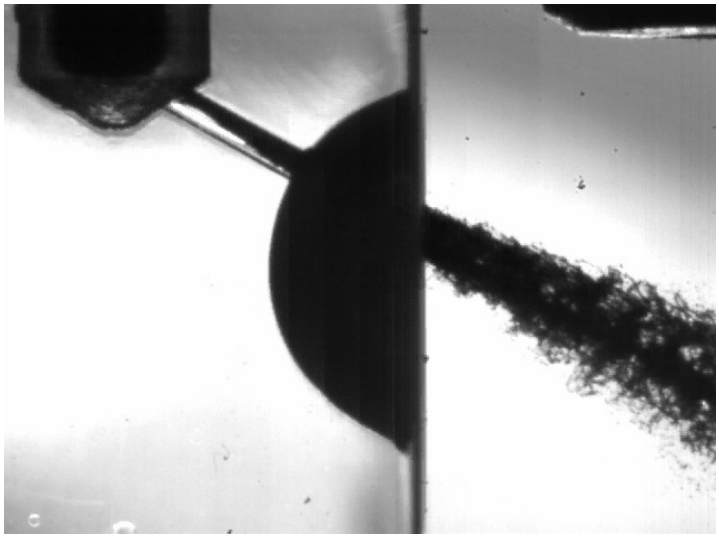

120 °C Fuel Temperature, 1.0 bar Gas Pressure

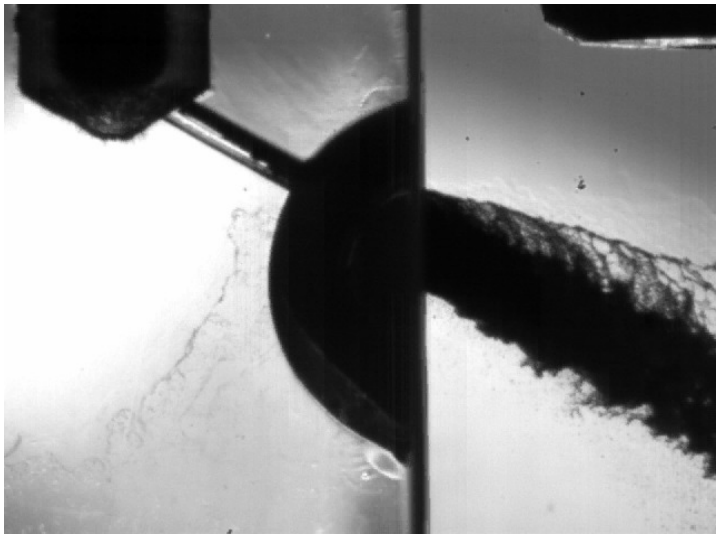

120 °C Fuel Temperature, 0.5 bar Gas Pressure

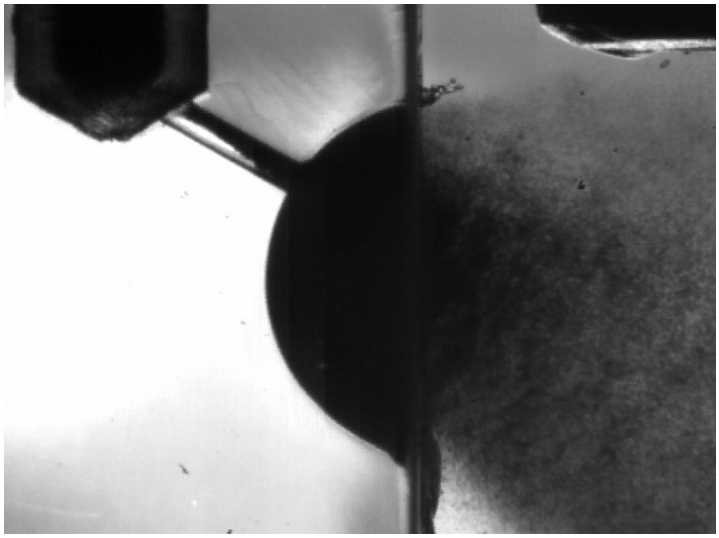

Figure 7-15 Nozzle A Fuel Flow, 30 bar Fuel Pressure, Standard Gasoline

In general, a dark area is seen along the top of the nozzle passage, suggesting the presence of vapour in this area, although the similarity of the dark region along the top of the channel suggests that some obscuration of the light due to the presence of the channel, or due to machining roughness, might be occurring in this region. The presence of a dark region at the bottom of the channel at the nozzle exit, where the channel meets the bowl, appears to occur with increased fuel temperature. This effect is augmented when the gas pressure is further reduced to 0.5 bar. At 1.0 bar gas pressure with hot fuel, the dark region at the bottom of the channel is larger around the nozzle exit than at 20 °C, and the spray form is similar to that seen at the cold fuel condition. However, the spray appears to be somewhat denser at the hot fuel condition, with more pronounced break-up along the top of the imaged plume. At the hot fuel, low pressure condition shown at the bottom of Figure 7-15, the dark region along the bottom of the channel clearly reaches the nozzle exit and the spray is seen to have broken up within the cut-out bowl. Although the spray produced is not dramatically affected by this temperature difference the hot spray is generally wider (larger cone angle due to plume swelling) and in particular has more pronounced break-up along the top side of the imaged plume.

The effects of collapsing cavitation bubbles outside the nozzle can contribute to downstream spray break-up and this seems to occur even at 20 °C; for hot conditions at the same gas pressure, it is likely that this collapse has an increased effect on the spray break-up as a result of different fluid properties e.g. lower surface tension, viscosity and higher vapour pressure, which all support faster bubble growth rates.

At the 120 °C fuel temperature, low gas pressure condition, the dark region along the bottom of the channel has expanded nearly a quarter to a third of the length into the nozzle and the subsequent spray is seen to be severely affected within the distance of the cut-out bowl (~2 mm). Cavitation structures, however do not appear to be that different compared to the 1.0 bar condition within the spatial resolution of the experiment. This is not altogether unsurprising since cavitation inside the nozzle will be governed mainly by liquid temperature, through its effect on the vapour pressure. Although gas backpressure also affects cavitation and is included in the definition of cavitation number, the CN at these conditions becomes somewhat meaningless since the vapour pressure is much greater than the gas pressure, resulting in negative values of CN. The relative difference between the vapour pressures at high temperatures and for a 0.5 bar change in gas pressure therefore has a small effect on the cavitation number.

The effect of low gas pressure is demonstrated strongly outside the nozzle by two mechanisms; the first is the lower resistance to vapour-bubble growth and the second is the reduction of the liquid boiling point and resultant increase in the level of superheat experienced by the fuel constituents. The result is rapid bursting of vapour bubbles within the spray upon exit causing the enhanced disintegration of the jet. This dramatically improves atomization and 'destroys' the nominal 'solid'-cone structure. The increased level of superheat also drives the rapid evaporation process of the newly formed ligaments and droplets, so that fine atomization is nearly instantaneous.

The presence of the cut-out bowl made it unclear as to how the bowl itself interfered with the spray formation process, particularly at the extreme conditions of pressure and temperature; therefore a second nozzle design iteration was used to improve the experimental arrangement, confirm these effects and allow a more detailed study of the effects of fuel properties on primary break-up. Individual images captured with the modified optical Nozzle A and developed Nozzle B are presented for the test fuels in Figure 7-16 to Figure 7-20. Since the imaging of the nozzle channel was unchanged using this new nozzle design, in general the same features discussed for the nozzle with the bowl cut-out apply for the grooved nozzle using gasoline. However, the fuels will be discussed individually first before direct comparisons are made between their primary break-up characteristics.

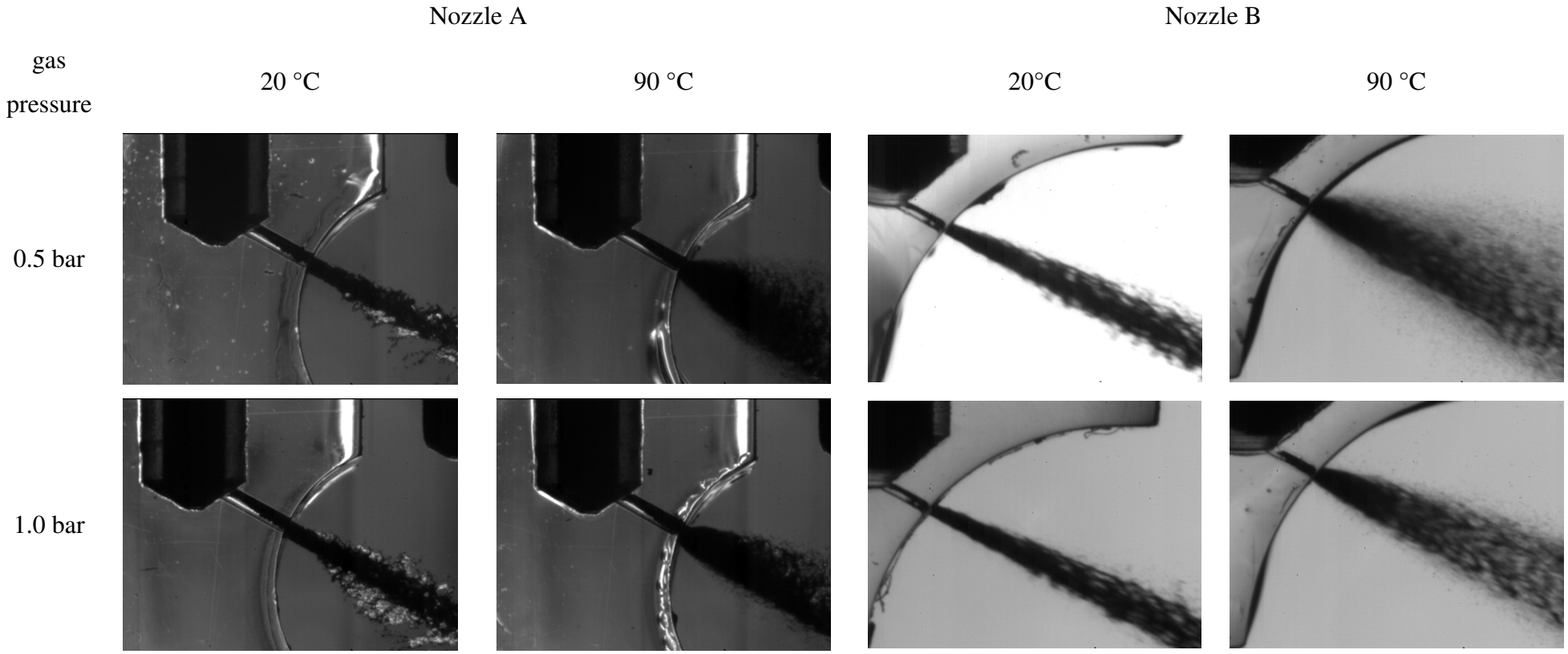

Figure 7-16 In-Nozzle Fuel Flow, Standard Gasoline

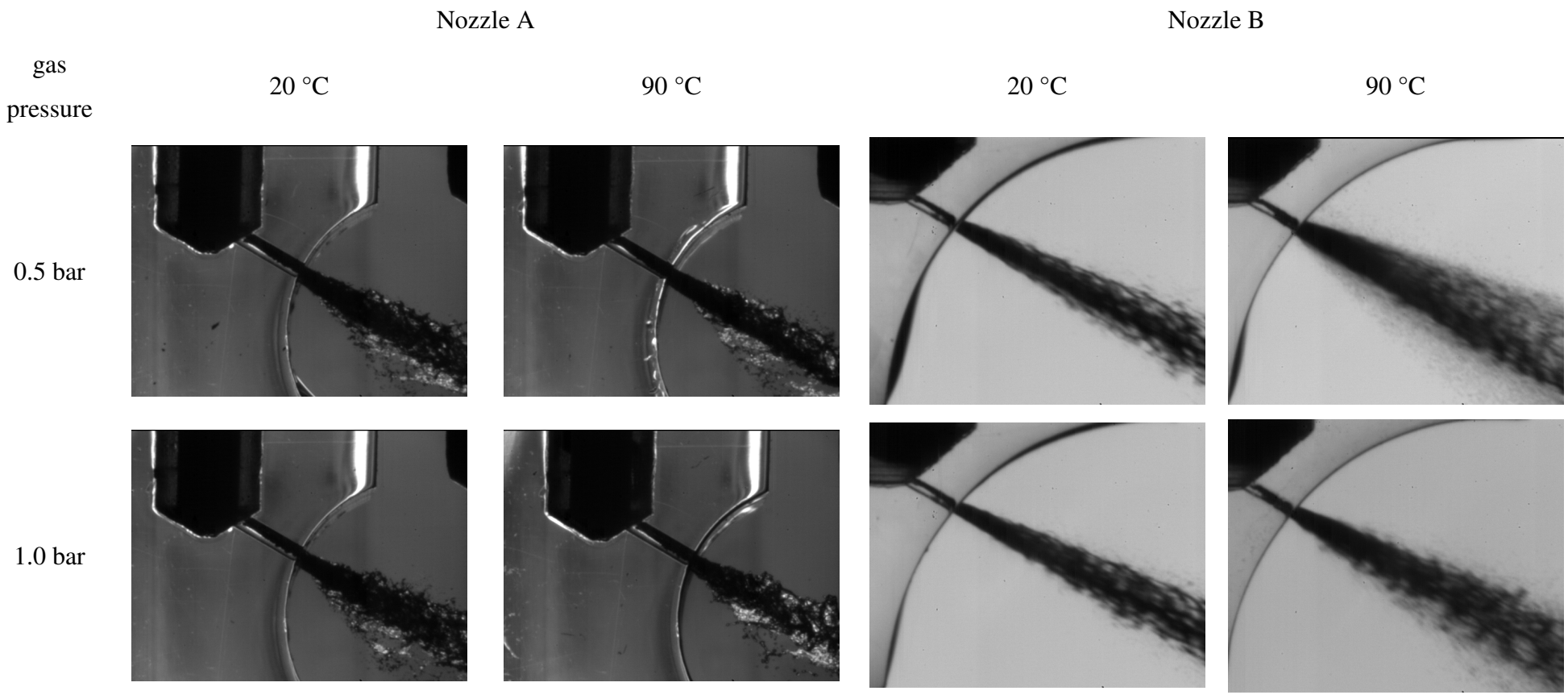

Figure 7-17 In-Nozzle Fuel Flow, *iso*-Octane

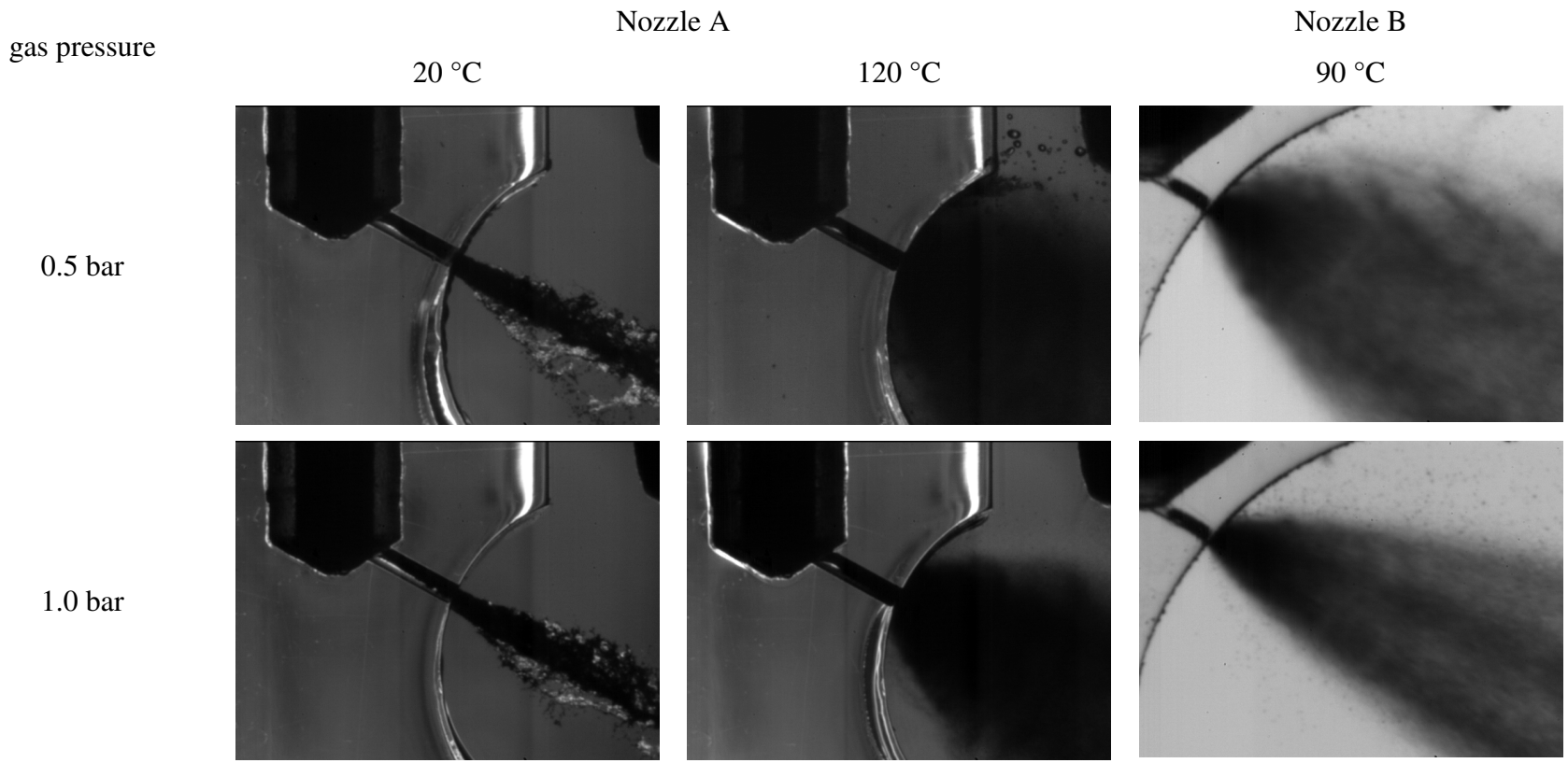

Figure 7-18 In-Nozzle Fuel Flow, *n*-Pentane

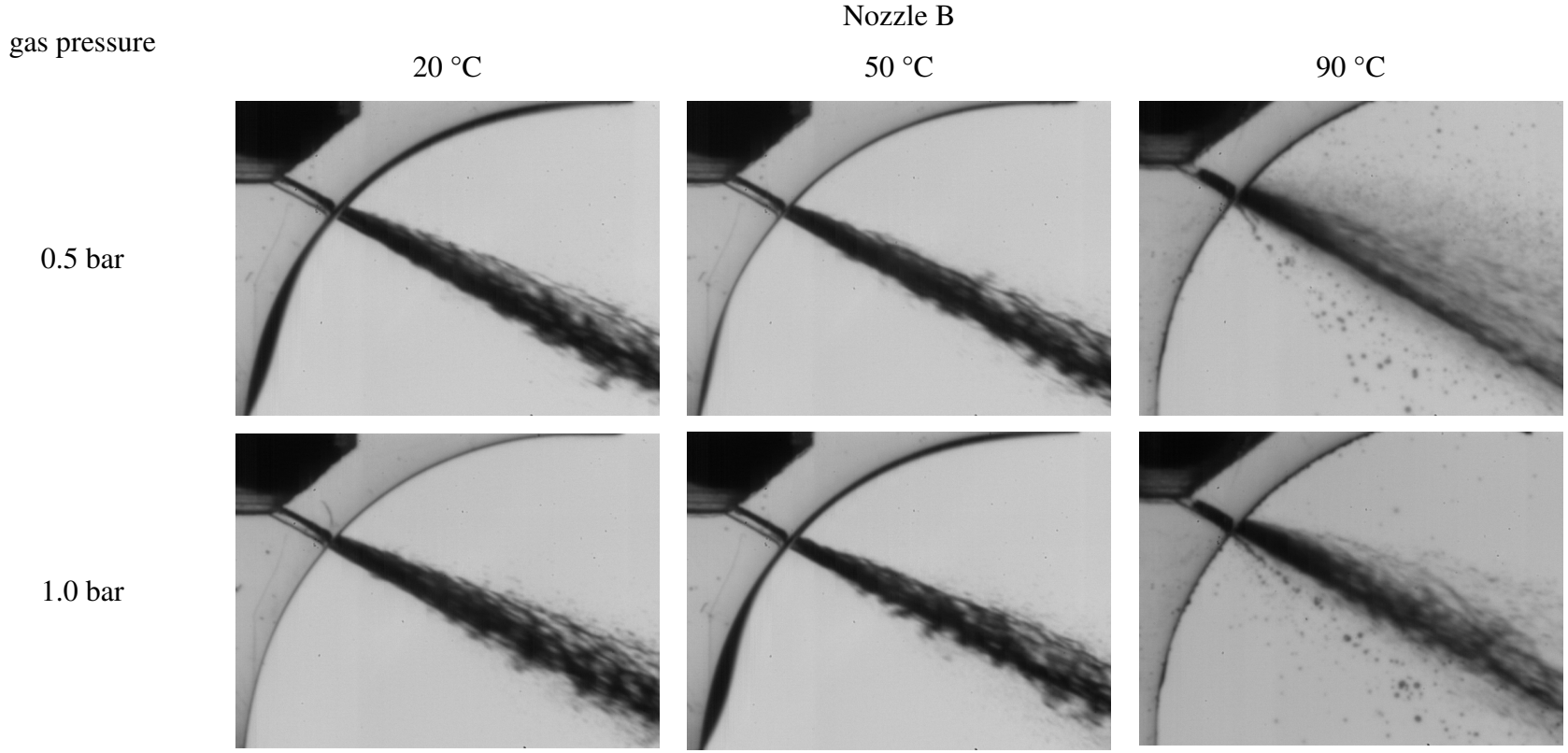

Figure 7-19 In-Nozzle Fuel Flow, Butanol

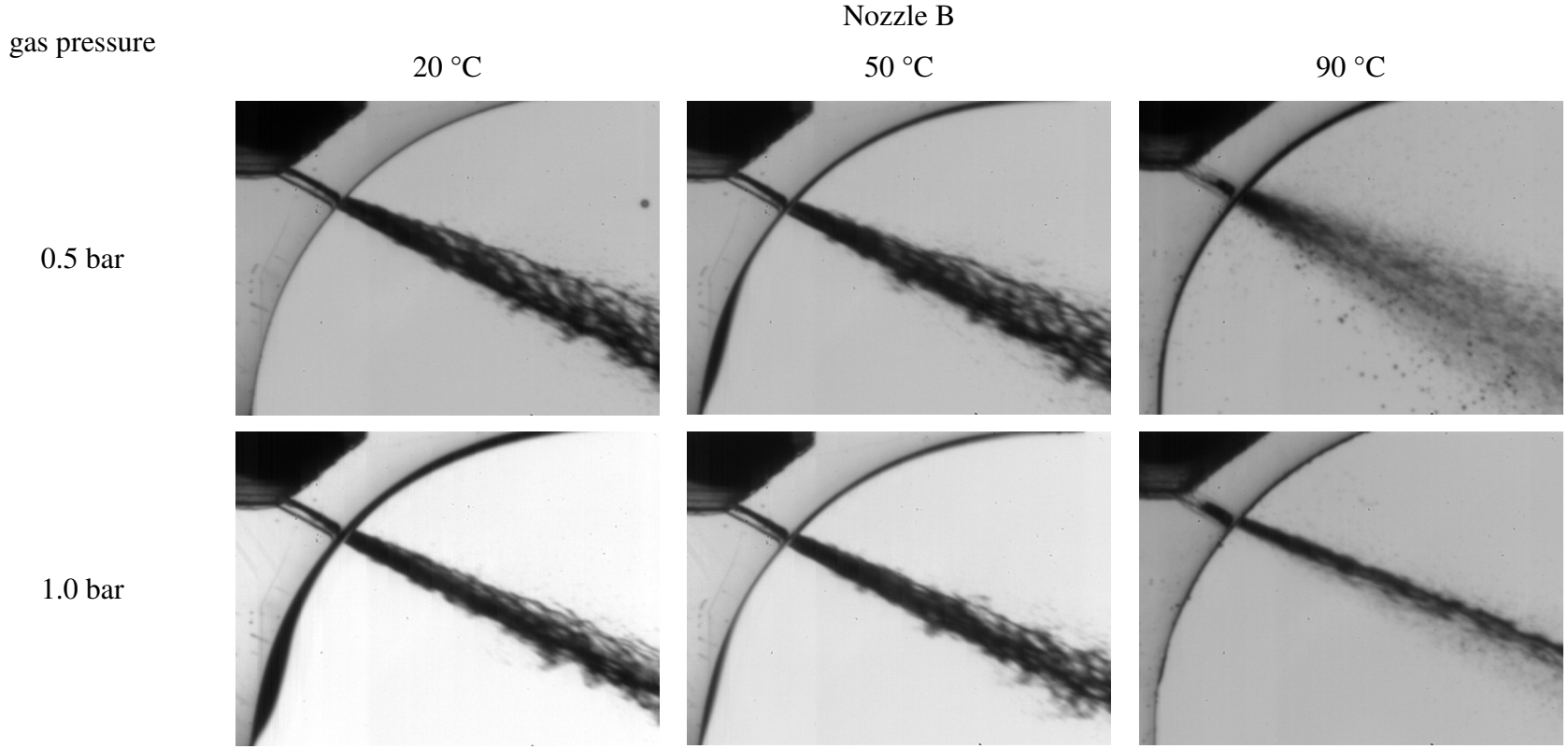

Figure 7-20 In-Nozzle Fuel Flow, Ethanol

A close analysis of the images in Figure 7-16 shows the dark cavitation region at the bottom of the nozzle passage extends upwards towards the nozzle's inlet with an increase in temperature. One common feature of all the images is the asymmetric nature of the spray with the cone angle being greater at the top side of the spray plume on the nozzle side where cavitation occurs; the spray clearly experiences stronger break-up at the top, as also observed by Gilles-Birth *et al*. [2005, 2006], Ganippa *et al*. [2001] and Hyun and Chang [2008]. Collapsing cavitation bubbles outside injector nozzles is known to contribute to spray break-up and this seems to occur even at 20 °C. For hot conditions at the same gas pressure, it is likely that this collapse has an increased effect on the spray break-up as a result of different fluid properties *e.g.* lower surface tension, viscosity and higher vapour pressure, which all support faster bubble growth rates. The lighter spray for hot conditions probably also indicates a higher concentration of vapour within the liquid fuel and/or higher concentration of fine droplets within the spray, as cavitation bubbles expand and burst rather than collapse, thus the 'swelling' seen in the primary break-up. These observations are compatible with similar plume swelling observed in the global imaging of the spray from the real multi-hole injector.

From the images of Standard Gasoline in Figure 7-16 it can be seen that at 20 °C the effect of a gas pressure reduction from 1.0 bar to 0.5 bar is relatively small. Although the Standard Gasoline spray is slightly wider at 0.5 bar gas pressure, the levels of cavitation inside the nozzle are comparable. It can also be observed that the in-nozzle cavitation pattern is different between the two nozzles at 20 °C fuel temperature. The cavitation film in Nozzle A with d = 0.5 mm never reaches the bottom of the nozzle passage even when gas pressure is reduced from 1.0 bar to 0.5 bar. This does not happen to be the case for Nozzle B with d = 0.2 mm. Here cavitation stretches down to the bottom of the nozzle passage at the outlet and extends to about a third of the nozzle length upstream of the outlet. However, both nozzles showed no significant change in cavitation structure when gas pressure was reduced from 1.0 bar to 0.5 bar. At 90 °C fuel temperature and 1.0 bar gas pressure there is a slight increase in cavitation in Nozzle A, accompanied by an asymmetric increase in the spray cone angle. The cavitation in Nozzle B has expanded significantly upstream of the nozzle's exit and occupies half to three quarters of the nozzle-hole passage, with a simultaneous increase in spray atomisation. The different cavitation patterns in the two nozzles are justified by the different cavitation numbers in Figure 7-3 to Figure 7-8. At 0.5 bar gas pressure and 90 °C fuel temperature, the spray cone angle is far greater than any of the other

conditions and the fuel begins to atomise immediately outside the nozzle. The spray is still asymmetric with the top half angle of the spray plume larger than the bottom one (*i.e.* on the side of the nozzle where cavitation is present). The difference in spray cone angle between the top and bottom of the nozzle holes could not be readily discerned in the macro spray imaging due to the overlap of the pairs of spray plumes from the side view (or trio of plumes from the end view). The increased levels of flash-boiling at low gas pressures are also seen to reduce the dense dark area significantly and in fact within only 4–7 nozzle diameters the dark spray 'core' is no longer 'intact' and the backlight is clearly visible through the atomised spray. This is in clear contrast to the 1.0 bar gas condition which even at 90 °C shows a much narrower spray exiting the nozzle. A further interesting observation is that at 90 °C, Standard Gasoline's in-nozzle cavitation at 1.0 bar gas pressure has extended upstream more than it has at 0.5 bar, particularly with Nozzle B. As will be shown later the same observation was made for all fuels at hot conditions, therefore, this is believed to be a real effect of the coupling between flash boiling and cavitation and the exact mechanism behind it required further study with higher magnification.

In Figure 7-17 *iso*-Octane appears less sensitive to operating conditions when compared to Standard Gasoline in Figure 7-16. At 20 °C there is no major difference in the spray produced or in the mechanisms of primary break-up; the locations and levels of cavitation are also broadly similar. However, upon close inspection, it is clear that the cavitation 'film' in Nozzle A rarely reached the bottom wall of the hole, in contrast to Standard Gasoline's behaviour in the same nozzle where even at 20 °C the cavitation film develops at the entrance of the nozzle hole and extends to the bottom part of the passage, filling the hole fully at the nozzle exit plane. Cavitation in Nozzle B appears as a thinner film adjacent to the top wall of the nozzle-hole passage for both *iso*-Octane and Standard Gasoline; in the case of Nozzle A cavitation is generally thicker from the inlet and increases more gradually as it expands downstream towards the nozzle's exit.

Reducing the gas pressure to 0.5 bar and maintaining the fuel temperature at 20 °C has no significant effect for *iso*-Octane and only a very small effect on the cone angle for Standard Gasoline. A rise in *iso*-Octane's temperature to 50 °C showed almost no macroscopic differences to 20 °C, even for 0.5 bar gas pressure. However, there were some more obvious differences when the temperature was raised further from 50 °C to 90 °C. In Figure 7-17, cavitation at 90 °C has extended upstream of the nozzle exit and

an increase in cone angle can be observed for Nozzle B, as the spray shows better atomisation. With a reduction in gas pressure at 90 °C, spray atomisation from Nozzle B is further enhanced as indicated by the lighter finer greyscales in the outer top region of the spray in the images. However, for Nozzle A, despite a change in cavitation similar to that of Nozzle B, no significant change in spray formation can be observed as the spray can be seen to break-up similarly at the top and bottom with almost no obvious increase in the cone angle at the top. A comparison between images of *iso*-Octane and Standard Gasoline gives a strong indication again that the levels of superheating of the fuel components contribute more towards the liquid jet's break-up and evaporation than the levels of cavitation in isolation, since cavitation structures are not very different between the two fuels over the full range of conditions but the sprays, particularly at 90 °C/hot fuel, are quite different indeed. Once again, it is observed that at 90 °C the dark cavitation region has extended upstream more at 1.0 bar gas pressure than at 0.5 bar.

Images of *n*-Pentane sprays through Nozzles A and B are presented in Figure 7-18. The sprays at 20 °C/cold fuel were not very different to those formed by *iso*-Octane and Standard Gasoline at the same temperature; a reduction in gas pressure showed no significant effect on the spray, apart from a slight increase in the cone angle, as also observed for Standard Gasoline. This similarity between *n*-Pentane and *iso*-Octane sprays can be explained by the similar *We* number of these two fuels at 20 °C. The vapour pressure graph (Figure 2-34) indicated at first that the level of cavitation would be higher for *n*-Pentane than for *iso*-Octane even at 20 °C because the vapour pressure of *n*-Pentane at this low temperature is about the same to that of *iso*-Octane at 90 °C. The similarity though is understandable, when one considers the very small effect of a raise in temperature from 20 °C to 90 °C on *iso*-Octane's cavitation. The Cavitation number *Ca* of *n*-Pentane at 20 °C is also very similar to that of *iso*-Octane at 90 °C.

By increasing the fuel temperature, similarities were observed in the atomisation of *n*-Pentane at 90 °C, 0.5 bar and Standard Gasoline at the same conditions, although interestingly, cavitation was observed to be much less with Standard Gasoline. This is further evidence that as a mechanism of atomisation enhancement, cavitation may not play as important a role compared to the levels of superheat experienced by the fuel components. At 90 °C fuel temperature and 1.0 bar gas pressure, *n*-Pentane shows excellent atomisation once again. However, the cone angle is smaller and there is some directionality in the spray. Differences in the spray formation should therefore stem

from the lower levels of superheat as a result of the higher boiling point at 1.0 bar. The viscosities do have a significant effect on the Reynolds number, which is nearly double for *n*-Pentane compared to that of *iso*-Octane along the plotted temperature range but although this will affect the levels of cavitation present, the vapour pressures will dictate the behaviour of the fuel as it exits from the nozzle. For example, an increase in fuel temperature increases the vapour pressure, requiring a smaller decrease in static pressure inside the nozzle before the onset of cavitation, i.e. increasing the degree of cavitation for a given fuel/gas pressure difference. It follows that the larger degree of superheat by a fuel's chemical components, the greater the degree of cavitation. It is also quite interesting that *n*-Pentane showed macroscopically very similar atomisation characteristics to those at 90 °C and 1.0 bar when it was heated to only 50 °C but with gas pressure reduced to 0.5 bar. In-nozzle cavitation levels at 90 °C, 1.0 bar appear comparable to those at 90 °C, 0.5 bar, but with a slightly longer extension upstream towards the nozzle's inlet, as also typically observed with Standard Gasoline and *iso*-Octane earlier.

For Butanol sprays in Figure 7-19, the in-nozzle cavitation structure does not appear very different to that with Ethanol, despite Butanol's much lower vapour pressure; however, upon closer inspection it was observed that the cavitation film that extends from the nozzle passage's inlet to the outlet appeared slightly thinner for Butanol. Another observation is that the dark cavitation region becomes greater towards the nozzle outlet but never touches the bottom of the passage, a similar behaviour to that of Ethanol. Despite Butanol's higher vapour pressure, the *Ca* of the two alcohols in Figure 7-3 is very similar at the same conditions, justifying to a degree the observed similarity in cavitation. Interestingly, Butanol's *Re* number in Figure 7-2 at 20 °C also indicates flow very close to laminar conditions. Cavitation remains approximately the same when pressure is reduced to 0.5 bar at 20 °C and 50 °C in Figure 7-19. No significant differences in the break-up mechanism can be observed in all four conditions, though at 20 °C, the spray break-up at the top of the spray occurs earlier at sub-atmospheric pressure. In comparison to Ethanol, at all these four conditions, Butanol exhibits 'surface waves' with larger wavelength and a darker continuous core without as many 'holes' as Ethanol. At 90 °C Butanol undergoes an increase in spray atomisation but large ligaments and fuel blobs can be observed around the main spray. This may have been the result of some corrosive deformation of the nozzle with the use of Butanol, and results cannot be confirmed as a typical representation of the fuel ability to cavitate and

atomise at this temperature. Nevertheless, these have been included here for completeness and for relative comparison to Ethanol's behaviour at the same temperature. The large fuel droplets that are showing up on the periphery of the Butanol spray images are most probably a result of Butanol's viscosity and surface tension (low *Re* and *We*) that restricts atomisation into as fine droplets as Ethanol does at the same conditions (higher *Re* and *We*). Specifically, Butanol's *Re* and *We* at 90 °C is similar to that of Ethanol at 50 °C, with a respective similarity also at 50 °C and 20 °C. The trend of a longer cavitation core at 90 °C with gas pressure of 1.0 bar than with 0.5 bar is again apparent as with all the other fuels discussed earlier.

Images obtained from the investigation of Ethanol using Nozzle B are shown in Figure 7-20. In-nozzle cavitation appears similar at most conditions investigated, apart from at 90 °C. Cavitation starts from the nozzle inlet and stretches all through to the nozzle outlet covering the top passage of the nozzle. Although the flow area covered by the dark cavitation region appears larger just close to the nozzle outlet, closer inspection shows that it never really touched the bottom side of the nozzle-hole passage for most conditions. In fact, the cavitation film appeared thinner than that observed with *iso*-Octane at the same conditions. However, the spray break-up mechanisms appear slightly different over the studied range of conditions. At cold fuel temperature and atmospheric pressure, the spray appears asymmetric and breaks up more at the top, on the side where cavitation occurs in the nozzle. When gas pressure is reduced to 0.5 bar, while maintaining the fuel temperature at 20 °C, Ethanol produces a slightly better atomised spray with more obvious ligaments on the side 'surface' of the spray, and an increase in cone angle, as can be justified by the thinner dark core in the spray when compared to the 1.0 bar gas pressure. No significant changes can be observed in both the in-nozzle cavitation and the spray break-up mechanism when Ethanol is heated from 20 °C to 50 °C at atmospheric pressure. The increase in fuel temperature at sub-atmospheric pressure brings about some increase to the atomisation, with just a lighter appearance of the dark core. At 50 °C, the in-nozzle cavitation also appears slightly different between atmospheric and sub-atmospheric pressure. With 0.5 bar gas pressure, the dark cavitation region in the nozzle appears to be touching the bottom of the nozzle passage; this does not seem to be the case for 1.0 bar gas pressure.

At high temperatures, Ethanol was found to react with the optical material of the nozzle resulting in some form of erosion to the nozzle-hole passage. Therefore, although at 90

°C cavitation occurs strongly inside the nozzle, it is difficult to give an informed description of its nature since the nozzle appears deformed at this condition, which in combination with Ethanol's lower refractive index at this temperature, lowers confidence in drawing solid conclusions. Nevertheless, the cavitation pattern is clearly longer at 1.0 bar than at 0.5 bar, as also observed at hot conditions with the other fuels too. Additionally, it is clear that fuel atomisation increases strongly when the gas pressure is reduced to 0.5 bar at 90 °C fuel temperature, as justified by the thin dark core and the wider cone angle of the spray. The case of 1.0 bar highlights further some of the complexities involved. Ethanol seems to behave quite differently at 1.0 bar when compared to the 0.5 bar gas pressure case, as well as to the trends observed with the other fuels. While the other fuels experienced an increase in cone angle with temperature increase and pressure reduction, ethanol at 1.0 bar gas pressure underwent a gradual reduction in the dark region of its relatively compact spray. Whether this is related to the reaction between ethanol and the optical nozzle, or it is a true effect potentially due to supercavitation, remains unclear and would require further study with a higher magnification lens and/or a nozzle of different optical material.

7.4 General Conclusions With Respect to Cavitation

Cavitation was observed at all conditions and with both nozzles as a film on the top surface of the nozzles, indicating cavitation initiation at the flow separation point just at the nozzle's inlet. In general, cavitation in Nozzle B appeared as a thinner film adjacent to the top wall of the nozzle-hole passage with an abrupt change in width close to the nozzle's outlet. In the case of Nozzle A cavitation was generally thicker from the inlet and increased in width more gradually as it expanded downstream towards the nozzle's exit. The cavitation region became thicker and extended upwards towards the nozzle inlet with increased temperature but this did not always result in a geometric change in spray formation or faster spray break-up compared with cold conditions. The cavitation films appeared thinner with the two alcohols, particularly Butanol, in comparison to the hydrocarbons. The lowest Cavitation numbers were in the range 12–18 for Nozzle B, whilst much larger numbers were calculated for Nozzle A. The relevant Reynolds numbers in the range 20–90 °C were 4,000–40,000.

One common feature in most of the spray images was the asymmetric nature of the spray with a greater cone angle at the top side of the spray plume, *i.e.* on the nozzle side where cavitation occurred. All fuels exhibited very similar cavitation patterns and

atomisation at 20 °C despite the calculated Reynolds and Cavitation numbers predicting higher levels of in-nozzle cavitation for some fuels. The sprays at 90 °C, especially at 0.5 bar pressure were wider with 'lighter' cores indicating higher concentration of vapour within the liquid fuel and/or higher concentration of fine droplets within the spray, as cavitation bubbles expand and burst rather than collapse, thus the 'swelling' seen in the primary break-up. For Standard Gasoline an increase in fuel temperature increased the levels of in-nozzle cavitation and resulted in an asymmetric spray at both 0.5 bar and 1.0 bar gas pressures with the higher spray angle on the same side as cavitation in the nozzle. Spray break-up and atomisation efficiency were clearly improved. At 90 °C it was observed that all fuels exhibited longer in-nozzle cavitation patterns at 1.0 bar gas pressure than at 0.5 gas pressure. This was not accompanied with enhanced atomisation and requires further study.

7.4.1 Effect of Fuel Properties

For pure substances with known properties, the static pressure relative to the vapour pressure within the nozzle hole will define the inception of cavitation. However for multi-component fuels, the combination of different chemical components and vapour pressures requires the 'bubble point' pressure to be used to indicate the inception of cavitation of the lowest boiling point components of the fuel. Bubble points calculated for this work and tabulated in Table 2-3 show that at 20 °C gasoline has a typical bubble pressure of ~0.3 bar. This is much larger compared to Ethanol's or *iso*-Octane's vapour pressure of ~0.1 bar at the same temperature. At 90 °C the percentage difference between Standard Gasoline's bubble point and Ethanol's vapour pressure is lower than at 20 °C, namely 2.4 bar bubble pressure for Standard Gasoline and 2.0 bar vapour pressure for Ethanol, whilst *iso*-Octane's vapour pressure is 0.8 bar. These trends are reflected in the observed spray images where the sprays produced by Ethanol are similar to those using Standard Gasoline at high injector body (fuel) temperatures but closer mimic those of *iso*-Octane at low injector body temperatures.

At high fuel temperatures, although the higher vapour pressures generally resulted in more cavitation inside the nozzle hole, it is the level of superheat, *i.e.* the extent to which the liquid temperature is above its boiling point at that gas pressure that determines the efficiency of atomisation. Cavitation is useful however because it supplies a plentiful source of vapour bubbles which act as nucleation sites to increase the rate at which superheated components in the spray can boil off. The biggest effect of

gas pressure was in influencing the effective level of superheating experienced by the fuels through its effect on the boiling point.

The key aspect of this analysis is that all the possible drivers of in-nozzle phenomena at a set operating condition appear to be aligned to affect the spray primary break-up in a similar manner, *i.e.* there are no competing effects amongst the main fluid properties, such that any one of them can be used to indicate the expected trends between sprays of two different fuels. This may be explained by considering each fuel property in turn: a) the fuel viscosity act to dampen turbulent eddies in the flow inside the nozzle established due to the fuel's vapour pressure relative to the local static pressure, b) the effects of viscosity in controlling the detachment of the boundary layer at the sharp inlet to the nozzle hole, a prime location for cavitation initiation, c) the fuel vapour pressure as the principal parameter governing the onset and intensity of cavitation and d) the effect of the fuel surface tension in governing the rate of bubble growth both inside the nozzle and upon injection of the liquid. As such the surface tension may be deemed to be the controlling factor in the energy balance between the kinetic energy of the smallest turbulent eddies in the gas outside the nozzle and the required surface energy necessary to produce droplets (as a result of Rayleigh break-up) from the corresponding eddy-sized ligaments at the jet surface, according to mechanisms described in Wu *et al*. [1995].

Although the exact hierarchy of mechanisms is difficult to define because cavitation and flash-boiling remain highly coupled, it can be hypothesised that the process occurs as follows: upon release into the low gas pressure atmosphere, micro-bubbles originating from cavitation are acting as nucleation sites for the rest of the superheated components which increase the rate at which these can boil. This cascade process continues to the point where vaporisation can be nearly instantaneous. Bubble growth and the energy released from bubble rupture, which is transferred to the surrounding liquid, is therefore important in the production of new ligaments. In this respect, the surface tension is a critical parameter as it will define the surface energy necessary for bubbles to grow and break up the spray into smaller ligaments and droplets. The surface tension is generally lower and the viscosity is also lower for *n*-Pentane and *iso*-Octane in comparison to the heavy component *o*-Xylene and to both Ethanol and Butanol, as indicated by the respective *We* and *Re* numbers throughout the studied range of fuel temperature; it is only at temperatures greater than ~120 °C (393 K) that Ethanol's *We* indicates better

ability to atomise than *iso*-Octane, whilst Butanol always shows a lower ability to atomise, similar to that of gasoline's heavy component *o*-Xylene. The mechanism can be further analysed when the relationship between cavitation and vapour pressure is considered. From the vapour pressure curves in Figure 2-34, it can be observed that under most of the conditions studied, the vapour pressure of Standard Gasoline and *n*-Pentane were greater than the ambient gas pressure. Cavitation inside the nozzle is governed mainly by the fuel temperature through its effect on vapour pressure, therefore, the relative difference between the vapour pressures at high temperatures and for a 0.5 bar change in gas pressure has a small effect. The effect of low gas pressure is demonstrated strongly outside the nozzle by two mechanisms; the first is the lower resistance to vapour-bubble growth and the second is the reduction of the liquid boiling point and resultant increase in the level of superheat experienced by the fuel constituents. This dramatically improves atomisation and destroys any remaining 'solid core' structure. The increased levels of superheat also drive the rapid evaporation process of the newly formed ligaments and droplets, so that fine atomisation can be nearly instantaneous.

7.5 Summary

Calculation of cavitation numbers implied that the liquid fuel in the injector nozzle used for the current study underwent cavitation under all examined experimental conditions based on comparison to critical cavitation number values published in the literature. Even at the highest gas pressure and lowest fuel temperature conditions examined in this work a calculated CN of 2.0 was above quoted values of 0.5 to 0.75 (*e.g.* Nouri *et al.* [2007]) for the critical CN. Imaging of the fuel flow in a real size optically accessible nozzle showed the fuel flow in the nozzle to be cavitating under all tested conditions, although difficulties in obtaining appropriate light intensities at high magnifications prevented quantification of the extent of cavitating under different conditions. Where cavitation voids were imaged at the nozzle exit a more disperse spray form was also seen to exit the nozzle under both low and high fuel temperature conditions.

Analysis of Cavitation numbers and in-nozzle flow images showed that the in-nozzle flow regime of Standard Gasoline is more sensitive to changes in fuel temperature than *iso*-Octane. This directly mirrors the trends observed in the global spray images with respect to spray convergence, and illustrates the link between the in-nozzle flow regime and the external rate of spray break-up. This also further shows that the high volatility

components within a multi-component fuels are those which most greatly affect the break-up rate, as they are the most sensitive to the prevailing conditions. This has important bearings on the use of single component fuels in engine research and modelling, where these are used to represent real-world multi component fuels. For example, *iso*-Octane is commonly used as a substitute for gasoline in many engine research applications. However, this work suggests that higher volatility components such as *n*-Pentane are better substitutes for gasoline when a single-component fuel is to be used to model gasoline especially at elevated temperature conditions. This is particularly important to spray modellers who are normally faced with modelling a complete gasoline blend and have to make decisions on which single components might be more appropriate to use.

8 Gas Turbulence Effect on Spray Development

The main intention of this work was to examine those factors affecting the spray break-up and its subsequent formation. To achieve this, the spray was isolated from any external influences. However, injectors and sprays for use in engines will be required to operate in more dynamic situations when used for their intended purpose, especially with respect to the gas body into which the spray is injected. For completeness, a small number of additional experiments were carried out as an initial investigation into the effect of gas motion affecting the spray development. To investigate whether bulk turbulence is a factor affecting spray development and break-up, sprays of Standard Gasoline were injected into a gas body with well characterised turbulence. Image analysis of these sprays was carried out to give an indication of the effect of turbulence on spray turbulence and evaporation rate for different fuel temperatures and gas pressures. Finally, for completeness, the spray which has formed the basis of this work was ignited in a controlled environment to illustrate its combustibility.

8.1 Consideration of In-Cylinder Turbulence

In gasoline direct injection engine operation, the spray is not injected in isolation of the in-cylinder air flow, as it has been in the quiescent chamber results presented in this work so far. In-cylinder air flow can be broken down into two, simultaneously occurring, air motions. The first is the large scale “bulk” air flow which constitutes a mass flow of air over a certain distance. Superimposed on this bulk flow is the localised, small scale turbulent air motion resulting from the fluid dynamic forces. The nature and coupling of these air flows, as well as their variability and effect on engine performance have been the subject of a large body of research (e.g. Arcoumanis and Whitelaw [1987], Heywood [1987], Ozdor *et al.* [1994], Rimmer *et al.* [2009]).

Work by Johansson [1991], Bianco *et al.* [1991] and Pajot *et al.* [2001] has shown that the large scale bulk flow structures predominantly control the air/fuel mixing within a direct injection engine, whilst small scale turbulent structures affect the rate of charge

consumption following ignition. Bradley *et al*. [2003] showed small scale turbulent structures acting to wrinkle the flame front, increasing the flame surface area and consequently increasing its local burning velocity. Furthermore, Rimmer *et al*. [2009] linked the flame front propagation rate at the start of the combustion process to the engine load, thereby showing the desirability of in-cylinder turbulence during the compression stroke for increased engine performance. The establishment of such turbulence at time of ignition would be expected to interact with a late injection strategy spray. Additionally, whilst there is some debate as to the relevance of in-cylinder flow structures during the induction stroke on the flow structure and turbulence during the compressions stroke (see for example Jarvis *et al*. [2006]), the presence of turbulent structures in the early stages of the induction stroke could also be expected to affect the break-up of an early injection spray.

However, the precise nature of the interaction between the bulk and local air motion and spray development are presently not well understood, with existing results and derived relationships largely based on the injection of diesel fuel into turbulent air bodies. A suitable investigation and analysis of these interactions is beyond the scope of this work. However, in order to guide the direction for potential further work in this area, some preliminary tests were carried out at Leeds University whereby the spray used throughout this work was injected into gaseous bodies of varying turbulence intensity.

8.2 Leeds Combustion Chamber

A number of additional experiments regarding spray evaporation, the effect of turbulence on spray development and spray combustion were carried out in a purpose designed high-pressure combustion chamber ("bomb") at Leeds University. This chamber consists of a spherical stainless steel pressure vessel as shown in Figure 8-1, with an internal diameter of 380 mm and orthogonal windows on the horizontal plane for spray and combustion imaging. The chamber has been designed to withstand peak pressures up to 100 bar and as such is suitable for the combustion of fuels. Four fans internal to the chamber on a tetrahedral layout generate isotropic turbulence with near zero mean (bulk flow) velocities in the central volume of the vessel. Each fan is independently driven by an 8 kW variable speed induction motor. The internal flow characteristics of the bomb have been fully characterised by Nwagwe *et al.* [2000] who found that the turbulence intensity is a linear function of the fan speed and that the integral length scales, measured using two LDA probes to measure the distance between

turbulent eddies, are 25 mm at low turbulence levels (u' < 1m/s) and 20 mm at all greater turbulence levels. The bomb has previously been used for many experiments published in a large volume of literature, which also contain further descriptions of the bomb and its operation, for example Bradley [1998], Lawes [2002], Verhelst [2004] and Jakubik [2006].

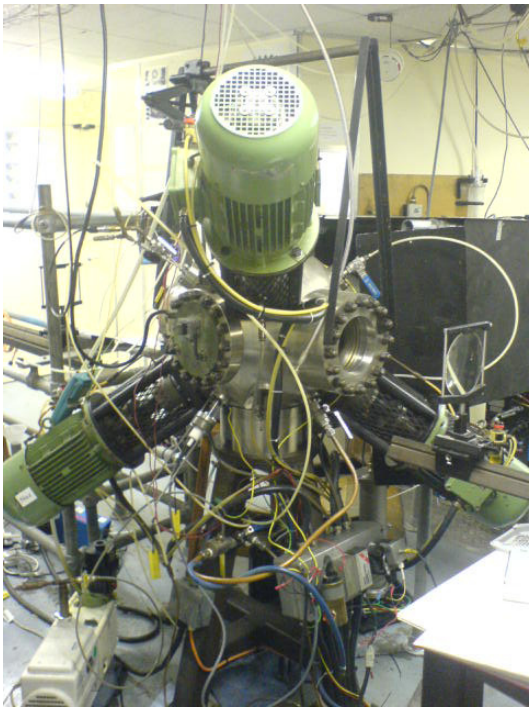

Figure 8-1 Photograph of Leeds University Combustion Bomb

One clear difference between the in-cylinder and Leeds chamber results is associated with the dimensional scaling of the turbulent eddies. Rimmer *et al.* [2009] report small scale vortices of the order 2 – 3 mm in diameter in the engine for which the injector used throughout this work was originally designed. By contrast, the integral length scale in the Leeds chamber is reported to be 20 mm (Jakubik *et al.* [2006]). Hence in the engine the length scale is approximately an order of magnitude less than in the Leeds chamber, and is more scaled to the physical dimensions of the spray and the facets of its break-up. An assessment of the Stokes Number in relation to the spray in the Leeds chamber shows that whilst an increased level of turbulence would be expected to lead to a reduction in vaporisation, the large scale turbulent eddies actually work to carry fuel vapour away from the spray. Hence the vaporisation rate is actually found to increase with an increase in turbulence intensity. At the smaller turbulence scales in an engine the small eddies would be expected to act to cluster the droplets around the spray

boundary, increasing the local vapour fraction and hence decreasing the rate of further evaporation/vaporisation. However, the purpose built turbulence and combustion chamber at Leeds University enabled control over the turbulence intensity whilst maintaining the same parameters as for the quiescent pressure chamber experiments. This facility also offers several other advantages over investigating the effect of turbulence in a running engine, including independent control of turbulence intensity and in-cylinder conditions, increased optical access and lack of bulk air flow to allow for a thorough investigation of the effect of turbulence.

Fuel injection into a turbulent gas field was carried out at conditions representative of both early injection, homogeneous charge conditions (0.5 bar gas pressure) and late injection, stratified charge injection (5.0 bar gas pressure). The in-chamber gas and injector body (and hence fuel) temperatures were maintained at 120 °C for comparison to the spray collapse condition, to encourage vaporisation and hence illustrate the effect of turbulence, and to represent the in-cylinder and injector nozzle temperatures in a running engine, particularly for late injection strategies. It should be noted that in a running engine the gas temperature during the compression stroke will be considerably higher (approx 160 - 200 °C) at time of late, compression stroke, injection but hardware limitation prevented these conditions being achieved in the Leeds chamber. All experiments in the Leeds combustion chamber for this work were carried out using Standard Gasoline.

8.3 Spray Development in Turbulent Gas Body

Turbulence intensities were set at nominal values of 2 m/s and 4 m/s average vector velocity (u') based on well calibrated fan speed correlated to in-chamber RMS turbulent velocity and turbulent eddy length scale. Typical, mean and RMS spray images for each condition are shown at 0.5 and 5.0 bar in Figure 8-2 and Figure 8-3 respectively using the Schlieren imaging technique, which shows both the liquid and vapour phases of the fuel. The mean and RMS images were calculated from the 20 images recorded at each condition during the experiment.

Time ASOI [µs]	Image	u’ = 0	u’ = 2	u’ = 4
475	Typical		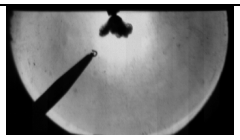	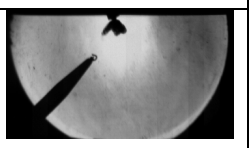
	Mean	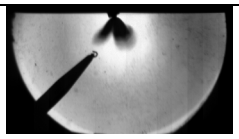	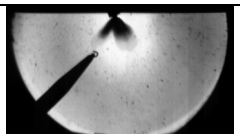	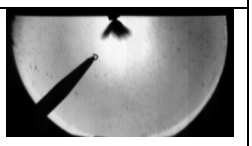
	RMS	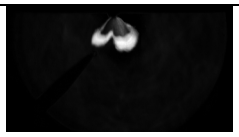	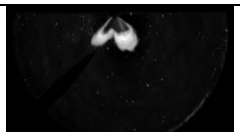	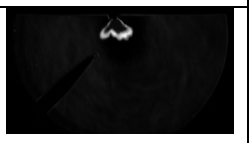
725	Typical	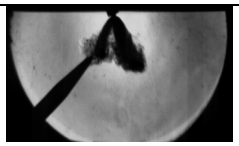	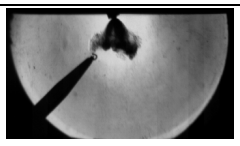	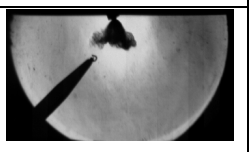
	Mean	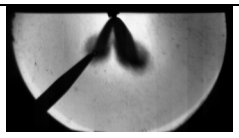	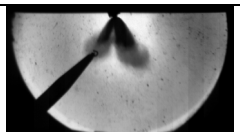	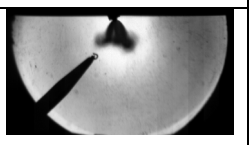
	RMS	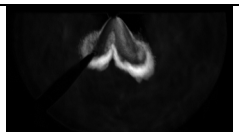	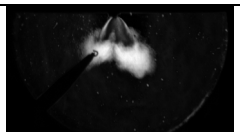	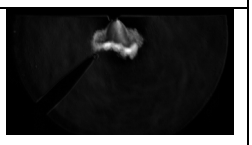
975	Typical	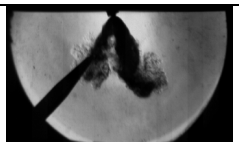	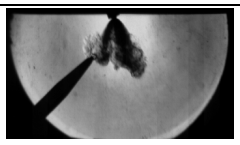	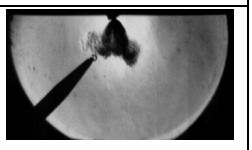
	Mean	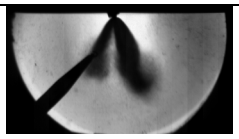	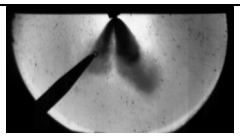	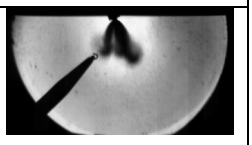
	RMS	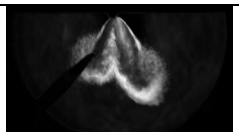	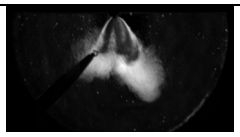	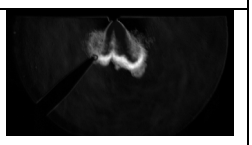

Figure 8-2 Effect of turbulence on spray – 0.5 bar

Time ASOI [µs]	Image	U' = 0	U' = 2	U' = 4
475	Typical	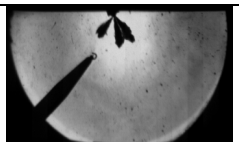	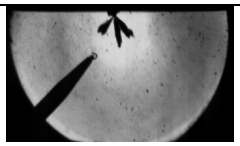	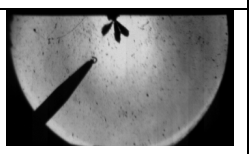
	Mean	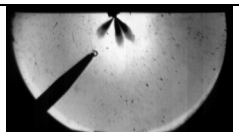	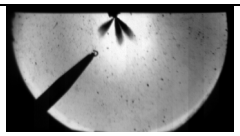	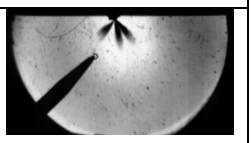
	RMS			
725	Typical	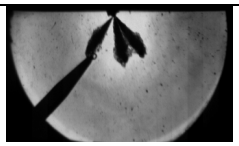	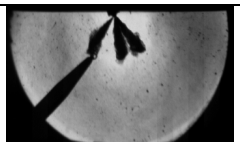	
	Mean	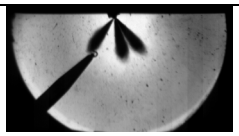	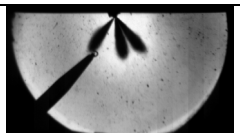	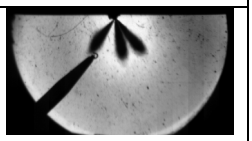
	RMS		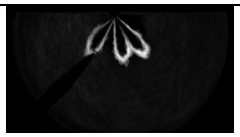	
975	Typical			
	Mean	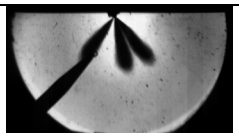	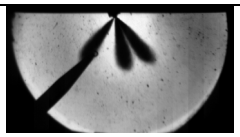	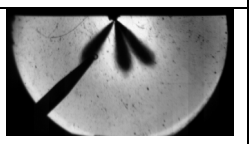
	RMS	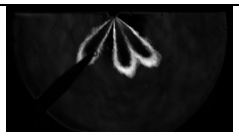		

Figure 8-3 Effect of turbulence on spray – 5.0 bar

The imaging results in Figure 8-2 and Figure 8-3 show that at the lower gas pressure (Figure 8-2), the effect of the turbulent air motion in increasing the rate of evaporation and hence reducing the volume of visible spray is much greater than for similar levels of turbulence at the higher gas pressure (Figure 8-3). The loss of liquid and detectable vapour gradients at the low gas pressure shows a rapid rate of vaporisation for this condition, which is analogous to those encountered in an engine for early injection strategies where the desire is to create a fully mixed, homogeneously dispersed air/fuel charge throughout the entire combustion chamber. Likewise, for later injection into a high pressure atmosphere (during the compression stroke prior to ignition), the desire is to create a highly stable, localised air/fuel charge around the spark plug which is not influenced by the turbulent flow structures. However, during these late injection conditions the turbulence intensity will be markedly higher than during the induction stroke due to the conservation of air flow momentum in the cylinder with a reduced cylinder volume.

The mean and RMS images in Figure 8-2 and Figure 8-3 show the effect of turbulence on the spray envelope variability. In these images, high variability is shown by white pixels with reducing greyscale tones to black representing no variability in tonal value over the different images. The mean and RMS images in Figure 8-2 show an increase in the width of the variability region around the spray at a turbulence intensity of 2 m/s relative to the quiescent condition (u' = 0 m/s), especially at the spray plume tips. At a turbulence intensity of 4 m/s the width of variation is greatly reduced. A similar level of variability is evident at all conditions at the high gas pressure condition (Figure 8-3), although a slightly wider band over which spray variability is detected is evident at a turbulence intensity of 4 m/s. If the effect of the turbulent air motion in entraining the droplets and vapour at the spray tip and boundary are considered, a clear trend in these variability observations emerges. At a gas pressure of 0.5 bar, the fuel droplets produced by aerodynamic break-up at and near the pray plume leading edge are entrained and clustered at a turbulence intensity of 2 m/s, reducing their localised vaporisation rate due to the dense clusters formed. Thereby the droplet residence time is increased and, allied to the "random" turbulent air motion, the variability in the detected liquid regions is increased. At a turbulence intensity of 4 m/s the droplets are entrained but the higher turbulent energy will lead to an increase in evaporation rate, and hence these smaller droplets are either fully vaporised or any remaining small droplets are not clustered but fully entrained into the airflow and swept away from the spray boundary.

The repeatability of this effect and reduction in clustering leads to a reduced variability in spray boundary location at these conditions. At a gas pressure of 5.0 bar the droplet size is greater and hence the probability of their entrainment into clusters is reduced, and so similar levels of variability are detected for all turbulence conditions, although at a turbulence intensity of 4 m/s some entrainment occurs and hence a slightly higher level of variability is detected.

The effect of gas turbulence on the measured spray plume penetration is quantified in Figure 8-4 for 5.0 bar chamber gas pressure and in Figure 8-5 for a gas pressure of 0.5 bar. Only a very minor effect of turbulence on the measured plume length is observed for the high pressure conditions in Figure 8-4, and the measured plume penetration lengths at this condition are similar to those measured in the quiescent chamber (Figure 4-8). In contrast, the effect of increasing turbulence intensity acting to decrease the measured spray plume lengths for the low gas pressure condition is clearly evident in Figure 8-5.

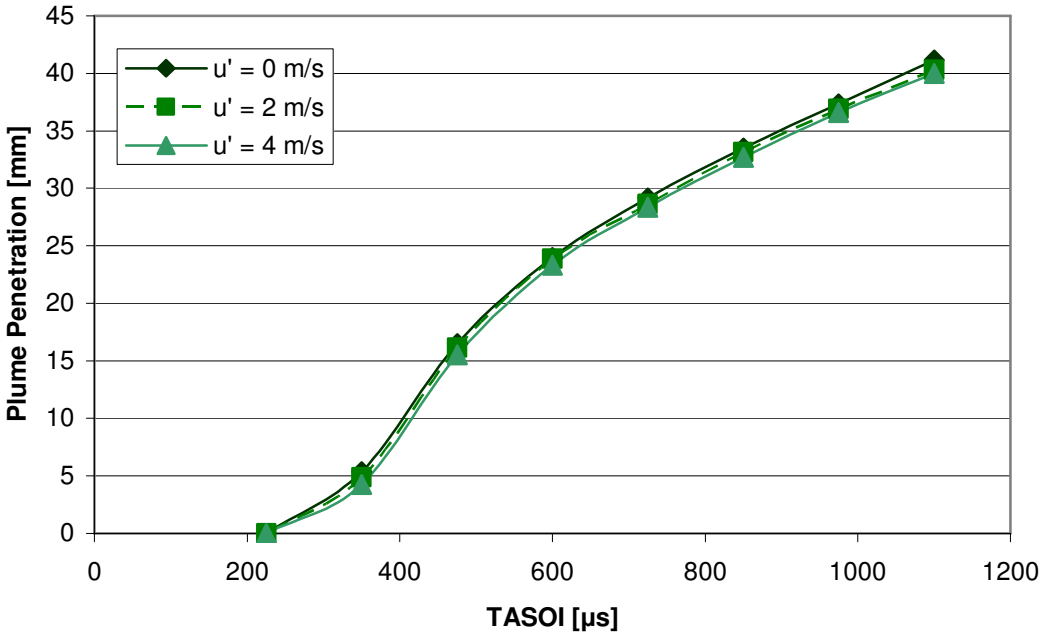

Figure 8-4 Effect of Turbulence on Spray Penetration; Standard Gasoline, 120 °C, 5.0 bar

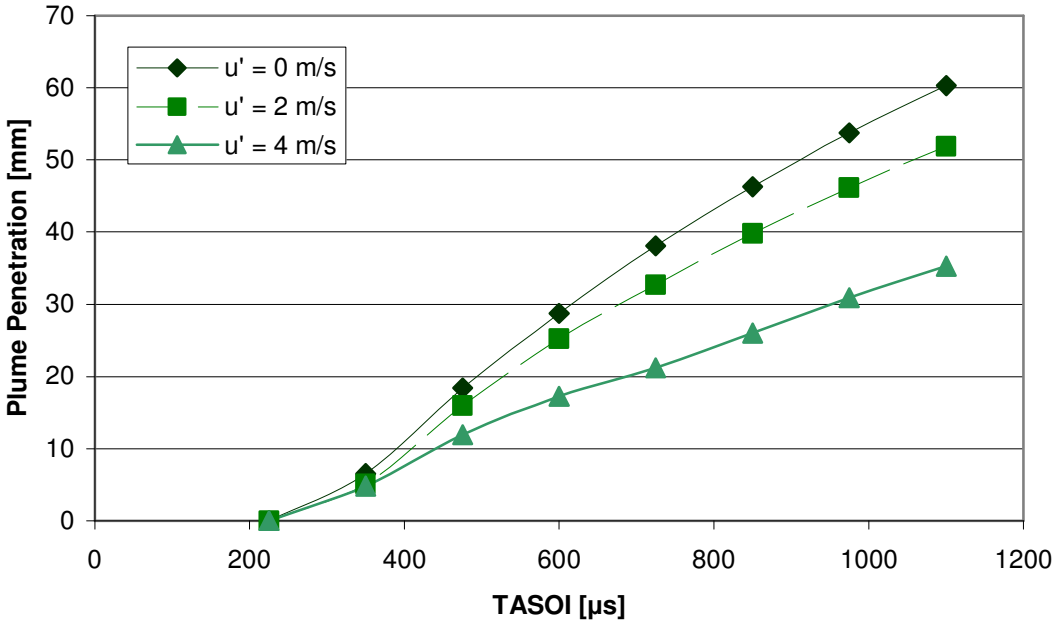

Figure 8-5 Effect of Turbulence on Spray Penetration; Standard Gasoline, 120 °C, 0.5 bar

The increase in plume penetration due to the effect of decreasing pressure between the 5.0 bar and 0.5 bar gas pressure conditions was measured to be approximately 17 % in the quiescent chamber (Figure 4-7 and Figure 4-8). At the low gas pressure condition, the plume penetration lengths measured in the Leeds chamber but without any gas motion (u' = 0 m/s, dark green line in Figure 8-5) shows a considerable increase over the lengths measured for similar conditions in the quiescent gas body experiments (Figure 4-7). This is likely to be due to the entire gas body being at the same temperature as the injector in the Leeds chamber (*i.e.* 120 °C), whereas the gas body in the quiescent chamber was monitored to be around 23 °C. Despite the increase in the measured plume penetration length at the low pressure condition in the Leeds chamber at the quiescent condition, an increase in turbulence intensity clearly shows a decrease in the measured plume lengths. This reduction in measured plume penetration length suggests that a certain volume of fuel is being convected or vaporised from the spray plume, thereby reducing the volume of fuel imaged and hence measured. The temporal development of this fully mixed and evaporated fuel, in terms of its volume and location, has considerable implications for engine operation, and is a key consideration of the spray interaction with the turbulent gas motion.

8.3.1 Effect of Turbulence on Fuel Evaporation Rate

An initial attempt to indicate the temporal development of the mass of Standard Gasoline fuel evaporated under different turbulence intensities was made from the projected area of the spray plumes for both the Schlieren and backlit images in the Leeds combustion chamber and UCL quiescent chamber respectively. Due to the presence of the spark plug obscuring spray plumes 1 and 6 in the schlieren images, this area analysis was based on the four closely spaced plumes. It was assumed that these four plumes formed a single cone, as shown in Figure 8-6, with a projected area as measured from the spray images. To calculate the volume of the fuel sprays within this projected cone, it was assumed that the liquid spray plumes comprised ¼ of the total cone volume. This assumption was based on engineering judgement, as for each spray the actual liquid volume proportion of its projected cone varies depending on the nozzle diameter, the plume cone angle(s) and the plume spacing, and hence values quoted in the literature are not able to be directly correlated to other spray forms.

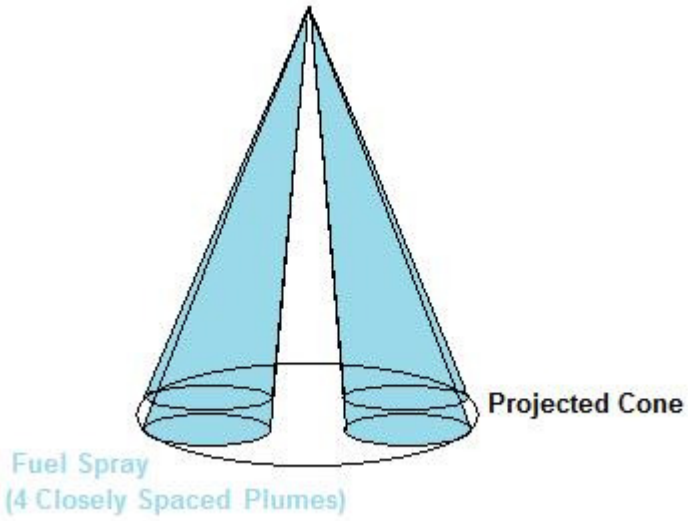

Figure 8-6 Projected Spray Volume Cone

The mass of fuel projected by each image was then calculated based on the assumption that the volume of fuel present in the last image assessed for each condition (*i.e.* showing the largest fuel volume of the captured images) was equivalent to 2/3 of the total injected fuel volume for each injection event (*i.e.* 0.2 grams). This total injected fuel mass was then apportioned to the 4 imaged spray plumes assuming an equal fuel mass flow for all 6 plumes, to give a value for the total mass of fuel present in the last captured spray image of 0.133 grams for the 4 closely spaced spray plumes.

The volume of fuel assumed as having been evaporated at each time interval was then calculated from the difference in projected spray volumes between the images captured using the backlighting technique in the quiescent chamber and those captured using the Schlieren technique in the turbulent chamber. The mass of fuel calculated as having evaporated was then divided by the total volume of fuel injected over each injection event to calculate the percentage volume of fuel which is thought to have been vaporised for each turbulence intensity at each injector body and gas pressure condition, as presented in Figure 8-7 and Figure 8-8.

For the images showing the spray at a gas pressure of 0.5 bar (Figure 8-7), those captured using the Schlieren imaging technique in the Leeds chamber present a smaller total area (and hence volume) of fuel than those captured for similar conditions in the quiescent chamber, even at nominally quiescent conditions in the Leeds chamber (u' = 0 m/s). These reduced projected spray areas, despite the increase in measured penetration lengths at u' = 0 m/s are likely to be due to the gas body temperature bringing about increased evaporation rates for all conditions. The Schlieren technique images density gradients which result from fuel vaporisation and hence fully vaporised fuel (*i.e.* areas of a constant concentration) is not depicted. Therefore the Schlieren images are not a measurement of the total volume of fuel vaporised but may be used to indicate regions where vaporisation occurs, and the volume of partially vaporised fuel present around the spray periphery. In this respect, these images have been assumed to capture the residual liquid spray at the high vaporisation case at a gas pressure of 0.5 bar and both the liquid spray and total fuel vapour at the low vaporisation case at a gas pressure of 5.0 bar (both at an injector body temperature of 120 °C). As such, for the 0.5 bar gas pressure case, the volume of fuel imaged as the difference between the backlit and Schlieren image was pro-rated based on the volume of fuel seen in the final backlit image. Conversely, the volume of fuel calculated from the difference in the Schlieren and backlit images was pro-rated to that captured in the final Schlieren image for the 5.0 bar gas pressure case.

It should be reiterated that the calculations based on this simple model and assumptions described above were carried out to examine whether the pictorial data could be used to attempt to indicate vaporisation rates. As such, the values derived from this model should be taken as purely indicative and not an accurate assessment of the volume of evaporated fuel with respect to time and turbulence intensity.

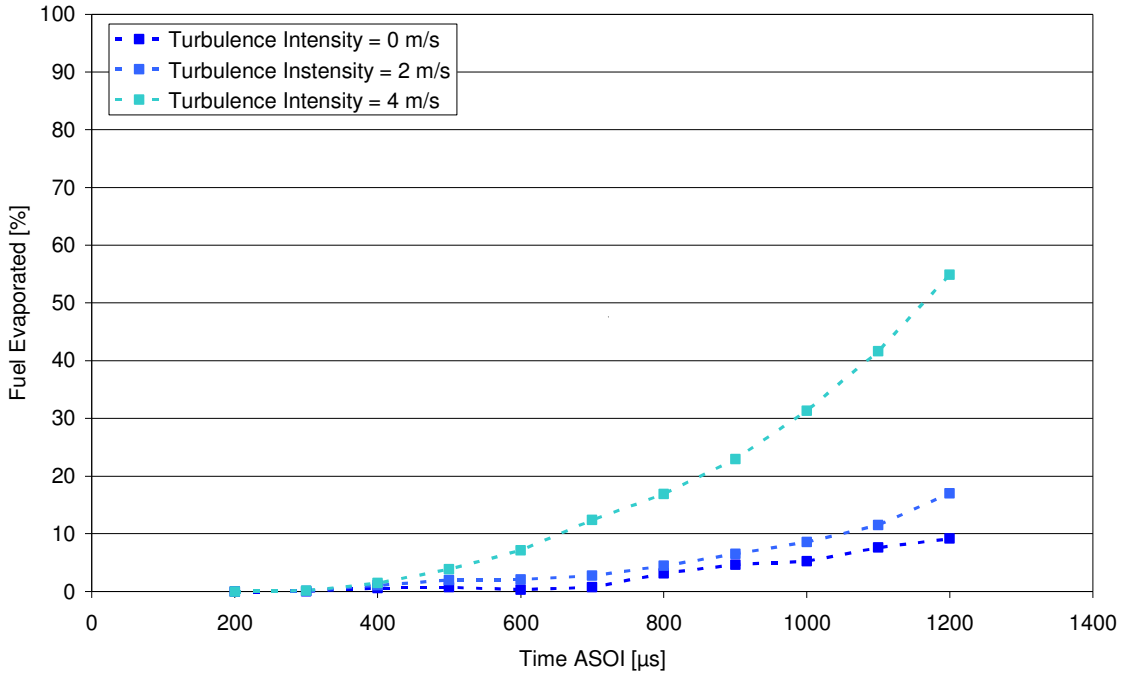

Figure 8-7 Evaporated Fuel Mass, 120 °C, 0.5 bar

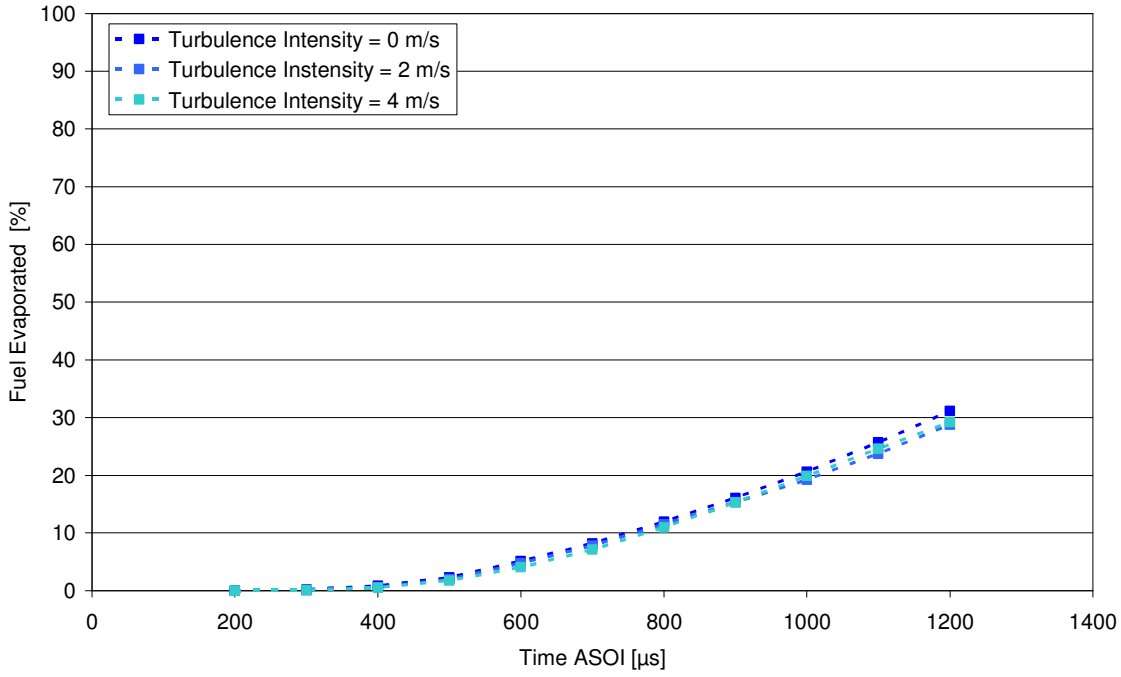

Figure 8-8 Evaporated Fuel Mass, 120 °C, 5.0 bar

Whilst the simplistic model and assumptions used to calculate temporal development of the mass of evaporated fuel for different turbulence intensities is clearly not perfect due to the coarse assumptions used in its derivation, as a first order approximation the calculation largely appears to show the expected trends. For the un-collapsed spray (5.0

bar gas pressure condition), a further iteration of the model could be made by assessing the imaged spray area projected by a single plume pair (in the side view) as a cone and comparing the single spray plume volumes calculated from the backlit and Schlieren images. This would eliminate ambiguities related to estimation of how much liquid is present in the imaged spray cone projected by the outer boundaries of the four closely spaced plumes. Additionally, such an assessment would allow a more accurate derivation of the actual proportion of the overall cone which is comprised of the liquid plumes, which may provide a more accurate estimation of the amount of fuel vapour present in the collapsed spray. Unfortunately image analysis software limitations and time constraints precluded this assessment being carried out for the present work

As the final outcome of any fuel spray into an engine is not the spray in its own right, but rather the fuel mixing with the air and subsequent combustion efficiency, the vaporisation and mixing rate of the fuel are critical parameters. Although only a very preliminary trial to assess whether an imaged based estimation of the liquid vapour present could be developed, this simplified model clearly suggests that there is a strong interaction between the vaporisation rate and the gas body's turbulence intensity.

8.4 Spray Interaction with Turbulent Gas Motion

The spray structure at the boundary can cause, and be influenced by, entrainment of the gaseous medium into which the spray is injected. If this gas carries its own motion, as is the case in in-cylinder flows, the interaction of the liquid and gas motions can affect the boundary spray structures and hence the evaporation and mixing regimes. Dan *et al.* [1997] identified the motion of the entrained air as the probable mechanism for the establishment of coherent liquid structures, determined to be dense clusters of droplets, around the periphery of diesel spray plumes. The authors also stated that their spatial distribution can be described by means of the aerodynamic response to the range of turbulent vortices present inside the spray. In relation to vaporising diesel sprays, Siebers [1998, 1999] concluded that the rate of vaporisation is controlled by the air entrainment and turbulent mixing of the liquid and gaseous phases. The vaporisation rate of the droplets, which is directly influenced by the local droplet concentration density, may be indicated by the Stokes number for these situations. However, for more dense sprays such as those relevant to gasoline DI, these assumptions are no longer strictly valid, and the applicability of the Stokes number becomes less well defined. Although Dan *et al.* [1997] suggest that the Stokes number is also valid in diesel-like DI

sprays, it is probable that the high droplet concentration density of such direct injection sprays alter the interaction between the turbulence and the fuel spray, limiting the validity of the application of the Stokes number. However, in absence of a more accurate assessment of the interaction of the gas motion and spray boundary, it can only be assumed that the characteristics of the ambient turbulence are a reasonable approximation of the turbulence acting at the spray boundary for high droplet concentration density sprays also, and that the Stokes number derived from these conditions will also give an indication of the spray boundary interactions for denser sprays.

8.4.1 Stokes Number

For general spray characterisation of the distribution of droplets in low droplet concentration density sprays, where creeping flow could be assumed to exist around the individual droplets, and large scales of turbulence are reported to affect the spray structure, the use of the Stokes number (St) has been found well suited to the qualitative indication of the likelihood of droplets around a spray being convected by the surrounding gas turbulence, Sornek *et al.* [2000].

The Stokes number can be mathematically expressed by;

Eq.1.1
$$St = \frac{\tau_D}{\tau_L}$$

Where τ_D is the droplet response time and τ_L is the integral time scale of the turbulence, Jakubik *et al.* [2006]. Bachalo [1995] states that the droplet response time, $\tau_{D,}$, is given by:

Eq.1.2
$$\tau_D = \frac{4D\rho_L}{3C_D\rho_g u}$$

Where D is the droplet diameter, ρ_L is the droplet density, C_D is the coefficient of drag, ρ_g is the gas density and u is the relative droplet velocity. By definition, τ_L is a function of the turbulence velocity.

According to Sornek *et al*. [2000] and Jakubik *et al*. [2006], based on the ratio of the droplet and gas turbulence response times, if St << 1 the droplet is likely to be captured in the turbulent eddy and follow the eddy's motion. Conversely, a high turbulent velocity gives short turbulent time scale and hence leads to an increase in Stokes number. In the extreme a droplet's inertia means that it does not have time to react to rapid changes in the turbulent air flow, and so if St >> 1 the droplet trajectory is notionally unaffected by the turbulent motion. At St = 1 the droplet is centrifuged towards the outer edge of the eddy, and the droplet trajectory is both vortical and perpendicular to that of the eddy, and the droplets spirals through the vortex.

The interaction of the spray with any in-cylinder turbulent gas motion is critical for the prediction of in-cylinder spray convection and evaporation. However, despite the importance of the fuel/air motion interaction, Jakubik *et al.* [2006] note that the effect of ambient turbulence on the spray structure is not currently well understood. Exceptions of note are Beard *et al.* [1994] who report a strong dependency of individual droplet trajectories on the large scale vortex dynamics in two phase flows, and Wark *et al.* [2000] who confirmed the presence of droplet clusters at the spray boundary and their dependence on the air flow turbulence. Lastly, Sornek *et al*. [2000] report a considerable qualitative change in the size and spatial distribution of the droplet clusters that were present inside the spray under different turbulence conditions. They also quantified the droplet-turbulence interactions by means of the centrifugal Stokes Number which is a measure of the turbulent vortex centrifugal force relative to the droplet drag force, and as such is another measure of the likelihood of droplet entrainment into the turbulent flow structure and subsequent vaporisation. They obtained values in the range of 0.1 to 1 for the centrifugal Stokes Number. At the lower limit, they reported nearly homogeneous droplet dispersion, whilst with an increasing Stokes Number the droplets tended to form droplet clusters of increasing size at the outer edge of the turbulent eddies. According to their findings, the mechanism of droplet clustering may exist up to a higher limits of St = 10, at which point dense clusters can result in non-transparent regions observable by optical techniques. Moreover, they also found that in these dense droplet clusters, the rate of vaporisation was reduced due to the near-droplet interactions.

Stokes Numbers were calculated for the turbulence intensity and gas pressure conditions illustrated in Figure 8-2 and Figure 8-3, and are shown graphically in Figure 8-9. Note

that for quiescent conditions (u' = 0 m/s), the response time for turbulent eddies does not have a value (due to no turbulent eddies being present), and so the Stokes Number is invalid for these conditions. The droplet sizes and velocities used in the calculation of the droplet response time were those measured from the main spray development analysis presented earlier in this work.

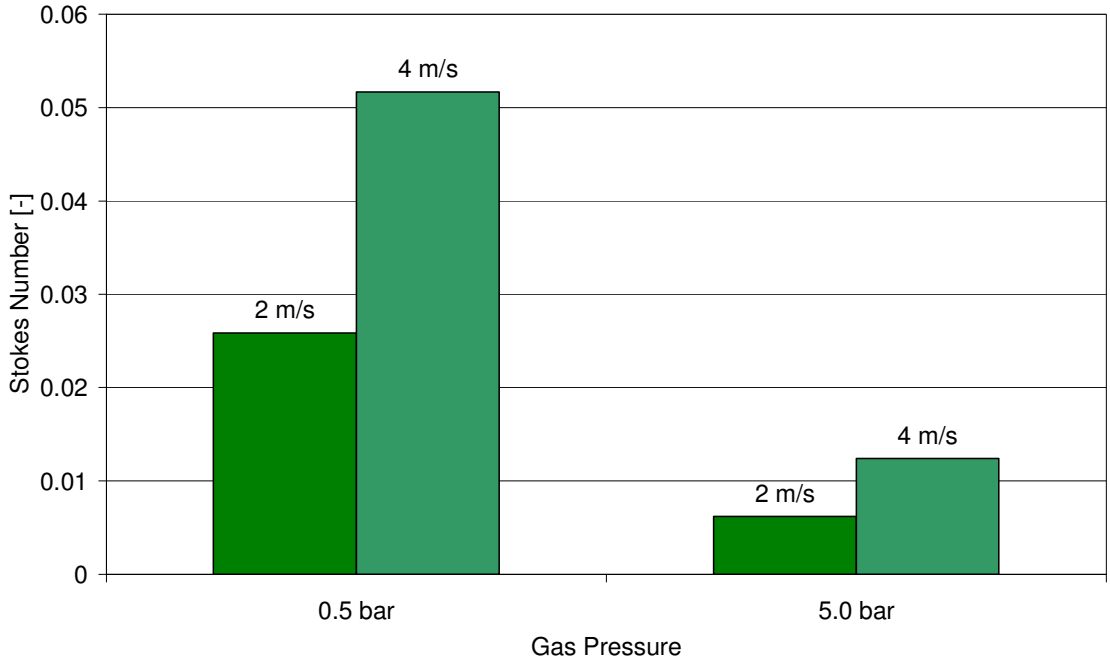

Figure 8-9 Integral Length Stokes Numbers for Gasoline Sprays

The Stokes Numbers calculated for the experimental conditions, as shown in Figure 8-9, were considerably lower than 1, suggesting that the droplets for all conditions would be likely to be entrained into the turbulent vortices. However, the previous assessment of the trends observed from the spray images would suggest that this was not case, and that entrainment and clustering was only strongly evident at 0.5 bar gas pressure and u' = 2 m/s. Similar Stokes Number values to those calculated for this work were obtained by Jakubik *et al*. [2006] for a single plume diesel spray, who calculated that an increased ambient turbulence from 2 m/s to 4 m/s led to an increase in the Stokes Number from 0.005 to 0.02. This was manifest by increased droplet clustering in the mixing region for a diesel spray, indicated by the increased size of the liquid structures and decreasing distance between them. However, both the results reported by Jakubik *et al*. [2006] and those calculated for this work were obtained in the Leeds chamber, which has an integral length scale of 20 mm (for the turbulence intensity conditions of interest). Whilst the length scale does not feature in the calculation of the Stokes Number, it may

be expected that the scale of the turbulence eddies in relation to the physical size of the spray form and droplets would influence their interaction and effect. For reference, in an engine air flow turbulent eddies have been measured to have a typical diameter of 2 – 3 mm, Rimmer *et al*. [2009].

As detailed above, this relationship between the spray break-up and Stokes Number was originally developed for low volatility sprays, where significant vaporisation which would influence that of the adjacent spray was not present. Whilst it has been suggested that this relationship holds for denser, higher volatility sprays (e.g. Dan *et al*. [1997]), this work suggests that these mechanisms are acting at different Stokes Number ranges than those with which they are usually associated. These results obtained with higher volatility fuels with dense droplet and vapour regions around the spray boundary also show clear differences in Stokes Number ranges over which droplets are conveyed away from the spray, over which clusters are formed and over which they are unaffected. However, these ranges appear not the be centred on a Stokes Number value of 1, but on a lower "critical" Stokes Number ("St_c"), at which clustering is most likely to occur. At either side of this critical Stokes Number, the likelihood (and hence effect) of clustering diminishes by a currently un-known function of the Stokes Number, as represented schematically in Figure 8-10. From the resolution of experimental data points in this work and the results obtained (particularly as illustrated in Figure 8-9), as well as those reported by Jakubik *et al*. [2006], the critical Stokes Number for this situation appears to fall in the range 0.02 – 0.03.

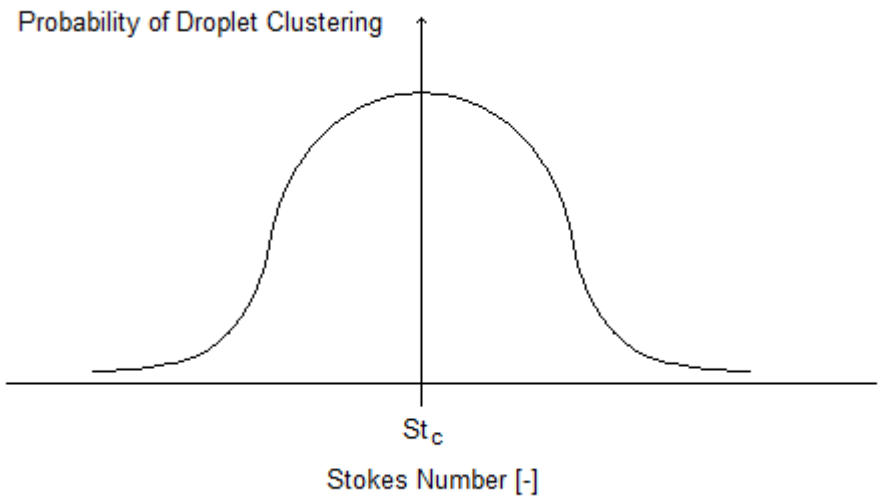

Figure 8-10 Probability of Droplet Clustering in relation to Stokes Number (Generalised)

Note that the distribution shown in Figure 8-10 is not intended to be representative of the actual function of drop clustering probability, as this is unknown, but is included to show that the results obtained in this work show that some form of "peaked" function is likely to exist between the probability of droplet clustering and the Stokes Number. This function may be of a linear or of a non-linear form. Investigation into the nature this relationship falls outside the scope of this work but would add significant value to the current state of knowledge where, as noted previously, the interaction between the spray and the in-cylinder air motion is critical for the robust operation of a direct injection gasoline engine. Despite this, this interaction is not well understood and any existing results and derived relationships are based on the injection of diesel fuel. In addition, the representation of these interactions through the Stokes or a further developed indicator number which clearly identifies the mechanics of the interaction would allow for a more precise prediction of conditions under which turbulence strongly influences the spray break-up and evaporation rate.

8.4.2 Prediction of Turbulence Effect for Different Fuels

Although the single component fuels examined in this work were not tested in the Leeds chamber with turbulent gas motion, Stokes Number were calculated for these fuels to enable a prediction of their break-up in turbulent flows based on the observed trends for Standard Gasoline. The Stokes number calculated for each fuel over the tested injector body (fuel) temperature range is shown in Figure 8-11 and Figure 8-12 for a turbulence intensity of u' = 2ms/ and in Figure 8-13 and Figure 8-14 for a turbulence intensity of u' = 4 m/s. The values calculated at u' = 4 m/s are double those calculated at u'= 2 m/s as the denominator of the definition of the Stokes number, given in Eq.1.1 is the time scale of the turbulent motion, which halves with a doubling of turbulence intensity.

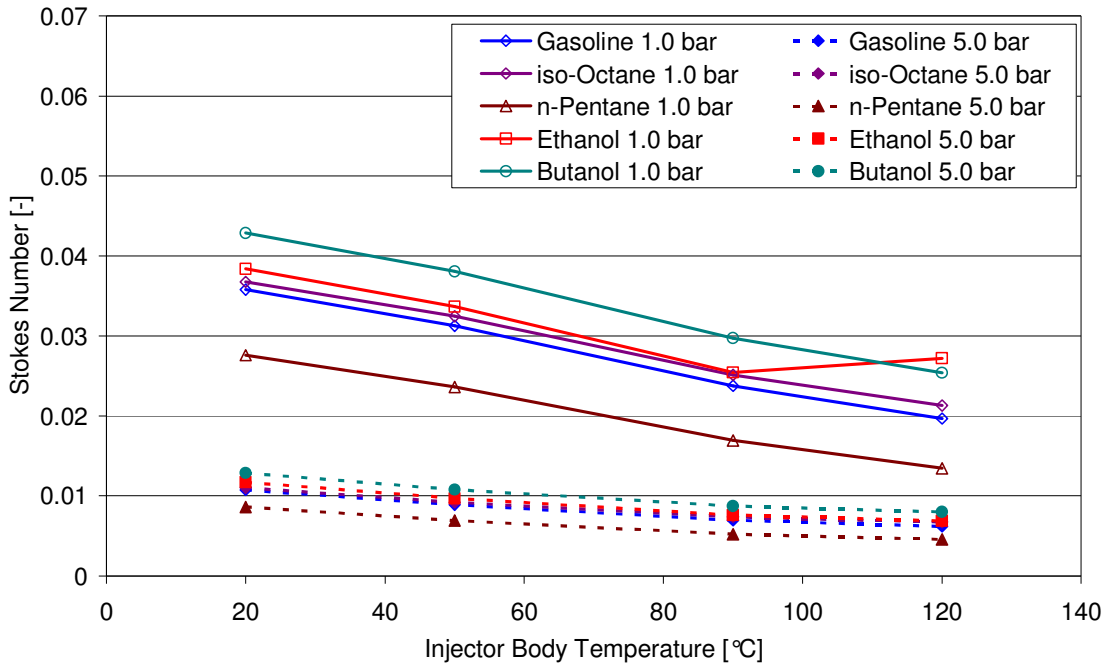

Figure 8-11 Integral Scale Stokes Numbers for Injector Body Temperatures at u' = 2 m/s (1.0 and 5.0 bar)

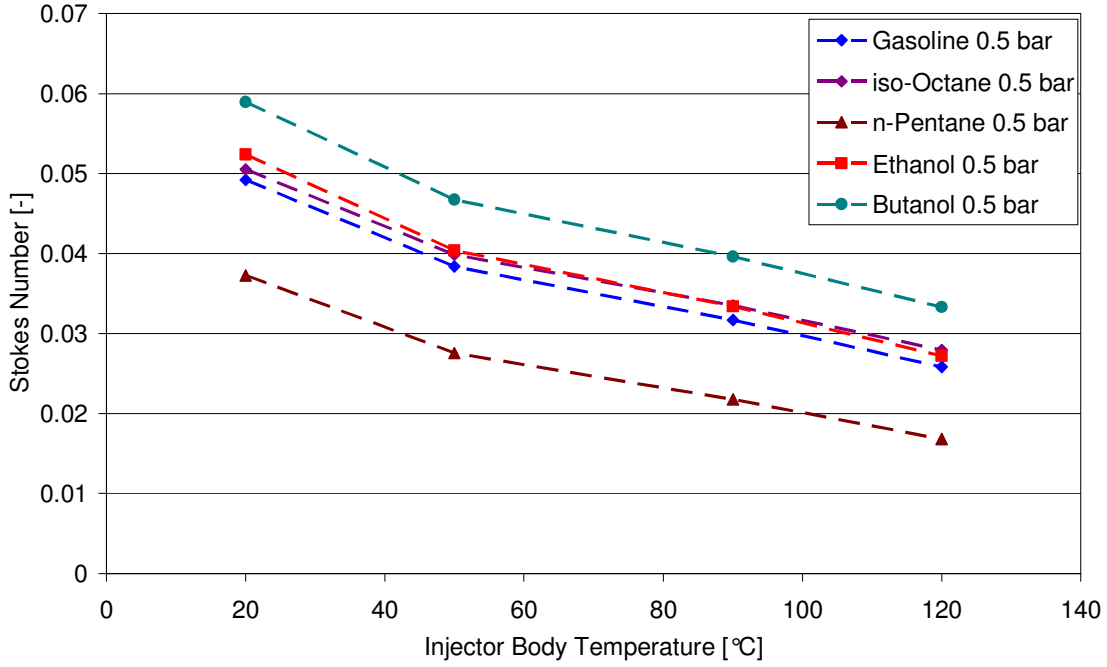

Figure 8-12 Integral Scale Stokes Numbers for Injector Body Temperatures at u' = 2 m/s (0.5 bar)

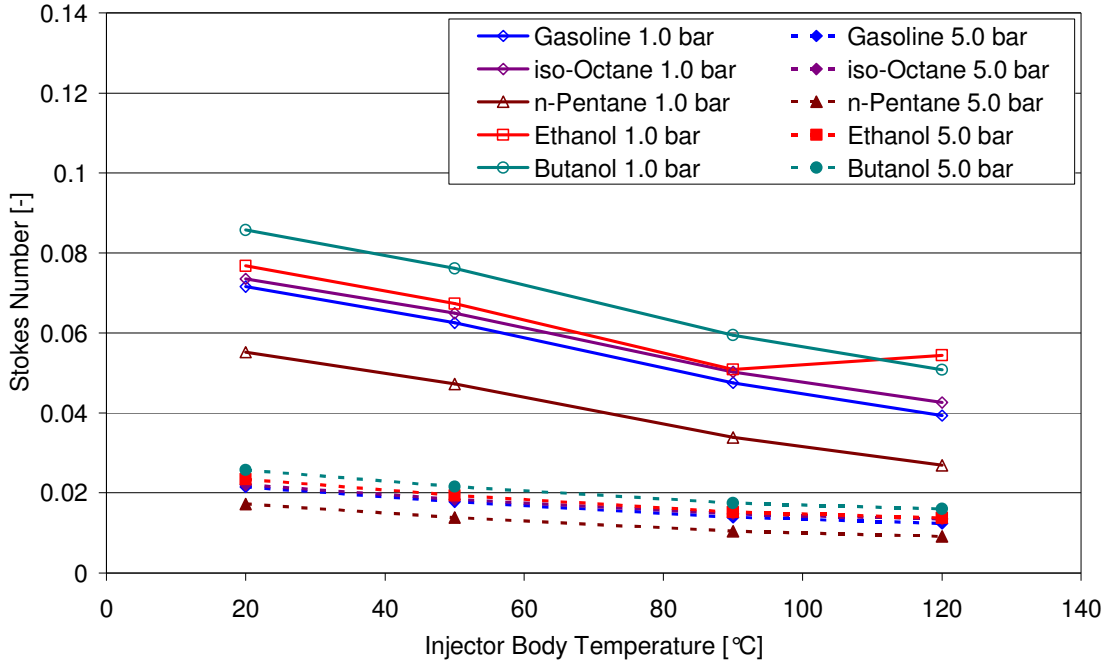

Figure 8-13 Integral Scale Stokes Numbers for Injector Body Temperatures at u' = 4 m/s (1.0 and 5.0 bar)

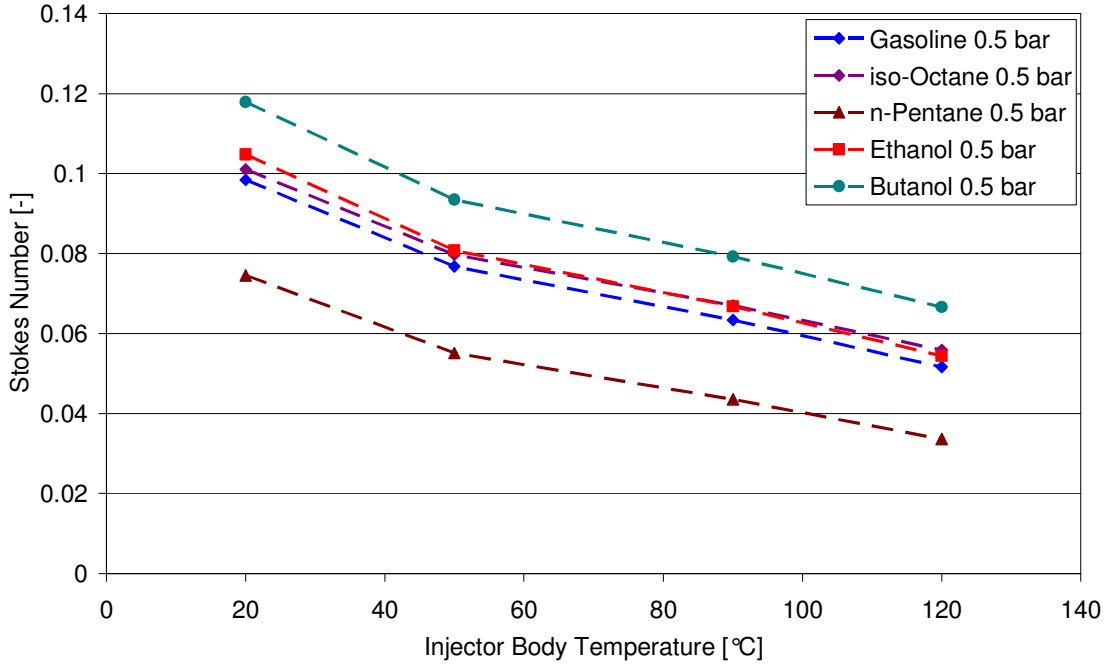

Figure 8-14 Integral Scale Stokes Numbers for Injector Body Temperatures at u' = 4 m/s (0.5 bar)

The graphs in Figure 8-11 and Figure 8-13 show a decrease in Stokes Number with an increase in temperature, principally due to a decrease in droplet size. A decrease in

Stokes number is also calculated for an increase in gas pressure, as the gas density is increased and the droplet response time decreases. For all conditions, the increased volatility leads to a reduction in the Stokes number at each temperature, mainly due to the reduction in droplet size as well as liquid density. Based on a critical Stokes Number Value of 0.025, at lower temperatures the larger droplets would be expected to remain unaffected by the turbulent gas motion although any fuel vapour (which would be low for all fuels at this condition) would be entrained and hence both variability in the spatial distribution of the fuel as well as a reduction in plume penetration would be expected to low. With increasing fuel temperature the effects of both of these mechanisms is expected to increase in line with the fuel volatility, with the highest volatility fuel (*n*-Pentane) being the most affected, and the relative extent of the effects being in the proportions relations of the lines plotted for the fuels in Figure 8-11 and Figure 8-13.

The relative positions of the fuels when plotted in terms of the Stokes Number shows an interesting correlation, in that *iso*-Octane and Gasoline are closely matched along with Ethanol, with a larger differences calculated for Butanol and *n*-Pentane. From the formulation of the Stokes Number, this is based on the ratio of the volatility to density for each fuel, showing this parameter to be a key indicator of a fuel's likely susceptibility to the influence of turbulence on spray break-up.

8.5 Spray Combustion

Whilst conducting experiments on the effect of turbulence on spray development in the Leeds combustion bomb, the opportunity was taken to ignite the spray and image the subsequent flame development. For completeness, these images and a brief discussion of their relevance is included here. However, the combustion of the spray and the detailed analysis of the flame propagation fall outside of the spray development scope of this work. A sister project was conducted in parallel to the presented work concerning these facets, and the reader is guided to publications which have arisen from that work for a thorough analysis of the mechanisms affecting the combustion and flame propagation of this spray in an optically accessed engine (*e.g.* Serras- Pereira *et al.* [2007a, 2007b], Aleiferis *et al.* [2008]).

For the combustion imaging, in-vessel conditions were set to be representative of typical direct-injection engine late injection, stratified charge operation conditions at

ignition. As such, they were a system temperature of 90 °C (injector body, fuel and air), 5.0 bar air pressure and a nominal turbulence intensity of 4 m/s. The spark plug was positioned to be located between spray plumes 1 and 6 and as near to its relative location as in the running engine examined in parallel to this project, with the confines of the physical bomb injector and spark plug mountings. The injection duration was maintained at 2 ms as for the spray imaging, and the ignition timing was set to 3 ms ASOI to ignite the spray at the same relative timing as it would be ignited in an engine operating at these conditions. Initial attempts were made to ignite the spray in a "pure" air mixture. However, it was found not to be possible to ignite the spray under these conditions, even under high spark energy conditions and by varying the ignition timing by as much as ± 2 ms. Although difficult to decipher from the images due to the spray obscuration of the spark plug tip, it is thought that this is due to the turbulent liquid spray "washing" the spark from the plug, and hence preventing the spark igniting the spray. This observation has potential implications for the robust ignition and combustion of the spray in an engine, although spray ignition was not found to be an issue in the running engine by Serras-Pereira *et al*. [2007a], most likely due to the smaller turbulence length scales found in the engine under these conditions, Rimmer *et al*. [2009]. For this work in the Leeds combustion bomb, it was found necessary to pre-inject fuel into the in-vessel air to establish a lean background air fuel mixture ($\lambda = 0.8$) in order to be able to ignite the spray. A sequence of a typical injection and ignition as imaged using the Schlieren system is shown in Figure 8-15.

The dark flame area in Figure 8-15 is seen to initially decrease slightly as the spark kernel produced at the plug electrodes is blown behind the spark plug wand. The flame then grows at an increasing rate until a steady growth rate is achieved at approximately 5000 μs ASOI. After this, examination of the images presented in Figure 8-15 shows that some clipping of the flame by the circular windows starts to occur, although the overall projected flame area continues to increase over the remaining imaged area.

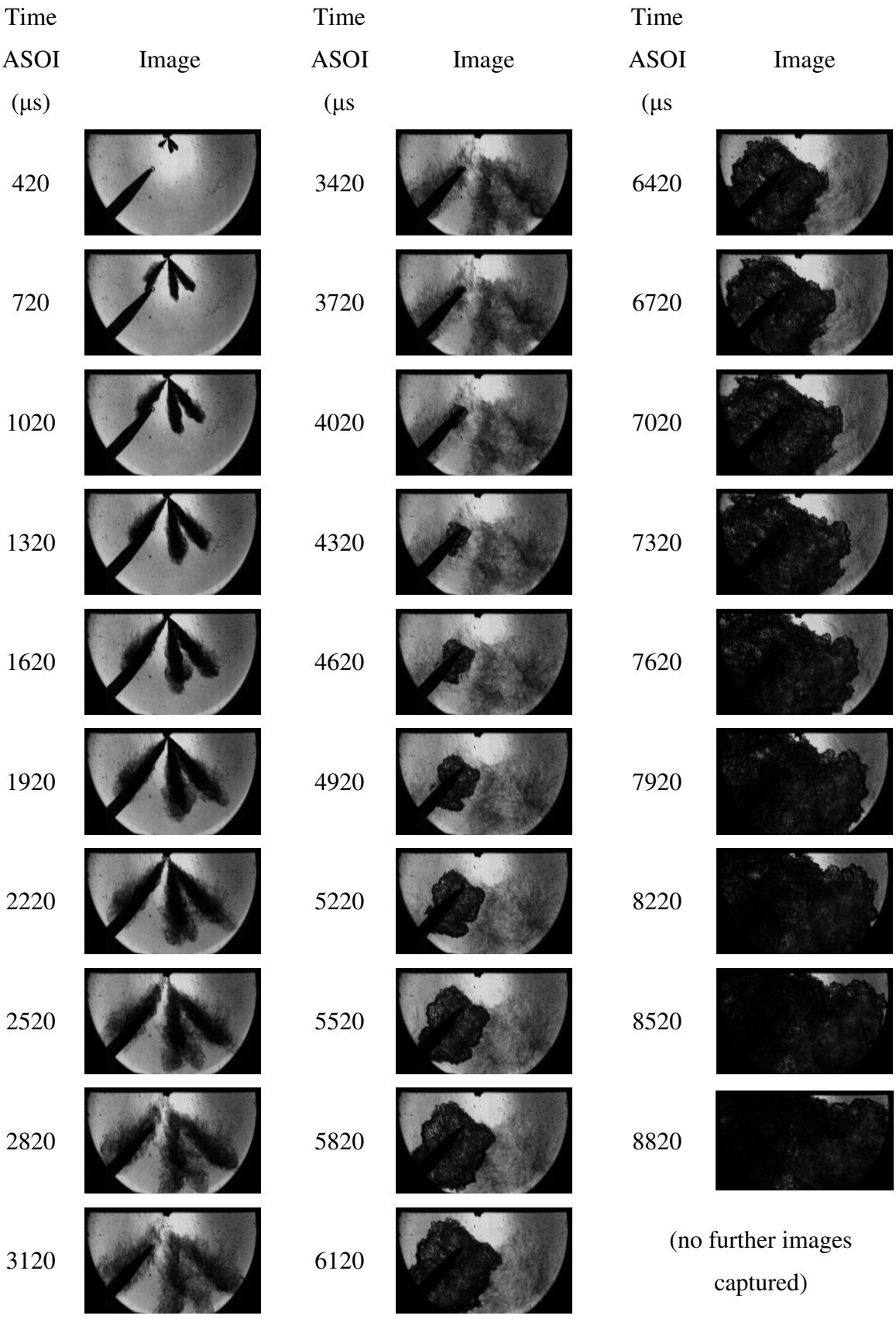

Figure 8-15 Injection and Spray Combustion Images

8.5.1 Flame Growth

The flame images presented in Figure 8-15 were processed in a similar manner as the spray images to measure the projected flame area. The measured area at each time interval was used to calculate the radius of the sphere that would have the same projected circular area as measured, as shown graphically in Figure 8-16 for the period until clipping of the imaged flame by the window prevents the flame area to be accurately measured.

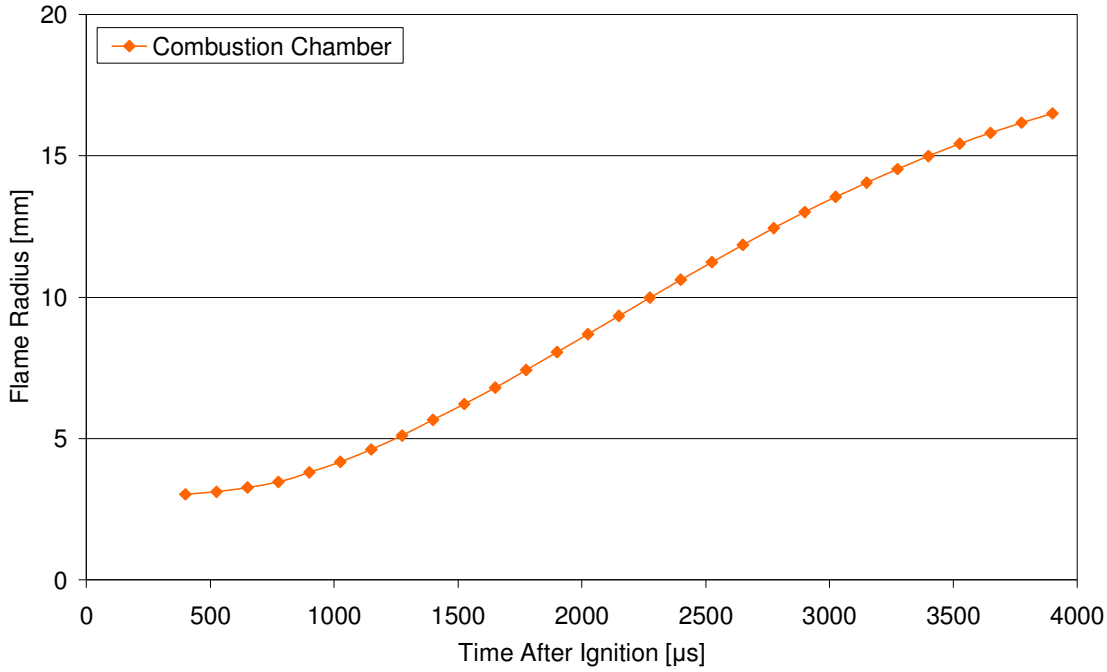

Figure 8-16 Flame Radius

The measured burning rates of the spray on which this work is based may be compared to those published by Lawes *et al.* [2006] from the combustion of well defined droplet and gaseous mixtures of *iso*-Octane in a quiescent air body in the Leeds combustion chamber, as presented in Figure 8-17. In this figure Lawes *et al.* also present the corresponding Schlieren images of the flames at r ≈ 48 mm. These photographs show the effect of droplet diameter on the flame structure for the centrally ignited aerosol *iso*-Octane-air mixtures. Although there are small difference in pressure, P, and temperature, T, between the conditions in the three images as an inevitable result of the droplet generation technique, the authors also showed that such small differences have a negligible effect on the flame structure.

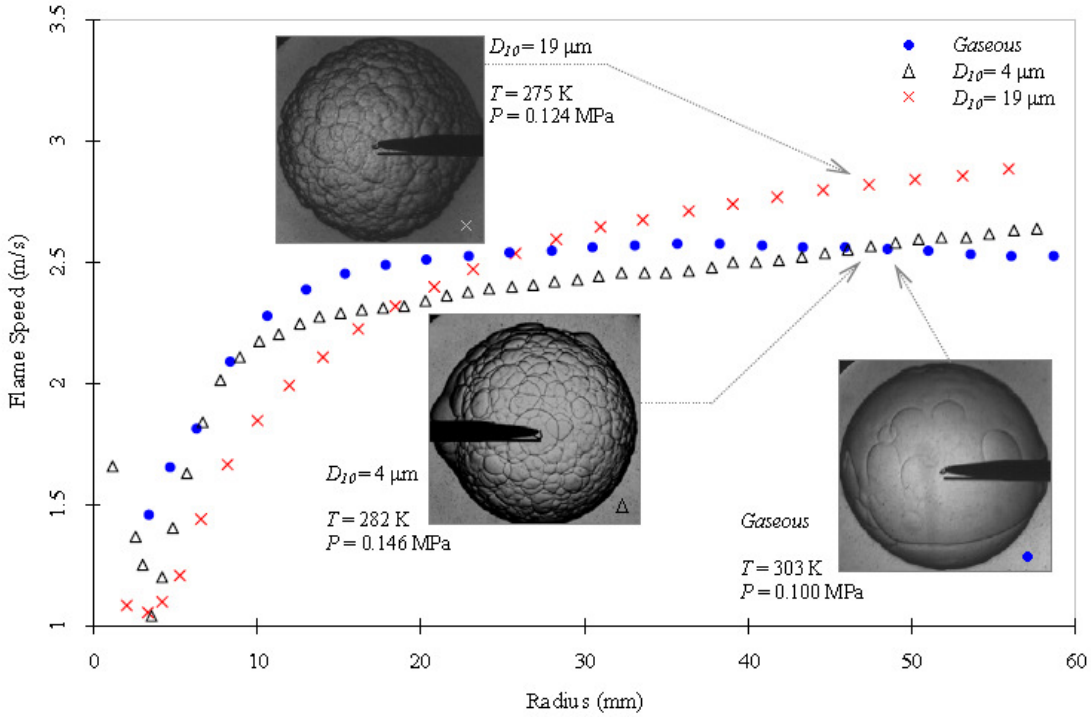

Figure 8-17 Flame speeds of *iso*-Octane-air mixtures at □ = 1.2, near atmospheric conditions and at different flame radii. Inset: the corresponding schlieren images at radius of approximately 48mm (Reproduced from Lawes *et al.* [2006])

It is clearly shown in Figure 8-17 that the effect of size of droplet on the flame structure, which increases the level of instabilities, correlates well with that of the flame propagation rate or burning rate as a result of increase in surface area. The Schlieren photographs superimposed on Figure 8-17 show that the flames of combusting droplets are, in general, more unstable than those of bodies of fully vaporised fuels (gaseous mixtures). The extent of this instability increases as the droplet size increases. Flame instabilities are manifested by a cellular surface structure, which increases the surface area of the flame front and consequently increases the flame speed. Lawes *et al.* suggest that droplet presence is therefore likely to play an important role in triggering instabilities in droplet-based flames by heat loss due to evaporation. As the droplet size increases the heat loss also increases, thereby resulting in a greater level of instability and a higher subsequent burning rate.

For the current work at the conditions at which the images in Figure 8-15 were captured, the mean droplet diameter (D_{10}) may be estimated to be around 8 µm from the droplet sizing results presented previously. The flame growth speed in relation to the flame radius is presented in Figure 8-18 for the measurements obtained for the current

work and for those taken from the same spray ignited in a running engine (Serras-Pereira *et al*. [2007a]).

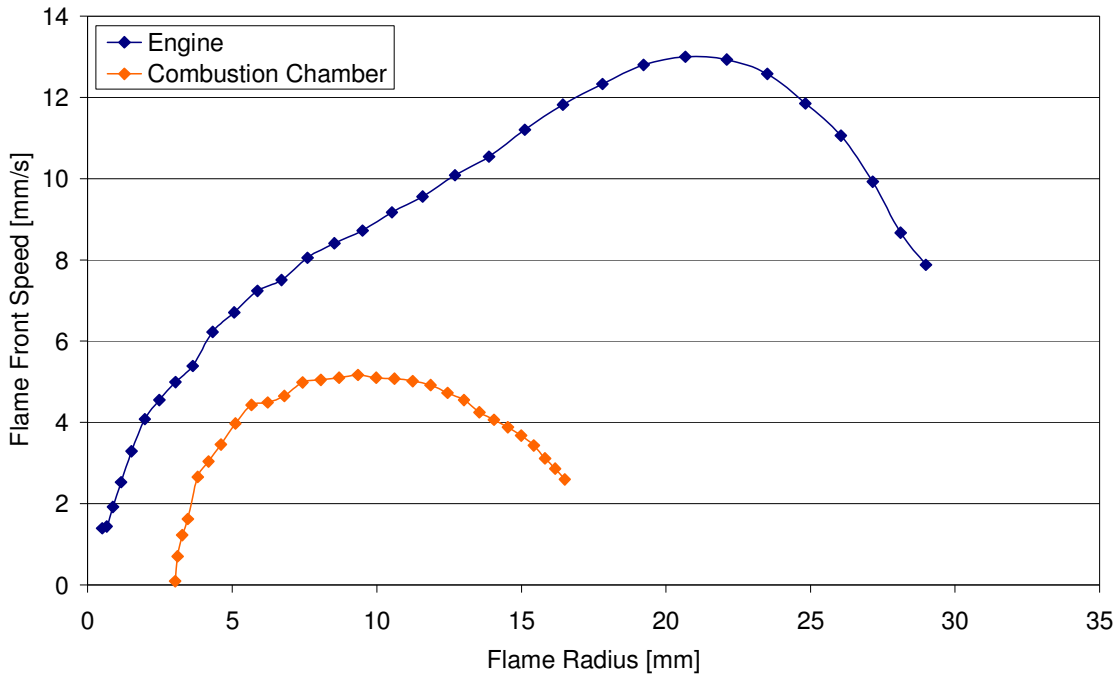

Figure 8-18 Flame Speed of Standard Gasoline Spray at □ = 0.8

The general form of flame growth measured from the ignition of the spray in the Leeds Combustion Chamber is comparable to that presented by Lawes *et al.* above. A reduction in growth rate is calculated for the current work due to the effect of frame clipping of the images occurring after approximately 5500 µs after the start of injection (ASOI). However, comparison of the graph scales between those presented in Figure 8-17 and Figure 8-18 show that the flame growth gate is considerably higher as measured for the images captured for the current work. In addition, the growth rate for the in-engine flame is measured to be even faster. This is likely to be due to both the difference in fuels used and the in-chamber/cylinder conditions present. Both the spray ignition and engine in-cylinder frame results presented in Figure 8-18 are based on Standard Gasoline sprays, whereas that presented by Lawes *et al.* is based on the lower volatility *iso*-Octane, where the previous results showed that the fuel volatility greatly affects the spray vaporisation rate, which may be expected to affect the combustion rate. Additionally, the higher fuel and gas body temperature at which this experiment was conducted relative to those conducted by Lawes *et al.* would be expected to increase the vaporisation rate. More importantly though, the spray ignition results obtained for this work were carried out at an in-cylinder turbulence intensity (u') of 4 m/s to represent

engine in-cylinder conditions. It may be expected that such a turbulence intensity would act to increase the instabilities at flame front, as can clearly be seen from the highly cellular structure of the flame imaged in Figure 8-15, thereby increasing the flame propagation rate. The further increase in flame propagation rates measured in the running engine also suggest that small scale turbulent eddies and possibly higher rates of in-cylinder local turbulence combined with in-cylinder gas temperature and pressure act to greatly increase flame instabilities and hence flame growth rate. Indeed, according to Lawes [2008], a doubling of burning velocity due to in-engine conditions is very readily achievable and flame speeds in an engine can be about four times higher than those observed in the combustion chamber due to expansion of the hot gas. In addition, the observed flame speed in an engine is influenced by convection velocities which further accelerate the flame growth.

8.6 Summary

This initial study into the affect of turbulence on the fuel spray has illustrated that the interaction of the fuel spray and gas body plays an important and significant role in the spray's development. The turbulent gas motion acts to affect the concentration of droplets and fuel vapour at the spray periphery, which in turn affect the local vaporisation rate through limiting the local concentration gradient. This alters the physical spray form in terms of penetration length and convergence which are impacted by the spray break-up and vaporisation rate as assessed in the main part of this work. The effect of turbulence altering the spray form may be expected to have a significant impact of fuel location, which is a critical parameter for gasoline direct injection engine operation, although for early injection stratified charge strategies where fuel direction is most crucial, in-cylinder turbulence would be expected to be at its lowest intensity.

This initial assessment also shows that the droplet size of the spray is not only critical to ensuring spray momentum, but also has a significant bearing on the rate of combustion and hence engine performance and emissions. Of course, the spray break-up and fuel vaporisation rate and resulting droplet size are not the only factors affecting the subsequent combustion event, and it has been shown that the intensity and length scale of localised turbulence greatly affects local droplet and fuel vapour concentrations, which affect the flame stability. The turbulent gas motion has also been shown to affect the flame propagation rate, by causing instabilities on the flame front which act to accelerate its burning rate. Although this aspect of the work is not intended to be a

comprehensive assessment, it shows the importance of turbulence in interacting with both the fuel spray itself and its subsequent combustion, and hence for it to be a major influence on engine performance.

9 Conclusions and Further Work

9.1 Factors Affecting Multihole Fuel Spray Development

This work makes its contribution to the prior state of knowledge by quantifying key spray break-up parameters in relation to the fuel properties, and by linking together the physical interactions in a logical sequential manner to provide an evidenced assessment of how those factors which affect spray development do so. The summary below sets out each of the factors examined and summarises their effect on the spray development as applicable to the multihole fuel spray on which this work is based. Prior to summarising these factors, consideration should be given to how the factors interact, as it is through this series of interactions that the overall spray form is produced.

The functional relationship between each of the factors is depicted schematically in Figure 9-1. Note that this hierarchy is intended to be a generic overview of the linkages, and hence that the specifics of each of the parameters (*e.g.* location of "droplet size") are not referred to, although the magnitude and nature of each of the parameters is highly dependant on such specific references as regards their affect on the spray. The linkages shown in Figure 9-1 also show that each factor is ultimately the results of a "design parameter", where this term has been used in reference to those aspects which are influenced by the design of the engine hardware or fuel blend. This is not to say that each of these parameters can be precisely controlled (*e.g.* turbulent eddy location) or can be altered without sacrifice to other factors affecting engine performance (*e.g.* gas pressure), but that these are (as suggested by this work) the fundamental parameters which ultimately lead to variations in the fuel spray formation in an engine.

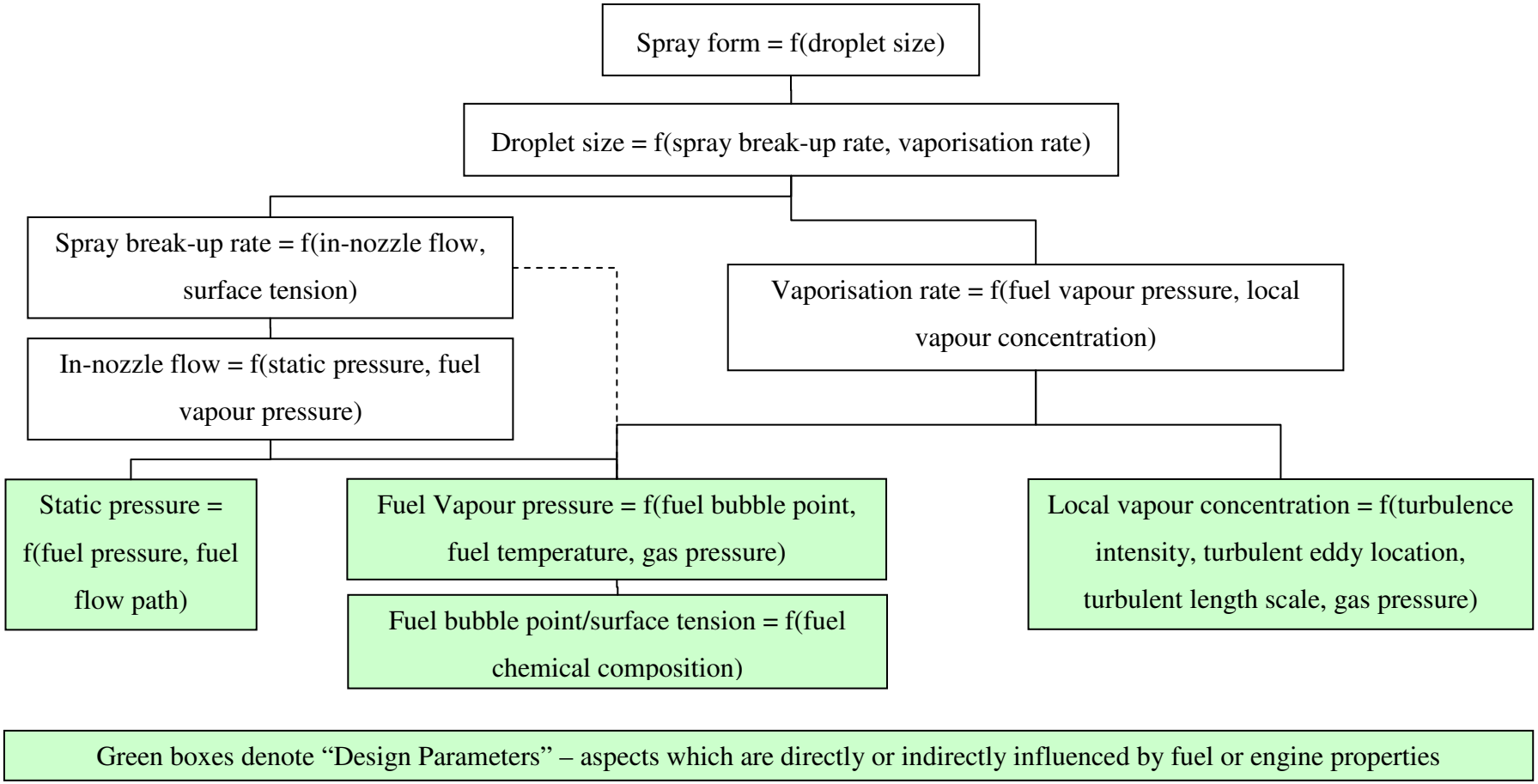

Figure 9-1 Functional Relationships between Factors Affecting Spray Development

This work has shown that the factors which affect the spray development initiate inside the injector nozzle. Starting in the injector nozzle, the sections below list the principal conclusions which may be drawn from this work on how these factors interact to affect the spray development.

9.1.1 In-Nozzle Flow

- Even at the highest gas pressure and lowest fuel temperature conditions examined in this work, the calculated Cavitation Number of 2.0 was above quoted critical values of 0.5 to 0.75, above which cavitation occurs.
- Imaging of the fuel flow in a real size optically accessible nozzle showed the fuel flow in the nozzle to be cavitating under all tested conditions.
- The larger the degree of liquid fuel superheat in the injector nozzle, the greater the extent of cavitation present in the nozzle.
- Cavitation voids imaged at the nozzle exit were seen to lead to a more disperse spray form.
- The in-nozzle flow regime of Standard Gasoline was observed to more sensitive to changes in fuel temperature than *iso*-Octane, illustrating the effect of the vapour pressure in determining the amount of cavitation present in the injector nozzle.
- The critical level of cavitation to induce spray collapse was observed to occur when the gas pressure was order of 10 below the fuel's bubble point.

9.1.2 Spray Break-Up

- The surface tension should be considered a critical parameter in determining the rate of spray break-up as it defines the surface energy necessary for bubbles to grow and break-up the spray into smaller ligaments and droplets.
- High speed near-nozzle imaging showed an initial similar well defined spray structure for all fuels under all conditions, even for those which in the subsequent frame showed the characteristics of a collapsed spray.
- Spontaneous and complete vaporisation of the fuel spray was not observed under any conditions.
- When "flash boiling" starts to occur, the vaporisation process takes heat away from the liquid and reduces its temperature, which in turn reduces the rate of liquid boiling and the establishment of new nucleation sites, inhibiting further "flash boiling.

- The level of liquid superheat in the injector nozzle is the thermodynamic driving force and as such determines the time taken for the spray to flash as it equilibrates
- For this work, a timescale in the order of 20 μs appeared to be one of the determining factors for the system to start to develop towards equilibrium conditions between the liquid fuel and surrounding gas.
- The time requirement for the establishment of equilibrium conditions leads to the existence of an external spray break-up length.

9.1.3 Spray Formation

- At high fuel temperatures and low gas pressures (*i.e.* high liquid superheat), the spray converges and ultimately collapses as a result of the movement of the atomised and vaporised fuel towards low pressure region between the high velocity spray plumes.
- Once the droplets are reduced to a size below a certain critical diameter (nominally ~12 μm SMD, 19 mm downstream of the injector nozzle for the injector used for this work), their momentum along the spray plume trajectory is diminished to the extent that they are drawn into the low pressure region in the centre of the spray, and their migration to this region acts to draw the plumes together.
- This effect increases up to the point where the spray becomes fully collapsed.
- Due to the extent of superheat driving the break-up rate, the break-up of multi-component fuel sprays such as those of commercial gasolines are driven by the superheat of the high volatility, low boiling point fractions.
- Multi-component fuel behaviour should not be approximated to a single component fuel unless a comprehensive sensitivity study has been previously carried out that justifies such an action.
- Using fluid properties that are closer to *n*-Pentane than *iso*-Octane would result in better accuracy when modelling real gasoline fuel injection processes.

9.1.4 Effect of Gas Turbulence

- The interaction of the fuel spray with gas turbulence plays an important and significant role in the spray's development.

- The turbulent gas motion acts to affect the concentration of droplets and fuel vapour at the spray periphery, which in turn affect the local vaporisation rate through limiting the local concentration gradient.
- Alteration of the vaporisation rate from that observed under quiescent gas conditions act to alter the physical spray form in terms of penetration length and convergence.

9.1.5 Biogenic Fuels

- The lower vapour pressure of Ethanol at 20 °C as compared to Standard Gasoline indicates that cavitation and the break-up rate are les severe with Ethanol.
- Sprays produced by Ethanol are similar to those using Standard Gasoline at high injector body (fuel) temperatures.
- Ethanol sprays mimic those of *iso*-Octane at low injector body temperatures.
- Sprays produced by Butanol reflect those produced by *iso*-Octane across the tested fuel temperature range.
- The similarity of spray behaviour between Ethanol and Standard Gasoline at engine operational temperatures suggest that the in-cylinder mixing will not be greatly affected.
- The lower specific energy content of Ethanol and its high viscosity relative to gasoline has implications for the injection duration and timing requirements to ensure the full mixing of the fuel prior to ignition.

9.2 Further Work

This work has used a number of techniques to examine the spray development using a range of fuels under different operating conditions. Whilst the work provides an overview of the principle mechanisms at each stage of spray development, the number of variables examined has precluded a highly detailed investigation of a more limited parameter space. Such an investigation would be expected to yield both theoretically and empirically derived relationships between pertinent physical quantities and reference values which would allow for the incorporation of these relationships into ever more comprehensive computer based models of spray development and break-up. Investigations of this nature may be recommended in a number of areas which the present work has identified as having a significant impact on the spray formation, but for which these relationships do not yet exist. Furthermore, the ongoing development of

sustainable automotive fuels will require future engines to be able to operate robustly on these fuels.

9.2.1 Investigation of Biogenic Fuels

Increasing environmental and fossil fuel availability concerns are driving interest in, and market uptake of, biogenically derived fuels. These drivers have led to the development of a range of biogenic fuels from various organic sources. In relation to compression ignition fuels, the range of fuels under development is illustrated by a recent call for project proposals by the Energy technologies institute, which is backed by the fuel producers BP and Shell, stating:

> *"There are currently a number of pathways to liquid diesel bio-fuels under exploration with no clear winners arising yet."*
> *(Energy Technologies Institute Website, [2010])*

A similar number of pathways and resulting bio-fuels are also under development in relation to spark-ignition fuels, as illustrated by the development of a "bio-gasoline" by Virent working with Shell (Virent Website, [2010]). Each of these fuels may be expected to have different physical and chemical properties, which in turn will affect their in-engine spray development and combustion characteristics. While there is some research being carried out into the spray and engine performance with these fuels, such as that being conducted by the University of Birmingham into the use of DMF (2.5-Dymethylfuran) (New Energy and Fuel, [2010]), the wide range of these fuels means that there is much research still to be conducted to identify those fuels which have the lowest life-cycle impacts, in terms of environmental emissions as well as engine development requirements to enable their sustained market uptake. As has been shown in this work, the different chemical composition and structure of these fuels is manifest in their different physical properties, which alter the fluid dynamics relative to fossil derived petroleum fuels. Hence, a deeper understanding of the effect in altering the transport properties and hence fluid dynamics and spray development of biogenically derived sustainable fuels, on their own and in blends of various ratios with fossil fuels, is required to be developed by the industry to enable these fuels to be successfully utilised and their benefits to be realised.

9.2.2 In-Nozzle Fuel Flow Visualisation

Visualisation and characterisation of the fuel flow in the real-size nozzle presents a number of areas worthy of further investigation in order to build a more comprehensive understanding of how the in-nozzle flow develops and influences the spray characteristics downstream.

Studies of in-nozzle flow have to date been limited to those of steady of quasi-steady state flow due to difficulties in repeatedly seating the pintle to seal the injector holes in the transparent materials of which optical nozzles have been made. Research and industry interest in the use of multiple injection events for charge establishment to aid mixing, such as those detailed by Serras- Pereira *et al*. [2007b] and Rimmer *et al*. [2009], mean an increasing proportion of the fuel will be injected under transient flow condition (i.e. dynamically changing nozzle inlet conditions). By developing the design of optical nozzles (*e.g*. through the insertion of a small metallic pintle seat in transparent nozzle to enable repeatable nozzle sealing), investigation of the fuel flow and establishment and break-down of cavitation structures may be possible. Considering the effect of cavitation on breaking-up the liquid spray in combination with the effect of liquid volumes present during combustion on engine emissions, particularly those of particulates and unburned hydrocarbons, understanding the rate of establishment and suppression of cavitating structures will be a key enabler in the optimisation of injection strategies and injector design.

The establishment and extent of in-nozzle cavitation could be examined in detail using a high resolution Particle Image Velocimetry (PIV) system in association with a suitably designed optical nozzle. Walther *et al*. [2000] showed the potential to carry out PIV in real size single and multi hole optical nozzles, and similar methodologies should be applied to a wide range of fuels over conditions representative on engine operation. Additionally, the PIV technique has latterly been developed to enable multiple images to be captured of the same injection event ("high speed PIV"). To date this technique has not yet been applied to the flow inside the injector nozzle. Characterising the in-nozzle flow using high speed PIV would enable investigation into the transient flow inside the nozzle, including the establishment of cavitation features.

While such an investigation would develop the understanding of the factors affecting the onset and extent of cavitation, the question would remain whether in-nozzle

cavitation is desirable or not. While cavitation brings about spray break-up and disintegration, it also limits the fuel flow rate. Combined with the demands places on the spray, particularly for spray guided late injection stratified charge operation, a fine balance between the benefits and drawbacks of cavitation emerges. Whether there is a particular 'optimum' level of cavitation which is sufficient to trigger the rapid disintegration of the spray at low and high temperatures is something that would need to be further investigated. Such a strategy would have to be carefully managed as excessive cavitation can limit the nozzle flow rate, which could have implications for biogenically derived fuels which have lower specific energy densities (due to the presence of oxygen in the fuel molecules), and hence already require longer injection pulse widths to bring about stoichiometry. Observations of the tested fuels suggest that levels of superheat of the fuel components contribute more towards the rapid jet disintegration and atomisation than levels of cavitation in isolation. It would therefore be interesting to reproduce the results presented in this work in a similar but non-cavitating nozzle in order to fully decouple the effects of cavitation and flash-boiling on spray formation. Whether this is possible while maintaining the same Reynolds Number would require further investigation, possibly by using rounded inlet holes or conical hole geometries in order to suppress cavitation at these conditions.

9.2.3 Spray Interaction with In-Cylinder Gas Turbulence

The interaction of the spray with any in-cylinder turbulent gas motion is critical for the prediction of in-cylinder spray convection and evaporation. However, despite the importance of the fuel/air motion interaction, Jakubik *et al.* [2006] note that the effect of ambient turbulence on the spray structure is not currently well understood. Exceptions of note are Beard *et al.* [1994] who report a strong dependency of individual droplet trajectories on the large scale vortex dynamics in two phase flows, and Wark *et al.* [2000] who confirmed the presence of droplet clusters at the spray boundary and their dependence o the air flow turbulence. Sornek *et al.* [2000] report a considerable qualitative change in the size and spatial distribution of the droplet clusters that were present inside the spray under different turbulence conditions, and also quantified the droplet-turbulence interactions by means of the centrifugal Stokes Number. The small number of experimental results collected for the present work appear to confirm an effect of turbulent gas motion in affecting the vaporisation rate, although the limited number of experiments conducted into this phenomena prevent any in-depth analysis of the mechanisms at work. However, considering the implications of the turbulence

intensity with respect to the air and fuel mixing rate and hence engine performance, it would seem that this area would benefit from further investigation.

One technique which could be applied to capture both the liquid and gas body motion simultaneously is Two Phase PIV applied downstream of the injector nozzle. In this technique, laser light of two different wavelengths (from two lasers or frequency shifting part of a split beam) is used to illuminate the area of interest containing both liquid and gas regions. Each of these fluids (phases) is separately doped with a different suitable media which is excited by the selected light wavelengths. The luminescence generated by the excited dopants can then be detected using a camera (one camera per frequency or split image capture using a single camera), using appropriate light frequency filtration to differentiate the luminescence from each doped phase.

Although the two phase PIV technique has been demonstrated, it has not to date been applied in conjunction with in-nozzle PIV imaging. If applied together over the same injection event, two phase PIV with in-nozzle high speed PIV would have the potential to present an extremely high resolution and comprehensive picture of the spray development. This is likely to vary considerably for different gas pressures in combination with different fuel properties, and hence has implications for different in-engine charge establishment strategies and for emissions with regard to large droplet formation at the end of the injection event. The use of Two Phase PIV in turbulent gas fields would add considerably to the volume of knowledge of how and the extent to which turbulence affect droplet transportation, clustering and vaporisation. Each of these elements have a large bearing on the subsequent charge mixing and location, and hence combustion event, and so a further investigation into these interactions would be highly valuable in developing the knowledge on the factors affecting both spray development and combustion variability

9.2.4 Fuel Spray Vaporisation Rate

In terms of engine operation, one of the key parameters affecting the combustion rate is the mixing and location of vaporised fuel. This is especially the case for gasoline direct injection engines under both homogeneous and stratified charge operation, where the location and concentration of fuel vapour are also desired to be controlled temporally. However, the direct measurement of the vaporisation rate of a dynamic liquid body, such as a fuel spray, would appear conceptually very difficult. It may be possible to

measure the vaporisation rate using Schlieren imaging to quantify the volume of vapour produced in two dimensions. However, the temporal resolution and 3-dimensional extrapolation of data acquired from such images would require careful consideration. The use of a Schlieren imaging based technique would have the advantage of visually capturing the spatial distribution and transportation of the vaporised fuel, especially if used in conjunction with a dynamic gaseous flow field representative of the engine-in-cylinder gas motion.

A second order measurement which may be used to derive the vaporised fuel volume and hence rate would be the measurement of drop sizes downstream of the spray break-up. In order to capture the variations in spatial distribution of different sized drops, a point based drop-sizing technique would be appropriate for use, such as Phase Doppler Anemometry. To build a complete picture of both the spatial and temporal development of the spray droplets, the drop-sizing technique would be best applied in a systematic three dimensional grid of measurement points located in and around the spray. Careful consideration would have to be given to the location of measurement locations to ensure adequate light penetration to establish and detect the measurement location at all points, especially for dense or multihole sprays. If used in conjunction with spray imaging and PIV data relating to the liquid droplets, a very comprehensive picture of spray development and vaporisation could be assembled.

In order to be able to use the drop size data to quantify the vaporised fuel volume and rate, accurate knowledge of the temporal fuel volume injection rate would also be required to be known, possibly for each individual spray plume for multihole type injectors. Although the measurement of this flow rate may appear trivial, the in-nozzle fluid dynamics with respect to a moving pintle and alterations in the fuel volume distribution between holes with different turning angles suggest that establishing and carrying out a robust fuel volume flow rate measurement technique is a worthy investigation in its own right.

9.3 Summary

In linking together and individually detailing the factors affecting the development of atomising sprays produced by multihole injectors for direct-injection spark-ignition (also known as gasoline direct injection) engine applications, this work has for the first time shown how the fuel properties and operational parameters relating to temperatures,

pressures and other external effects (*e.g.* injector design, gas motion) interact to generate the final spray form observed. As has been illustrated, this spray form and hence these interactions and their underlying mechanisms, which this work has also investigated, have important implications for the performance and emissions of internal combustion engines. In light of ever increasing commercial and legislative drivers for more efficient and lower emissions engines, knowledge of those parameters which may be controlled to indirectly control the fuel spray will better enable the engineering community to manipulate them through engine and fuel chemistry design for the continuation of affordable and convenient automotive transportation.

10 References

Aleiferis, P.G., Malcolm, J.S., Todd, A.R., Cairns, A. and Hoffmann, H., [2008] – "An Optical Study of Spray Development and Combustion of Ethanol, Iso-Octane and Gasoline in a DISI Engine", SAE Paper 2008-01-0073.

Aleiferis P.G., Taylor A.M.K.P., Ishii K., Urata Y. [2004] "The Relative Effects of Fuel Concentration, residual-Gas Fraction, Gas Motion, Spark Energy and Heat Losses to the Electrodes on Flame-Kernel Development in a Lean-Burn Spark Ignition Engine" Proceedings of the Institute of Mechanical Engineers, Journal of Automobile Engineering, Vol 218 Part D, 2004.

Aleiferis P.G. [2004] – "Flame Chemiluminescence studies of cyclic combustion variations and air-to-fuel ratio of the reacting mixture in a lean-burn stratified-charge spark-ignition engine" Combustion and Flame Vol. 136, pp. 72-90.

Aleiferis, P.G., Hardalupas, Y., Kolokotronis, D., Taylor, A.M.K.P., Arioka, A. and Saito, M., [2006] – "Experimental Investigation of the Internal Flow Field of a Gasoline Model Injector Using Micro-PIV", SAE Transactions, Journal of Fuels and Lubricants, Vol. 15, No. 4, pp. 597–606, Paper 2006-01-3374, 2006.

Aleiferis, P.G., Hardalupas, Y., Kolokotronis, D., Taylor, A.M.K.P. & Kimura, T., [2007a] – "Investigation of the Internal Flow Field of a Diesel Model Injector Using PIV and CFD", SAE Paper 2007-01-1897.

Aleiferis P.G., Serras-Pereira J., van Romunde R.Z., Richardson D., Wallace S., Cracknell R.F., Walmsley H.L. [2007b] – "Optical Studies of Spray Development in a Quiescent Chamber and in a Direct-Injection Spark-Ignition Engine." International Conference on Internal Combustion Engines: Performance, Fuel Economy and Emissions, Institution of Mechanical Engineers, pp. 3–13.

Aleiferis P., Serras-Pereira J., van Romunde Z., Caine J., Wirth M. [2010] – "Mechanisms of Spray Formation and Combustion from a Multi-Hole Injector with E85 and Gasoline", Combustion and Flame, Vol. 157, pp. 735–756.

Allen, J. and Hargrave, G., [2000] – "Fundamental Study of In-Nozzle Fluid Flow and its Effect on Liquid Jet Break-up in Gasoline Direct Injectors", Proceedings of ILASS-Europe, Darmstadt, Germany.

Allen, J., Hargrave, G.K. and Khoo, [2003] – Y.C., "In-Nozzle and Spray Diagnostic Techniques for Real Sized Pressure Swirl and Plain Orifice Gasoline Direct Injectors, SAE Paper 2003-01-3151.

Araneo L., Coghe A., Brunello G., Donde, R. [2000] "Effects of Fuel Temperature and Ambient Pressure on a GDI Swirled Injector Spray", SAE Paper 2000-01-1901.

Arcoumanis C., Flora H., Gavaises M. and Badami M. [2000] – "Cavitation in Real-Size Multi-Hole Diesel Injector Nozzles", SAE Paper 2000-01-1249.

Bachalo W.D., [1995] – "Spray Diagnostic techniques and the Application to the study of Spray interactions with Turbulent Flows" *Mechanics and Combustion of Droplets and Sprays*, Chiu H.H. and Chigier N. eds, Chap.4, pp. 297 – 327, Begell House, New York.

Badock C., Wirth R., Fath A. and Leipertz A. [1999] – "Investigation of Cavitation in Real Size Diesel Injection Nozzles", International Journal of Heat and Fluid Flow, Vol. 20, pp. 538–544.

Balabin, R.M., Syunyaev, R.Z. and Karpov, S.A., [2007] – "Quantitative Measurement of Ethanol Distribution over Fractions of Ethanol-Gasoline Fuel", Energy and Fuels, Vol. 21, pp. 2460–2465.

Baumgarten C., [2006] – "Mixture Formation in Internal Combustion Engines," Springer Verlag, Berlin, ISBN 3-540-30835-0

Baz I., Champoussin J-C., Lance M. and Marié J-L. [2002] – "Investigation of the Cavitation in High Pressure Diesel Injection Nozzles", Proc. ASME FEDSM'02, pp. 425–429, Montreal, Canada.

Beard P.J., Bissieres D., Lavregne G.D., Rompteaux A.A., [1994] – "Experimental and Numerical Studies of Droplet Turbulent Dispersion in Two-Phase Flows" *Numer. Methods Multiphase Flows*, vol. 185, pp 15-22.

Bergwerk W. [1959] – "Flow Pattern in Diesel Nozzle Spray Holes", Proc. Institution of Mechanical Engineers, Vol. 173, No. 25, pp. 655–660.

Bianco, Y., Cheng, W.K., Heywood, J.B. [1991] – "The Effects of Initial Flame Kernel Conditions on Flame Development in SI Engine" SAE Paper 912402.

Bradley D., Haq M.Z., Hicks R.A., Kitagawa T., Lawes M., Sheppard C.G.W., Woolley R. [2003] – "Turbulent Burning Velocity, burned Gas Distribution and Associated Flame Surface Definition", Combustion and Flame, Volume 133, Number 4, pp. 415-430.

Brown R., York., J.L., [1962] – "Sprays Formed By Flashing Liquid Jets" A.I.Ch.E. Journal, vol. 8, No. 2, pp. 149-153.

Chaves, H., Knapp, M., Kubitzek, A., Obermeier, F. & Schneider, T., [1995] – "Experimental Study of Cavitation in the Nozzle Hole of Diesel Injectors Using Transparent Nozzles", SAE Paper 950290,

Chaves H., Shuhbauer I. [2006] – "Cavitation in an Asymmetric Transparent Real Size VCO Nozzle" Proc Spray'06, Raumm Heilbronn, Germany.

Chehroudi B., Chen S.H., Bracco F.V, Onuma Y., [1985] – "On the Intact Core of Full-Cone Sprays" SAE Paper 850126.

Chen T-F., Davis J.R., [1964] – "Disintegration of a Turbulent Water Jet", Proceedings of the American Society of Civil Engineering, Journal of Hydrodynamics Division, Vol. 1, pp. 175-206.

Chigier N.A., Reitz R.D., [1996] – "Regimes of Jet Breakup and Breakup Mechanisms", in Kuo K (Ed.), Progress in Astronautics and Aeronautics, American Institute of Astronautics and Aeronautics, Reston, VA, Vol. 1, pp.109-136.

Dan T., Takagashi S., Senda J., Fujimoto H., [1997] – "Organised Structure and Motion in Diesel Sprays", SAE Paper 970641.

Davy, M.H., Williams, P.A. and Anderson, R.W., [2000] – "Effect of Fuel Composition on Mixture Formation in a Firing Direct Injection Spark Ignition (DISI) Engine: An Experimental Study using Mie-Scattering and Planar Laser-Induced Fluorescence (PLIF) Techniques", SAE Paper 2000-01-1904.

Dumouchel C., [2008] – "On the Experimental Investigation on Primary Atomisation of Liquid Streams" Exp Fluids, vol. 45, pp. 371-422.

Efthymiou E. [2004] – "Numerical Modelling of the Flow and Cavitation inside Automobile Injectors", MSc Thesis, UCL.

Energy Technologies Institute Website – [22/11/2010] http://www.energytechnologies.co.uk/Home/Technology-Programmes/Bio-Energy.aspx

Faeth G.M., Hsiang L.P., WuP.K., [1995] – "Structure and Break-up Properties of Sprays", International Journal of Multiphase Flow, Vol. 21, Suppl., pp. 99-127.

Ganippa L.C., Bark G., Andersson S., Chomiak J. [2001] – "Comparison of Cavitation Phenomena in Transparent Scaled-up Single Hole Diesel Nozzles" CAV 2001: Sessions A9.005, California.

Gilles-Birth I., Bernhardt S., Spicher U., Rechs M. [2005] – "A Study of the In-Nozzle Flow Characterisitics of Valve-Covered Orifice Nozzles for Gasoline Direct injection" SAE Paper 2005-01-3684.

Gilles-Birth I.., Rechs M., Spicher U., Bernhardt S. [2006] – "Experimental Investigation of the In-Nozzle Flow of Valve Covered Orifice Nozzles for Gasoline Direct Injection," Proc. of 7th International Symposium on Internal Combustion Diagnostics, pp. 59–78, AVL, ISBN 00-3-00-018208-X.

Global Renewable Fuels Alliance, Press Release. 21st March 2010, http://www.globalrfa.org/pr_032110.php. Accessed 02/08/2010

Grant R.P., Middleman S., [1966] – "Newtonian Jet Stability", A.I.Ch.E. Journal, Vol. 12, pp. 669 – 678.

Grimaldi C.N., Postrioti L., Stan C., Tröger R. [2000] – "Analysis Method for the Spray Characteristics of a GDI System with High Pressure Modulation", Sae Paper 2000-01-1043.

Gülder Ö.L., Smallwood G.J., Snelling D.R., [1992] – "Diesel Spray Structure Investigation by Laser Diffraction and Sheet Illumination" SAE Paper 920577.

Gülder Ö.L., Smallwood G.J., Snelling D.R., [1994] – "Internal Structure of Transient Full-Cone Dense Diesel Sprays" Commodia 94, pp 355-360.

Haenlein A., [1932] – "Disintegration of a Liquid Jet" National Advisory Committee for Aeronautics, Technical Memorandum 659.

Hirleman E.D., Bachalo W.D., Felton P.G., [1990] –"Liquid Particle Size Measurement Techniques" ASTM International, ISBN-10: 0803114591

Hiroyasu, H., Arai, M. and Tabata, M., [1989] – "Empirical Equations for the Sauter Mean Diameter of a Diesel Spray", SAE Paper 890464.

Hiroyasu, H. and Arai, M., [1990] – "Structure of Fuel Sprays in Diesel Engines", SAE Paper 900475.

Hiroyasu H., Shimizu M., Arai M [1991] – "Break-Up Length of a Liquid Jet and Internal Flow in a Nozzle" ICLASS-91.

Hiroyasu, H., [1998] – "The Structure of Fuel Sprays and the Combustion Processes in Diesel Engines", ASME 1998 Fall Technical Conference, Paper No. 98-ICE-117, ICE-Vol. 31-1, pp. 3-15.

Hiroyasu H., [2000] – "Spray Break-up Mechanism from the Hole-Type Nozzle and its Applications", Atomisation and Sprays, Vol. 10, pp.S253-S257.

Hochgreb S., van der Wege B.A. [2000] "The Effect of Fuel Volatility on Early Spray Development from High-Pressure Swirl Injectors", *Proc. Of International Congress on Direkteinspritzung im Ottomotor II (Gasoline Direct Injection Engines)*, 16-17 November, Munich, Germany, pp. 110-135, Ed. Spicher, U.A., Expert-Verlag, ISBN 3-8169-1822-0.

Honda T., Kawamoto M., Katashiba H., Sumida M., Fukutomi N., Kawajiri K. [2004] – "A Study of Mixture Formation and Combustion for Spray Guided DISI", SAE Paper 2004-01-0046.

Hu L., Ruiz F., [1995] – "Effect of Cavitation on Flow and Turbulence in Plain Orifices for High Speed Atomisation." Atomisation and Sprays, Vol 5, pp 569-584.

Hung D.L.S., Chimiel D.M., Markle L.E. [2003] – "Application of an Imaging-based Diagnostic Technique to Quantify the Fuel Spray Variations in a Direct-Injection Spark-Ignition Engine", SAE Paper 2003-01-0062.

Hwang S.S., Liu Z., Reitz R.D., [1996] – "Break-up Mechanisms and Drag Coefficients of High Speed Vapourising Liquid Drops." Atomisation and Sprays, vol. 6, pp 353-376.

Hyun K.S., Chang S.L. [2008] – "Effect of Cavitation in Nozzle Orifice on the Diesel Fuel Atomisation Characteristics." International Journal of Heat and Fluid Flow, Vol. 29, No. 4, pp 1001-1009.

Ipp W., Wagner V., Krämer H., Wensing M., Leipertz A., Arndt S., Jain A., [1999] – "Spray Formation of High Pressure Swirl Gasoline Injectors Investigated by Two-Dimensional Mie and LIEF Techniques" SAE Paper 1999-01-0498.

Iwamoto Y., Noma K., Nakayama O., Yamauchi T., Ando H. [1997] – "Development of Gasoline Direct Injection Engine" SAE Paper 970541.

Jakubik T, Lawes M., Woolley R., Jicha M. [2006] – "Study of Ambient Turbulence Effects on Diesel Sprays in a Fan-Stirred Vessel" Atomization and Sprays, vol. 16, oo 687 – 703.

Jarvis, S., Justham, T., Clarke, A., Garner, C.P., Hargrave, G.K. and Richardson, D., [2006] – "Motored SI IC Engine In-Cylinder Flow Field Measurement Using time Resolved Digital PIV for Characterisation of Cyclic Variation", SAE Paper 2006-01-1044.

Johansson, B. [1991] – "Influence of the Velocity near the Spark Plug on Early Flame Development" SAE Paper 930481, 1991.

Justham, T., "Cyclic Variability of Engine Intake and In-Cylinder Flows" PhD Thesis, Loughborough University, Wolfson School of Mechanical and Manufacturing Engineering, UK, in Preparation, 2009.

Kashdan, J.T., Shrimpton, J.S. and Acroumanis, C. [2002] – "Dynamic Structure of Direct Injection Gasoline Engine Sprays: Air Flow and Density Effects", Atomization and Sprays, Vol. 12, pp. 539–557.

Kaye, G.W.C., Laby, T.H., [1995] – "Tables of Physical and Chemical Constants", 16th Ed., Longman.

Kenneth, K., Last, T., Haywood, C. and Raine, R.R. [2008] – "Measurement of Vapour Pressures and Enthalpies of Vaporisation of Gasoline and Ethanol Blends and Their Effects on Mixture Preparation in an SI Engine", SAE Paper 2008-01-0317.

Khoo, Y.C. and Hargrave, G.K., [2006] – "Real-Sized Pressure Swirl GDI Injector Investigation with HSFV and FPIV", Journal of Physics: Conference Series, Vol. 45, pp. 77–84, 2nd ICOLAD.

Kolokotronis D. [2007] – "Experimental Investigation of the Internal Flow Field of Model Fuel Injectors", PhD Thesis, University of London

von Kuensberg Sarre C, Kong S.C., Reitz R.D., [1999] – "Modelling the Effects of Injector Nozzle Geometry on Diesel Sprays." SAE Paper 1999-01-0912

Laoonual Y., Youle A.J., Walmsley S.J., [2001] "Internal Fluid Flow and Spray Visualisation for a Large Scale Valve Covered Orifice (VCO) injector Nozzle" ILASS-Europe

Lawes M., Sulaiman S.A., Wooley R., [2006] –"Effect of Droplets on the Flame Speed ff Laminar iso-Octane and Air Aerosols", ICLASS 2006, Kyoto, Japan. Paper ID ICLASS06-258.

Lawes, M. [2008] Doctorate of Combustion and Energy, University of Leeds. Personal Communication.

Lefebvre A.H. [1989] – "Atomisation and Sprays," Hemisphere Publishing Company, New York. ISBN 0-89116-603-3.

Lemmon E.W., McLinden M.O. and Friend D.G. – [2005] "Thermophysical Properties of Fluid Systems" in NIST Chemistry WebBook, NIST Standard Reference Database Number 69, Eds. P.J. Linstrom and W.G. Mallard, June 2005, National Institute of Standards and Technology, Gaithersburg MD, 20899 (http://webbook.nist.gov).

Lide D.R. [2007] – "CRC Handbook of Chemistry and Physics". 88th Edition. CRC Press, Boca Raton, Florida, USA. ISBN 0-8493-0488-1.

Lienhard J.H., [1966] – "An Influence of Sperheat Upon the Spray Configurations of Superheated Liquid Jets" Journal of Basic Engineering, Trans. ASME vol. 88, Series D, pp. 685-687.

Lienhard J.H., Day J.B., [1970] – "The Breakup of Liquid Jets" Journal of Basic Engineering, Trans. ASME vol. 92, Series D, pp. 515-521.

Liggett J.A., [1994] – "Fluid Mechanics," McGraw-Hill, International Edition. ISBN 0-07-113449-2.

Lousalan P., [2004] PhD Thesis, University College London.

Loustalan P.W., Davey M.H., Williams P.A. [2003] – "Experimental Investigation into the Liquid Sheet Break-Up of High-Pressure DISI Swirl Atomizers", SAE Paper 2003-01-3102.

Marriott C.D., Wiles M., Gwidt M., Parrish S.E., [2002] – "Development of a Naturally Aspirated Spark Ignition Direct Injected Flex Fuel Engine" SEA Paper 2008-01-0319.

Mitroglou N., Nouri J.M., Gavaises M., Acroumanis C. [2006] – "spray Characteristics of a Multi-Hole Injector for Direct-Injection Gasoline Engines", International Journal of Engine Research, vol. 7, pp. 255-270.

Mitroglou N., Nouri J.M., Acroumanis C. [2009] – "In-nozzle Cavitating flow and ambient temperature effects in high-pressure multi hole gasoline sprays" City University, London.

Moon, S., Choi, J., Abo-Serie, E. and Bae, C. [2005] – "The Effects of Injector Temperature on Spray and Combustion Characteristics in a Single-Cylinder DISI Engine", SAE Paper 2005-01-0101.

Moon S., Bae C., Abo-Serie E.F., Choi J. [2007] – "Internal and Near-Nozzle Flow of a Pressure-Swirl Atomizer Under Varied Fuel Temperature" Atomization and Sprays, vol. 17, pp 1-22.

New Energy and Fuel Website, [22/11/2010] – http://newenergyandfuel.com/http:/newenergyandfuel/com/2010/05/24/get-ready-for-some-dmf/

Neyfey A.H., [1968] – "Non Linear Stability of a Liquid Jet" physics of Fluids, Vol. 13, No. 4, pp 841-847.

Nouri J.M., Mitroglou N., Yan Y., Arcoumanis C., [2007] – "Internal Flow and Cavitation in a Multi-hole Injector for Gasoline Direct-Injection Engines" SAE Paper 2007-01-1405.

Nwagwe I.K., Weller H.G., Tabor G.R., Gosman A.D., Lawes M., Sheppard C.W.G., Woolley R., [2000] – "Measurements and Large Eddy Simulations of Turbulent Premixed Flame Kernel Growth" *Proc. Combust. Inst*., vol. 28, pp 59-65.

Ohnesorge W., [1931] – "Die Bildung von Trpfen an Düsen und die Auflösung flüssiger Strahlen." Zeitschrift für Angewandtw Mathmatik und Mechanik, Bd. 16, Heft 6, pp 355-358.

Ortmann R. Arndt S., Raimann J., Grzeszik R., Würfel G. [2001] – "Methods and Analysis of Fuel Injection, Mixture Preparation and Charge Stratification in Different Direct Injected SI Engines, SAE Paper 2001-01-0970.

Pajot, O., Mounaim-Rousselle, C., Queiros-Conde, D. [2001] – "New Data on Flame Behaviour in Lean Burn S.I. Engine" SAE Paper 2001-01-1956.

Pitcher G., Wigley G., Saffman M [1990] – "Velocity and Drop Size Measurements in Fuel Sprays in a Direct Injection Diesel Engine". Particles and Particle Systems Characterisation, vol. 7, pp 160 – 168, Wiley InterScience.

Pitcher G., Wigley G., Saffman M. [1991] – "Sensitivity of Dropsize Measurements by Phase Doppler Anemometry to Refractive Index Changes in Combusting Fuel Sprays", Applications of Laser Techniques to Fluid Mechanics: 5th International Symposium, Lisbon, Portugal 9-12 July 1990, Eds. R.J. Adrian, D.F.G. Durao, F. Durst, M. Maeda and J.H. Whitelaw, (Springer Verlag, New York, 1991), 227-247.

Pontoppidan M. Gaviani G., Bella G., Demaio N. [2002] – "Study of the Benefits and Drawbacks of a Substantial Increase of Rail-Pressure in GDI-Injector Assemblies", SAE Paper 2002-01-1132.

Preussner C. Döring C., Fehler S., Kampmann S. [1998] – "GDI: Interaction Between Mixture Preparation, Combustion System and Injector Performance" SAE Paper 980498.

Rayleigh, Lord F.R.S. [1878] "On the Instability of Jets," *Proc. London Math. Soc.*, Vol. 10, pp4-13.

Redlich, O. and Kwong, J.N.S., [1949] – “Thermodynamics of Solutions: V. An Equation of State: Fugacities of Gaseous Solutions”, Chemical Reviews, Vol. 44, pp. 233–244.

Reitz, R.D. and Bracco, F.V., [1982] – “Mechanisms of Atomization of a Liquid Jet”, Physics of Fluids, Vol. 25, pp. 1730–42.

Reitz R.D. and Bracco F.V., [1986] – “Mechanisms of Breakup of Round Liquid Jets.” Encyclopaedia of Fluid Mechanics, Vol. 3, pp 233-249.

Rimmer J.E.T., Long E.J., Garner C.P., Hargrave G.K., Richardson D., Wallace S. [2009] – “The Influence of Single and Multiple Inejction Strategies on In-Cylinder Flow and Combustion within a DISI Engine” SAE Paper 2009-01-0660.

Rutland D.F., Jameson G.J., [1970] – “Theoretical Prediction of the Size of Drops Formed in the Breakup of Capillary Jets” Chem Eng Science, Vol. 25, p 1689.

Sallam K.A., Dai Z., Faeth G.M., [2002] – “Liquid Break-Up at the Surface of Turbulent round Liquid Jets in Still Gases”, international Journal of Multiphase Flow, vol. 28, pp. 427-449.

Schmidt D.P., Su T.F., Goney K.H., Farrell, P.V., Corradini. M.L., [1996] – "Detection of Cavitation in Fuel Injector Nozzles." Transport Phenomena in Combustion. Ed. S. H. Chan, Taylor and Francis.

Schmidt D.P., Corradini M.L, [2001] – “The Internal Flow of Diesel Fuel Injector Nozzles: A Review,” International Journal of Engine Research, Vol. 2, pp. 1–22.

Schwarzenbch, R.E., Gschwend, P.M., Imboden, D.M., [1993] – “Environmental Organic Chemistry”, John Wiley and Sons.

Serras-Pereira J., Aleiferis P.G., Richardson D., Wallace S. [2007a] – “Spray Development, Flow Interactions and Wall Impingement in a Direct-Injection Spark-Ignition Engine” SAE Paper 2007-01-2712

Serras-Pereira J., Aleiferis P.G., Richardson D., Wallace S. [2007b] – “Mixture Preparation and Combustion Variability in a Spray-Guided DISI Engine” SAE Paper 2007-01-4033

Serras-Pereira J., Aleiferis P.G., Richardson D., Wallace S. [2008] – "Characteristics of Ethanol, Butanol, Iso-Octane and Gasoline Sprays and Combustion from a Multi-Hole Injector in a DISI Engine" SAE Paper 2008-01-1591

Settles G.S., [2006] – "Schlieren and Shadowgraph Techniques" Springer Verlag, Berlin, ISBN 3-54066155-7.

Sheppard C.G.W., Progress Meeting of EPSRC/Jaguar/Shell "Sources of Cyclic Variability" Project Meeting, Leeds, 03/02/04.

Siebers D.L., [1998] – "Liquid Phase Fuel Penetration in Diesel Sprays" SAE Paper 980809.

Siebers D.L., [1999] – "Scaling Liquid-Phase Fuel Penetration in Diesel Sprays Based on Mixing-Limited Vaporisation" SAE Paper 1999-01-0528.

Silbey R.J., Alberty R.A., Bawendi M.G. [2005] – "Physical Chemistry", 4th Edition, J. Wiley & Sons, Inc, NJ. ISBN 0-471-21504-X.

Sornek R.J., Dobashi R., Hirano T., [2000] – "Effect of Turbulence on Vaporisation, Mixing and Combustion of Liquid Fuel Sprays" Combust. Flame, vol. 120, pp. 479 – 491.

Soteriou C., Andrews R., Smith M., [1995] – "Direct Injection Diesel Sprays and the Effect of Hydraulic Flip on Atomisation" SAE Paper 950080.

Soteriou, C., Andrews, R. & Smith, M., [1999] – "Further Studies of Cavitation and Atomization in Diesel Injection", SAE Paper 1999-01-1486.

Sou A., Hosokawa S., Tomiyama A., [2007] – "Effects of Cavitation in a Nozzle on Liquid Jet Atomisation", International Journal of Heat and Mass transfer, Vol. 50, pp. 3575-3582.

Speight J. [2005] –"Lange's Handbook of Chemistry", McGraw-Hill Professional; 16th edition, ISBN 0071432205.

Stevens, R.E., Ma, H. and Stone, C.R. [2006] "On Planar Laser-Induced Fluorescence with Multi-Component Fuel and Tracer Design for Quantitative Determination of Fuel Concentration in IC Engines", Proceedings of the Institution of Mechanical Engineers (IMechE), Part D, Journal of Automobile Engineering.

Suh H.K., Lee C.S., [2008] – "Effect of Cavitation in Nozzle Orifice on Diesel Fuel Atomization Characteristics", International Journal of Heat and Fluid Flow, vol. 29, pp. 1001-1009.

Viren Website [22/11/2010] – http://www.virent.com/News/press/03-23-10_Virent_and_Shell_Start_Worlds_First_Biogasoline_Demonstration_Plant.pdf

Walther, J., Schaller, J.K., Wirth, R. & Tropea, C., [2000] – "Characterisation of Cavitating Flow Fields in Transparent Diesel Injection Nozzles Using FPIV", ILASS-Europe, Darmstadt, Germany.

Walther, J., Schaller, J.K., Wirth, R. and Tropea, C., [2000b] – "Investigation of Internal Flow in Transparent Diesel Injection Nozzles using Fluorescent Particle Image Velocimetry (FPIV)", Proceedings of ICLASS, Pasadena, USA.

Wark C., Eickmann K., Richards C., [2000] – "The Structure of an Acoustically Forced, reacting Two-Phase Jet" *Cobust. Flame*, vol. 120, pp. 479-491.

van der Wege B.A., Hochgreb S. [2000] – "Effects of Fuel Volatility and Operating Conditions on Fuel Sprays in DISI Engines: (1) Imaging Investigation," SAE Paper 2000-01-0535.

van der Wege B.A., Hochgreb S. [2000, a] – "Effects of Fuel Volatility and Operating Conditions on Fuel Sprays in DISI Engines: (2) PDPA Investigation," SAE Paper 2000-01-0536.

van der Wege B.A., Lounsberry T.H., Hochgreb S. [2000, c] – " Numerical Modelling of Fuel Sprays in DISI Engines Under Early-Injection Operating Conditions", SAE Paper 2000-01-0273.

Wigley G., Goodwin M., Pitcher G., Blondel D., [2004] – "Imaging and PDA Analysis of a GDI Spray in the Near Nozzle Region" Experiments in Fluids, Vol. 36, No. 4, April 2004 , pp. 565-574(10)

Wigley G., Mehdi M., Williams M., Pitcher G., Helie J., [2006] – "The Effect of Fuel Properties on Liquid Breakup and Atomisation in GDI Sprays" ICLASS, Kyoto, Japan, ICLASS06-075.

Williams B., Ewart P., Stone R., Ma H., Walmsley H., Qiao J., Wallace S. [2008] – "Multi-Component Quantitative PLIF: Robust Engineering Measurements of Cyclic Variation in a Firing Spray-Guided Gasoline Direct Injection Engine" SAE Paper 2008-01-1073.

Wu P.K, Faeth G.M., [1993] – "Aerodynamic Effects on Primary Break-up of Turbulent Liquids", Atomisation and Sprays, Vol. 3, pp. 265-289.

Wu P.K., Miranda R.F., Faeth G.M., [1995] – "Effects of Initial Flow Conditions on Primary break-Up id Non Turbulent and Turbulent Round liquid jets", Atomisation and Sprays, vol. 5, pp. 175-196.

Yaws C.L., [2006] – "Yaws Handbook of Thermodynamic Properties of Hydrocarbons and Chemicals", Gulf Publishing Company, ISBN: 978-1933762074.

Yue Y., Powell C.F., Poola R., Wang J., Schaller j., [2001]- "Quantitative Measurements of Diesel Fuel Spray Characteristics in the near-Nozzle region using X-Ray Absorption", Atomisation and Sprays, Vol. 11, pp. 471-490.

Yuen M.C., [1968] – "Non Linear Capillary Instability of a Liquid Jet." J Fluid Mech, Vol. 33, p151.

Yule A.J., Salters D.G., [1994] – "A Conductivity Probe Technique for Investigating the Break-Up of Diesel Sprays" Atomisation and Sprays, Vol. 4, No. 1, pp 41-63.

Zigan L., Schmitz I., Flügel A., Wensing M., Leipertz A., [2009] – "Influence of Fuel Properties on Spray Formation and Evaporation Measured on a Piezoelectric Injector for the 2nd Generation Gasoline Direct Injection" Injection Systems for IC Engines Conference, IMechE, May 2009.